Synthesis and Characterization of $BiVO_4$-based photocatalysts

MENG Sopheak

Abstract

Solar energy is one of the most abundant resources on Earth. Utilizing this energy is the key for the future sustainable development. Photocatalytic technology is a technique that can harness such energy using a photocatalyst. It absorbs the photon of light to make various reactions, which are useful in a wide range of applications, such as water splitting (H_2 and O_2 generation), self-cleaning surface, air purification, and pollutant degradation. In recent years, $BiVO_4$ has emerged as a promising photocatalyst because it shares some similar advantages comparable to the traditional photocatalyst, TiO_2, including high chemical stability, low production cost, abundance, and non-toxicity. In addition to this, $BiVO_4$ possesses a narrow bandgap (~2.4 eV), which allows $BiVO_4$ to function in visible light region, unlike TiO_2 with a wide bandgap (3.2 eV), which can only absorb ultraviolet light. However, the photocatalytic activity of $BiVO_4$ is still considered to be low for commercial use. In this thesis, different techniques were used to enhance the photocatalytic activity of $BiVO_4$-based photocatalysts in organic pollutant degradation via controlling properties of $BiVO_4$ (morphology and bandgap) and incorporation with SnS_2.

The first approach began with KCl as a directing agent used in $BiVO_4$ precursor for hydrothermal method of $BiVO_4$. The result showed KCl concentration influenced the formation of BiOCl intermediate, crystal growth, and bandgap of $BiVO_4$. As a result, it altered the morphology of $BiVO_4$ and increased the relative intensity ratio of (040) to ($\bar{1}$21) plane, corresponding to the increase in exposed {010} facets of $BiVO_4$. Consequently, the photocatalytic performance of $BiVO_4$ is improved, the $BiVO_4$ sample with shuriken-like structure exhibits the highest photocatalytic activity, owing to its narrow bandgap and highest exposed {010} facets of $BiVO_4$. The KCl concentration in the precursor affects the bandgap of $BiVO_4$ by introducing defects to $BiVO_4$. The shuriken-like $BiVO_4$ was used to study the defects by calcination at various temperature in different atmospheric condition. Oxygen vacancies was found to be the defects and exhibited a linear correlation

with bandgap of the $BiVO_4$. Finally, KCl concentration in the precursor and calcination conditions were found to influence oxygen vacancies in $BiVO_4$. Therefore, bandgap of $BiVO_4$ can be tunable by controlling these two factors.

Another technique used a polyhedral $BiVO_4$ to incorporate with SnS_2 via solvothermal synthesis to produce $BiVO_4/B_2S_3/SnS_2$ composite. Various molar ratios of $BiVO_4$ to SnS_2 were used to achieve high photocatalytic performance for the composite. The sample with a ratio of 0.03:1 ($BiVO_4$ to SnS_2) was found to demonstrate the highest photocatalytic activity for rhodamine B degradation among the samples. The photodegradation rate of this sample is 2.9 times that of a single $BiVO_4$. The enhancement in the photocatalytic performance could be ascribed to the formation of heterojunction in the composite, which in turn facilitates the charge migration between individual components in the composite. A dual Z-scheme model was proposed to explain pathway of charge migration in the system. To further understand the incorporation technique, the shuriken-like $BiVO_4$ was also incorporated with SnS_2 via the same procedure and molar ratios of 0.03:1 ($BiVO_4$ to SnS_2) as the composite with the polyhedral $BiVO_4$. The comparison results of both composites showed that they shared a lot of similarities except for morphology, which could be the cause behind their difference in the photocatalytic activity. The composite with the shuriken-like $BiVO_4$ exhibits the highest photocatalytic performance due to the narrow bandgap and the morphology of the shuriken-like $BiVO_4$, which could enhance the electron transfer efficiency in the composite.

This thesis work presents two effective techniques to enhance the photocatalytic performance of $BiVO_4$-based materials in photodegradation of rhodamine B. The composite produced using the shuriken-like $BiVO_4$ demonstrates superior photocatalytic activity, and its dual Z-scheme process may extend its potential application to CO_2 reduction. This thesis provides an insight to the morphology modification and bandgap engineering of $BiVO_4$ as well as incorporation technique via chemical reaction by two materials.

Contents

Acknowledgment

First of all, I would like express my most sincere gratitude to my supervisor, Prof. Keiichi N. Ishihara, whose advice, guidance, and insight has a tremendous help on the completion of my thesis work. His academic freedom in the laboratory creates a creative environment for my research. I also would like express my profound appreciation to Prof. Hideyuki Okumura and Prof. Takaya Ogawa for their helpful and valuable comments as well as suggestions on my research.

I would like to thank to Japan Internation Cooperation Agency (JICA) for AUN/SEED-net PhD program scholarship for their financial support throughout my doctoral degree. I would like to thank to Mr. Yohei Takemonto, who has helped me purchase materials and laboratory equipment for my research and assisted me in other technical stuff. I also appreciate Prof. Takeshi Yabutsuka for allowing me to use the FESEM and EDX measurement.

Last but not least, I would like extend my gratitude to my beloved parents and family for their continuous support and encouragement. Special thanks to my Cambodia friends and my lab mates for being supportive and encouraging to me during our time we has spent together.

List of Tables

List of Figures

1. Introduction

1.1. Background

Technology advancement provides a favorable condition for humanity to thrive and accelerate industrialization. However, it does not come without a cost; the rapid growth in both the human population and industrialization produces overwhelmingly man-made pollutions, leading to a tremendous impact upon the environment, eco-system, and human health. Thus, the removal of that pollution from the environment requires an effective technique. Among various approaches used to tackle pollution problems, photocatalytic technology is one of the effective approaches for solving environmental issues, such as wastewater treatment, air purification, and CO_2 reduction [1,2]. A photocatalyst harnesses light energy to directly oxidize organic pollutants or generate reactive oxygen species (ROS) for eliminating contamination in the environment [3].

A widely used photocatalyst is titanium dioxide (TiO_2) due to its high reactivity, photostability, non-toxicity, chemical stability, and low cost [4]. Despite its many advantages, TiO_2 photocatalyst possesses a wide bandgap of ~3.2 eV, which can absorb only ultraviolet light, constituting only about 5% of sunlight at the surface of the Earth [5,6]. As a result, an alternative photocatalyst such as monoclinic bismuth vanadate ($BiVO_4$) has been extensively studied in recent years [7–9] because it has a narrow bandgap of 2.4–2.5 eV, which can harness the visible light, in addition to other benefits similar to those of TiO_2, such as photostability, non-toxicity, and low production cost [10,11]. Moreover, $BiVO_4$-based photocatalysts have demonstrated their promising photocatalytic performance under visible light in the degradation of various pollutants in an aqueous medium

[12–18]. Nevertheless, $BiVO_4$ is not without problems. Its photocatalytic performance is hindered by poor charge separation and high recombination rate of electron-hole pairs [19,20]. Therefore, $BiVO_4$-based photocatalyst still needs further research and development to enhance its photocatalytic activity to become an efficient photocatalyst for commercial use.

The photocatalytic performance of $BiVO_4$ is influenced by several factors, such as morphology, crystal structure, exposed facet, optical properties (e.g., bandgap), and electron-hole recombination rate [16,21–23]. Hence, developing a technique that can manipulate one or more of these factors is highly desirable to make an improvement on $BiVO_4$. Moreover, the development and understanding of a technique influencing the properties of a photocatalyst are essential to advance the knowledge on not only $BiVO_4$, but also the photocatalysis field.

1.2. Aims and objectives

As mentioned above, developing a novel technique is essential for further pushing a limit of the photocatalytic performance of $BiVO_4$ under visible light and for its future in photocatalysis applications. The aims of this thesis are to prepare, characterize, and study the $BiVO_4$-based photocatalysts via different techniques for enhanced photocatalytic performance with regard to organic pollutant degradation. Rhodamine B is used as a model organic (dye) pollutant in this thesis since it is widely used in textile industries and one of the most common contaminants in industrial wastewater [24–27].

The different approaches are conducted to control the morphology and optical properties of the $BiVO_4$-based photocatalyst in order to improve its photocatalytic activity. Therefore, the objectives of the thesis are stated as follows:

1) Use potassium chloride (KCl) as a directing agent in $BiVO_4$ preparation to control crystal growth, morphology, and bandgap of the $BiVO_4$.

2) Calcine the $BiVO_4$, prepared with KCl in precursor, to investigate its optical properties

3) Incorporate $BiVO_4$ with SnS_2 through chemical reaction via solvothermal method to produce composite photocatalyst.

4) Compare and study two different $BiVO_4$-based composites prepared with different morphologies of $BiVO_4$.

1.3. Thesis outline

This thesis structure is presented below:

Chapter 1 overviews the background of the project and presents the aims and objectives of the thesis. The framework of the thesis is also outlined.

Chapter 2 reviews the basic understanding and mechanism of photocatalysis, including the type of photocatalyst and the application in photodegradation of organic pollutants. The most recent and relevant literature related to $BiVO_4$-based photocatalyst and the strategic approaches to enhance its photocatalytic performance are demonstrated and discussed.

Chapter 3 describes the methods for experiment, characterization, and photocatalytic activity evaluation.

Chapter 4 investigates and discusses the effect of KCl concentration in a precursor of $BiVO_4$ on morphology, crystal growth, optical properties, and photocatalytic activity of the final product of $BiVO_4$.

Chapter 5 studies the defects in the $BiVO_4$, prepared with KCl in the precursor, via calcination in different conditions. The effect of calcination condition and KCl concentration on optical properties of the $BiVO_4$ are also studied and discussed.

Chapter 6 investigates the enhanced photocatalytic activity of $BiVO_4$-based composites ($BiVO_4/Bi_2S_3/SnS_2$) under visible light to determine a suitable molar ratio of SnS_2:$BiVO_4$ for the composite. Possible mechanisms of charge-transfer pathways in the composite, leading to photocatalytic activity enhancement, are studied and discussed.

Chapter 7 compares and studies two $BiVO_4$-based composites ($BiVO_4/Bi_2S_3/SnS_2$) prepared with the same procedure used in Chapter 6, using two different morphologies of $BiVO_4$ (polyhedral $BiVO_4$ and shuriken-like $BiVO_4$).

Chapter 8 discusses the findings of this study. In addition, the chapter also compares the photocatalytic performance (rhodamine B degradation) of the $BiVO_4$-based photocatalysts produced in this thesis and examines their potential applications. Finally, recommendations are proposed for future research.

Chapter 9 presents summary and conclusion of this thesis work.

Reference

[1] D.D. Dionysiou, G. Li Puma, J. Ye, J. Schneider, D. Bahnemann, Photocatalysis, The Royal Society of Chemistry, 2016. https://doi.org/10.1039/9781782627104.

[2] Z.H. Wei, Y.F. Wang, Y.Y. Li, L. Zhang, H.C. Yao, Z.J. Li, Enhanced photocatalytic CO_2 reduction activity of Z-scheme CdS/$BiVO_4$ nanocomposite with thinner $BiVO_4$ nanosheets, J. CO_2 Util. 28 (2018) 15–25. https://doi.org/10.1016/j.jcou.2018.09.008.

[3] R. V. Prihod'ko, N.M. Soboleva, R. V Prihod, N.M. Soboleva, Photocatalysis: Oxidative processes in water treatment, 2013. https://doi.org/10.1155/2013/168701.

[4] J. Schneider, M. Matsuoka, M. Takeuchi, J. Zhang, Y. Horiuchi, M. Anpo, D.W. Bahnemann, Understanding TiO_2 Photocatalysis: Mechanisms and Materials, Chem. Rev. 114 (2014) 9919–9986. https://doi.org/10.1021/cr5001892.

[5] C. Dette, M.A. Pérez-Osorio, C.S. Kley, P. Punke, C.E. Patrick, P. Jacobson, F. Giustino, S.J. Jung, K. Kern, TiO_2 anatase with a bandgap in the visible region, Nano Lett. 14 (2014) 6533–6538. https://doi.org/10.1021/nl503131s.

[6] W. Qin, D. Zhang, D. Zhao, L. Wang, K. Zheng, Near-infrared photocatalysis based on YF3:Yb^{3+}, Tm^{3+}/TiO_2 core/shell nanoparticles, Chem. Commun. 46 (2010) 2304–2306. https://doi.org/10.1039/b924052g.

[7] C. Cheng, Q. Fang, S. Fernandez-Alberti, R. Long, Controlling charge carrier trapping and recombination in $BiVO_4$ with the oxygen vacancy oxidation state, J. Phys. Chem. Lett. 12 (2021) 3514–3521. https://doi.org/10.1021/acs.jpclett.1c00713.

[8] C. Qin, H. Liao, F. Rao, J. Zhong, J. Li, One-pot hydrothermal preparation of Br-doped $BiVO_4$ with enhanced visible-light photocatalytic activity, Solid State Sci. 105 (2020) 106285. https://doi.org/10.1016/j.solidstatesciences.2020.106285.

[9] B. Xu, A. Zada, G. Wang, Y. Qu, Boosting the visible-light photoactivities of $BiVO_4$ nanoplates by Eu doping and coupling CeO:X nanoparticles for CO_2 reduction and organic oxidation, Sustain. Energy Fuels. 3 (2019) 3363–3369. https://doi.org/10.1039/c9se00409b.

[10] G. Zhao, W. Liu, Y. Hao, Z. Zhang, Q. Li, S. Zang, Nanostructured shuriken-like $BiVO_4$ with preferentially exposed {010} facets: Preparation, formation mechanism, and enhanced photocatalytic performance, Dalt. Trans. 47 (2018) 1325–1336. https://doi.org/10.1039/c7dt04431c.

[11] S. Meng, T. Ogawa, H. Okumura, K.N. Ishihara, The effect of potassium chloride on $BiVO_4$ morphology and photocatalysis, J. Solid State Chem. (2021) 122291. https://doi.org/10.1016/j.jssc.2021.122291.

[12] P. Pookmanee, S. Kojinok, S. Phanichphant, Photocatalytic degradation of 2,4-dichlorophenol using $BiVO_4$ powder prepared by the sol–gel method, Trans. Mater. Res. Soc. Japan. 39 (2014) 431–434. https://doi.org/10.14723/tmrsj.39.431.

[13] S.M. Thalluri, M. Hussain, G. Saracco, J. Barber, N. Russo, Green-synthesized $BiVO_4$ oriented along {040} facets for visible-light-driven ethylene degradation, Ind. Eng. Chem. Res. 53 (2014) 2640–2646. https://doi.org/10.1021/ie403999g.

[14] Y. Hu, D. Li, F. Sun, H. Wang, Y. Weng, W. Xiong, Y. Shao, One-pot template-free synthesis of heterophase $BiVO_4$ microspheres with enhanced photocatalytic activity, RSC Adv. 5 (2015) 54882–54889. https://doi.org/10.1039/c5ra09785a.

[15] D.P. Jaihindh, B. Thirumalraj, S.M. Chen, P. Balasubramanian, Y.P. Fu, Facile synthesis of hierarchically nanostructured bismuth vanadate: An efficient photocatalyst for degradation and detection of hexavalent chromium, J. Hazard. Mater. 367 (2019) 647–657. https://doi.org/10.1016/j.jhazmat.2019.01.017.

[16] J. Wang, J. Jin, X. Wang, S. Yang, Y. Zhao, Y. Wu, S. Dong, J. Sun, J. Sun, Facile fabrication of novel $BiVO_4/Bi_2S_3/MoS_2$ n-p heterojunction with enhanced photocatalytic activities towards pollutant degradation under natural sunlight, J. Colloid Interface Sci. 505 (2017) 805–815. https://doi.org/10.1016/j.jcis.2017.06.085.

[17] M.L. Guan, D.K. Ma, S.W. Hu, Y.J. Chen, S.M. Huang, From hollow olive-shaped $BiVO_4$ to n-p core-shell $BiVO_4@Bi_2O_3$ microspheres: controlled synthesis and enhanced visible-light-responsive photocatalytic properties, Inorg. Chem. 50 (2011) 800–805. https://doi.org/10.1021/ic101961z.

[18] L. Song, Y. Pang, Y. Zheng, C. Chen, L. Ge, Design, preparation and enhanced photocatalytic activity of porous $BiOCl/BiVO_4$ microspheres via a

coprecipitation-hydrothermal method, J. Alloys Compd. 710 (2017) 375–382. https://doi.org/10.1016/j.jallcom.2017.03.283.

[19] F.F. Abdi, T.J. Savenije, M.M. May, B. Dam, R. Van De Krol, The origin of slow carrier transport in $BiVO_4$ thin film photoanodes: A time-resolved microwave conductivity study, J. Phys. Chem. Lett. 4 (2013) 2752–2757. https://doi.org/10.1021/jz4013257.

[20] T.D. Nguyen, V.H. Nguyen, S. Nanda, D.V.N. Vo, V.H. Nguyen, T. Van Tran, L.X. Nong, T.T. Nguyen, L.G. Bach, B. Abdullah, S.S. Hong, T. Van Nguyen, $BiVO_4$ photocatalysis design and applications to oxygen production and degradation of organic compounds: a review, Environ. Chem. Lett. 18 (2020) 1779–1801. https://doi.org/10.1007/s10311-020-01039-0.

[21] X. Qi, X. Zhu, J. Wu, Q. Wu, X. Li, M. Gu, Controlled synthesis of $BiVO_4$ with multiple morphologies via an ethylenediamine-assisted hydrothermal method, Mater. Res. Bull. 59 (2014) 435–441. https://doi.org/10.1016/j.materresbull.2014.08.004.

[22] D. Wang, H. Jiang, X. Zong, Q. Xu, Y. Ma, G. Li, C. Li, Crystal facet dependence of water oxidation on $BiVO_4$ sheets under visible light irradiation, Chem. - A Eur. J. 17 (2011) 1275–1282. https://doi.org/10.1002/chem.201001636.

[23] H.L. Tan, A. Suyanto, A.T. De Denko, W.H. Saputera, R. Amal, F.E. Osterloh, Y.H. Ng, Enhancing the photoactivity of faceted $BiVO_4$ via annealing in oxygen-deficient condition, Part. Part. Syst. Charact. 34 (2017). https://doi.org/10.1002/ppsc.201600290.

[24] A. Ajmal, I. Majeed, R.N. Malik, H. Idriss, M.A. Nadeem, Principles and mechanisms of photocatalytic dye degradation on TiO_2 based photocatalysts: a comparative overview, RSC Adv. 4 (2014) 37003–37026. https://doi.org/10.1039/c4ra06658h.

[25] K. Iqbal, A. Iqbal, A.M. Kirillov, B. Wang, W. Liu, Y. Tang, A new Ce-doped MgAl-LDH@Au nanocatalyst for highly efficient reductive degradation of organic contaminants, J. Mater. Chem. A. 5 (2017) 6716–6724. https://doi.org/10.1039/C6TA10880F.

[26] K. Iqbal, A. Iqbal, A.M. Kirillov, W. Liu, Y. Tang, Hybrid metal-organic-framework/inorganic nanocatalyst toward highly efficient discoloration of organic dyes in aqueous medium, Inorg. Chem. 57 (2018) 13270–13278.

https://doi.org/10.1021/acs.inorgchem.8b01826.

[27] P. Singh, A. Borthakur, P.K. Mishra, D. Tiwary, Nano-materials as photocatalysts for degradation of environmental pollutants: challenges and possibilities, Elsevier, 2019.

2. Literature Review

This chapter comprehensively reviews the latest scientific literature on experimental discovery and development for $BiVO_4$-based photocatalysts. The first part of the chapter provides an overview of photocatalysis to understand the basic mechanism, application in the degradation of organic pollutants, and photocatalysts. The latter part focuses on $BiVO_4$ photocatalysts, such as crystal structure, phase transformation, hydrothermal method, and limitations. Finally, recent approaches and techniques used to improve the photocatalytic performance of $BiVO_4$–based photocatalysts are explored and discussed.

2.1. Photocatalysis

Ever since the breakthrough in photocatalysis made by Akira Fujishima and Kenichi Honda [1], the field of photocatalysis has been elevated and attracted much research due to its potential applications in solar energy conversion [2]. In recent years, a considerable amount of research on photocatalysis has focused more on applications for environmental decontamination, such as air and water purification, CO_2 reduction, and especially pollutant degradation [2–5]. Furthermore, since a photocatalyst can utilize solar energy, which is renewable and abundant energy on Earth, it perfectly fits an environmentally friendly material used for sustainable development in the future.

Photocatalysis involves photogeneration of electrons and holes by light energy, initiating a chemical reaction at the solid surface. At least two reactions, oxidation and reduction must happen simultaneously in order to balance the process and avoid any change on photocatalyst [2]. Fig. 2-1 illustrates the schematic representation of photocatalysis, using TiO_2 as an example. When photocatalyst absorbs incident photons with energy higher than its bandgap, electrons jump from

the valence band to conduction band, which in turn generates electron-hole pairs. For example, to produce photogenerated electron-hole pairs in TiO_2 with a bandgap of 3.2 eV, it requires light with a wavelength (λ) shorter than 390 nm (UV region). Thus, a photocatalyst with a narrower bandgap such as $BiVO_4$ (~2.5 eV) can absorb light with a longer wavelength locating in the visible light region, consequently having better light absorption efficiency than that of the wide-bandgap TiO_2. After excitation, the photogenerated electrons and holes migrate and perform a redox reaction at the surface of the semiconductor. The redox reaction in water can generate reactive oxygen species (ROS) that decompose organic pollutants into CO_2, H_2O, and other harmless substances [6]. The recombination of the electron and hole can happen both inside and at the surface of the semiconductor, releasing the absorbed photons as heat instead [7]. The high recombination rate greatly reduces the efficiency of photocatalytic activity and renders the photocatalyst useless. The recombination rate can be suppressed by controlling surface and bulk properties of the photocatalyst, such as crystallinity, oxygen vacancies, particle size, and surface trap state [8–10]. Additionally, incorporating two or more photocatalysts has also been found to suppress charge recombination due to the formation of heterojunction [4,11].

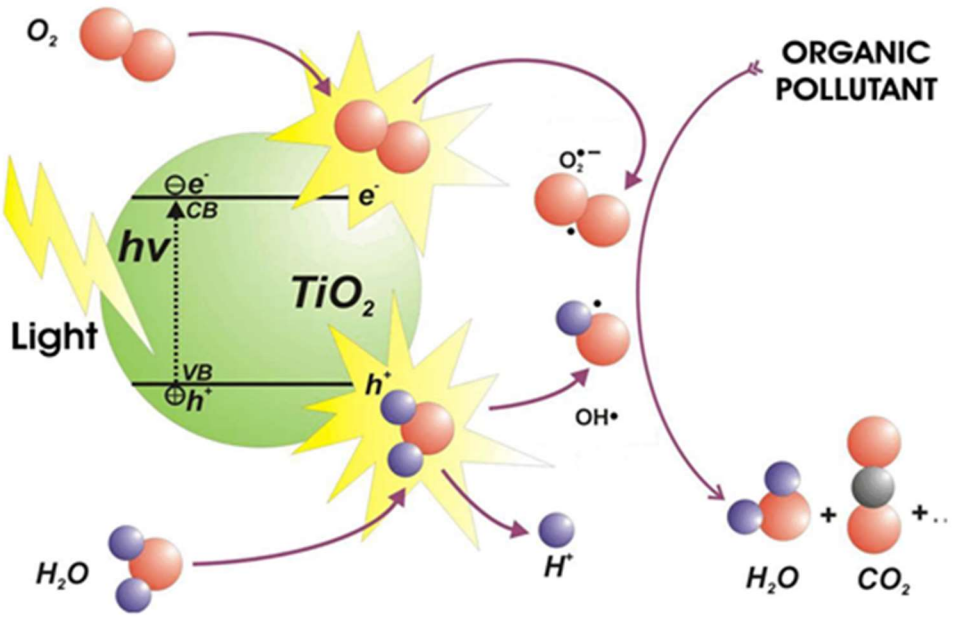

Fig. 2-1. Schematic representation of photocatalytic reaction [7].

2.1.1. Photodegradation of organic pollutants

As mentioned in Section 2.1, reactive oxygen species (ROS) are generated by a redox reaction at the photocatalyst surface. The ROS are highly reactive due to the unsaturated bonds and generally include free radicals (hydroxyl radical, •OH; superoxide radical, $O_2^{\bullet-}$; and perhydroxy radical, HO_2•) and molecular form (hydrogen peroxide, H_2O_2; and singlet oxygen, $^1O_2$) [3,12]. The ROS can react with organic pollutants and chemically alter them to form harmless by-products such as CO_2, H_2O, and mineral acid [3,6].

The photodegradation process of organic pollutants by photocatalyst consists of three potential mechanisms, as shown in Fig. 2-2 [13]. First one is a direct reduction-oxidation reaction with organic pollutants when electrons or holes reach the photocatalyst surface without recombination and react with pollutant directly [4,14,15]. The second one involves a two-step process in which electrons come into contact with O_2 and produce $O_2^{\bullet-}$ radicals, or holes oxidize H_2O to produce •OH. Then, both radicals can react and decompose the pollutant. The last one is similar to the second process, except that the radicals produced by electron-hole pairs can conduct further reaction to form more ROS (•OH, HO_2•, $O_2^{\bullet-}$, H_2O_2), which then degrade the pollutants to become by-product (H_2O, CO_2, inorganic acid).

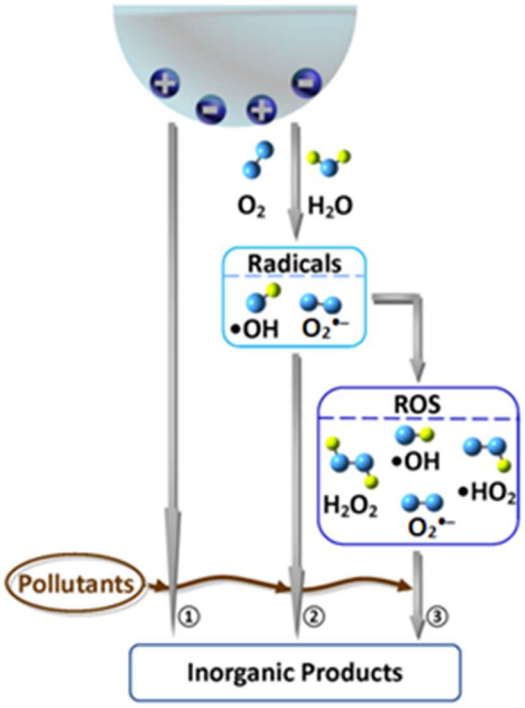

Fig. 2-2. Schematic diagram of pollutant degradation mechanism [13].

Rhodamine B (RhB) is one of the most common organic dyes in the textile industry and industrial wastewater [16–19]. This dye is hazardous to any organism because it exhibits carcinogenic and mutagenic behaviors [20,21]. As such, for many years, a lot of research has been extensively conducted to find a suitable photocatalyst for removing RhB [22–25]. Moreover, RhB is often used as a model dye monitoring photocatalytic activity of photocatalysts [17,26–28]. The RhB photodegradation process by photocatalyst involves several steps and finally produces CO_2 and H_2O as by-products [29], as demonstrated in Fig. 2-3. The RhB photodegradation by various photocatalysts are shown in Table 2-1.

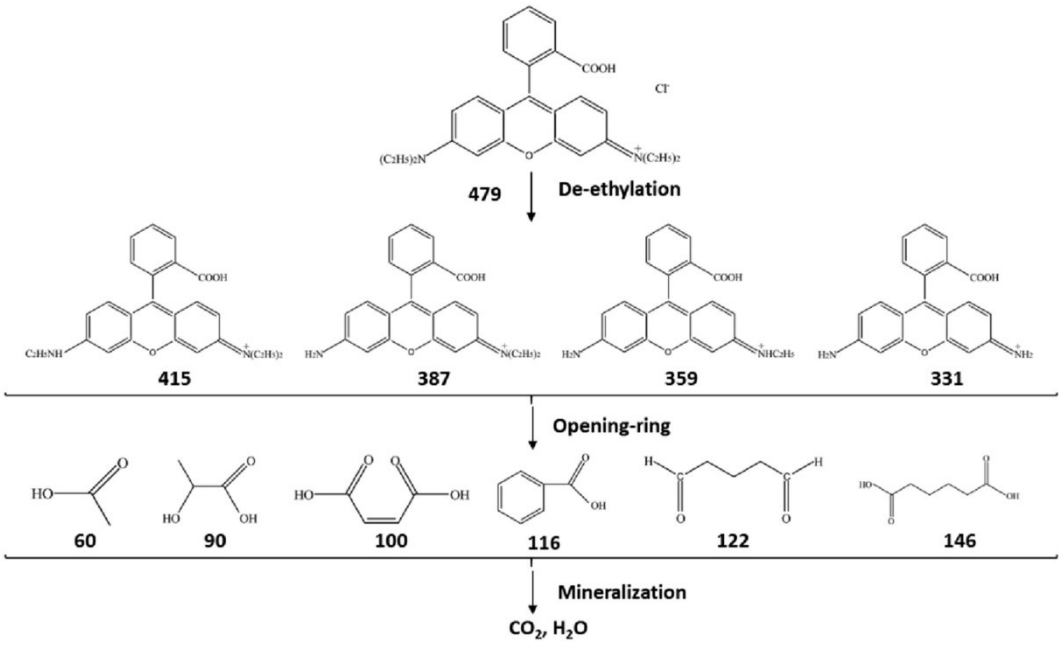

Fig. 2-3. The photodegradation pathway of rhodamine B by TiO_2 [29]

Table 2-1. RhB photodegradation with measurement condition by various photocatalysts and their bandgaps (E_g).

Photocatalyst	E_g (eV)	Light source	Reaction condition	Degradation efficiency (irradiation time)	Ref.
TiO_2	3.2	500 W Xe lamp, λ>420 nm	100 ml RhB (0.01 mmol L^{-1}), 0.05 g photocatalyst	~40% (4.5 h)	[29]
$BiVO_4$	2.48	500 W halogen lamp, λ>420 nm	80 ml RhB (0.01 mmol L^{-1}) , 0.08 g photocatalyst	~97% (6 h)	[30]
SnS_2	2.3	300 W Xe lamp, visible light	100 ml RhB (0.02 mmol L^{-1}), 0.05 g photocatalyst	~68% (2 h)	[31]
SnO_2	3.6	Mercury lamp, λ=365 nm	100 ml RhB (0.02 mmol L^{-1}), 0.045 g photocatalyst	~92% (4.5 h)	[32]
CdS	2.29	500 W mercury lamp	40 mL RhB (0.015 mmol L^{-1}), 0.05 g photocatalyst	~93% (2 h)	[33]

2.2. Photocatalysts

Metal oxides and metal sulfides are common types of photocatalysts, which are intensively studied in past decades [34,35]. The typical oxide and sulfide materials are listed in Table 2-2. These materials possess various values of the bandgap, which determine their ability to absorb light energy, corresponding to the wavelength of light. As a result, the bandgap greatly influences the photocatalytic performance of these materials.

Table 2-2. Crystal phase and optical properties of commonly studied photocatalysts.

Photocatalyst	Crystal phase	Bandgap (E_g)	Light absorption region	Reference
TiO_2 Rutile	Tetragonal	~3.0 eV	λ<414 nm	[36]
TiO_2 Anatase	Tetragonal	~3.2 eV	λ<388 nm	[36]
$BiVO_4$	Monoclinic	~2.5 eV	λ<496 nm	[30]
$BiVO_4$	Tetragonal	~2.9 eV	λ<428 nm	[37]
SnO_2	Tetragonal	~3.6 eV	λ<345 nm	[32]
ZnO	Hexagonal	~3.3 eV	λ<376 nm	[38]
SnS_2	Hexagonal	~2.2 eV	λ<564 nm	[39]
CdS	Hexagonal	~2.3 eV	λ<540 nm	[33]
Bi_2S_3	Orthorhombic	~1.4 eV	λ<886 nm	[40]

Besides the bandgap of the photocatalyst, band-edge positions, which refer to conduction band minimum (CBM) and valence band maximum (VBM) potentials, are another important factor in choosing a potential application for a photocatalyst [41]. As shown in Fig. 2-4, photocatalysts with a large positive potential of VBM possess strong oxidation abilities to produce •OH radicals and degrade pollutants. Moreover, they can induce the O_2 evolution process. Water splitting application requires a photocatalyst with CBM potential more negative than $2H^+/H_2$ potential and VBM potential more positive than H_2O/O_2 potential. If photocatalysts exhibit

strong reduction abilities due to large negative potential, they could be used for CO_2 reduction or H_2 evolution.

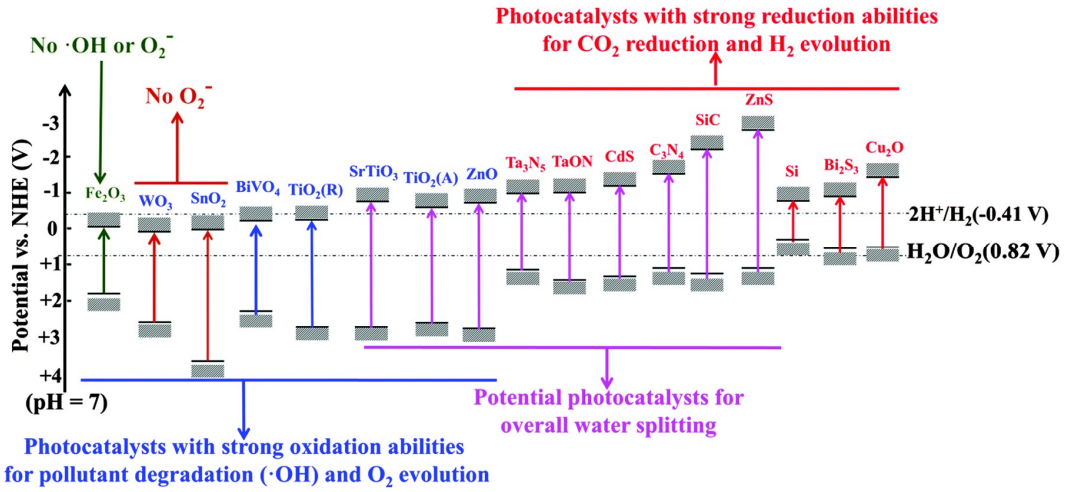

Fig. 2-4. Typical metal oxides, metal sulfides and their band positions for potential applications [41].

2.2.1. Metal oxides

Metal oxides are exceptionally important materials as photocatalysts. Their rise in popularity in photocatalysis has begun after the discovery of the Honda-Fujishima effect [1], in which TiO_2 was used to conduct water splitting using light irradiation. Metal oxides such as TiO_2, ZnO, and SnO_2 have been extensively studied in the photocatalysis field, owing to their abundance in nature, exceptional stability, biocompatibility, and low production cost [35]. However, their drawbacks are wide bandgaps (Fig. 2-4), which only work in the UV light region and limit their applications. As a result, an alternative oxide such as $BiVO_4$ has attracted a substantial amount of attention from many researchers. Its advantages are that it possesses similar benefits to the mentioned oxides above and narrower bandgap (~2.5 eV), which can harness visible light and increase its light absorption efficiency [30,42–44]. Further information on $BiVO_4$ is discussed later in Section 2.3.

2.2.2. Metal sulfides

Metal sulfides are known to possess relatively smaller bandgaps than metal oxides, and most of them can be used in the visible light region [34]. Although a narrow bandgap can absorb more light, it also provides a narrow gap for photoexcited electrons and holes to recombine, resulting in an increase in recombination rate and lowering the efficiency of photocatalytic performance. For example, Bi_2S_3 with a bandgap around 1.4 eV exhibits a low photocatalytic activity due to the fast recombination rate of charge carriers [45,46]. On the other hand, SnS_2 possesses a relatively wider bandgap (~2.2 eV) than that of Bi_2S_3 and demonstrates great photocatalytic activity for pollutant degradation [39] and H_2 production [47,48]. In addition, SnS_2 can be used in acid and neutral aqueous solution due to its chemical stability. Moreover, SnS_2 has been reported to exhibit strong adsorptivity for RhB dye, which is very useful for RhB removal even without light irradiation [49]. However, metal sulfides, including SnS_2 [50,51], suffer from photocorrosion due to S^{2-} ions prone to oxidation by photogenerated holes [52]. Therefore, incorporating metal sulfides with more stable materials like metal oxides is a common strategy not only for promoting their stability, but also for suppressing their rapid combination rate of photogenerated electron-hole pairs [53,54].

2.3. Bismuth vanadate ($BiVO_4$)

Bismuth Vanadate ($BiVO_4$), also known as bismuth vanadium oxide, is well known for its bright yellow color and its application in pigments. First use of $BiVO_4$ dates back almost a century ago when a patent of $BiVO_4$ was reported in the medical field in 1924. Later in 1976, $BiVO_4$ was first synthesized as a solid material [55]. In recent decades, the use of $BiVO_4$ extends to the photocatalysis field owing to its narrow bandgap, which can harness visible light [56–58]. In addition, $BiVO_4$ possesses other common advantages of oxide materials, including non-toxicity, low cost of production, stability, and abundance. As a photocatalyst, the most widely studied crystal phase of $BiVO_4$ is monoclinic scheelite structure because of its exceptionally high photocatalytic activity, compared with other crystal phases [59]. The physical properties of monoclinic $BiVO_4$ are listed in Table 2-3.

Table 2-3. Physical properties of monoclinic $BiVO_4$ [56,60]

Formula	$BiVO_4$
Color	Yellow
Molecular weight	323.92 g mol^{-1}
Melting point	~940 °C
Boiling point	1997 °C
Density	6.1 g m^{-3}
Bandgap	2.4 eV
Solubility	Insoluble, soluble in strong acids

2.3.1. Crystal structure and phase transition

In nature, $BiVO_4$ occurs as pucherite with an orthorhombic crystal structure [61]. In a laboratory setting, $BiVO_4$ can be synthesized in three crystal phases, such as monoclinic scheelite $BiVO_4$ (ms-$BiVO_4$), tetragonal scheelite (ts-$BiVO_4$), and tetragonal zircon-type $BiVO_4$ (tz-$BiVO_4$), as shown in Fig. 2-5. The zircon-type structure consists only of the tetragonal phase, while the scheelite type possesses two possible phases: tetragonal and monoclinic phases [59]. There is a difference between zircon-type and scheelite structures: six VO_4 surround one Bi ion for the former and eight VO_4 bound to one Bi ion for the latter [62]. On the other hand, the distinction between the two phases of the scheelite structure is the distortion of local environments of Bi and V ions in the monoclinic structure. ts-$BiVO_4$ has only one type of V-O bond with a length of 1.72 Å, while two types of V-O bond (1.69 Å and 1.77 Å) exist in ms-$BiVO_4$ [63].

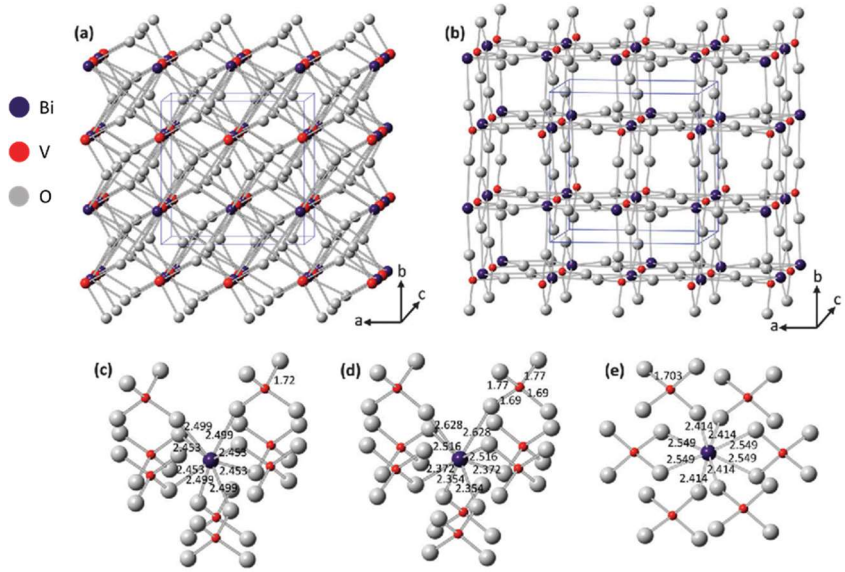

Fig. 2-5. Crystal structures of (a) tetragonal scheelite and (b) tetragonal zircon-type $BiVO_4$. The crystal structure of monoclinic scheelite is similar to tetragonal scheelite (a) except for some small changes in the atomic position of Bi, V, and O. The images showing Bi ions surrounded by VO_4 ions of (c) tetragonal scheelite (ts-$BiVO_4$), (d) monoclinic scheelite $BiVO_4$ (ms-$BiVO_4$), and (e) tetragonal zircon-type $BiVO_4$ (tz-$BiVO_4$), including local coordination of Bi-O and V-O bond lengths in Å. [62]

Among the three crystal structures, ms-$BiVO_4$ demonstrates the highest photocatalytic activity. Firstly, if ms-$BiVO_4$ is compared to tz-$BiVO_4$, the superior photocatalytic performance is due to the bandgap of ms-$BiVO_4$ (2.4 eV), which is narrower than that (2.9 eV) of tz-$BiVO_4$ [64]. The O-O bond length in ms-$BiVO_4$ is longer than that of tz-$BiVO_4$, which in turn decreases the repulsion between Bi^{3+} lone electrons and O 2p, resulting in narrowing the bandgap of ms-$BiVO_4$, as illustrated in Fig. 2-6 [65]. On the other hand, Tokunaga et al. [64] reported that ms-$BiVO_4$ (2.41 eV) and ts-$BiVO_4$ (2.34 eV) had similar bandgaps and electronic structures. However, ms-$BiVO_4$ shows greater photocatalytic activity in O_2 production than st-$BiVO_4$. They suggested that the high photocatalytic activity of ms-$BiVO_4$ under visible light was attributed to the distortion of the Bi-O polyhedron in ms-$BiVO_4$ by a $6s^2$ lone pair of Bi^{3+} [64].

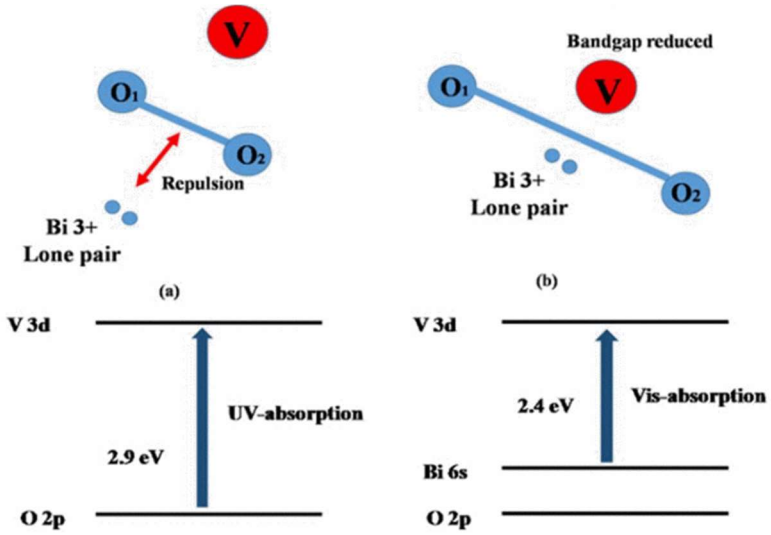

Fig. 2-6. Schematic representation of optical bandgap of (a) tz-$BiVO_4$ and (b) ms-$BiVO_4$ [65].

$BiVO_4$ with the tetragonal zircon-type structure is commonly obtained via low temperature synthesis [59,66,67]. The phase transition from tz-$BiVO_4$ to ms-$BiVO_4$ and ts-$BiVO_4$ can be achieved via thermal treatment [61,64], as shown in Fig. 2-7. An irreversible transformation from tz-$BiVO_4$ to ms-$BiVO_4$ happens at 670-770 K, while the ms-$BiVO_4$ reversibly transit to ts-$BiVO_4$ at 528 K [61]. Thus, it indicates that tetragonal zircon-type structure is a metastable state of $BiVO_4$. Nevertheless, ts-$BiVO_4$ and ms-$BiVO_4$ can be synthesized using an aqueous-solution process at room temperature by controlling the preparation time (4.5 h for ts-$BiVO_4$ and 46 h for ms-$BiVO_4$) [64]. Other factors and synthesis methods can also influence the crystal structures of $BiVO_4$. For example, the crystal phases of $BiVO_4$ (tetragonal zircon-type and monoclinic scheelite phases) could be determined by the pH of the $BiVO_4$ precursor for the hydrothermal method [66]. Another report utilized microwave-hydrothermal reaction to transform tz-$BiVO_4$ to ms-$BiVO_4$ by controlling the irradiation time (10-22 min) at a fixed 800 W of the irradiation power [68]. Another study reported that mechanical crushing of $BiVO_4$ powder at room temperature could also cause an irreversible phase transition from tz-BiVO to ms-$BiVO_4$ [61].

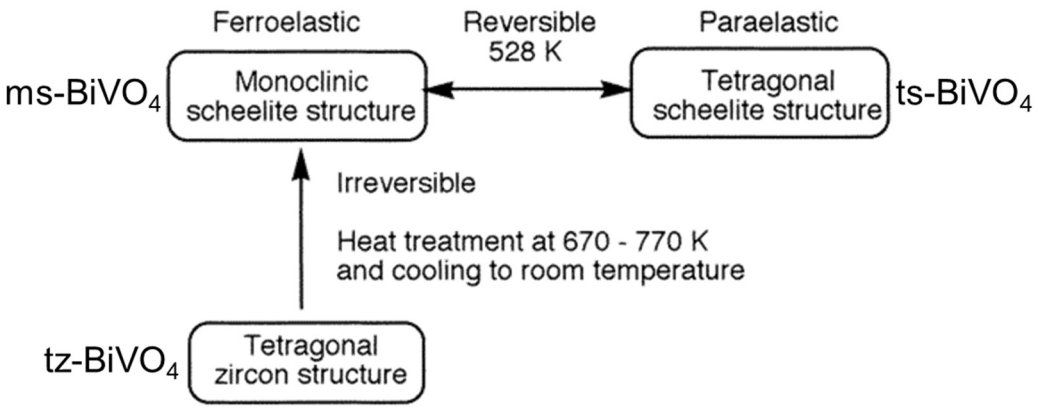

Fig. 2-7. Phase transition of $BiVO_4$ via thermal treatment. [64]

2.3.2. Hydrothermal synthesis

$BiVO_4$ can be prepared by various methods, including solid state synthesis [69,70], hydrothermal or solvothermal route [71,72], phytosynthesis [73], sol gel process [74], and homogeneous precipitation [75]. Among them, the hydrothermal method is one of the most commonly used techniques for the preparation of $BiVO_4$, owing to its ability to control the crystal growth, morphology, and crystal structure via synthesis parameters, such as pH of precursor, structure-directing agent, synthesis time and temperature, reactant concentration [66,76–78].

In the hydrothermal method, the common starting materials for $BiVO_4$ are $Bi(NO_3)_3 \cdot 5H_2O$ (Bi^{3+} source) and NH_4VO_3 (V^{5+} source). Both starting materials are often dissolved separately in a nitric acid solution for $Bi(NO_3)_3 \cdot 5H_2O$ and a basic solution (NaOH or ammonia solution) for NH_4VO_3 to ensure a complete dissolution prior to mixing [76,79,80]. It is noted that NH_4VO_3 is more soluble in hot water and basic solution (ammonia) [81]. However, one-pot hydrothermal synthesis in ultrapure water is also possible to produce $BiVO_4$ [82]. A possible chemical reaction in the preparation stage of $BiVO_4$ can be expressed as follows [66,67]:

$$Bi^{3+} + 2H_2O \rightleftharpoons BiOH^{2+} + H_3O^+ \quad (2\text{-}1)$$

$$BiOH^{2+} + H_2O \rightleftharpoons BiO^+ + H_3O^+ \quad (2\text{-}2)$$

$$BiO^+ + NO_3^- \rightleftharpoons BiONO_3 \downarrow \quad (2\text{-}3)$$

$$BiONO_3 \downarrow + VO_3^- \rightleftharpoons \text{tz-}BiVO_4 \downarrow + NO_3^- \quad (2\text{-}4)$$

Firstly, $Bi(NO_3)_3 \cdot 5H_2O$ is hydrolyzed in an aqueous solution, as can be seen in the reaction (2-1) and (2-2), generating BiO^+ and H_3O^+. In reaction (2-3), BiO^+ reacts with NO_3^- to produce slightly soluble $BiONO_3$. After that, the slightly soluble $BiONO_3$ further reacts VO_3^- to form $BiVO_4$ [reaction (2-4)]. The $BiVO_4$ forming at this stage often is tz-$BiVO_4$ because the formation of tz-$BiVO_4$ is kinetically favorable when there is a sudden increase in pH due to the introduction of the basic solution of NH_4VO_3 [66,83]. The transition from tz-$BiVO_4$ to ms-$BiVO_4$ can occur by prolonging the aging period [64] or using hydrothermal route [66,67].

As mentioned above, the monoclinic scheelite structure exhibits high photocatalytic activity. Thus, it is preferable to obtain ms-$BiVO_4$ as the final product via synthesis. Tan et al. [66] demonstrated the effect of pH of precursor on the crystal structure of $BiVO_4$ using hydrothermal synthesis (200 °C for 40 min). He found that pure ms-$BiVO_4$ could be obtained at either pH of 0.59 (a strong acid condition) or pH range of 4.26–9.76. This result was supported by another study [84], in which pure ms-$BiVO_4$ was attained at pH values of 4 and 7 via hydrothermal method (185 °C for 6 h). In contrast, Ressnig et al. [85] obtained pure ms-$BiVO_4$ at a pH range of 1–4 (hydrothermal route, 160 °C for 5 h), while Zhang et al. [86] reported that pure ms-$BiVO_4$ was obtained at pH value of 8.8 and 11.5. These contradicting results indicate that although the pH of the precursor influences the crystal phase of $BiVO_4$, it cannot be solely used to determine the crystal phase of the final product of $BiVO_4$. Thus, other parameters of hydrothermal synthesis, such as heating duration, should be taken into consideration for the preparation of pure ms-$BiVO_4$. For instance, Zhao et al. [67] suggested that prolonging the heating

duration of the synthesis up to 10 h could completely transform tz-$BiVO_4$ to ms-$BiVO_4$. Furthermore, pure ms-$BiVO_4$ could be acquired at a wide pH range of value of 1–9 by prolonging hydrothermal duration up to 24 h at 180 °C.

2.3.3. Limitation of monoclinic $BiVO_4$

Although $BiVO_4$ has a narrow bandgap (2.4–2.5 eV) and can harness visible light, its photon absorption is limited to the wavelength of light shorter than 517 nm. Thus, there is still a significant number of photons of sunlight in the visible light region that $BiVO_4$ is unable to absorb. Previous studies suggested that reducing the bandgap of photocatalysts could improve their light absorption efficiency, in turn enhancing their photocatalytic performance [87–90].

Furthermore, the photocatalytic activity of $BiVO_4$ is inhibited by poor charge separation and rapid combination rate of photogenerated electrons and holes [91,92]. Abdi et al. [91] revealed that the said issues were caused by the remarkably low charge mobility (~4×10^{-2} cm^2 V^{-1} s^{-1}) of $BiVO_4$, compared with that of other metal oxides, such as Fe_2O_3 (0.5 cm^2 V^{-1} s^{-1}), WO_3 (10 cm^2 V^{-1} s^{-1}), and Cu_2O (6 cm^2 V^{-1} s^{-1}). Various methods have been used to improve the charge separation and suppress the recombination rate of charge carriers, such as reduction of particle size [93], forming heterojunctions [94], and doping with atoms [43,95]. Another interesting technique is facet engineering of $BiVO_4$. The well-known facets of $BiVO_4$ responsible for the reduction and oxidation reactions upon irradiation are {010} and {110}, respectively [96–98]. The preferential redox reactions of {010} and {110} facets are attributed to the difference in energy band levels of both facets (Fig. 2-8) [97], which enable the charge transfer, resulting in the accumulation of electrons and holes on {010} and {110} facets, respectively. Tan et al. [98] suggested that $BiVO_4$ with dominant {010} facets possesses a large number of available photogenerated electrons at the surface of $BiVO_4$, promoting the electron transfer efficiency and lowering the rate of electron-hole recombination [98]. As a result, photocatalytic activity of $BiVO_4$ is enhanced with the increase in the exposed {010} facets, which is consistent with many experimental studies [44,79,99–101].

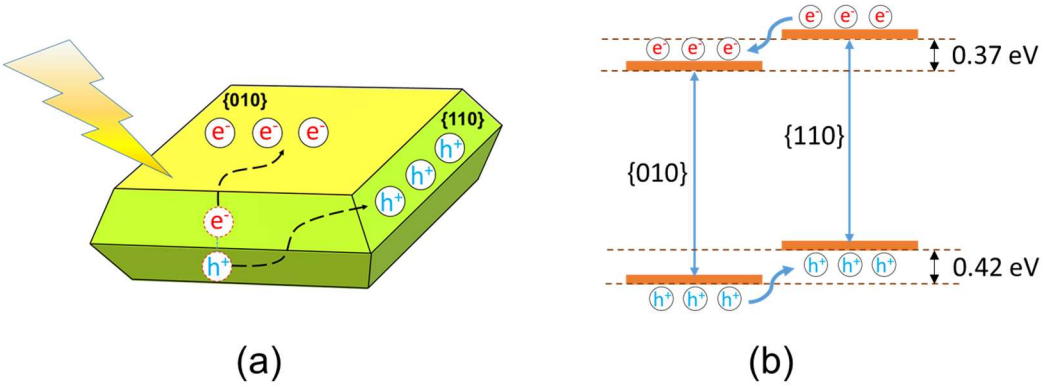

Fig. 2-8. Schematic diagram of (a) spatial separation of photogenerated electrons and holes on the {010} and {110} facets [102] and (b) difference in energy band levels for both facets of $BiVO_4$. [97]

Another limitation of $BiVO_4$ is related to its band energy structure, as depicted in Fig. 2-9. Although $BiVO_4$ possesses the valence band potential positive enough to oxidize H_2O for O_2 evolution, its conduction band potential lacks overpotential for H_2 evolution (-0.41 V for $2H^+/H_2$) and CO_2 reduction (at least -0.05 V for $HCHO/CO_2$) [62,103,104]. Incorporating $BiVO_4$ with other photocatalysts (e.g., Bi_2S_3 [105], CdS [106], and Cu_2O [107]) is one of the solutions to extend its potential applications to H_2 production and CO_2 reduction.

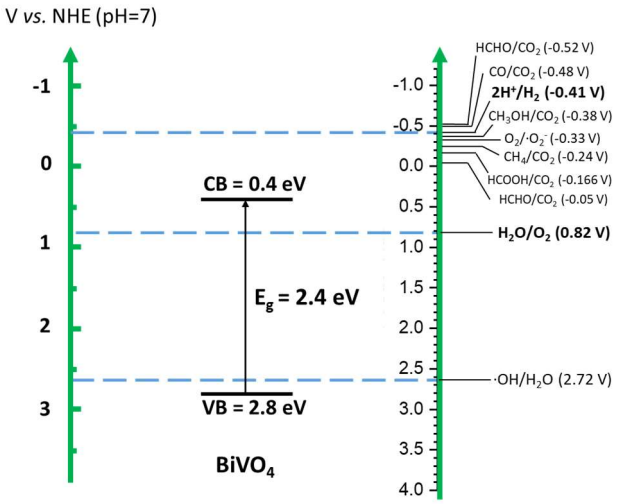

Fig. 2-9. Conduction band and valence band of $BiVO_4$ [108] respective to redox potentials at pH 7 of various compounds [109].

2.4. Strategy for improvement

As described in previous sections, $BiVO_4$ is a promising photocatalyst with many advantages. However, its photocatalytic performance needs further improvement for commercial use. This section aims to review and discuss strategies, such as morphological control, bandgap modification, producing composite, for enhancing the photocatalytic activity and overcoming the limitation of $BiVO_4$.

2.4.1. Morphological control

As described in Section 2.3.3, maximizing the exposure of {010} facets is important to enhance the photocatalytic performance of $BiVO_4$. Controlling the morphology and crystal growth of $BiVO_4$ is a common approach to increase the exposed {010} facets of $BiVO_4$. Several studies reported that $BiVO_4$ with dendritic or shuriken-like structures exhibited high exposed {010} facets and enhanced photocatalytic activity [95,99,110–113].

First of all, it should be noted that the mentioned facets, corresponding to the enhanced photocatalytic activity of $BiVO_4$, are {010} facets of the space group no. 15 with *I2/a* setting. While most research used the *I2/a* setting [44,80,99], *I2/b and C2/c* settings were also used in some studies [114–116]. Thus, the low indices of crystal facets in *I2/a* and their corresponding facets in the *I2/b and C2/c* settings are listed in Table 2-4.

Table 2-4. Low indices of crystal face in *I2/a* for monoclinic $BiVO_4$, and the matching ones in the settings *I2/b and C2/c.* [115]

Settings	Low indices of crystal face						
*I*2/*a*	{001}	{100}	{010}	{011}	{110}	$\{10\bar{1}\}$	$\{11\bar{1}\}$
*I*2/*b*	{100}	{010}	{001}	{101}	{011}	{110}	{111}
*C*2/*c*	{100}	$\{\bar{1}01\}$	{010}	$\{\bar{1}10\}$	$\{\bar{1}11\}$	{001}	{011}

A common strategy to control the morphology and increase the exposure of {010} facets of $BiVO_4$ is to utilize a structure-directing agent in the synthesis, such

as $TiCl_3$ [80], NaCl [100,117,118], ammonium carbonate [79], ethylenediamine [76], and glycerol [119]. It is worth mentioning that both $TiCl_3$ and NaCl contain Cl^- ions, which could be the main reason for the increase in the exposed {010} facets of $BiVO_4$ because Cl^- ions were found to stabilize the {010} facets, as reported by Xie et al. [118]. They conducted density functional theory (DFT) calculations and found that the surface energy of {010} facet was reduced when Cl^- ions were adsorbed on the said facet. Thus, the crystals of $BiVO_4$ grew slowly in [010] direction, resulting in preferential crystal growth along the {010} planes and promoting the exposure of {010} facets [118]. However, another study conducted by Wang et al. [80] demonstrated that some metal chloride, such as $AlCl_3$, CuCl, $ZrCl_4$, and $FeCl_2$, exhibited no significant effect on the {010} facets of $BiVO_4$. It might be due to the synthesis condition and Cl^- concentration in the solution.

The enhanced {010} facets of $BiVO_4$ are also reported in some research, using $BiCl_3$ as a source of Bi^{3+} for $BiVO_4$ synthesis [99,114]. $BiCl_3$ also contains Cl^- ions, which could be the cause of the enhanced {010} facets. However, the synthesis route of $BiVO_4$ using $BiCl_3$ may be different from the one using the directing agent containing Cl^- ions. Generally, the directing agent containing Cl^- was used at a later stage of $BiVO_4$ preparation [80,118], thus, tz-$BiVO_4$ would be formed before the addition of Cl^- ions, as shown in reaction (2-4). Whereas, when $BiCl_3$ is hydrolyzed, the reaction (2-1) and (2-2) occur to produce BiO^+, which then reacts with Cl^- to form BiOCl precipitate [reaction (2-5) below] [120]. In this synthesis route, the formation of BiOCl happens before the addition of VO_3^- ions. As a result, BiOCl may act as an intermediate before transforming into $BiVO_4$, as shown in reaction (2.6). The possible reactions are shown as follows [114,120,121]:

$$BiO^+ + Cl^- \rightleftharpoons BiOCl \downarrow \quad (2\text{-}5)$$

$$BiOCl \downarrow + VO_3^- \rightleftharpoons BiVO_4 \downarrow + Cl^- \quad (2\text{-}6)$$

Moreover, the Cl^- concentration is reported to affect the formation of BiOCl [122]. Therefore, in addition to the effect on the {010} facets of $BiVO_4$, changing

in Cl^- concentration in the preparation route with BiOCl as intermediate would significantly influence the properties of $BiVO_4$, especially its crystal growth and morphology. Moreover, this technique may produce $BiVO_4$ with various morphologies, possibly including the shuriken-like or dendritic structure since there is a report [112] of the dendritic structure obtained via $BiVO_4$ preparation with BiOCl as intermediate. However, the effect of Cl^- concentration on $BiVO_4$ using this approach has not yet been explored.

2.4.2. Bandgap modification

Bandgap engineering is one of the important techniques to improve light absorption efficiency and photocatalytic activity of photocatalysts. Many approaches have been carried out for bandgap modification, including doping [88,123], modifying oxygen vacancies [89,124], and building composites with other photocatalysts [125]. Among them, controlling oxygen vacancies is one of the promising techniques and is often used to tune the bandgap of the oxide materials.

Oxygen vacancies are common point defects found in metal oxides [126,127]. The oxygen vacancies in the oxides are reported to create defect levels inside the electronic bandgap, either just below the bottom end of the conduction band or just above the upper end of the valence band [127,128]. It would result in a decrease of the bandgap due to overlapping of the defect states with either the conduction band minimum or the valence band maximum [127,128]. The techniques for introducing oxygen vacancies in the oxides involve the oxygen-deficient environment, chemical reduction, plasma treatment and hydrogen treatment [89,127,129]. In addition, thermal treatment is also an effective technique to control oxygen vacancies in oxide materials because calcining the oxide in air (oxygen-rich atmosphere) could reduce oxygen vacancies [130,131], while an opposite outcome was obtained if the oxide was calcined in an oxygen-deficient atmosphere (N_2, H_2, and Ar) [88,89,132].

Although the effect of calcination in the oxygen-deficient atmosphere on oxygen vacancies has been studied on $BiVO_4$ [88,89,132], studies on calcination in the oxygen-rich atmosphere have not been focused regarding oxygen vacancies in

$BiVO_4$ [70,133–136]. Since either atmospheric conditions of thermal treatment (oxygen-rich or oxygen-deficient atmosphere) may alter oxygen vacancies in $BiVO_4$, research on the influence of both calcination conditions is needed to achieve greater insight in controlling oxygen vacancies and tuning bandgap of $BiVO_4$.

2.4.3. Producing composite

Composite photocatalyst has proved very effective in achieving greater photocatalytic performance, compared with pure photocatalyst [23,54,137,138]. It is attributed to the heterojunction and its hybrid energy band structure, allowing charge transfer between photocatalysts, which in turn promotes charge separation and suppresses the photoinduced electron–hole recombination [11,54,139].

The heterojunction composite can be categorized into three types [140], as shown in Fig. 2-10. Type I heterojunction involves transferring electrons and holes from both CB and VB of a wider-bandgap material (TiO_2), respectively, to those of narrower-bandgap material (Fe_2O_3). Although the formation of heterojunction in type I can enhance the photocatalytic activity by facilitating charge transfer and improving the charge separation efficiency, redox ability of the heterojunction is weakened due to accumulation of electrons and holes at the narrower-bandgap material [141]. In type II heterojunction, a material possesses both CB and VB positions more positive than those of another material. In this system, there are two possible charge migration pathways between both materials. Taking WO_3 and $BiVO_4$ as an example of the first pathway, electrons from CB of $BiVO_4$ migrate to that of WO_3, while holes from VB of WO_3 transfer to that of $BiVO_4$, ascribed to the nature of charge transfer. The result of this system is similar to type I, in which the charge separation efficiency is improved at the cost of weakening the redox ability. However, if a Z-scheme is established in the heterojunction, the second charge transfer pathway occurs. In the Z-scheme system, electrons from CB of material combine with holes from VB of another material, as shown in Fig. 2-10, in which $BiVO_4$ and g-C_3N_4 [142] are used as an example. It is a desirable pathway because not only is the charge separation efficiency improved, but also the redox ability of the heterojunction is enhanced. Lastly, type III heterojunction represented by

$BiVO_4$ and Sb_3Se_3 is displayed in Fig. 2-10. The band structure of Sb_3Se_3 is exceptionally more negative than that of $BiVO_4$. The benefit of type III is similar to that of Z-scheme in type II as both charge transfer and redox ability are enhanced due to the recombination of electrons from CB of $BiVO_4$ and holes from VB of Sb_3Se_3 [140,142].

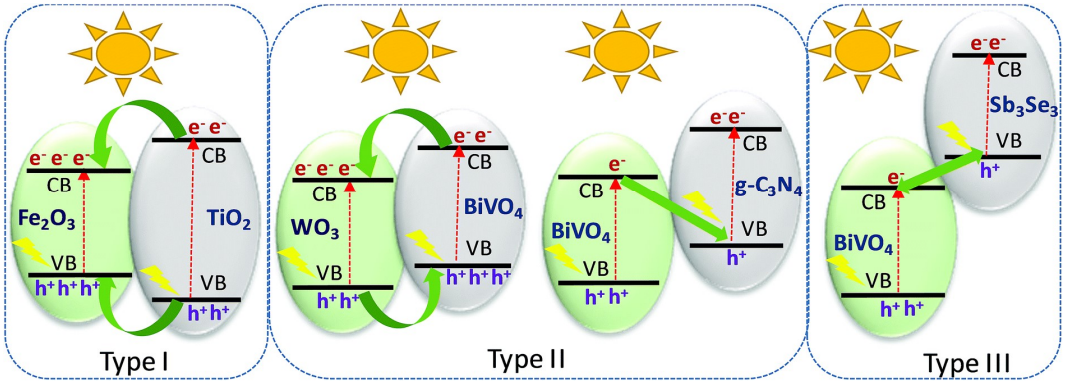

Fig. 2-10. Schematic representation of three different types of heterojunctions and their band alignments [140]. The green arrows represent the charge (electrons and holes) migration.

$BiVO_4$ has been successfully incorporated with other materials, such as Bi_2S_3 [105], CdS [5], TiO_2 [108], BiOCl [143], and $LaVO_4$ [138]. The photocatalytic performances of the $BiVO_4$-based composites are greatly improved. Some studies have reported that the Z-scheme process was established in the system when incorporated with CdS [5], Cu_2O [107], and g-C_3N_4 [137]. As a result, the redox ability and the photocatalytic activity of the composite were enhanced simultaneously, which are very useful for applications such as water splitting and CO_2 reduction.

Although there have been many reports focusing on $BiVO_4$-based composites as described above, those studies did not focus on the chemical reaction between two photocatalysts that could produce another material. One of the possible reasons is that those materials may not easily react with $BiVO_4$ due to the high chemical stability of $BiVO_4$. However, Wang et al. [4] have suggested that Bi^{3+} and S^{2-} ions have a strong chemical interaction, which could produce Bi_2S_3. In their study, they

produced a ternary $BiVO_4/Bi_2S_3/MoS_2$ composite by synthesizing MoS_2 in the presence of $BiVO_4$ via hydrothermal synthesis. During the reaction, not only did S^{2-} ions from thioacetamide react with Mo^{4+}, but also $BiVO_4$, in turn producing both MoS_2 and Bi_2S_3. Another study from Yu et al. [144] has also reported the preparation of ternary $Bi_2S_3/SnS_2/Bi_2O_3$ composite via a one-pot solvothermal method, in which $Bi(NO_3)_3 \cdot 5H_2O$, $SnCl_2 \cdot 2H_2O$, and CH_4N_2S were mixed together. The formation of Bi_2S_3 was also due to the interaction between Bi^{3+} and S^{2-} ions during the synthesis. Thus, in both studies, the formation of Bi_2S_3 happened when S^{2-} ions reacted either with $BiVO_4$ or with Bi^{3+} ions in the solution.

To date, there is no research on the formation of Bi_2S_3 from the chemical reaction between $BiVO_4$ and another metal sulfide as starting materials. This research can be intriguing to study and explore because individual photocatalysts can be prepared and designed separately to achieve desirable photocatalytic performance. Then, the photocatalytic activity may be further improved by incorporation of both photocatalysts via a chemical reaction, resulting in producing Bi_2S_3 as interface and facilitating charge transfer between both photocatalysts.

2.5. Summary

The photocatalysis field has garnered much attention from both academic and industrial sectors due to its potential applications, especially pollutant degradation, for future sustainable development. The literature provides an overview and recent progress in photocatalysts, especially $BiVO_4$, which has emerged as a promising photocatalyst owing to its many merits. However, $BiVO_4$ still suffers from drawbacks (poor charge separation and rapid combination rate of photogenerated electrons and holes), which hinder its photocatalytic performance. Many approaches have been employed to improve the photocatalytic activity by either remedying the problems (controlling exposed facets of $BiVO_4$ and incorporating with other photocatalysts) or enhancing another aspect of $BiVO_4$ such as light absorption efficiency (bandgap reduction). Despite the fact that many effective techniques have been done for enhancing the photocatalytic performance of $BiVO_4$

thus far, some parts of research areas have not been explored and studied. These interesting areas are revealed as follows:

Firstly, morphology and crystal growth of $BiVO_4$ may be influenced by BiOCl intermediate when there is a change in concentration of Cl^- in the precursor for $BiVO_4$ preparation via hydrothermal synthesis. Thus, various morphologies (possibly including shuriken-like structure) of $BiVO_4$ may be obtained using this technique. Secondly, thermal treatment of $BiVO_4$ under different atmospheric conditions may be used to control oxygen vacancies and modify bandgap of $BiVO_4$. Lastly, incorporating $BiVO_4$ with another photocatalyst via chemical reaction may further enhance their photocatalytic performance due to the formation of another component, which potentially acts as an interface connecting both photocatalysts, consequently facilitating the charge transfer in the composite.

Reference

[1] A. Fujishima, K. Honda, Electrochemical photolysis of water at a semiconductor electrode, Nature. 238 (1972) 37–38. https://doi.org/10.1038/238037a0.

[2] A. Fujishima, X. Zhang, D.A. Tryk, TiO_2 photocatalysis and related surface phenomena, Surf. Sci. Rep. 63 (2008) 515–582. https://doi.org/10.1016/j.surfrep.2008.10.001.

[3] D.D. Dionysiou, G. Li Puma, J. Ye, J. Schneider, D. Bahnemann, Photocatalysis, The Royal Society of Chemistry, 2016. https://doi.org/10.1039/9781782627104.

[4] J. Wang, J. Jin, X. Wang, S. Yang, Y. Zhao, Y. Wu, S. Dong, J. Sun, J. Sun, Facile fabrication of novel $BiVO_4/Bi_2S_3/MoS_2$ n-p heterojunction with enhanced photocatalytic activities towards pollutant degradation under natural sunlight, J. Colloid Interface Sci. 505 (2017) 805–815. https://doi.org/10.1016/j.jcis.2017.06.085.

[5] Z.H. Wei, Y.F. Wang, Y.Y. Li, L. Zhang, H.C. Yao, Z.J. Li, Enhanced photocatalytic CO_2 reduction activity of Z-scheme $CdS/BiVO_4$ nanocomposite with thinner $BiVO_4$ nanosheets, J. CO2 Util. 28 (2018) 15–25. https://doi.org/10.1016/j.jcou.2018.09.008.

[6] R. V. Prihod'ko, N.M. Soboleva, R. V Prihod, N.M. Soboleva, Photocatalysis: Oxidative processes in water treatment, 2013. https://doi.org/10.1155/2013/168701.

[7] A.O. Ibhadon, P. Fitzpatrick, Heterogeneous photocatalysis: recent advances and applications, Catal. . 3 (2013). https://doi.org/10.3390/catal3010189.

[8] Y. Peng, H. Wu, M. Yuan, F.F. Li, X. Zou, Y.H. Ng, H.Y. Hsu, Chemical reduction-induced surface oxygen vacancies of $BiVO_4$ photoanodes with enhanced photoelectrochemical performance, Sustain. Energy Fuels. 5 (2021) 2284–2293. https://doi.org/10.1039/d0se01901a.

[9] J. Xiao, H. Huang, Q. Huang, L. Zhao, X. Li, X. Hou, H. Chen, Y. Li, Suppressing the electron–hole recombination rate in hematite photoanode with a rapid cooling treatment, J. Catal. 350 (2017) 48–55. https://doi.org/https://doi.org/10.1016/j.jcat.2017.02.001.

[10] Q.P. Zhang, X.N. Xu, Y.T. Liu, M. Xu, S.H. Deng, Y. Chen, H. Yuan, F. Yu,

Y. Huang, K. Zhao, S. Xu, G. Xiong, A feasible strategy to balance the crystallinity and specific surface area of metal oxide nanocrystals, Sci. Rep. 7 (2017) 46424. https://doi.org/10.1038/srep46424.

[11] F. Li, D.Y.C. Leung, Highly enhanced performance of heterojunction $Bi_2S_3/BiVO_4$ photoanode for photoelectrocatalytic hydrogen production under solar light irradiation, Chem. Eng. Sci. 211 (2020) 115266. https://doi.org/10.1016/j.ces.2019.115266.

[12] S.S. Gill, N. Tuteja, Reactive oxygen species and antioxidant machinery in abiotic stress tolerance in crop plants, Plant Physiol. Biochem. 48 (2010) 909–930. https://doi.org/10.1016/j.plaphy.2010.08.016.

[13] H. Ren, Semiconducting $BiVO_4$ and TiO_2 thin films for photoelectrochemical water splitting and photodegradation, doctoral dissertation, University of New South Wales, 2019. http://handle.unsw.edu.au/1959.4/61365

[14] L. Yu, X. Zhang, G. Li, Y. Cao, Y. Shao, D. Li, Highly efficient $Bi_2O_2CO_3$/BiOCl photocatalyst based on heterojunction with enhanced dye-sensitization under visible light, Appl. Catal. B Environ. 187 (2016) 301–309. https://doi.org/10.1016/j.apcatb.2016.01.045.

[15] T. Tachikawa, S. Tojo, K. Kawai, M. Endo, M. Fujitsuka, T. Ohno, K. Nishijima, Z. Miyamoto, T. Majima, Photocatalytic oxidation reactivity of holes in the sulfur- and carbon-doped TiO_2 powders studied by time-resolved diffuse reflectance spectroscopy, J. Phys. Chem. B. 108 (2004) 19299–19306. https://doi.org/10.1021/jp0470593.

[16] A. Ajmal, I. Majeed, R.N. Malik, H. Idriss, M.A. Nadeem, Principles and mechanisms of photocatalytic dye degradation on TiO_2 based photocatalysts: a comparative overview, RSC Adv. 4 (2014) 37003–37026. https://doi.org/10.1039/c4ra06658h.

[17] K. Iqbal, A. Iqbal, A.M. Kirillov, B. Wang, W. Liu, Y. Tang, A new Ce-doped MgAl-LDH@Au nanocatalyst for highly efficient reductive degradation of organic contaminants, J. Mater. Chem. A. 5 (2017) 6716–6724. https://doi.org/10.1039/C6TA10880F.

[18] K. Iqbal, A. Iqbal, A.M. Kirillov, W. Liu, Y. Tang, Hybrid metal-organic-framework/inorganic nanocatalyst toward highly efficient discoloration of organic dyes in aqueous medium, Inorg. Chem. 57 (2018) 13270–13278. https://doi.org/10.1021/acs.inorgchem.8b01826.

[19] P. Singh, A. Borthakur, P.K. Mishra, D. Tiwary, Nano-materials as photocatalysts for degradation of environmental pollutants: challenges and possibilities, Elsevier, 2019.

[20] C. Lops, A. Ancona, K. Di, B. Dumontel, N. Garino, Sonophotocatalytic degradation mechanisms of Rhodamine B dye via radicals generation by micro- and nano-particles of ZnO, Appl. Catal. B Environ. 243 (2019) 629–640. https://doi.org/10.1016/j.apcatb.2018.10.078.

[21] A. Akbar, A. Payan, M. Fattahi, S. Jor, B. Kakavandi, Photocatalytic degradation of rhodamine B and real textile wastewater using Fe-doped TiO_2 anchored on reduced graphene oxide (Fe-TiO_2/rGO): Characterization and feasibility , mechanism and pathway studies, Appl. Surf. Sci. 462 (2018) 549–564. https://doi.org/10.1016/j.apsusc.2018.08.133.

[22] E. Huang, X. Yao, W. Wang, G. Wu, N. Guan, SnS_2 nanoplates with specific facets exposed for enhanced visible-light-driven photocatalysis, ChemPhotoChem. (2017) 60–69. https://doi.org/10.1002/cptc.201600026.

[23] Z. Zhang, C. Shao, X. Li, Y. Sun, M. Zhang, J. Mu, P. Zhang, Z. Guo, Y. Liu, Hierarchical assembly of ultrathin hexagonal SnS_2 nanosheets onto electrospun TiO_2 nanofibers: Enhanced photocatalytic activity based on photoinduced interfacial charge transfer, Nanoscale. 5 (2013) 606–618. https://doi.org/10.1039/c2nr32301j.

[24] J. Cao, B. Xu, H. Lin, B. Luo, S. Chen, Novel Bi_2S_3-sensitized BiOCl with highly visible light photocatalytic activity for the removal of rhodamine B, Catal. Commun. 26 (2012) 204–208. https://doi.org/10.1016/j.catcom.2012.05.025.

[25] X. Xu, Y. Sun, Z. Fan, D. Zhao, S. Xiong, B. Zhang, S. Zhou, G. Liu, Mechanisms for $\cdot O^{2-}$ and ·OH production on flowerlike $BiVO_4$ photocatalysis based on electron spin resonance, Front. Chem. 6 (2018) 1–12. https://doi.org/10.3389/fchem.2018.00064.

[26] K.K. Bera, M. Chakraborty, M. Mondal, S. Banik, S.K. Bhattacharya, Synthesis of α-β Bi_2O_3 heterojunction photocatalyst and evaluation of reaction mechanism for degradation of RhB dye under natural sunlight, Ceram. Int. 46 (2020) 7667–7680. https://doi.org/10.1016/j.ceramint.2019.11.269.

[27] H. Luo, J. Guo, T. Shen, H. Zhou, J. Liang, S. Yuan, Study on the catalytic performance of $LaMnO_3$ for the RhB degradation, J. Taiwan Inst. Chem. Eng.

109 (2020) 15–25. https://doi.org/10.1016/j.jtice.2020.01.011.

[28] D. Li, W. Shi, W. Zheng, Controlled synthesis of m-$BiVO_4$ dendrites for enhanced photocatalytic activity, J. Cryst. Growth. 448 (2016) 93–96. https://doi.org/10.1016/j.jcrysgro.2016.05.028.

[29] G. Cheng, Y. Wei, J. Xiong, F. Xu, J. Ding, S. Guo, R. Chen, Sorbitol-employed hydrothermal carbonization to TiO_2@C mesoporous hybrids with promoted visible light utilization and excellent photosensitization stability, J. Alloys Compd. 723 (2017) 948–959. https://doi.org/10.1016/j.jallcom.2017.06.317.

[30] Y. Hu, D. Li, F. Sun, H. Wang, Y. Weng, W. Xiong, Y. Shao, One-pot template-free synthesis of heterophase $BiVO_4$ microspheres with enhanced photocatalytic activity, RSC Adv. 5 (2015) 54882–54889. https://doi.org/10.1039/c5ra09785a.

[31] W. Zhao, Z. Wei, L. Ma, J. Liang, X. Zhang, Ag_2S quantum dots based on flower-like SnS_2 as matrix and enhanced photocatalytic degradation, Mater. . 12 (2019). https://doi.org/10.3390/ma12040582.

[32] Y. Li, Q. Yang, Z. Wang, G. Wang, B. Zhang, Q. Zhang, D. Yang, Rapid fabrication of SnO_2 nanoparticle photocatalyst: computational understanding and photocatalytic degradation of organic dye, Inorg. Chem. Front. 5 (2018) 3005–3014. https://doi.org/10.1039/C8QI00688A.

[33] Y. Tan, Z. Zhang, F. Guo, R. Guo, H. Bai, B. Zhang, X. Li, Q. Yang, X. Liu, Effect of morphology transformation on photocatalytic performance of CdS crystal, J. Mater. Sci. Mater. Electron. 31 (2020) 20315–20324. https://doi.org/10.1007/s10854-020-04551-9.

[34] H. Hao, X. Lang, Metal sulfide photocatalysis: visible-light-Induced organic transformations, ChemCatChem. 11 (2019) 1378–1393. https://doi.org/10.1002/cctc.201801773.

[35] M.M. Khan, S.F. Adil, A. Al-Mayouf, Metal oxides as photocatalysts, J. Saudi Chem. Soc. 19 (2015) 462–464. https://doi.org/10.1016/j.jscs.2015.04.003.

[36] A.J. Haider, Z.N. Jameel, I.H.M. Al-Hussaini, Review on: Titanium Dioxide Applications, Energy Procedia. 157 (2019) 17–29. https://doi.org/https://doi.org/10.1016/j.egypro.2018.11.159.

[37] G. Li, Y. Bai, W.F. Zhang, Difference in valence band top of $BiVO_4$ with

different crystal structure, Mater. Chem. Phys. 136 (2012) 930–934. https://doi.org/https://doi.org/10.1016/j.matchemphys.2012.08.023.

[38] S. Mridha, D. Basak, Aluminium doped ZnO films: electrical, optical and photoresponse studies, J. Phys. D. Appl. Phys. 40 (2007) 6902–6907. https://doi.org/10.1088/0022-3727/40/22/008.

[39] Y.C. Zhang, Z.N. Du, K.W. Li, M. Zhang, Size-controlled hydrothermal synthesis of SnS_2 nanoparticles with high performance in visible light-driven photocatalytic degradation of aqueous methyl orange, Sep. Purif. Technol. 81 (2011) 101–107. https://doi.org/10.1016/j.seppur.2011.07.016.

[40] H.C. Liao, M.C. Wu, M.H. Jao, C.M. Chuang, Y.F. Chen, W.F. Su, Synthesis, optical and photovoltaic properties of bismuth sulfide nanorods, CrystEngComm. 14 (2012) 3645–3652. https://doi.org/10.1039/C2CE06154F.

[41] X. Li, J. Yu, M. Jaroniec, Hierarchical photocatalysts, Chem. Soc. Rev. 45 (2016) 2603–2636. https://doi.org/10.1039/c5cs00838g.

[42] D.P. Jaihindh, B. Thirumalraj, S.M. Chen, P. Balasubramanian, Y.P. Fu, Facile synthesis of hierarchically nanostructured bismuth vanadate: An efficient photocatalyst for degradation and detection of hexavalent chromium, J. Hazard. Mater. 367 (2019) 647–657. https://doi.org/10.1016/j.jhazmat.2019.01.017.

[43] T. Zhang, Y. Liu, S. Jiang, B. Li, J. Wang, X. Shao, D. Wang, K. Wang, Z. Yan, Bacitracin-assisted synthesis of spherical $BiVO_4$ nanoparticles with C doping for remarkable photocatalytic performance under visible light, CrystEngComm. 22 (2020) 1812–1821. https://doi.org/10.1039/c9ce01908a.

[44] G. Zhao, W. Liu, Y. Hao, Z. Zhang, Q. Li, S. Zang, Nanostructured shuriken-like $BiVO_4$ with preferentially exposed {010} facets: Preparation, formation mechanism, and enhanced photocatalytic performance, Dalt. Trans. 47 (2018) 1325–1336. https://doi.org/10.1039/c7dt04431c.

[45] J. Cao, J. He, J. Ye, K. Ge, Y. Zhang, Y. Yang, Urchin-like Bi_2S_3/Ag nanostructures for photocatalytic reduction of Cr(VI), ACS Appl. Nano Mater. 4 (2021) 1260–1269. https://doi.org/10.1021/acsanm.0c02858.

[46] Z. Wu, L. Chen, C. Xing, D. Jiang, J. Xie, M. Chen, Controlled synthesis of Bi_2S_3/ZnS microspheres by an in situ ion-exchange process with enhanced visible light photocatalytic activity, J. Chem. Soc. Dalt. Trans. 42 (2013)

12980–12988. https://doi.org/10.1039/c3dt50984b.

[47] J. Yu, C.Y. Xu, F.X. Ma, S.P. Hu, Y.W. Zhang, L. Zhen, Monodisperse SnS_2 nanosheets for high-performance photocatalytic hydrogen generation, ACS Appl. Mater. Interfaces. (2014). https://doi.org/10.1021/am506396z.

[48] G. Li, R. Su, J. Rao, J. Wu, P. Rudolf, G.R. Blake, R.A. de Groot, F. Besenbacher, T.T.M. Palstra, Band gap narrowing of SnS_2 superstructures with improved hydrogen production, J. Mater. Chem. A. 4 (2016) 209–216. https://doi.org/10.1039/C5TA07283B.

[49] G. Zhang, X. Du, Y. Wang, H. Wang, W. Wang, Z. Fu, Controllable synthesis of SnS_2 nanostructures with high adsorption and photocatalytic activities, Mater. Sci. Semicond. Process. 64 (2017) 77–84. https://doi.org/10.1016/j.mssp.2017.03.010.

[50] I. Shown, S. Samireddi, Y.C. Chang, R. Putikam, P.H. Chang, A. Sabbah, F.Y. Fu, W.F. Chen, C.I. Wu, T.Y. Yu, P.W. Chung, M.C. Lin, L.C. Chen, K.H. Chen, Carbon-doped SnS_2 nanostructure as a high-efficiency solar fuel catalyst under visible light, Nat. Commun. 9 (2018). https://doi.org/10.1038/s41467-017-02547-4.

[51] S. Guo, P. Yang, Y. Zhao, X. Yu, Y. Wu, H. Zhang, B. Yu, B. Han, M.W. George, Z. Liu, Direct Z-scheme heterojunction of SnS_2/sulfur-bridged covalent triazine frameworks for visible-light-driven CO_2 photoreduction, ChemSusChem. 13 (2020) 6278–6283. https://doi.org/https://doi.org/10.1002/cssc.202000712.

[52] H. Ahmad, S.K. Kamarudin, L.J. Minggu, M. Kassim, Hydrogen from photo-catalytic water splitting process: A review, Renew. Sustain. Energy Rev. 43 (2015) 599–610. https://doi.org/https://doi.org/10.1016/j.rser.2014.10.101.

[53] S.L. Lee, C.-J. Chang, Recent Progress on Metal sulfide composite nanomaterials for photocatalytic hydrogen production, Catal. . 9 (2019). https://doi.org/10.3390/catal9050457.

[54] Y.C. Zhang, Z.N. Du, K.W. Li, M. Zhang, D.D. Dionysiou, High-performance visible-light-driven SnS_2/SnO_2 nanocomposite photocatalyst prepared via in situ hydrothermal oxidation of SnS_2 nanoparticles, ACS Appl. Mater. Interfaces. 3 (2011) 1528–1537. https://doi.org/10.1021/am200102y.

[55] E.B. Faulkner, R.J. Schwartz, High performance pigments, John Wiley &

Sons, 2009.

[56] S.S. Dunkle, R.J. Helmich, K.S. Suslick, $BiVO_4$ as a visible-light photocatalyst prepared by ultrasonic spray pyrolysis, J. Phys. Chem. C. 113 (2009) 11980–11983. https://doi.org/10.1021/jp903757x.

[57] C. Ravidhas, A. Juliat Josephine, P. Sudhagar, A. Devadoss, C. Terashima, K. Nakata, A. Fujishima, A. Moses Ezhil Raj, C. Sanjeeviraja, Facile synthesis of nanostructured monoclinic bismuth vanadate by a co-precipitation method: Structural, optical and photocatalytic properties, Mater. Sci. Semicond. Process. 30 (2015) 343–351. https://doi.org/10.1016/j.mssp.2014.10.026.

[58] H.S. Han, S. Shin, D.H. Kim, I.J. Park, J.S. Kim, P.S. Huang, J.K. Lee, I.S. Cho, X. Zheng, Boosting the solar water oxidation performance of a $BiVO_4$ photoanode by crystallographic orientation control, Energy Environ. Sci. 11 (2018) 1299–1306. https://doi.org/10.1039/c8ee00125a.

[59] A. Kudo, K. Omori, H. Kato, A novel aqueous process for preparation of crystal form-controlled and highly crystalline $BiVO_4$ powder from layered vanadates at room temperature and its photocatalytic and photophysical properties, J. Am. Chem. Soc. 121 (1999) 11459–11467. https://doi.org/10.1021/ja992541y.

[60] V. Rajalingam, Synthesis and Characterization of $BiVO_4$ nanostructured materials : application to photocatalysis, doctoral dissertation, Université du Maine, 2014. https://tel.archives-ouvertes.fr/tel-01150464/file/2014LEMA1018.pdf.

[61] A.K. Bhattacharya, K.K. Mallick, A. Hartridge, Phase transition in $BiVO_4$, Mater. Lett. 30 (1997) 7–13. https://doi.org/https://doi.org/10.1016/S0167-577X(96)00162-0.

[62] Y. Park, K.J. Mc Donald, K.-S.S. Choi, K.J. McDonald, K.-S.S. Choi, Progress in bismuth vanadate photoanodes for use in solar water oxidation, Chem. Soc. Rev. 42 (2013) 2321–2337. https://doi.org/10.1039/C2CS35260E.

[63] J. Yu, A. Kudo, Effects of structural variation on the photocatalytic performance of hydrothermally synthesized $BiVO_4$, Adv. Funct. Mater. 16 (2006) 2163–2169. https://doi.org/10.1002/adfm.200500799.

[64] S. Tokunaga, H. Kato, A. Kudo, Selective preparation of monoclinic and

tetragonal $BiVO_4$ with scheelite structure and their photocatalytic properties, Chem. Mater. 13 (2001) 4624–4628. https://doi.org/10.1021/cm0103390.

[65] M. Noor, M.A. Al Mamun, M.A. Matin, M.F. Islam, S. Haque, F. Rahman, M.N. Hossain, M.A. Hakim, Effect of pH variation on structural, optical and shape morphology of $BiVO_4$ photocatalysts, ICECE 2018 - 10th Int. Conf. Electr. Comput. Eng. (2019) 81–84. https://doi.org/10.1109/ICECE.2018.8636721.

[66] G. Tan, L. Zhang, H. Ren, S. Wei, J. Huang, A. Xia, Effects of pH on the hierarchical structures and photocatalytic performance of $BiVO_4$ powders prepared via the microwave hydrothermal method, ACS Appl. Mater. Interfaces. 5 (2013) 5186–5193. https://doi.org/10.1021/am401019m.

[67] Y. Zhao, R. Li, L. Mu, C. Li, Significance of crystal morphology controlling in semiconductor-based photocatalysis: a case study on $BiVO_4$ photocatalyst, Cryst. Growth Des. 17 (2017) 2923–2928. https://doi.org/10.1021/acs.cgd.7b00291.

[68] T.S. Dabodiya, P. Selvarasu, A.V. Murugan, Tetragonal to monoclinic crystalline phases change of $BiVO_4$ via microwave-hydrothermal reaction: in correlation with visible-light-driven photocatalytic performance, Inorg. Chem. 58 (2019) 5096–5110. https://doi.org/10.1021/acs.inorgchem.9b00193.

[69] Z. Liang, Y. Cao, H. Qin, D. Jia, Low-heating solid-state chemical synthesis of monoclinic scheelite $BiVO_4$ with different morphologies and their enhanced photocatalytic property under visible light, Mater. Res. Bull. 84 (2016) 397–402. https://doi.org/https://doi.org/10.1016/j.materresbull.2016.08.038.

[70] M.F. Rahman, M.S. Haque, M. Hasan, M.A. Hakim, Fabrication of bismuth vanadate ($BiVO_4$) nanoparticles by a facile route, Trans. Electr. Electron. Mater. 20 (2019) 522–529. https://doi.org/10.1007/s42341-019-00144-4.

[71] T. Senasu, S. Youngme, K. Hemavibool, S. Nanan, Sunlight-driven photodegradation of oxytetracycline antibiotic by $BiVO_4$ photocatalyst, J. Solid State Chem. 297 (2021) 122088. https://doi.org/10.1016/j.jssc.2021.122088.

[72] G.S. Kamble, Y.C. Ling, Solvothermal synthesis of facet-dependent $BiVO_4$ photocatalyst with enhanced visible-light-driven photocatalytic degradation of organic pollutant: assessment of toxicity by zebrafish embryo, Sci. Rep.

10 (2020) 1–11. https://doi.org/10.1038/s41598-020-69706-4.

[73] H.E.A. Mohamed, S. Afridi, A.T. Khalil, T. Zohra, M.M. Alam, A. Ikram, Z.K. Shinwari, M. Maaza, Phytosynthesis of $BiVO_4$ nanorods using hyphaene thebaica for diverse biomedical applications, AMB Express. 9 (2019) 1–14. https://doi.org/10.1186/s13568-019-0923-1.

[74] L. Zhang, Z. Dai, G. Zheng, Z. Yao, J. Mu, Superior visible light photocatalytic performance of reticular $BiVO_4$ synthesized via a modified sol-gel method, RSC Adv. 8 (2018) 10654–10664. https://doi.org/10.1039/c8ra00554k.

[75] A. Helal, S.M. El-Sheikh, J. Yu, A.I. Eid, S.A. El-Haka, S.E. Samra, Novel synthesis of $BiVO_4$ using homogeneous precipitation and its enhanced photocatalytic activity, J. Nanoparticle Res. 22 (2020). https://doi.org/10.1007/s11051-020-04861-3.

[76] M. Hojamberdiev, G. Zhu, Z.C. Kadirova, J. Han, J. Liang, J. Zhou, X. Wei, P. Liu, Morphology-controlled growth of $BiVO_4$ crystals by hydrothermal method assisted with ethylene glycol and ethylenediamine and their photocatalytic activity, Mater. Chem. Phys. 165 (2015) 188–195. https://doi.org/10.1016/j.matchemphys.2015.09.015.

[77] X. Qi, X. Zhu, J. Wu, Q. Wu, X. Li, M. Gu, Controlled synthesis of $BiVO_4$ with multiple morphologies via an ethylenediamine-assisted hydrothermal method, Mater. Res. Bull. 59 (2014) 435–441. https://doi.org/10.1016/j.materresbull.2014.08.004.

[78] J.A. Darr, J. Zhang, N.M. Makwana, X. Weng, Continuous hydrothermal synthesis of inorganic nanoparticles: applications and future directions, Chem. Rev. 117 (2017) 11125–11238. https://doi.org/10.1021/acs.chemrev.6b00417.

[79] S.M. Thalluri, M. Hussain, G. Saracco, J. Barber, N. Russo, Green-synthesized $BiVO_4$ oriented along {040} facets for visible-light-driven ethylene degradation, Ind. Eng. Chem. Res. 53 (2014) 2640–2646. https://doi.org/10.1021/ie403999g.

[80] D. Wang, H. Jiang, X. Zong, Q. Xu, Y. Ma, G. Li, C. Li, Crystal facet dependence of water oxidation on $BiVO_4$ sheets under visible light irradiation, Chem. - A Eur. J. 17 (2011) 1275–1282. https://doi.org/10.1002/chem.201001636.

[81] M.J. O'Neil, R.S. of C. (Great Britain), The Merck index : an encyclopedia of chemicals, drugs, and biologicals, Royal Society of Chemistry, Cambridge, UK, 2013. p. 96

[82] S. Meng, T. Ogawa, H. Okumura, K.N. Ishihara, The effect of potassium chloride on $BiVO_4$ morphology and photocatalysis, J. Solid State Chem. 302 (2021) 122291. https://doi.org/10.1016/j.jssc.2021.122291.

[83] L. Zhou, W. Wang, L. Zhang, H. Xu, W. Zhu, Single-crystalline $BiVO_4$ microtubes with square cross-sections: microstructure, growth mechanism, and photocatalytic property, J. Phys. Chem. C. 111 (2007) 13659–13664. https://doi.org/10.1021/jp065155t.

[84] S. Phiankoh, R. Munprom, Effect of pH on crystal structure and morphology of hydrothermally-synthesized $BiVO_4$, Mater. Today Proc. 5 (2018) 9447–9452. https://doi.org/https://doi.org/10.1016/j.matpr.2017.10.123.

[85] D. Ressnig, R. Kontic, G.R. Patzke, Morphology control of $BiVO_4$ photocatalysts: PH optimization vs. self-organization, Mater. Chem. Phys. 135 (2012) 457–466. https://doi.org/10.1016/j.matchemphys.2012.05.008.

[86] A. Zhang, J. Zhang, N. Cui, X. Tie, Y. An, L. Li, Effects of pH on hydrothermal synthesis and characterization of visible-light-driven $BiVO_4$ photocatalyst, J. Mol. Catal. A Chem. 304 (2009) 28–32. https://doi.org/10.1016/j.molcata.2009.01.019.

[87] J.K. Cooper, S.B. Scott, Y. Ling, J. Yang, S. Hao, Y. Li, F.M. Toma, M. Stutzmann, K. V. Lakshmi, I.D. Sharp, Role of hydrogen in defining the n-type character of $BiVO_4$ photoanodes, Chem. Mater. 28 (2016) 5761–5771. https://doi.org/10.1021/acs.chemmater.6b01994.

[88] T.W. Kim, Y. Ping, G.A. Galli, K.S. Choi, Simultaneous enhancements in photon absorption and charge transport of bismuth vanadate photoanodes for solar water splitting, Nat. Commun. 6 (2015) 1–10. https://doi.org/10.1038/ncomms9769.

[89] H.L. Tan, A. Suyanto, A.T. De Denko, W.H. Saputera, R. Amal, F.E. Osterloh, Y.H. Ng, Enhancing the photoactivity of faceted $BiVO_4$ via annealing in oxygen-deficient condition, Part. Part. Syst. Charact. 34 (2017). https://doi.org/10.1002/ppsc.201600290.

[90] S. Na, S. Seo, H. Lee, Recent developments of advanced Ti^{3+}-self-doped TiO_2 for efficient visible-light-driven photocatalysis, Catal. . 10 (2020).

https://doi.org/10.3390/catal10060679.

[91] F.F. Abdi, T.J. Savenije, M.M. May, B. Dam, R. Van De Krol, The origin of slow carrier transport in $BiVO_4$ thin film photoanodes: A time-resolved microwave conductivity study, J. Phys. Chem. Lett. 4 (2013) 2752–2757. https://doi.org/10.1021/jz4013257.

[92] I. Abdellaoui, M.M. Islam, M. Remeika, Y. Higuchi, T. Kawaguchi, T. Harada, C. Budich, T. Maeda, T. Wada, S. Ikeda, T. Sakurai, Photocarrier recombination dynamics in $BiVO_4$ for visible light-driven water oxidation, J. Phys. Chem. C. 124 (2020) 3962–3972. https://doi.org/10.1021/acs.jpcc.9b10621.

[93] T.W. Kim, K.-S. Choi, Nanoporous $BiVO_4$ photoanodes with dual-layer oxygen evolution catalysts for solar water splitting, Science (80-.). 343 (2014) 990 LP – 994. https://doi.org/10.1126/science.1246913.

[94] M. Zhu, Q. Liu, W. Chen, Y. Yin, L. Ge, H. Li, K. Wang, Boosting the visible-light photoactivity of BiOCl/$BiVO_4$/N-GQD ternary heterojunctions based on internal Z-scheme charge transfer of N-GQDs: simultaneous band gap narrowing and carrier lifetime prolonging, ACS Appl. Mater. Interfaces. 9 (2017) 38832–38841. https://doi.org/10.1021/acsami.7b14412.

[95] C. Regmi, Y.K. Kshetri, R.P. Pandey, S.W. Lee, Visible-light-driven S and W co-doped dendritic $BiVO_4$ for efficient photocatalytic degradation of naproxen and its mechanistic analysis, Mol. Catal. 453 (2018) 149–160. https://doi.org/10.1016/j.mcat.2018.05.008.

[96] R. Li, F. Zhang, D. Wang, J. Yang, M. Li, J. Zhu, X. Zhou, H. Han, C. Li, Spatial separation of photogenerated electrons and holes among {010} and {110} crystal facets of $BiVO_4$, Nat. Commun. 4 (2013). https://doi.org/10.1038/ncomms2401.

[97] H.L. Tan, X. Wen, R. Amal, Y.H. Ng, $BiVO_4$ {010} and {110} relative exposure extent: governing factor of surface charge population and photocatalytic activity, J. Phys. Chem. Lett. 7 (2016) 1400–1405. https://doi.org/10.1021/acs.jpclett.6b00428.

[98] B. Zhang, Y. Xiang, M. Guo, J. Wang, K. Liu, W. Lin, G. Ma, Fabrication of a facet-oriented $BiVO_4$ photoanode by particle engineering for promotion of charge separation efficiency, ACS Appl. Energy Mater. 4 (2021) 4259–4268. https://doi.org/10.1021/acsaem.1c00694.

[99] Y. Li, Z. Sun, S. Zhu, Y. Liao, Z. Chen, D. Zhang, Fabrication of $BiVO_4$ nanoplates with active facets on graphene sheets for visible-light photocatalyst, Carbon N. Y. 94 (2015) 599–606. https://doi.org/10.1016/j.carbon.2015.07.042.

[100] L. Xia, J. Li, J. Bai, L. Li, S. Chen, B. Zhou, $BiVO_4$ photoanode with exposed (040) facets for enhanced photoelectrochemical performance, Nano-Micro Lett. 10 (2018) 1–10. https://doi.org/10.1007/s40820-017-0163-3.

[101] B. Baral, K. Parida, {040/110} Facet isotype heterojunctions with monoclinic scheelite $BiVO_4$, Inorg. Chem. (2020). https://doi.org/10.1021/acs.inorgchem.0c01465.

[102] R. Li, H. Han, F. Zhang, D. Wang, C. Li, Highly efficient photocatalysts constructed by rational assembly of dual-cocatalysts separately on different facets of $BiVO_4$, Energy Environ. Sci. 7 (2014) 1369–1376. https://doi.org/10.1039/c3ee43304h.

[103] B. Xu, A. Zada, G. Wang, Y. Qu, Boosting the visible-light photoactivities of $BiVO_4$ nanoplates by Eu doping and coupling CeO_x nanoparticles for CO_2 reduction and organic oxidation, Sustain. Energy Fuels. 3 (2019) 3363–3369. https://doi.org/10.1039/C9SE00409B.

[104] Y. Yang, S. Ajmal, X. Zheng, L. Zhang, Efficient nanomaterials for harvesting clean fuels from electrochemical and photoelectrochemical CO_2 reduction, Sustain. Energy Fuels. 2 (2018) 510–537. https://doi.org/10.1039/c7se00371d.

[105] M.A. Mahadik, H.-S. Chung, S.-Y. Lee, M. Cho, J.S. Jang, In-situ noble fabrication of $Bi_2S_3/BiVO_4$ hybrid nanostructure through a photoelectrochemical transformation process for solar hydrogen production, ACS Sustain. Chem. Eng. 6 (2018) 12489–12501. https://doi.org/10.1021/acssuschemeng.8b03140.

[106] F.Q. Zhou, J.C. Fan, Q.J. Xu, Y.L. Min, $BiVO_4$ nanowires decorated with CdS nanoparticles as Z-scheme photocatalyst with enhanced H_2 generation, Appl. Catal. B Environ. 201 (2017) 77–83. https://doi.org/10.1016/j.apcatb.2016.08.027.

[107] C. Kim, K.M. Cho, A. Al-Saggaf, I. Gereige, H.T. Jung, Z-scheme photocatalytic CO_2 conversion on three-dimensional $BiVO_4$/carbon-coated Cu_2O nanowire arrays under visible light, ACS Catal. 8 (2018) 4170–4177. https://doi.org/10.1021/acscatal.8b00003.

[108] Y. Hu, D. Li, Y. Zheng, W. Chen, Y. He, Y. Shao, X. Fu, G. Xiao, $BiVO_4/TiO_2$ nanocrystalline heterostructure: A wide spectrum responsive photocatalyst towards the highly efficient decomposition of gaseous benzene, Appl. Catal. B Environ. 104 (2011) 30–36. https://doi.org/https://doi.org/10.1016/j.apcatb.2011.02.031.

[109] W. Tu, Y. Zhou, Z. Zou, Photocatalytic conversion of CO_2 into renewable hydrocarbon fuels: State-of-the-art accomplishment, challenges, and prospects, Adv. Mater. 26 (2014) 4607–4626. https://doi.org/10.1002/adma.201400087.

[110] L. Chen, J. Wang, D. Meng, X. Wu, Y. Wang, E. Zhong, The pH-controlled {040} facets orientation of $BiVO_4$ photocatalysts with different morphologies for enhanced visible light photocatalytic performance, Mater. Lett. 162 (2016) 150–153. https://doi.org/10.1016/j.matlet.2015.09.138.

[111] Y. Lu, H. Shang, F. Shi, C. Chao, X. Zhang, B. Zhang, Preparation and efficient visible light-induced photocatalytic activity of m-$BiVO_4$ with different morphologies, J. Phys. Chem. Solids. 85 (2015) 44–50. https://doi.org/10.1016/j.jpcs.2015.04.016.

[112] Y. Zhu, M.W. Shah, C. Wang, Insight into the role of Ti^{3+} in photocatalytic performance of shuriken-shaped $BiVO_4/TiO_{2-x}$ heterojunction, Appl. Catal. B Environ. 203 (2017) 526–532. https://doi.org/10.1016/j.apcatb.2016.10.056.

[113] S. Sun, W. Wang, L. Zhou, H. Xu, Efficient methylene blue removal over hydrothermally synthesized starlike $BiVO_4$, Ind. Eng. Chem. Res. 48 (2009) 1735–1739. https://doi.org/10.1021/ie801516u.

[114] G. Xi, J. Ye, Synthesis of bismuth vanadate nanoplates with exposed {001} facets and enhanced visible-light photocatalytic properties, Chem. Commun. 46 (2010) 1893–1895. https://doi.org/10.1039/b923435g.

[115] G.L. Li, First-principles investigation of the surface properties of fergusonite-type monoclinic $BiVO_4$ photocatalyst, RSC Adv. 7 (2017) 9130–9140. https://doi.org/10.1039/c6ra28006d.

[116] Z. Zhao, W. Luo, Z. Li, Z. Zou, Density functional theory study of doping effects in monoclinic clinobisvanite $BiVO_4$, Phys. Lett. A. 374 (2010) 4919–4927. https://doi.org/https://doi.org/10.1016/j.physleta.2010.10.014.

[117] X. Yu, V. V. Ordomsky, A.Y. Khodakov, Selective deposition of cobalt and

copper oxides on $BiVO_4$ facets for enhancement of CO_2 photocatalytic reduction to hydrocarbons, ChemCatChem. 12 (2020) 740–749. https://doi.org/10.1002/cctc.201901115.

[118] S. Xie, Z. Shen, H. Zhang, J. Cheng, Q. Zhang, Y. Wang, Photocatalytic coupling of formaldehyde to ethylene glycol and glycolaldehyde over bismuth vanadate with controllable facets and cocatalysts, Catal. Sci. Technol. 7 (2017) 923–933. https://doi.org/10.1039/c6cy02510b.

[119] G. Zhao, W. Liu, J. Li, Q. Lv, W. Li, L. Liang, Facile synthesis of hierarchically structured $BiVO_4$ oriented along (010) facets with different morphologies and their photocatalytic properties, Appl. Surf. Sci. 390 (2016) 531–539. https://doi.org/10.1016/j.apsusc.2016.08.126.

[120] D. Diemente, Why is bismuth subchloride soluble in acid?, J. Chem. Educ. 74 (1997) 398–399. https://doi.org/10.1021/ed074p398.

[121] X. Zhu, F. Zhang, M. Wang, X. Gao, Y. Luo, J. Xue, Y. Zhang, J. Ding, S. Sun, J. Bao, C. Gao, A shuriken-shaped m-$BiVO_4$/{001}-TiO_2 heterojunction: Synthesis, structure and enhanced visible light photocatalytic activity, Appl. Catal. A Gen. 521 (2016) 42–49. https://doi.org/10.1016/j.apcata.2015.10.017.

[122] M.N. Ackermann, Why is Bismuth Subchloride Soluble in Acid?, J. Chem. Educ. 75 (1998) 523. https://doi.org/10.1021/ed075p523.

[123] C. Qin, H. Liao, F. Rao, J. Zhong, J. Li, One-pot hydrothermal preparation of Br-doped $BiVO_4$ with enhanced visible-light photocatalytic activity, Solid State Sci. 105 (2020) 106285. https://doi.org/10.1016/j.solidstatesciences.2020.106285.

[124] H. Liu, F. Zeng, Y. Lin, G. Wang, F. Pan, Correlation of oxygen vacancy variations to band gap changes in epitaxial ZnO thin films, Appl. Phys. Lett. 102 (2013). https://doi.org/10.1063/1.4804613.

[125] M.R.U.D. Biswas, W.C. Oh, Synthesis of $BiVO_4$-GO-PVDF nanocomposite: An excellent, newly designed material for high photocatalytic activity towards organic dye degradation by tuning band gap energies, Solid State Sci. 80 (2018) 22–30. https://doi.org/10.1016/j.solidstatesciences.2018.03.021.

[126] C. Künneth, R. Batra, G.A. Rossetti, R. Ramprasad, A. Kersch, Thermodynamics of phase stability and ferroelectricity from first principles,

2019. https://doi.org/10.1016/B978-0-08-102430-0.00006-1.

[127] F. Gunkel, D. V. Christensen, Y.Z. Chen, N. Pryds, Oxygen vacancies: The (in)visible friend of oxide electronics, Appl. Phys. Lett. 116 (2020). https://doi.org/10.1063/1.5143309.

[128] S. Wang, T. He, P. Chen, A. Du, K. Ostrikov, W. Huang, L. Wang, In situ formation of oxygen vacancies achieving near-complete charge separation in planar $BiVO_4$ photoanodes, Adv. Mater. 32 (2020) 1–10. https://doi.org/10.1002/adma.202001385.

[129] Q. Wang, S. Zhang, H. He, C. Xie, Y. Tang, C. He, M. Shao, H. Wang, Oxygen vacancy engineering in titanium dioxide for sodium storage, Chem. - An Asian J. 16 (2021) 3–19. https://doi.org/10.1002/asia.202001172.

[130] W. Yu, F. Chen, Y. Wang, L. Zhao, Rapid evaluation of oxygen vacancies-enhanced photogeneration of the superoxide radical in nano-TiO_2 suspensions, RSC Adv. 10 (2020) 29082–29089. https://doi.org/10.1039/d0ra06299e.

[131] K. Yamada, H. Yamane, S. Matsushima, H. Nakamura, K. Ohira, M. Kouya, K. Kumada, Effect of thermal treatment on photocatalytic activity of N-doped TiO_2 particles under visible light, Thin Solid Films. 516 (2008) 7482–7487. https://doi.org/10.1016/j.tsf.2008.03.041.

[132] G. Wang, Y. Ling, X. Lu, F. Qian, Y. Tong, J.Z. Zhang, V. Lordi, C. Rocha Leao, Y. Li, Computational and photoelectrochemical study of hydrogenated bismuth vanadate, J. Phys. Chem. C. 117 (2013) 10957–10964. https://doi.org/10.1021/jp401972h.

[133] M. Ganeshbabu, N. Kannan, P.S. Venkatesh, G. Paulraj, K. Jeganathan, D. MubarakAli, Synthesis and characterization of $BiVO_4$ nanoparticles for environmental applications, RSC Adv. 10 (2020) 18315–18322. https://doi.org/10.1039/d0ra01065k.

[134] P. Pookmanee, S. Kojinok, R. Puntharod, S. Sangsrichan, S. Phanichphant, Preparation and characterization of $BiVO_4$ powder by the sol-gel method, Ferroelectrics. 456 (2013) 45–54. https://doi.org/10.1080/00150193.2013.846197.

[135] S.R.M. Thalluri, C. Martinez-Suarez, A. Virga, N. Russo, G. Saracco, Insights from crystal size and band gap on the catalytic activity of monoclinic $BiVO_4$, Int. J. Chem. Eng. Appl. (2013) 305–309.

https://doi.org/10.7763/ijcea.2013.v4.315.

[136] Y. Shen, X. Wang, G. Zuo, F. Li, Y. Meng, Influence of heat treatment on photocatalytic performance of $BiVO_4$ synthesized by hydrothermal method, High Temp. Mater. Process. 2015 (2015) 853–856. https://doi.org/10.1515/htmp-2015-0070.

[137] J. Safaei, H. Ullah, N. Aida, M. Firdaus, M. Noh, M. Fairus, A.A. Tahir, N. Ahmad, M. Adib, Enhanced photoelectrochemical performance of Z-scheme g-C_3N_4/$BiVO_4$ photocatalyst, Appl. Catal. B Environ. 234 (2018) 296–310. https://doi.org/10.1016/j.apcatb.2018.04.056.

[138] N. Kumar, N. Krishnarao, S.A. Singh, Cocatalyst free Z-schematic enhanced H_2 evolution over $LaVO_4$/$BiVO_4$ composite photocatalyst using Ag as an electron mediator, Appl. Catal. B Environ. 220 (2018) 512–523. https://doi.org/10.1016/j.apcatb.2017.08.082.

[139] X. Li, Y. Li, J. Shen, M. Ye, A controlled anion exchange strategy to synthesize Bi_2S_3 nanoparticles/plate-like Bi_2WO_6 heterostructures with enhanced visible light photocatalytic activities for Rhodamine B, Ceram. Int. 42 (2016) 3154–3162. https://doi.org/10.1016/j.ceramint.2015.10.105.

[140] K. Afroz, M. Moniruddin, N. Bakranov, S. Kudaibergenov, N. Nuraje, A heterojunction strategy to improve the visible light sensitive water splitting performance of photocatalytic materials, J. Mater. Chem. A. 6 (2018) 21696–21718. https://doi.org/10.1039/c8ta04165b.

[141] B.J. Ng, L.K. Putri, X.Y. Kong, Y.W. Teh, P. Pasbakhsh, S.P. Chai, Z-Scheme photocatalytic systems for solar water splitting, Adv. Sci. 7 (2020). https://doi.org/10.1002/advs.201903171.

[142] S.N.F.M. Nasir, H. Ullah, M. Ebadi, A.A. Tahir, J.S. Sagu, M.A. Mat Teridi, New Insights into Se/$BiVO_4$ heterostructure for photoelectrochemical water splitting: A combined experimental and DFT study, J. Phys. Chem. C. 121 (2017) 6218–6228. https://doi.org/10.1021/acs.jpcc.7b01149.

[143] L. Song, Y. Pang, Y. Zheng, C. Chen, L. Ge, Design, preparation and enhanced photocatalytic activity of porous BiOCl/$BiVO_4$ microspheres via a coprecipitation-hydrothermal method, J. Alloys Compd. 710 (2017) 375–382. https://doi.org/10.1016/j.jallcom.2017.03.283.

[144] C. Yu, K. Wang, P. Yang, S. Yang, C. Lu, Y. Song, S. Dong, J. Sun, J. Sun, One-pot facile synthesis of Bi_2S_3/SnS_2/Bi_2O_3 ternary heterojunction as

advanced double Z-scheme photocatalytic system for efficient dye removal under sunlight irradiation, Appl. Surf. Sci. 420 (2017) 233–242. https://doi.org/10.1016/j.apsusc.2017.05.147.

3. Methods

This chapter describes materials and their purity used in this study as well as methods for characterization and photocatalytic measurement of the samples. As for sample preparation for each sample, it is described later in its respective chapter.

3.1. Materials

Thioacetamide (C_2H_5NS, 98%), acetic acid (CH_3COOH, 99.7%), ethylene glycol ($(CH_2OH)_2$, 99.5%), L-ascorbic acid ($C_6H_8O_6$, 99.6%), and thiourea (H_2NCSNH_2, 98%) were purchased from FUJIFILM Wako Pure Chemical Corporation (Osaka, Japan). The tin(IV) chloride pentahydrate ($SnCl_4 \cdot 5H_2O$, 98%), ammonium vanadate (V) (NH_4VO_3, 99.0%), bismuth (III) nitrate pentahydrate ($Bi(NO_3)_3 \cdot 5H_2O$ 99.5%), methanol (CH_3OH, 99.8%), and isopropyl alcohol ($(CH_3)_2CHOH$, 99.7%) were supplied by Nacalai Tesque (Kyoto, Japan). The rhodamine B ($C_{28}H_{31}ClN_2O_3$, > 95%) was purchased from Tokyo Chemical Industry (Tokyo, Japan). All chemicals were analytical grade and used without further purification. Deionized water (DI water) was obtained from the Direct-Q water purification system (Millipore).

3.2. Characterization

3.2.1. X-ray diffraction (XRD)

X-ray diffraction (XRD) is a widely used technique to determine crystal structures of materials. This thesis work used XRD data to investigate the crystal structures of the samples. XRD measurement was conducted using a Rigaku RINT2100 at 40 kV and 30 mA with Cu Kα radiation (λ = 0.15418 nm). Each sample was scanned in a 2θ angle range from 10° to 80°. The obtained diffraction

patterns were identified by matching with the standard pattern from ICDD (The International Centre for Diffraction Data) database.

3.2.2. Field emission scanning electron microscopy (FESEM)

Field Emission Scanning Electron Microscopy is one of the most used methods to study the morphology and microstructure of materials. FESEM uses electrons instead of light to capture micrograph images produced by detecting secondary and backscattered electrons. It requires a high vacuum in order to avoid the disturbance caused by gas molecules, which can interfere with the emitted secondary and backscattered electrons [1].

In this study, the microstructure and morphology of each sample were observed using an FESEM (Hitachi SU6600 Scanning Electron Microscope). It was performed at 15-20 kV with a working distance of around 10 mm. A small quantity of each sample powder was spread on a double-sided carbon tape. All samples were sputtered with Au to avoid a charging effect prior to FESEM analysis.

3.2.3. Energy dispersive x-ray spectroscopy (EDX or EDS)

Energy Dispersive X-ray spectroscopy is an analytical technique used to identify the element in the sample for elemental composition analysis. EDS is often included as a part of SEM due to the benefit of carrying out the elemental analysis and microstructure examination at the same time [1]. In this study, EDX data were obtained using Bruker EDX detector attached with FESEM and operated with accelerating voltage of 20 kV.

3.2.4. UV-Vis spectroscopy (UV-Vis)

UV-Vis spectroscopy is a characterization method to record absorption spectra of materials using ultraviolet (UV) and visible (Vis) light. The UV-Vis diffuse reflectance spectroscopy (DRS) is a useful technique to measure reflectance spectra of solid and powder samples.

Present work used DRS to study optical properties of the samples using reflectance spectrum obtained from a Lambda 750S UV/Vis/NIR

Spectrophotometer with $BaSO_4$ as reference. The reflectance spectra were converted to absorption spectra via the Kubelka–Munk function as shown below, in Eq. (3.1) [2,3]:

$$F(R) = \frac{\alpha}{S} = \frac{(1-R)^2}{2R} \tag{3.1}$$

where *F(R)*, *α*, *S*, and *R* are the Kubelka–Munk function, absorption coefficient, scattering coefficient, and reflectance, respectively. The calculated F(R) was plotted against wavelength to realize a light absorption graph.

The bandgaps (E_g) can be estimated using the following formula [2–4]:

$$\alpha h\upsilon = A(h\upsilon - E_g)^{\frac{n}{2}} \tag{3.2}$$

where α, hυ, and A are absorption coefficient, incident photon energy, and a constant associated with the material, respectively. The F(R) from Eq (3.1) is commonly used to replace α in the Tauc's plot ($(\alpha h\upsilon)^{2/n}$ vs. hυ) [3,5,6]. The value of n depends on transition types of semiconductors; 1 and 4 are for direct and indirect transition, respectively. In the case of this study, SnS_2, Bi_2S_3, and $BiVO_4$ are direct transition semiconductors; hence, n = 1 is used in Eq (3.2) [3,7]. Thus, the estimated E_g value of the sample was determined by extrapolating the linear part of the curve to intercept the x-axis in the graph of Tauc's plot. Fig 1 in Appendix D also demonstrates the estimated bandgaps of SnS_2 and $BiVO_4$ using n = 1 is more consistent with those reported by other research [2,4,8–10].

3.2.5. X-ray photoelectron spectroscopy (XPS)

X-ray Photoelectron Spectroscopy is a surface analytical technique based on the photoelectric effect to identify the chemical elements and their chemical state near the surface of the samples. This technique works by measuring the kinetic energy and photoelectron when X-ray of particular energy is used to excite the

surface of a sample. Binding energy can be calculated using the energy of incident X-ray minus the known kinetic energy and work function of element. Since each electron possesses a characteristic value of binding energy, this can be used to determine elements in the sample.

This thesis work used a JPS-9030 X-ray photoelectron spectrometer to obtain XPS data for studying the chemical state and composition of the samples. XPS was operated with Mg Kα radiation on the sample powder, which was evenly spread over a carbon tape on the sample holder.

3.2.6. Specific surface area measurement

In this study, the specific surface area was measured and evaluated using nitrogen gas adsorption with a FlowSorb III 2305 Micromeritics Instrument (Shimadzu, Japan). The measurement of the specific surface area is based on Brunauer-Emmett-Teller (BET) theory, which explains the gas molecules adsorbed on the surface of a solid. Flowsorb III determines the area of a sample by calculating the amount of adsorbate gas molecules on the sample at or near the boiling point of the said gas, assuming a form of a monomolecular layer.

3.3. Measurement of photocatalytic activity for rhodamine B degradation

Evaluation of photocatalytic activity was conducted via the photodegradation of RhB dye under visible light irradiation using a 500 W Xe lamp (Ushio, UXL-500D-O) equipped with a UV cutoff filter (λT = 420 nm). The intensity of light from the Xe lamp was 100 mW/cm^2 calibrated using a Spectroradiometer (S-2440 model II). After passing through the cutoff and water filters, the sample solution received around 40 mW/cm^2 of light intensity.

In each measurement process, 30 mg of the photocatalyst was put into a certain quantity of RhB solution (5 mg/L, 0.01 mmol/L) in a beaker with 100 mL capacity. Specific experimental condition of each sample for RhB degradation is

further described in their respective chapter. The solution was magnetically stirred and maintained at 25 °C during irradiation. About 3 mL of sample solution was taken every 60 min, and the photocatalyst powder was filtered out by a syringe filter (0.22 µm, PTFE). The absorbance of each RhB solution was measured using a UV–Vis spectrophotometer (Lambda 750S UV/Vis/NIR). Then, the concentration of RhB was determined from the absorbance intensity at λ_{max} = 554 nm. Before irradiation, the establishment of adsorption-desorption equilibrium between photocatalyst and RhB solution was achieved to ensure an accurate result of photocatalytic activity. The measurement setup for photocatalytic degradation of RhB dye is shown in Fig. 3.1.

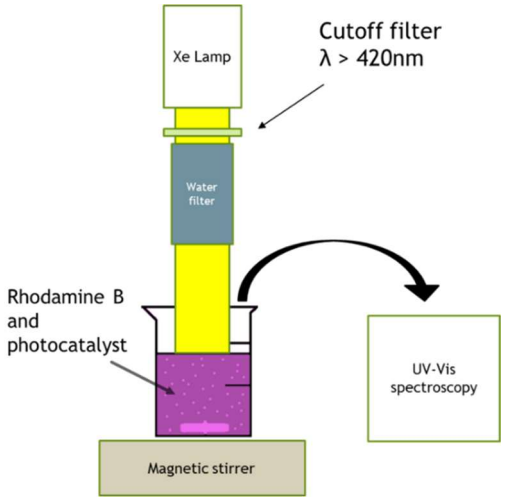

Fig. 3-1. Schematic of apparatus setup for the photocatalytic RhB degradation measurement.

Degradation efficiency (%) of the dye was determined using Eq (3.3):

$$\text{Degradation efficiency (\%)} = \left[\frac{(C_0 - C_t)}{C_0}\right] \times 100\% \qquad (3.3)$$

where C_0 and C_t are initial dye concentration (t=0) and dye concentration at any sampling time, respectively.

In addition, the photodegradation rate constant (k) was determined using a pseudo-first-order reaction expressed as follows:

$$ln\left(\frac{C_0}{C_t}\right) = kt \tag{3.4}$$

where k and t are photodegradation rate constants and irradiation time, respectively.

Reference

[1] D.K. Schroder, Semiconductor material and device characterization, 3rd ed., John Wiley & Sons, 2015.

[2] Y.C. Zhang, Z.N. Du, K.W. Li, M. Zhang, Size-controlled hydrothermal synthesis of SnS_2 nanoparticles with high performance in visible light-driven photocatalytic degradation of aqueous methyl orange, Sep. Purif. Technol. 81 (2011) 101–107. https://doi.org/10.1016/j.seppur.2011.07.016.

[3] X. Gao, G. Huang, H. Gao, C. Pan, H. Wang, J. Yan, Y. Liu, H. Qiu, N. Ma, J. Gao, Facile fabrication of Bi_2S_3/SnS_2 heterojunction photocatalysts with efficient photocatalytic activity under visible light, J. Alloys Compd. 674 (2016) 98–108. https://doi.org/10.1016/j.jallcom.2016.03.031.

[4] G. Zhao, W. Liu, Y. Hao, Z. Zhang, Q. Li, S. Zang, Nanostructured shuriken-like $BiVO_4$ with preferentially exposed {010} facets: Preparation, formation mechanism, and enhanced photocatalytic performance, Dalt. Trans. 47 (2018) 1325–1336. https://doi.org/10.1039/c7dt04431c.

[5] G. Zhang, X. Du, Y. Wang, H. Wang, W. Wang, Z. Fu, Controllable synthesis of SnS_2 nanostructures with high adsorption and photocatalytic activities, Mater. Sci. Semicond. Process. 64 (2017) 77–84. https://doi.org/10.1016/j.mssp.2017.03.010.

[6] Y.C. Zhang, Z.N. Du, K.W. Li, M. Zhang, D.D. Dionysiou, High-performance visible-light-driven SnS_2/SnO_2 nanocomposite photocatalyst prepared via in situ hydrothermal oxidation of SnS_2 nanoparticles, ACS Appl. Mater. Interfaces. 3 (2011) 1528–1537. https://doi.org/10.1021/am200102y.

[7] A. Walsh, Y. Yan, M.N. Huda, M.M. Al-Jassim, S.H. Wei, Band edge electronic structure of $BiVO_4$: Elucidating the role of the Bi s and V d orbitals, Chem. Mater. 21 (2009) 547–551. https://doi.org/10.1021/cm802894z.

[8] Z.Y. Bian, Y.Q. Zhu, J.X. Zhang, A.Z. Ding, H. Wang, Visible-light driven degradation of ibuprofen using abundant metal-loaded $BiVO_4$ photocatalysts, Chemosphere. 117 (2014) 527–531. https://doi.org/10.1016/j.chemosphere.2014.09.017.

[9] S. Tokunaga, H. Kato, A. Kudo, Selective preparation of monoclinic and tetragonal $BiVO_4$ with scheelite structure and their photocatalytic properties, Chem. Mater. 13 (2001) 4624–4628. https://doi.org/10.1021/cm0103390.

[10] N.G. Deshpande, A.A. Sagade, Y.G. Gudage, C.D. Lokhande, R. Sharma, Growth and characterization of tin disulfide (SnS_2) thin film deposited by successive ionic layer adsorption and reaction (SILAR) technique, J. Alloys

Compd. 436 (2007) 421–426. https://doi.org/10.1016/j.jallcom.2006.12.108.

4. The Effect of Potassium Chloride on $BiVO_4$ Morphology and Photocatalysis for Rhodamine B Degradation

4.1. Introduction

Over past decades, bismuth vanadate ($BiVO_4$) has become one of the most widely-studied photocatalysts ascribed to its favorable properties such as nontoxicity, low cost, narrow bandgap (E_g~2.4 eV), and stability [1]. As a photocatalyst, $BiVO_4$ has been known for its usage in the degradation of organic pollutants [2–4] and oxygen evolution in water splitting [5,6]. Of all three existing phases of $BiVO_4$, only monoclinic scheelite $BiVO_4$ is commonly used due to its superior photocatalytic performance compared with tetragonal scheelite and tetragonal zircon-type counterpart [7–9]. Besides the crystal phase of $BiVO_4$, morphology has a significant impact on the photocatalytic activity of $BiVO_4$ as well.

As discussed in Section 2.4.1 (Chapter 2), increasing exposed {010} facets leads to a remarkable enhancement of the photocatalytic activity of $BiVO_4$ [2,10–13]. Directing agents ($TiCl_3$ [6] and NaCl [14]) containing Cl^- could be used to enhance the exposed {010} facets [6,14]. In addition to the effect on the {010} facets, Cl^- ions may also influence the crystal growth and morphology of $BiVO_4$ in the synthetic route involving BiOCl intermediate because the change in Cl^- concentration could alter the formation of BiOCl intermediate in the precursor [15]. To date, no study has focused on the effect of Cl^- concentration influencing the formation of BiOCl intermediate (in the precursor of $BiVO_4$), which may play a significant role in controlling the morphology of $BiVO_4$.

In this study, $BiVO_4$ is synthesized via one-pot hydrothermal synthesis, in which KCl is used as a source of Cl^- ions. Although KCl was used in the $BiVO_4$ synthesis to compare with NaCl in the previous report [14], the effect of KCl on $BiVO_4$ has not been thoroughly studied yet. Thus, the present study investigates and discusses the effect of KCl concentration on the $BiVO_4$ synthesis route, morphology, crystal structure, photocatalytic activity, and other properties. Rhodamine B (RhB) is selected as a model dye to evaluate the photocatalytic performance of each sample because, as mentioned in Section 2.1.1 (Chapter 2), it represents one of the most common organic dyes in the textile industry and industrial wastewater [21–24]. The $BiVO_4$ prepared with 3 mmol of KCl, exhibiting "shuriken-like" morphology, demonstrates a superior photocatalytic degradation of RhB dye under visible light illumination because of the enhanced exposed {010} facets and the narrow bandgap.

4.2. Experimental

4.2.1. Preparation of $BiVO_4$ samples

$BiVO_4$ was synthesized via hydrothermal synthesis. Briefly, 0.485 g of $Bi(NO_3)_3 \cdot 5H_2O$ (1 mmol) was hydrolyzed in 30 ml of ultrapure water and magnetically stirred for 5 min. Then, a certain amount of KCl (0, 1, 2, 3, and 5 mmol) was added to the solution to form a white suspension (slightly soluble BiOCl). After 2 min of stirring, 117 g of NH_4VO_3 (1 mmol) was put into the white suspension, whose color then turned yellowish orange. The pH of the suspension was adjusted to 1.8 using ethanolamine. The suspension remained under stirring for 1 h and agitated under ultrasonication (45 Hz) for another 1 h. Then, it was transferred to a 50 ml stainless-steel autoclave with a Teflon liner, heated in an electric oven at 160 °C for 12 h. After the heat treatment, the autoclave was allowed to cool down to room temperature. The $BiVO_4$ samples were then collected and washed several times with ultrapure water and ethyl alcohol, further dried at 90 °C overnight. The samples were labeled as Bi0, Bi1, Bi2, Bi3, and Bi5 based on the amount of KCl (0, 1, 2, 3, and 5 mmol) used in the precursor. The schematic illustration of the preparation procedure can be seen in Fig. 4-1.

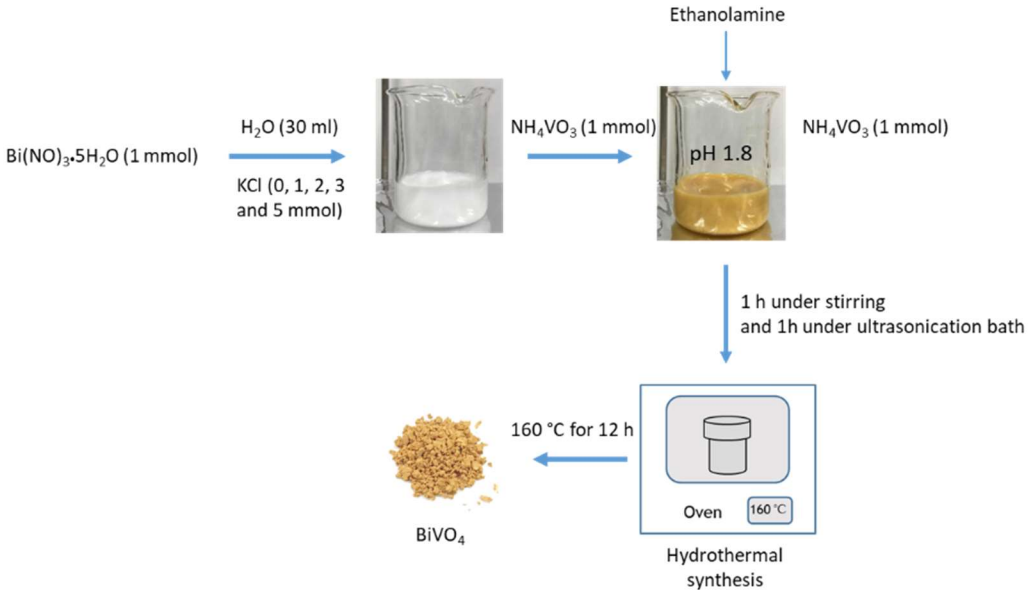

Fig. 4-1. Schematic illustration of the preparation procedure of the $BiVO_4$ samples.

4.2.2. Characterization

The crystal phase of the sample was determined using an X-ray diffraction (XRD) diffractogram obtained from a Rigaku RINT2100 with Cu Kα radiation (λ = 0.15418 nm). Microstructures and morphologies of each sample were investigated using an FE-SEM (Hitachi SU6600 Scanning Electron Microscope) operated at 20 kV, where Au was sputtered on all samples prior to the analyses. UV-vis diffuse reflectance spectra (DRS) were obtained using a Lambda 750S UV/Vis/NIR Spectrophotometer equipped with a 60 mm integrating sphere. X-ray photoelectron spectroscopy (XPS, JPS-9030 X-ray photoelectron spectrometer) was conducted with Mg Kα radiation using O 1s = 530.0 eV as reference. The Brunauer–Emmett–Teller specific surface area (S_{BET}) of the samples was measured via the single-point BET method using N_2 gas adsorption with a Flowsorb III 2305 Micromeritics instrument (Shimadzu, Japan).

4.2.3. Measurement of photocatalytic activity for rhodamine B degradation

Evaluation of photocatalytic activity was conducted via the photodegradation of rhodamine B (RhB) dye under visible light irradiation. The experimental setup is described in Section 3.3 (Chapter 3). For each photocatalytic measurement, 40

ml of RhB solution (0.01 mmol L^{-1}) that contained 30 mg of the photocatalyst was poured in a 100 ml capacity beaker. Before light irradiation, the solution was agitated in the dark under ultrasonication for 10 min and magnetically stirred for another 50 min to achieve adsorption-desorption equilibrium between the photocatalyst and RhB solution. The detailed sampling process and analysis are explained in Section 3.3 (Chapter 3).

4.3. Results and discussions

4.3.1. Crystal structures of the samples

Fig. 4-2 shows XRD patterns of $BiVO_4$ with different concentrations of KCl. All the samples exhibit characteristic peaks of monoclinic $BiVO_4$ (ICDD PDF No. 00-014-0688), especially the two split peaks at 18.5° and 35°, which are often used to distinguish between tetragonal and monoclinic phases. The former (18.5°) correspond to (110) and (011) planes, while the latter (35°) can be assigned to (200) and (002) planes. It is also noticeable that the intensity of the peak at 30.5°, corresponding to (040) plane of $BiVO_4$, becomes more intense as the concentration of KCl is increased. To make a comparison, the relative intensity ratio of (040) to ($\bar{1}21$) plane ($I_{(040)}/I_{(\bar{1}21)}$) for each sample was calculated (Table 4-1). The $I_{(040)}/I_{(\bar{1}21)}$ intensity ratio rises from 0.46 to 2.46 as KCl concentration is increased from 0 to 3 mmol, while it decreases when KCl content reaches 5 mmol. It demonstrates that the addition of KCl influences the preferential growth of $BiVO_4$ crystals along {010} planes. A previous study [14] using NaCl as a directing agent reported that Cl^- anions played an important role in stabilizing and controlling the exposed {010} facets. The mentioned study also suggested that Cl^- anions were adsorbed on the said facets, in turn reducing the surface energy of {010} facets and slowing the growth rate in [010] direction. A similar result was also reported for the synthesis utilizing $TiCl_3$ [6].

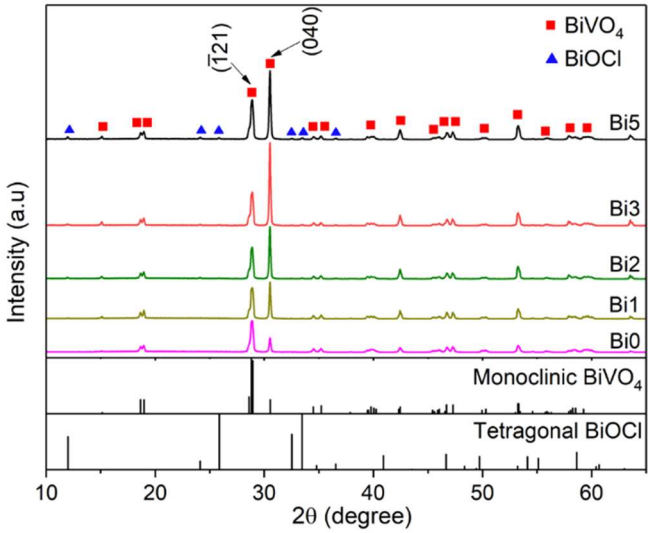

Fig. 4-2. XRD patterns of $BiVO_4$ with a different amount of KCl (mmol).

Table 4-1. Relative intensity ratio, physical properties and photocatalytic performance of $BiVO_4$ with a different amount of KCl.

Sample	$I_{(040)}/I_{(\bar{1}21)}$	E_g[a] (eV)	S_{BET}[b] (m^2 g^{-1})	RhB degradation efficiency (%)	k[c] ($\times10^{-3}$ min^{-1})	k/S_{BET}[d] ($\times10^{-2}$ min^{-1} /m^2 g^{-1})
Bi0	0.46	2.48	2.8	70.1	5.03	0.18
Bi1	1.17	2.45	1.1	81.7	6.60	0.60
Bi2	1.68	2.43	0.84	93.4	10.2	1.2
Bi3	2.46	2.34	0.63	94.7	11.4	1.8
Bi5	1.72	2.35	0.51	63.9	4.75	0.93

[a] E_g is Bandgap value; [b] S_{BET} is BET specific surface area; [c] k is photodegradation rate constant; [d] k/S_{BET} is ratio of photodegradation rate constant over BET specific surface area

The additional content of KCl not only affects the crystal growth of $BiVO_4$ but also produces another phase in the samples, as seen in Fig. 4-2. The small peaks at 12°, 24.1°, 25.9°, 32.5°, 33.5, and 36.5° can be assigned to (001), (002), (101), (110), (102), and (003) plane diffraction of tetragonal BiOCl (ICDD PDF No. 00-006-0249), respectively. These peaks become more visible in samples with higher KCl concentrations. The BiOCl could be an intermediate material before the growth

of $BiVO_4$ crystals. A possible chemical reaction can be expressed as follows [18,19]:

$$Bi^{3+} + 2H_2O \rightleftharpoons BiOH^{2+} + H_3O^+ \quad (4.1)$$

$$BiOH^{2+} + H_2O \rightleftharpoons BiO^+ + H_3O^+ \quad (4.2)$$

$$BiO^+ + Cl^- \rightleftharpoons BiOCl \downarrow \quad (4.3)$$

$$BiOCl \downarrow + VO_3^- \rightleftharpoons BiVO_4 \downarrow + Cl^- \quad (4.4)$$

The synthetic reaction begins with the hydrolysis of $Bi(NO_3)_3 \cdot H_2O$ [reaction (4.1) and (4.2)]. The BiO^+ derived from hydrolysis reacts with Cl^- to form the BiOCl precipitate [reaction (4.3)], which further reacts with VO_3^- to form $BiVO_4$ [reaction (4.4)]. Both $BiVO_4$ and BiOCl are present in the precursor, as shown in Fig. 4-3. In addition, the elevated temperature and pressure during the hydrothermal process may accelerate the conversion from BiOCl to $BiVO_4$. Fig. 4-3 demonstrates that the conversion from BiOCl to $BiVO_4$ was nearly completed when the sample was heated for 45 min, and prolonging the heating duration to 12 h exhibits no significant change in terms of the crystal structure. Moreover, an incomplete transformation can be seen, as the residual BiOCl is still present in the sample due to the excess amount of Cl^- present in the solution.

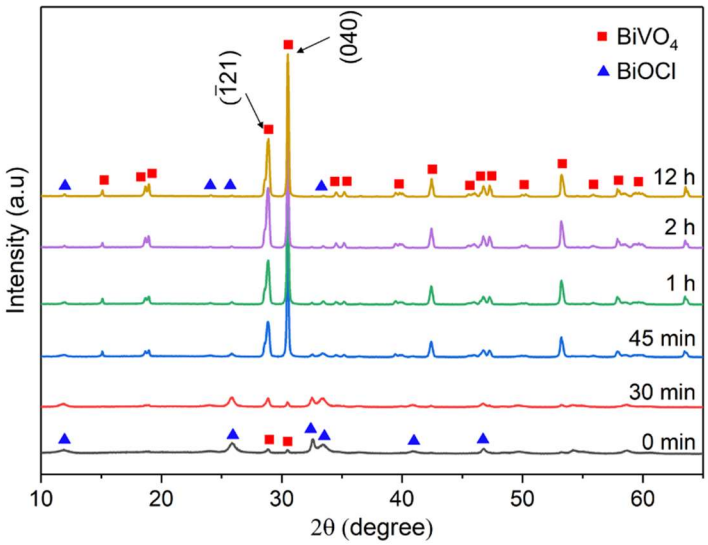

Fig. 4-3. XRD diffractograms of Bi3 with a different heating duration of hydrothermal synthesis at 160 °C.

4.3.2. Morphology of $BiVO_4$ samples

Morphologies of $BiVO_4$ prepared with a different molar amount of KCl are depicted in SEM micrographs, as can be seen in Fig. 4-4. A rod-like $BiVO_4$ (Fig. 4-4a) can be obtained when the synthesis is prepared without KCl. The anisotropic growth of rod-like structure may be attributed to the pH~1.8 of the precursor [9]. The shape of particles has been found to transform from polyhedron to rod-like structure due to an increase in pH value, which in turn lowers the solute concentration [9,20,25,26]. When 1 mmol of KCl is added, the $BiVO_4$ particles take a short rod-like form, as shown in Fig. 4-4b. As the amount of KCl further rises to 2 mmol, the $BiVO_4$ particles assume a form of cruciate structure (Fig. 4-4c). Further additional amount of KCl (3 mmol) allows a suitable condition for dendritic structure with small branches grown out from four arms to assume a shuriken-like structure, as can be seen in Fig. 4-4d. Fig. 4-4e illustrates the $BiVO_4$ structure resembles a tabular block with an uneven assembly of small particles as the concentration of KCl reaches 5 mmol.

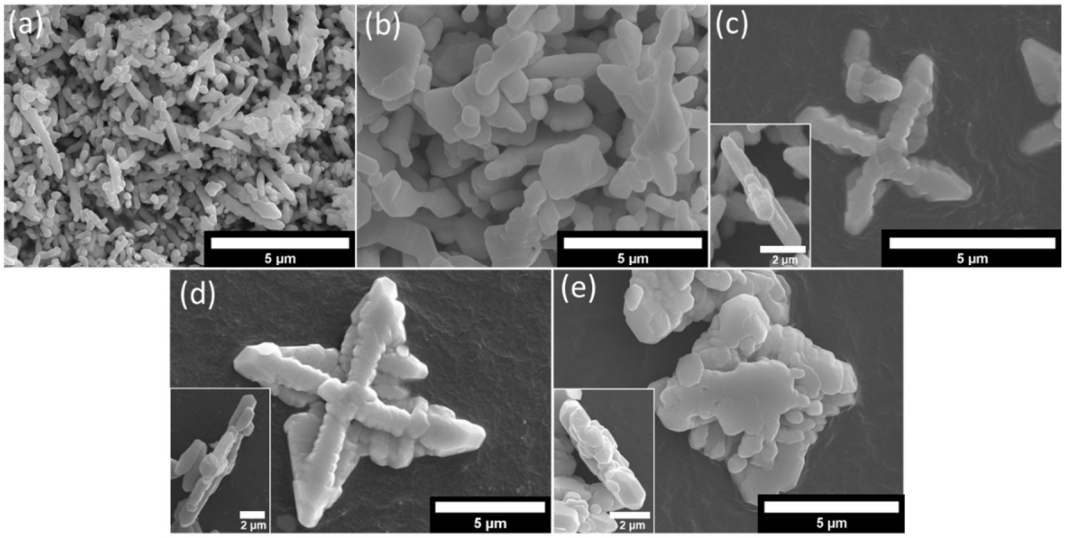

Fig. 4-4. FE-SEM micrographs of (a) Bi0 (0 mmol KCl) and (b) Bi1 (1 mmol KCl); and the top-view and side-view micrographs of (c) Bi2 (2 mmol KCl), (d) Bi3 (3 mmol KCl), and (e) Bi5 (5 mmol KCl).

The morphology evolution of $BiVO_4$ from rod-like structure to dendrite and then to tabular form visibly correlates with the increase in KCl concentration as depicted in Fig. 4-4. A similar transformation of $BiVO_4$ has been reported by Xi and coworkers [5], except that the phenomenon occurs when the acidity of the precursor is increased. It is worth mentioning that they synthesized $BiVO_4$ using $BiCl_3$ as a source of Bi^{3+}. Thus, the chemical reaction involving the BiOCl intermediate could be similar to the current study. According to this study and theirs, either increasing acidity or Cl^- concentration could provide a similar outcome of the morphological evolution of $BiVO_4$. A plausible reason is related to the solubility of BiOCl. Since BiOCl is the intermediate phase followed by its transformation into $BiVO_4$, the number of BiOCl particles in the precursor could dictate the crystal growth of $BiVO_4$ because the particle number influences the free Bi^{3+} ions, which react with VO_3^- ions during the $BiVO_4$ formation. It is known that both H_3O^+ and Cl^- ions play a major role in the dissolution of BiOCl to form $BiCl_4^-$ through a chemical reaction (4.5) [15]:

$$BiO^+ + 2H_3O^+ + 4Cl^- \rightleftharpoons BiCl_4^- + 3H_2O \qquad (4.5)$$

In the case of this study, the additional Cl^- ions (more than 1 mmol of KCl) could dissolve more BiOCl, decreasing the number of BiOCl particles in the precursor and increasing the concentration of the Bi^{3+} solute in the precursor solution. The detailed calculation of the $BiCl_4^-$ concentration, corresponding to Cl^- content in the precursor, is included in Appendix A.

The morphology of $BiVO_4$ can be explained as follows. The BiOCl precipitates during the preparation stage due to homogeneous nucleation. Its growth rate is relatively slow as they take the form of nanoparticles, as shown in Fig. 4-5 and 4-6. At 1 mmol addition of KCl, the number of particles of BiOCl is large. Also, the concentration of free Bi^{3+} ions in the solution is substantially low, leading to difficulty in the nucleation of $BiVO_4$. Thus, the formation and growth of the $BiVO_4$ crystals mainly depend on the transformation from BiOCl to $BiVO_4$ via the reaction (possibly, also diffusion) with VO_3^-. As the concentration of KCl is increased, the number of BiOCl particles decreases, and more free Bi^{3+} ions are generated. Since the homogeneous nucleation of $BiVO_4$ is rather difficult, the $BiVO_4$ particles transform from the BiOCl particles and can grow larger in volume by the reaction between the free Bi^{3+} and VO_3^- ions. As a result, raising the concentration of KCl leads to different morphologies of the samples, as depicted in Fig. 4-4c to 4-4e. The formation of $BiVO_4$ with different morphologies, corresponding to the concentration of KCl, is depicted in Fig. 4-5. It is worth mentioning that the shuriken-like $BiVO_4$ (the dendritic structure) in Fig. 4-4d can be obtained with the addition of 3 mmol KCl. The directional growth of the $BiVO_4$ crystals may be attributed to the variation in the relative growth rate of each crystal facet. Additionally, the dendrite $BiVO_4$ tends to have a crystal preferential growth in the [001] direction [27–29] due to the high surface energy of {001} facets [30].

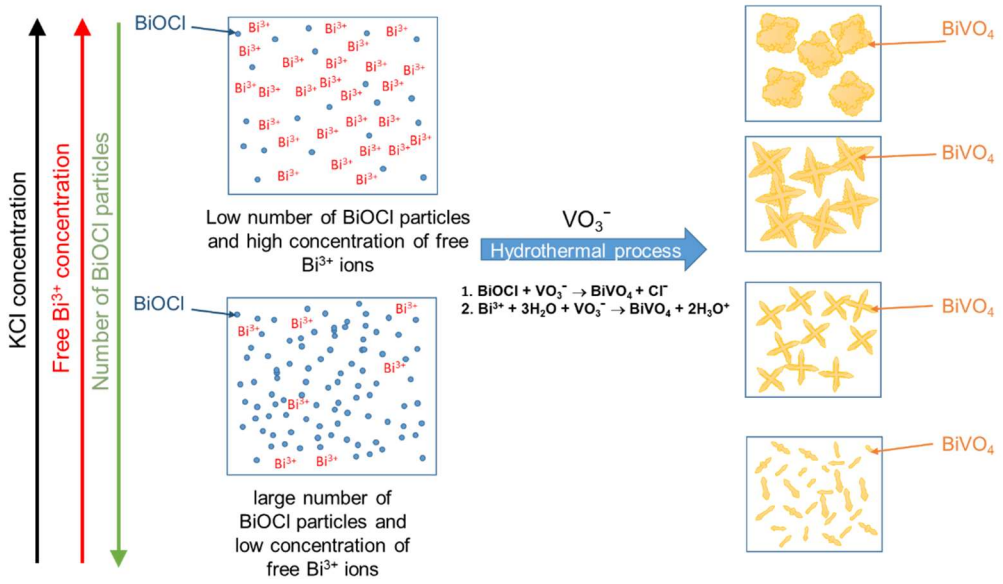

Fig. 4-5. Schematic illustration of $BiVO_4$ formation with different morphologies, corresponding to KCl concentrations.

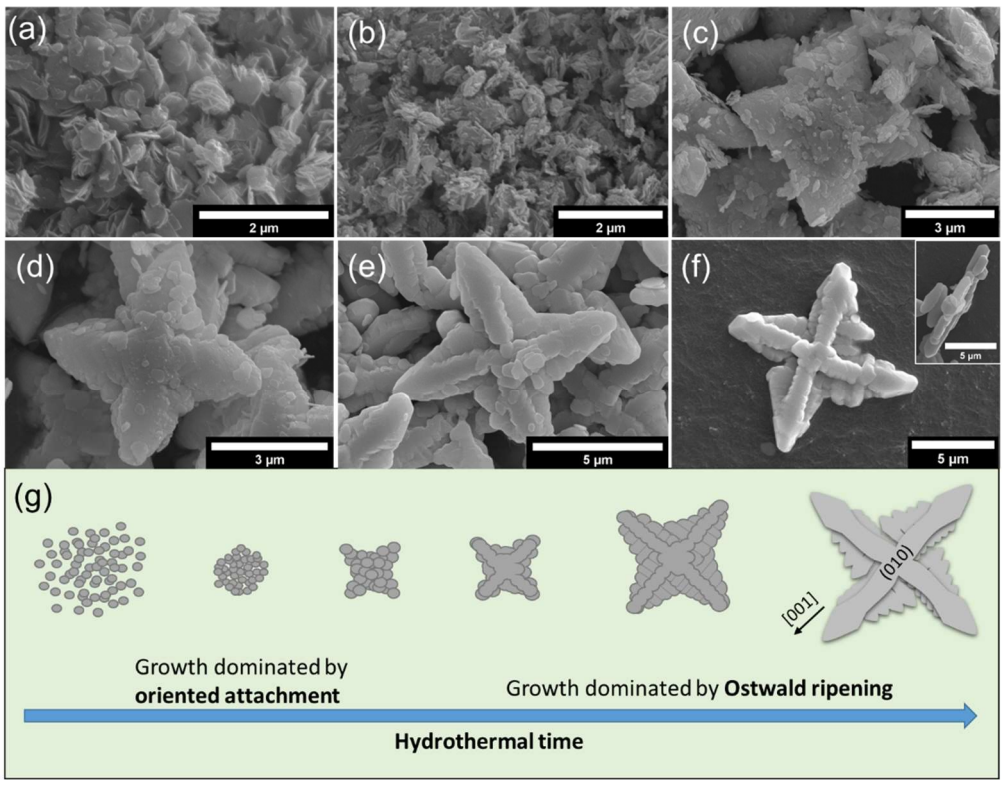

Fig. 4-6. FE-SEM micrograph of Bi3 heated in the autoclave at 160 °C for (a) 0 min (precursor), (b) 30 min, (c) 45 min, (d) 1 h, (e) 2 h, and (f) 12 h. (g) Schematic representation of crystal growth of the shuriken-like $BiVO_4$.

The morphological evolution of the shuriken-like $BiVO_4$ (Bi3) at different stages of the hydrothermal route is depicted in Fig. 4-6. Fig. 4-6a shows a micrograph of nanoplates (a thickness of 30 –40 nm), which are BiOCl based on the XRD pattern in Fig. 4-3. The aggregation of nanoplates can be seen at the reaction time of 30 min under elevated temperature and pressure in Fig. 4-6b. The BiOCl nanoplate would go through a self-assembly process via oriented attachment, which involves particle coalescence by rotating and interacting to match a mutual crystallographic orientation[31]. At the reaction time of 45 min, as shown in Fig. 4-6c, the nanoplates stacked and joined together to form a star-shaped structure through oriented attachment. During the formation process, BiOCl also transformed to $BiVO_4$ when they reacted with VO_3^- ions in the solution, according to the XRD result in Fig. 4-3. Based on Fig. 4-6d to 4-6f, the crystal growth of $BiVO_4$ from 1 h to 12 h was dominated by Ostwald ripening process in which dissolution occurs on small particles, and their ions reprecipitate on the larger particles[32,33]. The variation in the relative growth rate of each individual facet promoted the uneven deposition rate to form a defined shuriken shape as it grew larger. The $BiVO_4$ crystals grow faster in the [001] direction due to the high surface energy of {001} facets[30]. It is worth mentioning that the $BiVO_4$ crystals also grew along {010} planes because the Cl^- ions stabilized {010} facets and significantly reduced the growth rate in the [010] direction [14]. The final product of the shuriken-like BiVO4 with a smooth surface possesses a diagonal length of around 12 μm with a thickness of 1–1.5 μm. Fig. 4-6g illustrates the crystal growth of the shuriken-like $BiVO_4$ during the hydrothermal process.

In addition to the role of the BiOCl formation and its dissolution, the Cl^- ions also decrease the surface energy and stabilize {010} facets of $BiVO_4$ during the hydrothermal synthesis [14]. Therefore, it is understandable that $BiVO_4$ has the preferential growth in a 2D plane along the {010} planes with a smooth surface as the concentration of Cl^- increases. The preferential growth along the {010} planes in relation to the concentration of Cl^- ion is consistent with the XRD results.

4.3.3. Optical absorption properties of the samples

Absorption properties of as-synthesized samples were evaluated by UV-Vis diffuse reflectance spectra. Fig. 4-7a shows absorption spectra of the samples, converted from reflectance data of the samples using Kubelka-Munk function in Eq. (3.1). It is observed that the absorption edge of $BiVO_4$ has a redshift correlating with the increase in the content of KCl, which is consistent with the color of $BiVO_4$ as it changes from yellow to orange. Thus, it indicates $BiVO_4$ samples prepared with higher KCl content can absorb a broader wavelength of visible light. However, there is no significant difference in absorption edge of the sample after further addition of KCl content from 3 mmol (Bi3) to 5 mmol (Bi5), as shown in Fig. 4-7a.

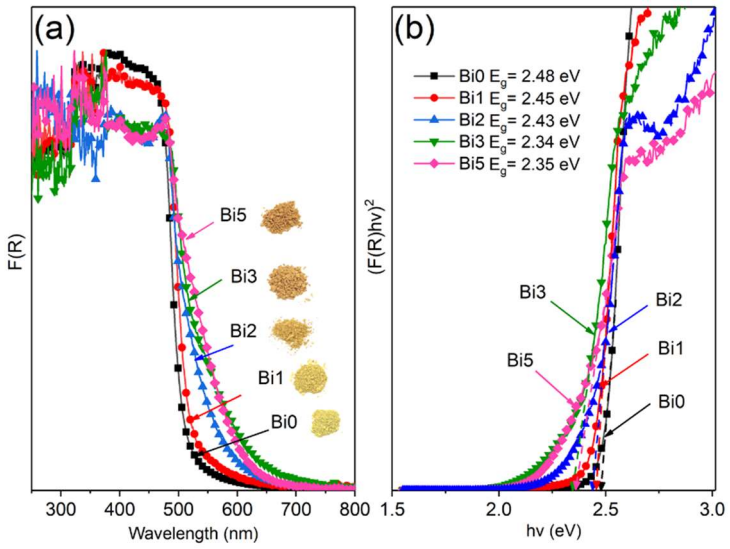

Fig. 4-7. (a) UV-Vis absorption spectra and (b) Tauc's plot of $BiVO_4$ with a different amount of KCl.

Bandgap of each sample is determined using Eq (3.2) and Tauc's plot [$(F(R)hv)^2$ *vs.* hv], as illustrated in Fig. 4-7b, where the bandgap of the samples can be estimated by extrapolating the linear part of the curve to intercept x-axis. The estimated E_g values of the samples are listed in Table 4-1 (p61). The Bi0 has E_g value of 2.48 eV, which is similar to a previous report [10]. Interestingly, the E_g value of the sample is decreased as the KCl content rises, indicating that the addition of KCl in the precursor influences the optical absorption properties of $BiVO_4$.

Unlike absorption spectra, the Tauc plot (Fig. 4-7b) visibly reveals that the E_g value of Bi3 (2.34 eV) is narrower than that of Bi5 (2.35 eV). Therefore, E_g values of the $BiVO_4$ sample follow the order of Bi0 > Bi1 > Bi2 > Bi5 > Bi3.

The current finding differs from prior studies [6,14], which reported that the concentration of Cl^- from NaCl and $TiCl_3$ had no obvious effect on the absorption edge and bandgap value of the $BiVO_4$ sample. It could be ascribed to the different conditions of synthesis, in which Cl^- was added in different orders. Both previous studies added the Cl^- after NH_4VO_3; thus, $BiVO_4$ could have already formed, whereas Cl^- in this study was introduced before NH_4VO_3 addition. In order to confirm this, two $BiVO_4$ samples were prepared via changing the order of adding KCl to the precursor, under otherwise identical conditions (3 mmol of KCl).

The absorption spectra of the samples are shown in Fig 4-8. When Cl^- was introduced into the precursor after NH_4VO_3, the absorption spectrum of the sample exhibit no significant difference from that of the sample without KCl, which is consistent with the previous studies [6,14]. It could be said that if Cl^- was added after NH_4VO_3, the tetragonal zircon-type $BiVO_4$ intermediate had already formed due to its low formation temperature [7]. Thus, the sample prepared with KCl addition after NH_4VO_3, in a sense, goes through a similar formation process as the one without KCl addition. On the other hand, the sample prepared with KCl addition before NH_4VO_3 would go through a different formation route, in which the monoclinic $BiVO_4$ was converted from BiOCl intermediate, as revealed in XRD patterns in Fig. 4-3. To further confirm this, pure BiOCl powder (1 mmol) was used as a starting material with the addition of KCl (2 mmol) in a solution with a pH value of 1.8 to simulate the preparation of the Bi3 sample. The results demonstrate that the absorption spectrum (Fig. 4-8) and the XRD patterns (Fig. 4-9) of the $BiVO_4$ sample prepared using pure BiOCl as a Bi^{3+} source are indeed similar to those of the Bi3 sample prepared with KCl addition before NH_4VO_3. Moreover, both samples exhibit tails in their absorption spectra, indicating defects present in the samples. The result suggests that the synthetic route used in the current study may introduce defects into $BiVO_4$ and create impurity levels, influencing the optical

properties of $BiVO_4$. Further study on this matter will be conducted and discussed later in Chapter 5.

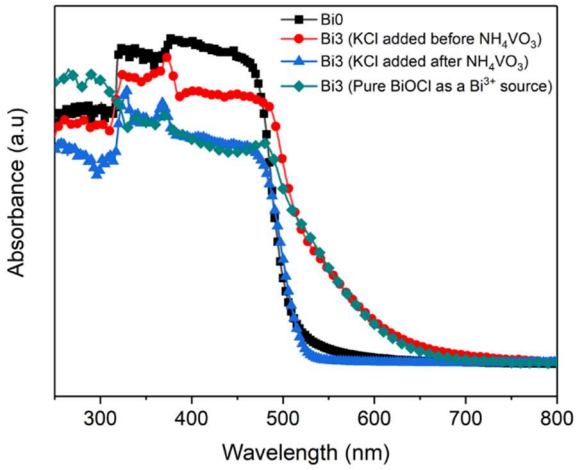

Fig. 4-8. UV-Vis absorption spectra of the $BiVO_4$ samples without KCl addition (Bi0), with 3 mmol KCl (Bi3) added before NH_4VO_3, with 3 mmol KCl (Bi3) added after NH_4VO_3, and $BiVO_4$ prepared using pure BiOCl (1 mmol) as a source of Bi^{3+} with the addition of KCl (2 mmol) and NH_4VO_3 (1 mmol) in a solution with a pH value of 1.8 to simulate the procedure of the Bi3 sample.

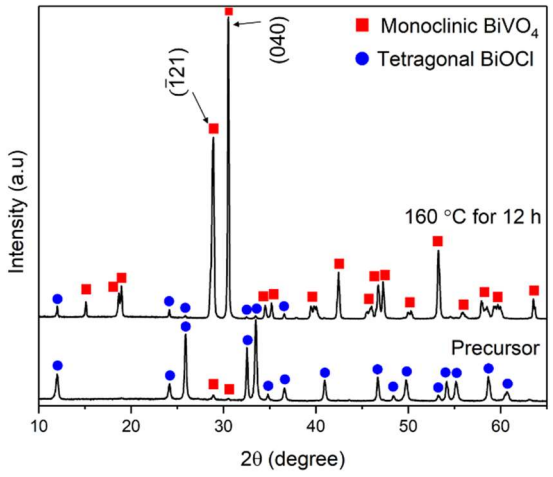

Fig. 4-9. XRD diffraction patterns of the precursor and $BiVO_4$ prepared using pure BiOCl (1 mmol) as a source of Bi^{3+} with the addition of KCl (2 mmol) and NH_4VO_3 (1 mmol) in a solution with pH value of 1.8 to simulate the procedure of the Bi3 sample.

4.3.4. X-ray photoelectron spectroscopic (XPS) analyses of the samples

Elemental composition and chemical state of various samples were analyzed using XPS spectra. In Fig. 4-10a, the XPS survey spectra of the as-synthesized Bi0, Bi3, and Bi5 samples confirmed the presence of Bi, V, and O elements. Fig. 4-10b shows two peaks at 164.6 and 159.3 eV, which are assigned to Bi $4f_{5/2}$ and Bi $4f_{7/2}$, respectively. In Fig. 4-10c, the V $2p_{1/2}$ (524.4 eV) and V $2p_{3/2}$ (516.8 eV) spectra of V 2p orbitals correspond to V−O bonds, indicating the existence of V^{5+} in the samples [4]. Fig. 4-10d displays O 1s spectra with a peak at 530 eV, assigned to the bonding with the lattice oxygen (Bi−O) of $BiVO_4$ [34–37]. Based on high-resolution XPS spectra, the different amount of KCl has no significant influence on the chemical state of $BiVO_4$. However, a small amount of Cl is detected for $BiVO_4$ prepared with additional KCl (Bi3 and Bi5). In Fig. 4-10e, two spin orbital peaks of Bi3 located at 199.5 and 198.2 eV, respectively, associate with Cl $2p_{1/2}$ and Cl $2p_{3/2}$ of Cl^- in BiOCl [35]. Whereas, the Cl 2p orbital peaks of the Bi5 sample exhibit a slight blueshift to 200.3 and 198.6 eV, respectively, when KCl and BiOCl content is increased, in accordance with the XRD result (Fig.4-2).

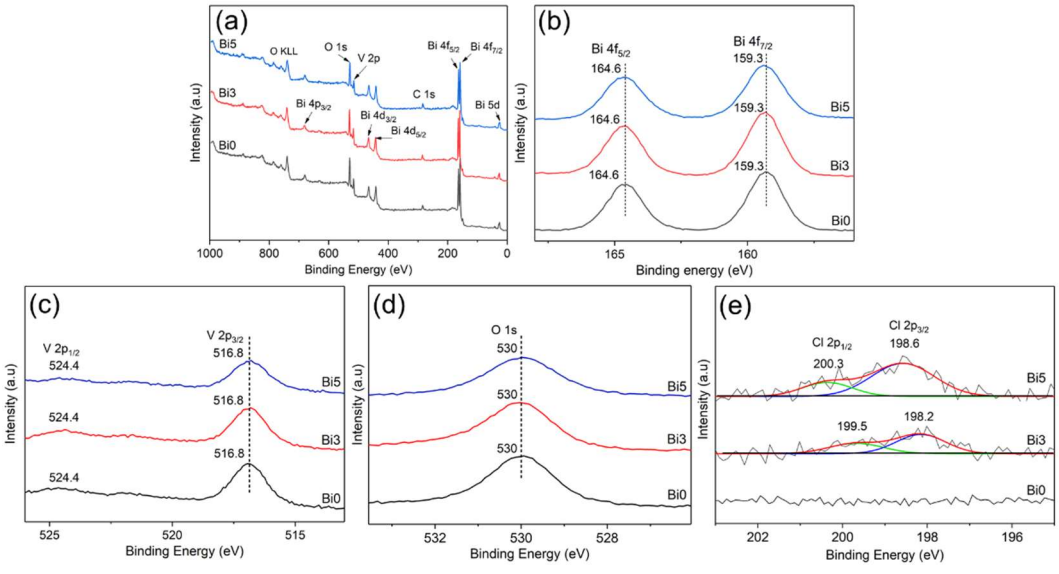

Fig. 4-10. (a) XPS survey spectra of $BiVO_4$ samples and high-resolution XPS spectra of (b) Bi 4f, (c) V 2p, (d) O 1s, and (e) Cl 2p.

4.3.5. Photocatalytic activities of the samples for rhodamine B degradation

Photocatalytic activities of the as-synthesized $BiVO_4$ with different concentrations of KCl were evaluated by plotting the photodegradation of RhB (C_t/C_0) against irradiation time (t), as shown in Fig. 4-11. To determine the stability of the RhB solution in the test condition, a photolysis of the blank RhB solution was also conducted without any photocatalyst. As a controlled test, the photolysis of the blank RhB solution showed no significant decrease in concentration over 240 min, implying RhB solution remained stable in this photocatalytic test condition. Under the same condition, the concentration of all RhB solutions containing the photocatalyst was drastically reduced over a period of time. After 240 min of irradiation, the Bi3 sample exhibited the highest photocatalytic performance as about 94.7% of RhB was degraded. It was followed by Bi2 (93.4%) with only a slight difference. Whereas, Bi5 only degraded about 63.9% of RhB, which demonstrated the lowest photocatalytic activity among the samples. The temporal absorption spectra of RhB solution in the presence of each sample are shown in Fig. 1 (Appendix B).

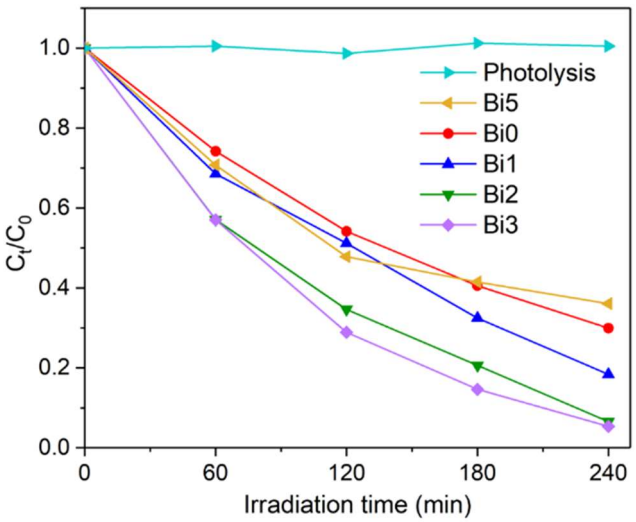

Fig. 4-11. Photodegradation of RhB solution without any photocatalyst and with $BiVO_4$ samples prepared with a different amount of KCl under visible light ($\lambda > 420$ nm).

To further study and compare the photocatalytic performance of the samples, photodegradation rate constants were determined utilizing a pseudo-first-order

reaction equation as in Eq. (3.4). The values of k obtained from $ln(C_0/C_t)$ vs. kt plot in Fig. 4-12a are also listed in Table 4-1 (p61). Using the specific surface area (S_{BET} in Table 4-1) of each sample, the photodegradation rate k per specific surface area (k/S_{BET}) is used to compare the photocatalytic degradation of RhB for each sample.

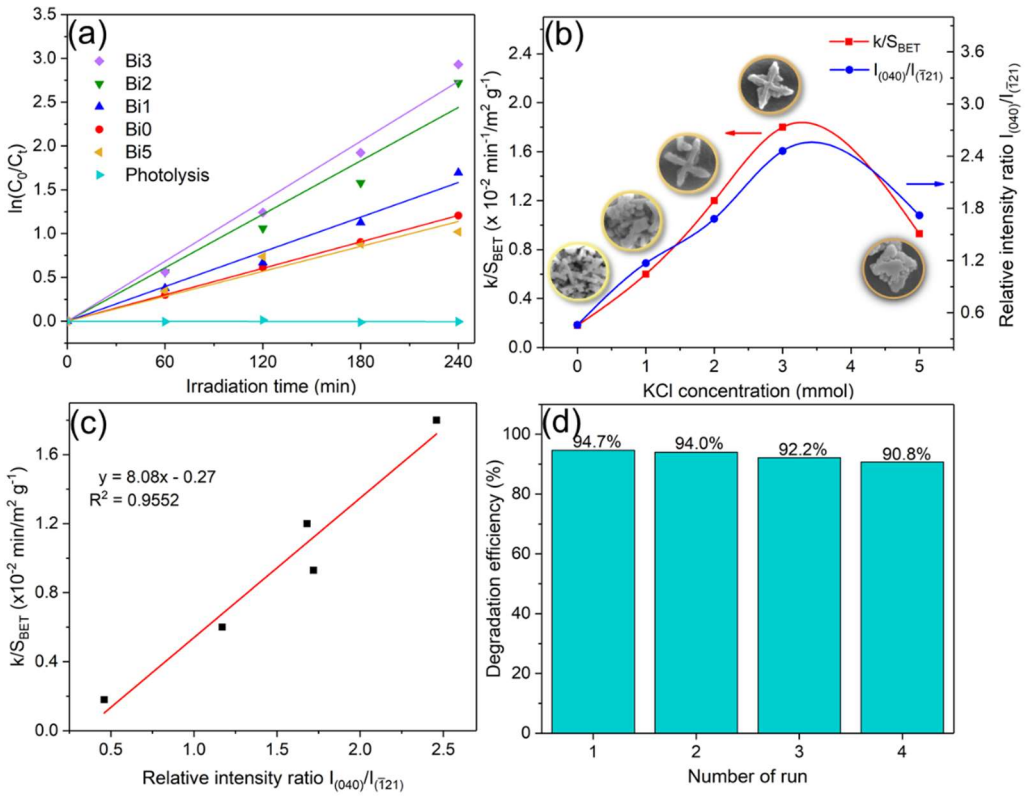

Fig. 4-12. (a) Pseudo-first-order kinetic degradation of RhB by $BiVO_4$ prepared with a different amount of KCl precursor; (b) Variation of both photocatalytic degradation rate constant (k) over S_{BET} (k/S_{BET}) and relative intensity ratio $I_{(040)}/I_{(\bar{1}21)}$ with respect to the KCl concentration in precursor; (c) Linear relationship between k/S_{BET} and relative intensity ratio $I_{(040)}/I_{(\bar{1}21)}$; and (d) Reusability test of the Bi3 sample for RhB degradation over four cycles under visible light ($\lambda > 420$ nm).

Fig. 4-12b demonstrates the relationship between k/S_{BET} and relative intensity ratio $I_{(040)}/I_{(\bar{1}21)}$ with respect to the concentration of KCl. The k/S_{BET} value surges along with the $I_{(040)}/I_{(\bar{1}21)}$ ratio when KCl content is increased until it reaches around 3 mmol and then goes down when it reaches 5 mmol. Both the k/S_{BET} values and the $I_{(040)}/I_{(\bar{1}21)}$ ratios follow a very similar trend, and they can be used to create a linear relationship between them, as plotted in Fig. 4-12c. The figure indicates the

linear dependency of k/S_{BET} on the intensity ratio $I_{(040)}/I_{(\bar{1}21)}$ of the samples. It is commonly known that a combination of various aspects, such as morphology, bandgap, crystal structure, and specific surface area influences the photocatalytic performance of photocatalysts. Based on the results in this study, the relative intensity ratio $I_{(040)}/I_{(\bar{1}21)}$ plays a major role in the enhanced photocatalytic degradation of the RhB dye. The increase in the $I_{(040)}/I_{(\bar{1}21)}$ intensity ratio associates with the enhanced exposure of {010} facets, promoting the photocatalytic activity of the $BiVO_4$ [2,5,6,10–12]. The shuriken-like $BiVO_4$ with a molar ratio of 1:3 (Bi:Cl) exhibits the highest RhB photodegradation ascribed to the highest relative intensity ratio $I_{(040)}/I_{(\bar{1}21)}$. The narrowest bandgap of the Bi3 sample among the samples may also contribute, to some extent, to the enhancement of the photocatalytic performance as it could provide superior visible-light absorption. Based on the above experimental results and analyses, it could be concluded the KCl concentration (via modification of the reaction path) is one of the key factors that influence the crystal growth, crystal structure, morphology, and optical property of $BiVO_4$, which in turn affect the photocatalytic performance of $BiVO_4$.

Reusability test was conducted for the Bi3 sample in order to study its stability. The test was repeatedly run for fours cycles under identical conditions. After each cycle, the photocatalyst was collected and recovered via centrifuge and put in a fresh RhB solution for another run. It should be noted that the weight of the sample might be reduced each time due to the recovery process. Fig. 4-12d shows that the Bi3 sample exhibits good stability, as the RhB degradation efficiency of the Bi3 sample only decreases slightly from 94.7% to 90.8% after four cycles. A loss of photocatalyst during the recovery process might be responsible for the reduction in RhB degradation efficiency. Moreover, there is no significant change in the crystal structure of the Bi3 sample after irradiation for four cycles, based on the XRD result in Fig. 4-13.

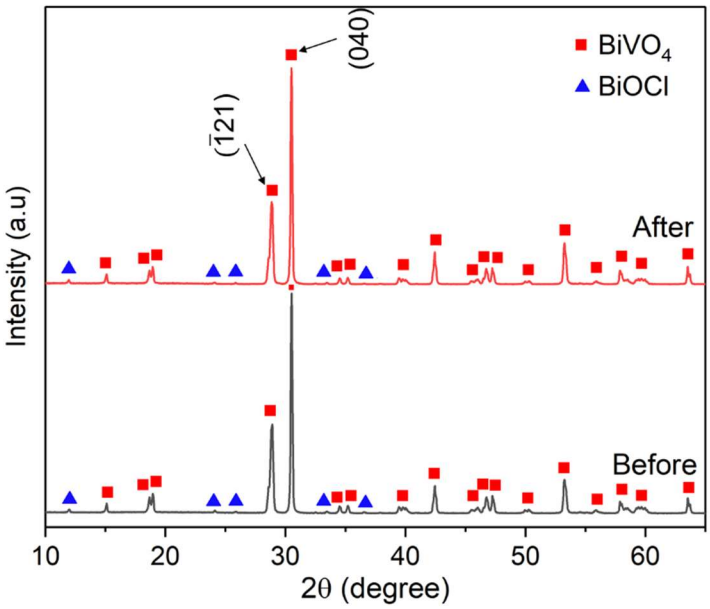

Fig. 4-13. XRD patterns of the Bi3 sample before* and after irradiation (4 cycles) under visible light (λ > 420 nm). * It is the same data as indicated in Fig. 4.2.

4.4. Conclusion

The $BiVO_4$ samples with different morphologies were synthesized using a varied amount of KCl in the hydrothermal synthesis. The concentration of Cl^- ions from KCl played a major role in the crystal growth of $BiVO_4$ via the formation of BiOCl intermediate and the order of the KCl addition in the precursor that altered the intermediate phase, which influenced the final morphology of the $BiVO_4$. The shuriken-like $BiVO_4$ (Bi3) with the molar ratio of 1:3 (Bi:Cl) exhibits the highest photocatalytic performance for RhB degradation among the as-synthesized samples owing to the high relative intensity ratios of $I_{(040)}/I_{(\bar{1}21)}$ and the narrow bandgap. The present work contributes to the development of various dye degradation systems. The findings provide an important clue into the effect of Cl^- concentration on BiOCl intermediate, influencing the crystal growth, light absorption property, and morphology as well as the photocatalytic performance of $BiVO_4$.

Reference

[1] H.L. Tan, R. Amal, Y.H. Ng, Alternative strategies in improving the photocatalytic and photoelectrochemical activities of visible light-driven $BiVO_4$: A review, J. Mater. Chem. A. 5 (2017) 16498–16521. https://doi.org/10.1039/c7ta04441k.

[2] S.M. Thalluri, M. Hussain, G. Saracco, J. Barber, N. Russo, Green-synthesized $BiVO_4$ oriented along {040} facets for visible-light-driven ethylene degradation, Ind. Eng. Chem. Res. 53 (2014) 2640–2646. https://doi.org/10.1021/ie403999g.

[3] M. Hojamberdiev, G. Zhu, Z.C. Kadirova, J. Han, J. Liang, J. Zhou, X. Wei, P. Liu, Morphology-controlled growth of $BiVO_4$ crystals by hydrothermal method assisted with ethylene glycol and ethylenediamine and their photocatalytic activity, Mater. Chem. Phys. 165 (2015) 188–195. https://doi.org/10.1016/j.matchemphys.2015.09.015.

[4] T. Senasu, S. Youngme, K. Hemavibool, S. Nanan, Sunlight-driven photodegradation of oxytetracycline antibiotic by $BiVO_4$ photocatalyst, J. Solid State Chem. 297 (2021) 122088. https://doi.org/10.1016/j.jssc.2021.122088.

[5] G. Xi, J. Ye, Synthesis of bismuth vanadate nanoplates with exposed {001} facets and enhanced visible-light photocatalytic properties, Chem. Commun. 46 (2010) 1893–1895. https://doi.org/10.1039/b923435g.

[6] D. Wang, H. Jiang, X. Zong, Q. Xu, Y. Ma, G. Li, C. Li, Crystal facet dependence of water oxidation on $BiVO_4$ sheets under visible light irradiation, Chem. - A Eur. J. 17 (2011) 1275–1282. https://doi.org/10.1002/chem.201001636.

[7] A. Kudo, K. Omori, H. Kato, A novel aqueous process for preparation of crystal form-controlled and highly crystalline $BiVO_4$ powder from layered vanadates at room temperature and its photocatalytic and photophysical properties, J. Am. Chem. Soc. 121 (1999) 11459–11467. https://doi.org/10.1021/ja992541y.

[8] S. Tokunaga, H. Kato, A. Kudo, Selective preparation of monoclinic and tetragonal $BiVO_4$ with scheelite structure and their photocatalytic properties, Chem. Mater. 13 (2001) 4624–4628. https://doi.org/10.1021/cm0103390.

[9] Y. Zhao, R. Li, L. Mu, C. Li, Significance of crystal morphology controlling in semiconductor-based photocatalysis: a case study on $BiVO_4$ photocatalyst,

Cryst. Growth Des. 17 (2017) 2923–2928. https://doi.org/10.1021/acs.cgd.7b00291.

[10] G. Zhao, W. Liu, Y. Hao, Z. Zhang, Q. Li, S. Zang, Nanostructured shuriken-like $BiVO_4$ with preferentially exposed {010} facets: Preparation, formation mechanism, and enhanced photocatalytic performance, Dalt. Trans. 47 (2018) 1325–1336. https://doi.org/10.1039/c7dt04431c.

[11] Y. Li, Z. Sun, S. Zhu, Y. Liao, Z. Chen, D. Zhang, Fabrication of $BiVO_4$ nanoplates with active facets on graphene sheets for visible-light photocatalyst, Carbon N. Y. 94 (2015) 599–606. https://doi.org/10.1016/j.carbon.2015.07.042.

[12] L. Xia, J. Li, J. Bai, L. Li, S. Chen, B. Zhou, $BiVO_4$ photoanode with exposed (040) facets for enhanced photoelectrochemical performance, Nano-Micro Lett. 10 (2018) 1–10. https://doi.org/10.1007/s40820-017-0163-3.

[13] B. Baral, K. Parida, {040/110} Facet isotype heterojunctions with monoclinic scheelite $BiVO_4$, Inorg. Chem. (2020). https://doi.org/10.1021/acs.inorgchem.0c01465.

[14] S. Xie, Z. Shen, H. Zhang, J. Cheng, Q. Zhang, Y. Wang, Photocatalytic coupling of formaldehyde to ethylene glycol and glycolaldehyde over bismuth vanadate with controllable facets and cocatalysts, Catal. Sci. Technol. 7 (2017) 923–933. https://doi.org/10.1039/c6cy02510b.

[15] M.N. Ackermann, Why is Bismuth Subchloride Soluble in Acid?, J. Chem. Educ. 75 (1998) 523. https://doi.org/10.1021/ed075p523.

[16] B. Xu, A. Zada, G. Wang, Y. Qu, Boosting the visible-light photoactivities of $BiVO_4$ nanoplates by Eu doping and coupling CeO_x nanoparticles for CO_2 reduction and organic oxidation, Sustain. Energy Fuels. 3 (2019) 3363–3369. https://doi.org/10.1039/C9SE00409B.

[17] S.W. Cao, Z. Yin, J. Barber, F.Y.C. Boey, S.C.J. Loo, C. Xue, Preparation of Au-$BiVO_4$ heterogeneous nanostructures as highly efficient visible-light photocatalysts, ACS Appl. Mater. Interfaces. 4 (2012) 418–423. https://doi.org/10.1021/am201481b.

[18] X. Zhu, F. Zhang, M. Wang, X. Gao, Y. Luo, J. Xue, Y. Zhang, J. Ding, S. Sun, J. Bao, C. Gao, A shuriken-shaped m-$BiVO_4$/{001}-TiO_2 heterojunction: Synthesis, structure and enhanced visible light photocatalytic activity, Appl. Catal. A Gen. 521 (2016) 42–49. https://doi.org/10.1016/j.apcata.2015.10.017.

[19] D. Diemente, Why is bismuth subchloride soluble in acid?, J. Chem. Educ. 74 (1997) 398–399. https://doi.org/10.1021/ed074p398.

[20] G. Tan, L. Zhang, H. Ren, S. Wei, J. Huang, A. Xia, Effects of pH on the hierarchical structures and photocatalytic performance of $BiVO_4$ powders prepared via the microwave hydrothermal method, ACS Appl. Mater. Interfaces. 5 (2013) 5186–5193. https://doi.org/10.1021/am401019m.

[21] A. Ajmal, I. Majeed, R.N. Malik, H. Idriss, M.A. Nadeem, Principles and mechanisms of photocatalytic dye degradation on TiO_2 based photocatalysts: a comparative overview, RSC Adv. 4 (2014) 37003–37026. https://doi.org/10.1039/c4ra06658h.

[22] K. Iqbal, A. Iqbal, A.M. Kirillov, B. Wang, W. Liu, Y. Tang, A new Ce-doped MgAl-LDH@Au nanocatalyst for highly efficient reductive degradation of organic contaminants, J. Mater. Chem. A. 5 (2017) 6716–6724. https://doi.org/10.1039/C6TA10880F.

[23] K. Iqbal, A. Iqbal, A.M. Kirillov, W. Liu, Y. Tang, Hybrid metal-organic-framework/inorganic nanocatalyst toward highly efficient discoloration of organic dyes in aqueous medium, Inorg. Chem. 57 (2018) 13270–13278. https://doi.org/10.1021/acs.inorgchem.8b01826.

[24] P. Singh, A. Borthakur, P.K. Mishra, D. Tiwary, Nano-materials as photocatalysts for degradation of environmental pollutants: challenges and possibilities, Elsevier, 2019.

[25] P. McFadyen, E. Matijević, Copper hydrous oxide sols of uniform particle shape and size, J. Colloid Interface Sci. 44 (1973) 95–106. https://doi.org/10.1016/0021-9797(73)90196-3.

[26] Y. Sui, W. Fu, H. Yang, Y. Zeng, Y. Zhang, Q. Zhao, Y. Li, X. Zhou, Y. Leng, M. Li, G. Zou, Low temperature synthesis of Cu_2O crystals: Shape evolution and growth mechanism, Cryst. Growth Des. 10 (2010) 99–108. https://doi.org/10.1021/cg900437x.

[27] D. Li, W. Shi, W. Zheng, Controlled synthesis of m-$BiVO_4$ dendrites for enhanced photocatalytic activity, J. Cryst. Growth. 448 (2016) 93–96. https://doi.org/10.1016/j.jcrysgro.2016.05.028.

[28] L. Zhou, W. Wang, H. Xu, Controllable synthesis of three-dimensional well-defined $BiVO_4$ mesocrystals via a facile additive-free aqueous strategy, Cryst. Growth Des. 8 (2008) 728–733. https://doi.org/10.1021/cg0705761.

[29] S.S. Patil, D.P. Dubal, V.G. Deonikar, M.S. Tamboli, J.D. Ambekar, P. Gomez-Romero, S.S. Kolekar, B.B. Kale, D.R. Patil, Fern-like rGO/$BiVO_4$ hybrid nanostructures for high-energy symmetric supercapacitor, ACS Appl. Mater. Interfaces. 8 (2016) 31602–31610. https://doi.org/10.1021/acsami.6b08165.

[30] G.L. Li, First-principles investigation of the surface properties of fergusonite-type monoclinic $BiVO_4$ photocatalyst, RSC Adv. 7 (2017) 9130–9140. https://doi.org/10.1039/c6ra28006d.

[31] R.L. Penn, J.A. Soltis, Characterizing crystal growth by oriented aggregation, CrystEngComm. 16 (2014) 1409–1418. https://doi.org/10.1039/C3CE41773E.

[32] I.M. Lifshitz, V. V Slyozov, The kinetics of precipitation from supersaturated solid solutions, J. Phys. Chem. Solids. 19 (1961) 35–50. https://doi.org/https://doi.org/10.1016/0022-3697(61)90054-3.

[33] M. Lin, Z.Y. Fu, H.R. Tan, J.P.Y. Tan, S.C. Ng, E. Teo, Hydrothermal synthesis of CeO_2 nanocrystals: Ostwald ripening or oriented attachment?, Cryst. Growth Des. 12 (2012) 3296–3303. https://doi.org/10.1021/cg300421x.

[34] D.P. Jaihindh, B. Thirumalraj, S.M. Chen, P. Balasubramanian, Y.P. Fu, Facile synthesis of hierarchically nanostructured bismuth vanadate: An efficient photocatalyst for degradation and detection of hexavalent chromium, J. Hazard. Mater. 367 (2019) 647–657. https://doi.org/10.1016/j.jhazmat.2019.01.017.

[35] C. Feng, D. Wang, B. Jin, Z. Jiao, The enhanced photocatalytic properties of BiOCl/$BiVO_4$ p-n heterojunctions via plasmon resonance of metal Bi, RSC Adv. 5 (2015) 75947–75952. https://doi.org/10.1039/c5ra13886h.

[36] M. Zhu, Q. Liu, W. Chen, Y. Yin, L. Ge, H. Li, K. Wang, Boosting the visible-light photoactivity of BiOCl/$BiVO_4$/N-GQD ternary heterojunctions based on internal Z-scheme charge transfer of N-GQDs: simultaneous band gap narrowing and carrier lifetime prolonging, ACS Appl. Mater. Interfaces. 9 (2017) 38832–38841. https://doi.org/10.1021/acsami.7b14412.

[37] L. Zhang, Q. Luo, X. Chen, M.S. Tse, O.K. Tan, K.H.H. Li, Y.Y. Tay, C.K. Lim, X. Guo, H. holden, Mechanochemically synthesized CuO/m-$BiVO_4$ composite with enhanced photoelectrochemical and photocatalytic properties, RSC Adv. 6 (2016) 65038–65046. https://doi.org/10.1039/c6ra13411d.

5. The Effect of Calcination on Optical Properties of $BiVO_4$ Prepared via Hydrothermal Route

5.1. Introduction

Photocatalyst is a fascinating material, which can harness light energy to promote a chemical reaction for various applications such as water spitting [1], pollutant degradation [2], hydrocarbon production [3], and self-cleaning effect [4]. A commonly-used semiconductor photocatalyst is TiO_2, with a wide bandgap of 3.2 eV. This material, however, works only under ultraviolet light, which occupies only about 5% of sunlight at the surface of the Earth [5,6]. Therefore, numerous research has been performed to seek alternative photocatalysts with narrower bandgap, which can harness visible light energy, such as Fe_2O_3 [7], $BiVO_4$ [1], SnS_2 [8], CdS [9], etc.

In particular, the $BiVO_4$ with monoclinic structure has attracted significant interest from researchers due to its bandgap around ~2.5 eV [10] and other advantages such as low cost of production, non-toxicity, abundance, and stability [11]. However, although the $BiVO_4$ with a bandgap of 2.5 eV can harness visible light, its photon absorption is limited to a wavelength shorter than 500 nm. Considering that there are still a significant amount of photons of sunlight in wavelength of 500–600 nm, narrowing bandgap of $BiVO_4$ could further improve its light absorption efficiency and photocatalytic performance, as evidently shown by a previous study [12–14]. Hence, the ability to tune the bandgap of $BiVO_4$ is crucial for achieving optimal performance for various applications. Many studies have been conducted to modify the bandgap of a photocatalyst via various techniques, such as doping [13,15], controlling oxygen vacancies [14,16], incorporating with other photocatalysts [17], etc.

The study [18] in Chapter 4 reveals that an addition of KCl in the precursor of $BiVO_4$ influences not only the morphology but also the bandgap of $BiVO_4$. Furthermore, the photocatalytic performance of the $BiVO_4$ prepared with KCl is enhanced compared with that of pristine $BiVO_4$. Although KCl addition has been shown to narrow the bandgap of $BiVO_4$, the underlying cause behind the effect has not been clarified yet. Identifying the cause could lead to a discovery of a novel technique to control the bandgap of $BiVO_4$.

A possible explanation could be that KCl may induce defects in $BiVO_4$ during the synthesis, which introduces an impurity band inside the bandgap (of pristine $BiVO_4$) and extends the light absorption edge of $BiVO_4$ to the longer light wavelength range. The likely defects produced during synthesis could be oxygen vacancies in $BiVO_4$ since they are the common point defects found in metal oxides [19,20]. Oxygen vacancies have been demonstrated to reduce material bandgap by introducing defect levels inside the electronic bandgap [20,21].

Thermal treatment can be an effective method to study oxygen vacancies present in metal oxides. Calcining metal oxides with oxygen vacancies in air (oxygen-rich atmosphere) can cause oxygen to fill the vacancy, reducing the number of oxygen vacancies in the materials [22,23]. Whereas calcining them in an oxygen-deficient atmosphere including nitrogen (N_2) [13,23], hydrogen (H_2) [24], and argon (Ar) atmosphere [14] could retain the level of oxygen vacancies or further introduce oxygen vacancies in the material, depending on the calcination condition. Among oxygen-deficient calcination, H_2 gas may cause an undesirable reduction to the metal oxides due to its strong reducing ability [25], while N_2 gas may introduce an N-doping effect in the oxide materials [13,23]. On the other hand, Ar gas has been found to induce only a mild effect on oxygen vacancies in $BiVO_4$, and the doping effect by Ar gas has not been reported yet [14,26]. Considering this matter, Ar calcination is a suitable option to examine oxygen vacancies in the material to retain oxygen vacancies in $BiVO_4$ without introducing doping effect.

This study aims to control oxygen vacancies and bandgap of $BiVO_4$ using different calcination conditions (oxygen-rich and oxygen-deficient atmosphere).

The study also examines the correlation between oxygen vacancies and the bandgap of $BiVO_4$. In addition, the current work intends to clarify the underlying cause affecting the optical properties of $BiVO_4$, prepared with KCl addition in the precursor. In this study, the $BiVO_4$ sample was synthesized via a hydrothermal method, in which KCl was added to the $BiVO_4$ precursor. This work explores the change of oxygen vacancy level via heating the sample at different temperatures in either air (oxygen-rich atmosphere) or Ar gas (oxygen-deficient atmosphere). The morphology, crystal structure, surface chemical state, and optical properties were examined and discussed. The result showed that the bandgap value of the sample prepared with KCl almost restored to that of pristine $BiVO_4$ when calcined in air up to 600 °C, while the value was not changed if calcined in Ar up to 600 °C, strongly indicating an involvement of oxygen vacancies in the sample. The correlation of the KCl concentration with oxygen vacancies in the $BiVO_4$ sample will be also discussed.

5.2. Experimental

5.2.1. Materials

In this study, all chemicals with analytical grade were used without further purification. Bismuth (III) nitrate pentahydrate ($Bi(NO_3)_3 \cdot 5H_2O$, 99.5%), ammonium vanadate (NH_4VO_3, 99.0%), ethanolamine (2-aminoethanol, C_2H_7NO, ≥ 97.0%) were supplied by Nacalai Tesque. Potassium chloride (KCl, 99.5%) was purchased from FUJIFILM Wako Pure Chemical Corporation. Ultrapure water (18.2 MΩ.cm at 25 °C) used for synthesis was obtained via the Direct-Q water purification system (Millipore).

5.2.2. Preparation of $BiVO_4$ samples

$BiVO_4$ was prepared via a typical hydrothermal synthesis with additional KCl. First of all, 0.001 mol of $Bi(NO_3)_3 \cdot 5H_2O$ was put in 30 ml of ultrapure water. After 5 min of stirring, 0.003 mol of KCl was added into the solution to form barely soluble BiOCl. Then, 0.001 mol of NH_4VO_3 was put into the suspension. Then, the pH of the solution was adjusted to 1.8 using 0.6 ml of 1M ethanolamine. After 1 h

of constant stirring, ultrasonication (45 Hz) was used to agitate the suspension for another 1 h. Then, it was transferred to a 50 ml stainless-steel autoclave with a Teflon liner, which was sealed and placed in a pre-heated oven at 160 °C for 12 h. When the autoclave cooled down to room temperature, the as-synthesized $BiVO_4$ was taken out from the autoclave, washed several times with ultrapure water and ethyl alcohol, and dried at 90 °C overnight. This sample was denoted as KCl-$BiVO_4$. For comparison, a pristine $BiVO_4$ sample, without KCl addition in the precursor, was prepared via the same procedure. Finally, the KCl-$BiVO_4$ sample was calcined in a tube furnace either under ambient air or Ar atmosphere (pressure of 0.04 MPa) for 1 h at different temperatures of 400 °C, 500 °C, and 600 °C. The samples were denoted as KCl-$BiVO_4$ T-air and KCl-$BiVO_4$ T-Ar, where T represents the calcined temperature.

5.2.3. Characterization

The X-ray diffraction (XRD) diffractograms of as-prepared samples were measured using a Rigaku RINT2100 with Cu Kα radiation (λ = 0.15418 nm) operated at 40 kV and 30 mA. The microstructure and morphology of each sample were observed using an FE-SEM (Hitachi SU6600 Scanning Electron Microscope), where all samples were sputter-coated with thin Au film to prevent electronic charge-up. The x-ray photoelectron spectroscopy (XPS, JPS-9030 x-ray photoelectron spectrometer) was conducted with Mg Kα radiation using O 1s peak at 530 eV as reference. The UV-vis diffuse reflectance spectra (DRS) were obtained using a Lambda 750S UV/Vis/NIR Spectrophotometer equipped with a 60 mm integrating sphere.

5.3. Results and discussion

5.3.1. Morphology and microstructure of the samples

Morphologies of the samples are shown in SEM micrographs (Fig. 5-1). The pristine $BiVO_4$ sample (Fig. 5-1a) exhibits a rod-like structure, while the KCl-$BiVO_4$ sample (Fig. 5-1b) possesses a shuriken-like structure. The morphology of shuriken-like $BiVO_4$ caused by the addition of KCl has been discussed in Chapter 4 [18]. The KCl-$BiVO_4$ samples are calcined at different temperatures either under ambient air (Fig. 5-1c, 5-1e, and 5-1g) or under Ar atmosphere (Fig. 5-1d, 5-1f, and 5-1h). Based on Fig. 5-1c to 5-1f, there is no significant change when KCl-$BiVO_4$ is heated at 400 °C and 500 °C for both in air and Ar gas. However, the morphology of KCl-$BiVO_4$ is altered noticeably when the temperature becomes 600 °C either under air or Ar gas (Fig. 5-1g and 5-1h). The surface of KCl-$BiVO_4$ becomes smoother at 600 °C. Earlier studies have also found that the $BiVO_4$ particles become more spherical with a smoother surface at the temperature above 500 °C due to the $BiVO_4$ crystallization process [27,28].

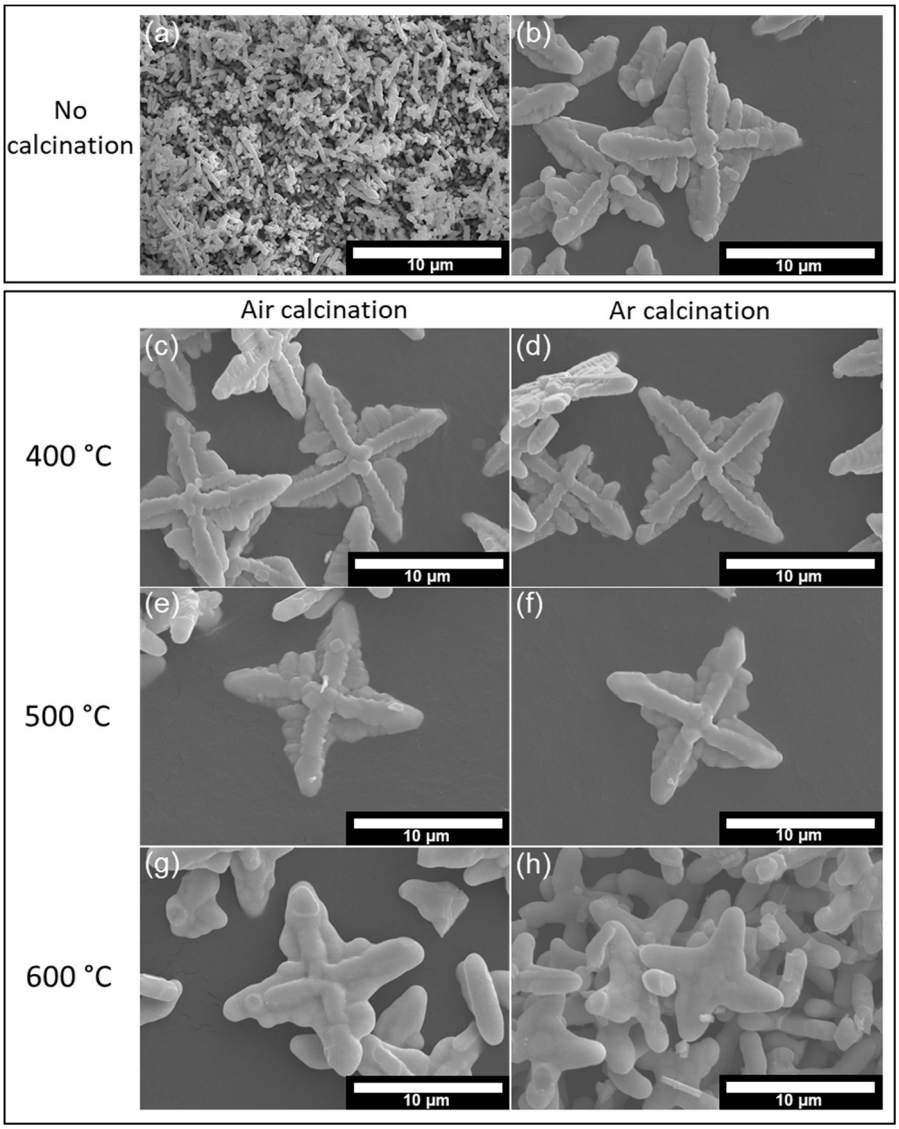

Fig. 5-1. SEM images of (a) pristine $BiVO_4$, (b) KCl-$BiVO_4$, (c) KCl-$BiVO_4$ 400-air, (d) KCl-$BiVO_4$ 400-Ar, (e) KCl-$BiVO_4$ 500-air, (f) KCl-$BiVO_4$ 500-Ar, (g) KCl-$BiVO_4$ 600-air, and (h) KCl-$BiVO_4$ 600-Ar.

5.3.2. Crystal structure of the samples

Fig. 5-2 shows XRD patterns of $BiVO_4$ with and without addition of KCl. Both samples exhibit monoclinic structure (ICDD PDF No. 00-014-0688), except that the KCl-$BiVO_4$ sample possesses a strong intensity at 30.5°, corresponding to (040) plane due to the effect of Cl^- on the crystal growth of $BiVO_4$ [29]. Furthermore, the XRD diffractogram of the KCl-$BiVO_4$ sample displays small

peaks of a tetragonal BiOCl at 12°, 24.1°, and 25.9°, assigned to (001), (002), and (101) planes (ICDD PDF No. 00-006-0249), respectively.

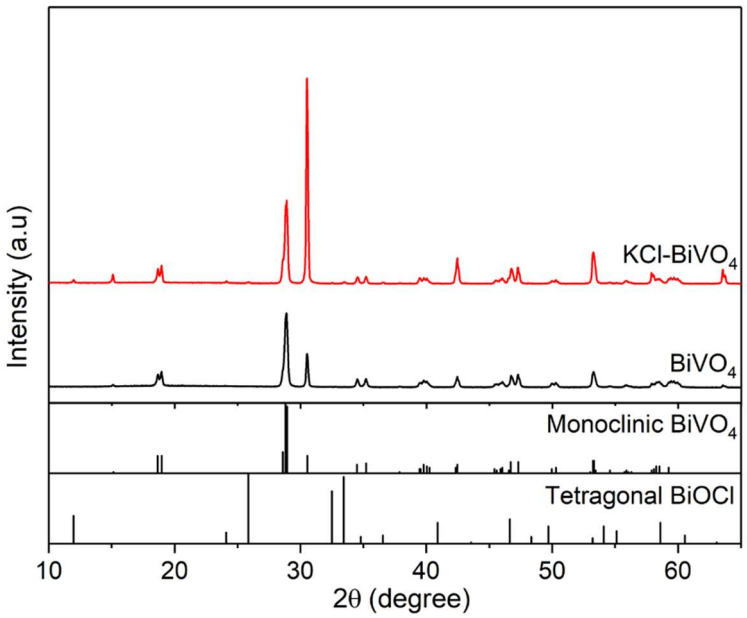

Fig. 5-2. XRD patterns of pristine $BiVO_4$ and KCl-$BiVO_4$.

The KCl-$BiVO_4$ samples are calcined at different temperatures in air (Fig. 5-3a) and Ar gas (Fig. 5-3b). The KCl-$BiVO_4$ sample retains the monoclinic structure of $BiVO_4$ after calcination either in air or in Ar gas. The peak intensity of BiOCl phase decreases as the temperature increases in either condition of calcination since BiOCl is reported to decompose and convert to $Bi_{24}O_{31}Cl_{10}$ at a temperature above 400 °C [30–32]. However, there is no $Bi_{24}O_{31}Cl_{10}$ phase observed in this study, as shown in Fig. 5-3. Instead, another crystal phase appears in Fig. 5-3b when KCl-$BiVO_4$ is heated to 600 °C in Ar atmosphere. The diffraction peaks of the mentioned crystal phase at 11.5°, 23.6°, and 32.6° can be assigned to (002), (013), and (200) planes of $Bi_4V_2O_{10}$ (ICDD PDF No. 01-086-1181) [33], respectively.

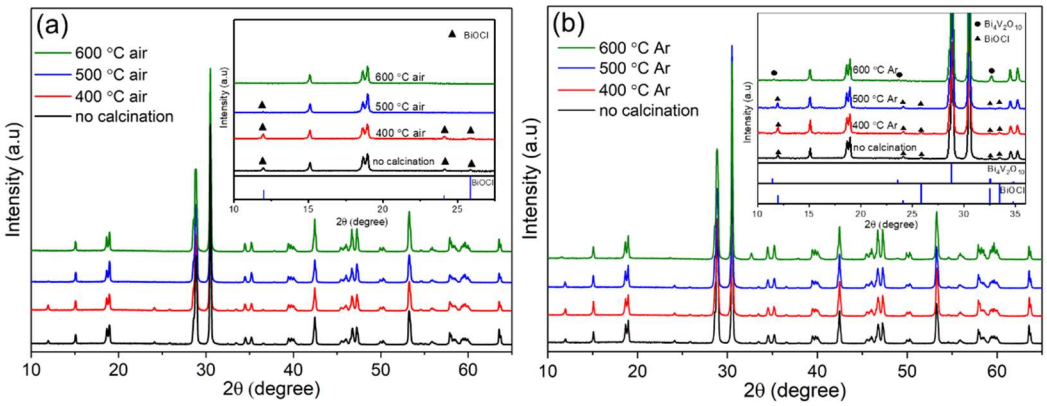

Fig. 5-3. XRD patterns of KCl-$BiVO_4$ calcined at different temperatures in (a) air and (b) Ar gas, including their respective magnification charts at 2θ = 10° to 27° and 2θ = 10° to 36°. All peaks without symbols correspond to the $BiVO_4$.

In the present study, the formation of $Bi_4V_2O_{10}$ in the KCl-$BiVO_4$ 600-Ar sample can be explained as follows. The $Bi_4V_2O_{10}$ belongs to Bi_2O_3–VO_2 system with V^{4+} instead of V^{5+} [33,34]. According to the previous works [33,35], $Bi_4V_2O_{10}$ can be synthesized by heating the mixture of Bi_2O_3 and VO_2 at a temperature higher than 550 °C in vacuum. To date, there is scarce research on $Bi_4V_2O_{10}$, and no report has indicated production of $Bi_4V_2O_{10}$ via the thermal treatment of $BiVO_4$; that is, no $Bi_4V_2O_{10}$ phase would be observed when $BiVO_4$ phase is annealed at a temperature range of 300–700 °C under Ar atmosphere, as demonstrated by an earlier study [14]. The plausible explanation of $Bi_4V_2O_{10}$ appearance in the KCl-$BiVO_4$ 600-Ar sample is that the pre-formed BiOCl decomposes and loses Cl at high temperatures, and further reacts with V^{4+} to form $Bi_4V_2O_{10}$ phase. It is worth mentioning that V^{4+} exists in $BiVO_4$ in response to oxygen vacancies in the $BiVO_4$ to maintain charge neutrality [36,37]. It is thus indicated that a considerable number of oxygen vacancies are already present in KCl-$BiVO_4$, and more vacancies are further introduced by oxygen-deficient calcination.

5.3.3. X-ray photoelectron spectroscopic (XPS) analyses of the samples

XPS analysis was used to study the surface chemical state, including vacancies and composition of the samples. XPS survey spectra in Fig. 5-4a demonstrate the existence of Bi, V, and O elements in both $BiVO_4$ and KCl-$BiVO_4$

heated at various temperatures in air. Fig. 5-4b shows Bi 4f XPS spectra of $BiVO_4$ and KCl-$BiVO_4$, corresponding to Bi^{3+} of $BiVO_4$. Both spectra are composed of two peaks at 164.6 and 159.3 eV, each corresponding to Bi $4f_{5/2}$ and Bi $4f_{7/2}$, respectively [38]. There is no significant change in the core level of Bi 4f when the KCl-$BiVO_4$ sample is calcined up to 600 °C in air. On the other hand, in Fig. 5-4c, an asymmetry spectrum of each sample, assigned to V $2p_{3/2}$ of $BiVO_4$, can be deconvoluted into two peaks, V^{5+} (516.9 eV) and V^{4+} (515.3 eV) [2,14]. The existence of V^{4+} has been reported to indicate the presence of oxygen vacancies in $BiVO_4$ [36,37]. The peak areas (in cps) of V^{5+} and V^{4+} are listed in Table 5-1. In Fig. 5-4d, it is displayed that the KCl-$BiVO_4$ sample possesses a small peak at 198.6 eV, assigned to Cl 2p of BiOCl [39]. The peak disappears when the temperature becomes 600 °C, which is in agreement with XRD patterns in Fig. 5-3a. Lastly, O 1s peaks of the samples (Fig. 5-4e) at 530 eV corresponds to the bonding of Bi−O in $BiVO_4$ [39,40].

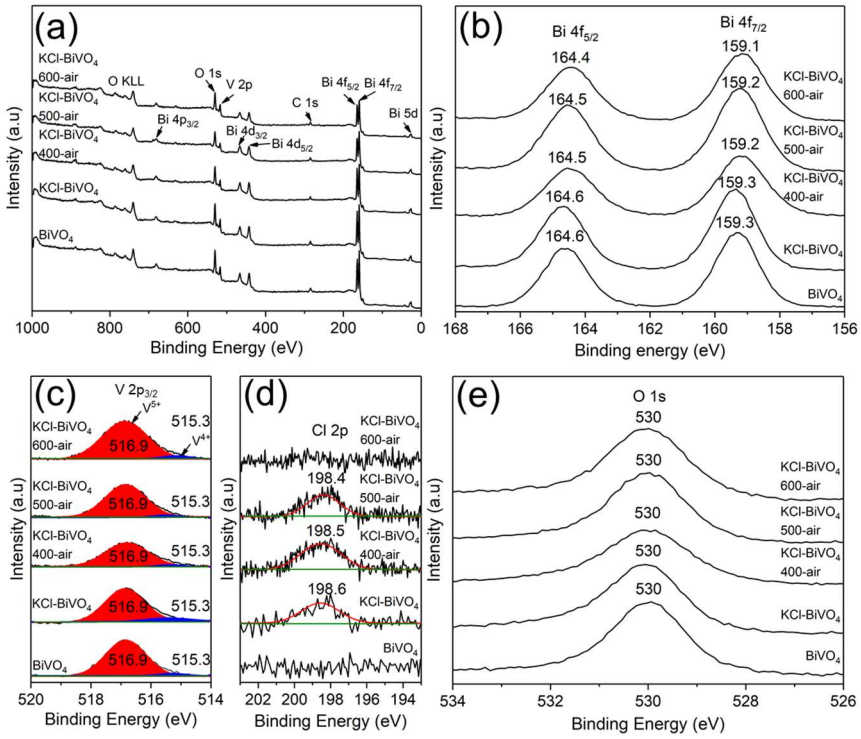

Fig. 5-4. XPS spectra of $BiVO_4$ and KCl-$BiVO_4$ samples calcined in air at various temperatures: (a) survey spectra and high-resolution spectra of (b) Bi 4f, (c) V 2p, (d) Cl 2p, and (e) O 1s orbitals.

Table 5-1. XPS relative peak areas of V^{5+} and V^{4+} from V $2p_{3/2}$, estimated % oxygen vacancies (V_o) and bandgaps (E_g) of the pristine $BiVO_4$ and the KCl-$BiVO_4$ calcined at various temperatures, either in Ar gas or in air.

Sample	Peak area V^{5+} (%)	Peak area V^{4+} (%)	% Oxygen Vacancy, V_o (%)	E_g (eV)
KCl-$BiVO_4$	91.2	8.8	4.4	2.34
KCl-$BiVO_4$ 400-Ar	91.2	8.8	4.4	2.34
KCl-$BiVO_4$ 500-Ar	91.2	8.8	4.4	2.34
KCl-$BiVO_4$ 600-Ar	90.8	9.2	—[a]	2.34
KCl-$BiVO_4$ 400-air	94.4	5.6	2.8	2.42
KCl-$BiVO_4$ 500-air	95.5	4.5	2.2	2.44
KCl-$BiVO_4$ 600-air	95.7	4.3	2.2	2.45
$BiVO_4$	96.1	3.9	2.0	2.48

[a] since KCl-$BiVO_4$ 600-Ar contains $Bi_4V_2O_{10}$ phase, V^{4+} may come from both $Bi_4V_2O_{10}$ and oxygen vacancies in $BiVO_4$. Thus, the oxygen vacancies in $BiVO_4$ cannot be estimated using relative areas of V^{5+} and V^{4+}.

The Bi, V, and O elements are also observed in XPS survey spectra (Fig. 5-5a) of the KCl-$BiVO_4$ sample calcined in Ar gas. Similar to the KCl-$BiVO_4$ sample calcined in air, the core level of Bi 4f (Fig. 5-5b) and O 1s (Fig. 5-5e) exhibits no apparent change when calcined up to 600 °C in Ar gas. Likewise, the V $2p_{3/2}$ spectra of the sample calcined in Ar gas are similar to those of the sample calcined in air except the relative peak area of V^{5+} and V^{4+} (Table 5-1), which is discussed later. Fig. 5-5d illustrates a small peak of Cl 2p (198.6 eV) of BiOCl [39] in the KCl-$BiVO_4$ 600-Ar sample, indicating residual Cl remains in the sample even though BiOCl phase disappears in XRD patterns (Fig. 5-3b). It suggests that either residual BiOCl may still exist in the form of amorphous or residual chlorine is present in the sample.

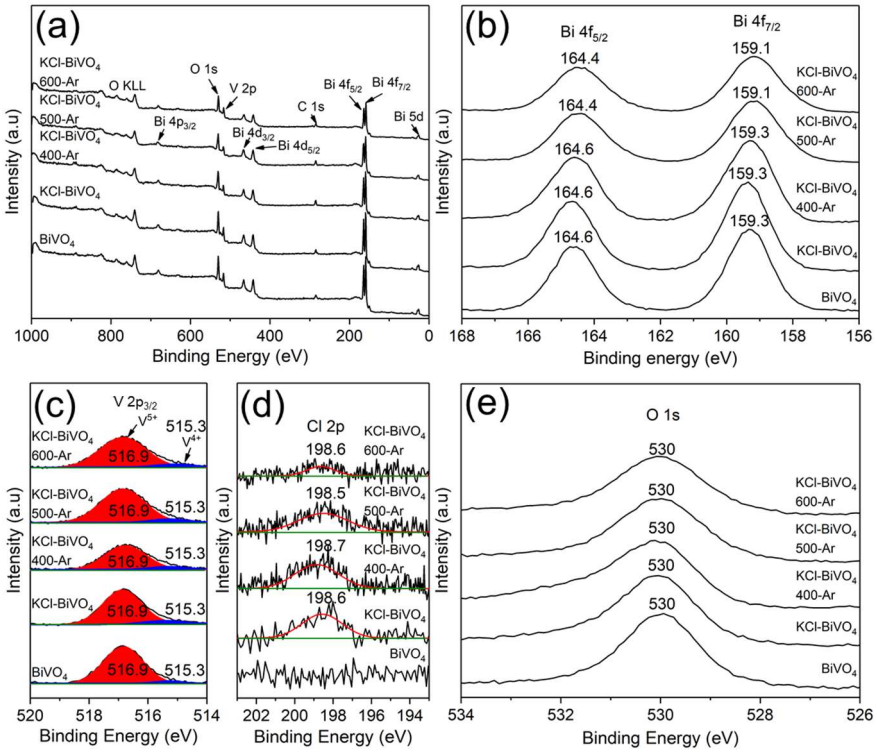

Fig. 5-5. XPS survey spectra of $BiVO_4$ and KCl-$BiVO_4$ samples calcined in Ar gas at different temperatures and high-resolution XPS spectra of (b) Bi 4f, (c) V 2p, (d) Cl 2p, and (e) O 1s orbitals.

The % oxygen vacancies (V_o) in Table 5-1 can be estimated using the peak area of V^{5+} and V^{4+} in the V $2p_{3/2}$ XPS spectra, assuming that each oxygen vacancy site generates two equivalent of V^{4+}. Thus, the % oxygen vacancies (V_o) is calculated using the following Eq (5-1) [37].

$$V_o = \left(\frac{Peak\ area\ V^{4+}}{Peak\ area\ V^{4+} + Peak\ area\ V^{5+}} \right) \times 0.5 \times 100\% \qquad (5.1)$$

5.3.4. Optical properties of the samples

Fig. 5-6 illustrates the different colors of all the samples. Pristine $BiVO_4$ exhibits bright yellow color while KCl-$BiVO_4$ is orange in color. When KCl-$BiVO_4$

is calcined at different temperatures in Ar gas, its color changes from orange to dark green. Likewise, when KCl-$BiVO_4$ is calcined in air at 400 °C, it also shows similar dark green in color. However, the color alters to bright yellow, similar to pristine $BiVO_4$ when the temperature is increased to 500 °C and 600 °C.

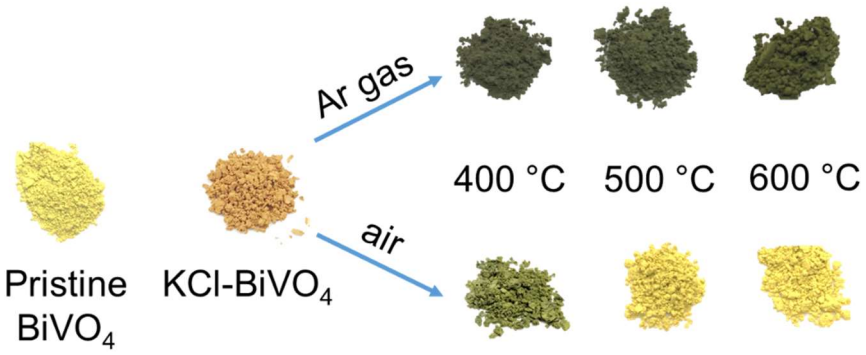

Fig. 5-6. Photographs of pristine $BiVO_4$, KCl-$BiVO_4$, and calcined KCl-$BiVO_4$ at various temperatures in air and Ar gas.

The optical properties of the samples are investigated using UV-vis diffuse reflectance spectra (DRS). Absorption spectra are transformed from reflectance spectra using Kubelka-Munk function, $F(R) = (1-R)^2/2R$, where R is diffuse reflectance. The absorption spectrum of each sample is depicted in Fig. 5-7a and 5-7c. Since $BiVO_4$ is a direct transition semiconductor, the plot, $F(R)hv)^2$ vs. hv, can be used to estimate the bandgaps [10,40,41], where each bandgap value (E_g), as shown in Table 5-1, is determined by extrapolating the linear part of the curve in Fig. 5-7b and 5-7d. Based on Fig. 5-7, the pristine $BiVO_4$ sample exhibits the E_g value of 2.48 eV, similar to that of pristine $BiVO_4$ reported by an earlier study [10]. On the other hand, the KCl-$BiVO_4$ sample possesses a narrower E_g of 2.34 eV, indicating that the addition of KCl (in precursor) reduces the E_g value of $BiVO_4$. Figure 5-7 also demonstrates the absorption spectra and bandgap of the KCl-$BiVO_4$ sample, calcined at various temperatures either in air (oxygen-rich gas) or in Ar gas (oxygen-deficient gas).

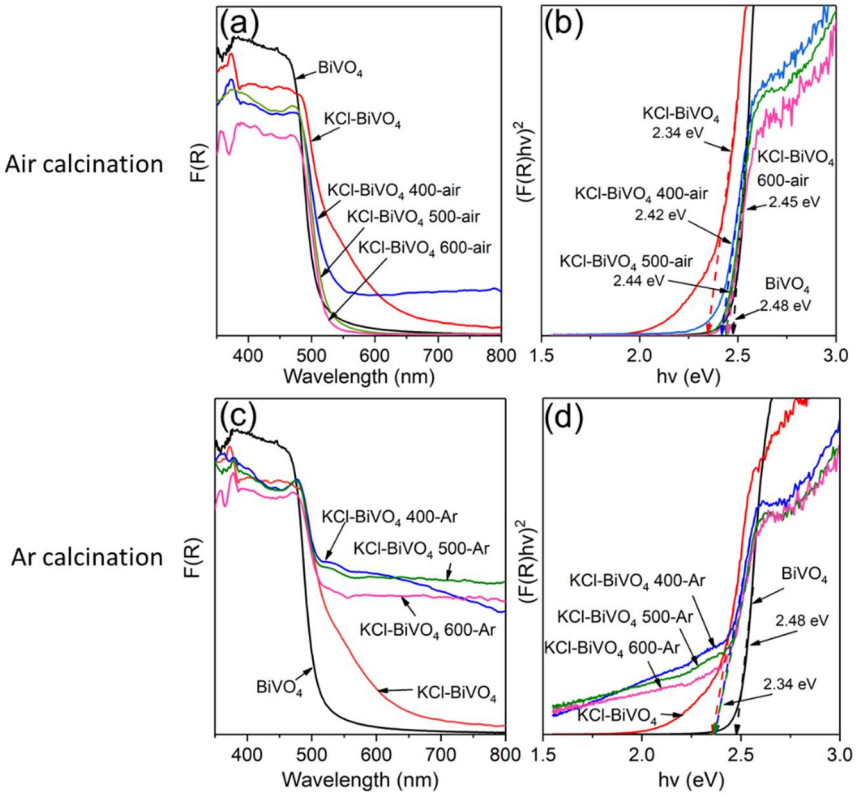

Fig. 5-7. UV-vis absorption spectra (left) and $(F(R)hv)^2$ *vs hv* plot (right) of pristine $BiVO_4$ and KCl-$BiVO_4$ calcined at different temperatures in (a-b) air and (c-d) Ar gas.

As shown in Fig. 5-7a and 5-7b, the absorption edge of the KCl-$BiVO_4$ sample calcined in air exhibits a blueshift, and the E_g value of the sample calcined at 600 °C in air is almost that of the pristine $BiVO_4$. On the other hand, the E_g value of the KCl-$BiVO_4$ sample remains to be at 2.34 eV, as shown in Fig. 5-7c and 5-7d. Since BiOCl possesses a bandgap of about 3.3 eV [42], which is substantially wider than that (2.34–2.48 eV) of $BiVO_4$, it may not influence the bandgap of $BiVO_4$. Moreover, earlier study [42] reported no significant change in bandgap of $BiVO_4$ in BiOCl/$BiVO_4$ composite even with their interface formed at a nanosized level. Thus, the modification of the bandgap may not be originated from the residual BiOCl in the samples (XRD result in Fig. 5-3). The $Bi_4V_2O_{11}$ phase, on the other hand, is only observed in KCl-$BiVO_4$ 600-Ar (Fig. 5-3b), whose E_g value is equal to those of KCl-$BiVO_4$, KCl-$BiVO_4$ 400-Ar, and KCl-$BiVO_4$ 500-Ar. Thus, the small amount of $Bi_4V_2O_{11}$ might not influence the bandgap of $BiVO_4$. Hence, the change in the bandgap is more likely to be attributed to oxygen vacancies, which

had been found to influence the light absorption and bandgap of $BiVO_4$ [36,37]. This result is consistent with the presence of oxygen vacancies from the XPS result. The oxygen vacancies in metal oxides are reported to create defect levels inside the electronic bandgap, either just below the bottom end of the conduction band or just above the upper end of the valence band. This would result in a decrease of the bandgap due to overlapping of the defect states with either the conduction band minimum or the valence band maximum [20,21].

The present study shows the bandgaps of KCl-$BiVO_4$ samples before and after Ar-calcination (400, 500, and 600 °C) are unchanged. This result defers from that of earlier report [14], which revealed that bandgap values of Ar-calcination $BiVO_4$ were slightly reduced by 0.02 and 0.05 eV at temperatures of 500 and 700 °C, respectively, compared with untreated $BiVO_4$. It was attributed to an increase in oxygen vacancies. The different outcomes between the said report and this study could be a large number of oxygen vacancies already present in the untreated KCl-$BiVO_4$ (from the XPS results). Thus, calcining the KCl-$BiVO_4$ sample in Ar could not further induce more oxygen vacancies in the sample. To confirm this, the KCl-$BiVO_4$ sample was first calcined at 600 °C (1 h) in air, then at 600 °C (1 h) in Ar gas. The sample was allowed to cool to room temperature in between both calcinations. Bandgaps of the samples were determined using the Tauc's plot, as shown in Fig. 5-8. The result showed that the bandgap of the said sample increased from 2.34 to 2.45 eV when calcined in air (600 °C for 1 h), and then decreases to 2.40 eV when calcined in Ar (600 °C for 1 h). It implies that if the amount of oxygen vacancies in KCl-$BiVO_4$ is relatively low, Ar calcination could induce oxygen vacancies and reduce the bandgap of KCl-$BiVO_4$. The results of this study are in agreement with those of previous study [43], in which the $BiVO_4$ was annealed in air at 450 °C for 2 h before being heated in Ar gas (300 – 400 °C for 2 h).

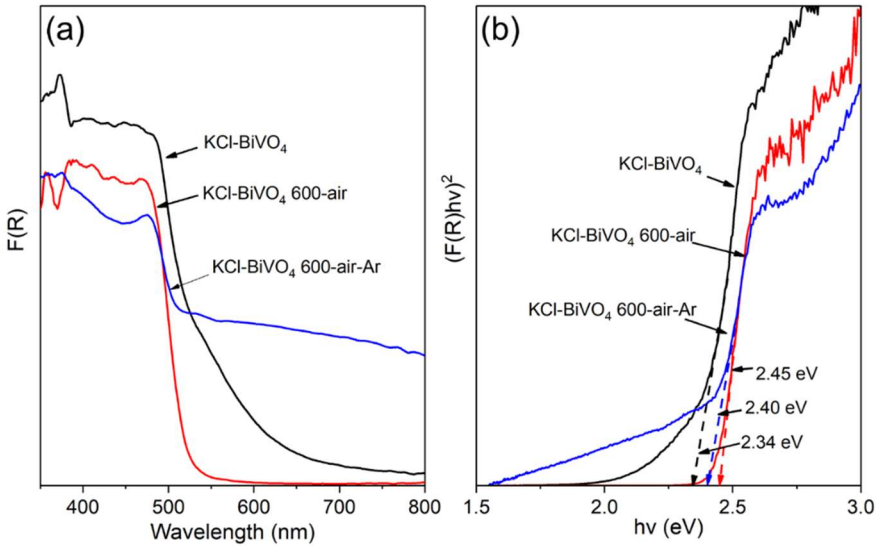

Fig. 5-8. (a) UV-vis absorption spectra and (b) *(F(R)hv)*^{2} *vs hv* plot of KCl-$BiVO_4$, KCl-$BiVO_4$ 600-air, and KCl-$BiVO_4$ 600-air-Ar (KCl-$BiVO_4$ was calcined at 600 °C in air and then Ar gas).

It is worth mentioning that although absorption edges and bandgaps remain unchanged for the Ar-calcination samples (Fig. 5-7c and 5-7d), their baselines of absorption spectra (550–800 nm) shift upward, which could be ascribed to the change in color (dark green) of Ar-calcination samples in Fig. 5-6. This phenomenon has also been observed by Qin et al. [44], who treated $BiVO_4$ film by electrochemical and chemical ($NaBH_4$) reduction. They mentioned the dark green color occurred after the electrochemical and chemical reduction treatment, which generated a considerable amount of V^{4+} in $BiVO_4$. Hence, the dark green color of $BiVO_4$ might be caused by electrical energy and the large amount of V^{4+} present in the $BiVO_4$. In the case of the current study, a likely cause of the color change is heat energy (instead of electrical energy) and the large amount of V^{4+} present in the KCl-$BiVO_4$ sample, which would explain the dark green color of Ar-calcination samples. It suggests that high temperature may modify the surface state of $BiVO_4$ that possesses a considerable amount of V^{4+}. It is further confirmed by the KCl-$BiVO_4$ 400-air sample, which exhibits a greenish-yellow color (Fig. 5-6) due to a moderate amount of V^{4+} still present in the sample. On the other hand, the KCl-

$BiVO_4$ 500-air and KCl-$BiVO_4$ 600-air samples display bright yellow, comparable to the pristine $BiVO_4$, because of their low amount of V^{4+}.

Table 5-1 shows the relationship between V_o and E_g of all the samples. The E_g value decreases along with an increase in the V_o value, strongly suggesting that an increase in oxygen vacancies narrows the bandgap of the sample, which is consistent with earlier research [36,37,45]. As a result, the correlation between bandgap and oxygen vacancies in present study can be constructed in a linear relationship, as plotted in Fig. 5-9. A similar linear relationship between bandgap and oxygen vacancies has been reported in ZnO thin films, produced via varying the oxygen partial pressure [16]. It should be noted that the data of KCl-$BiVO_4$ 600-Ar are not used to construct Fig. 5-9 because the said sample contains $Bi_4V_2O_{10}$ phase (from XRD results), possessing V^{4+} states that are not responsible for oxygen vacancies in $BiVO_4$.

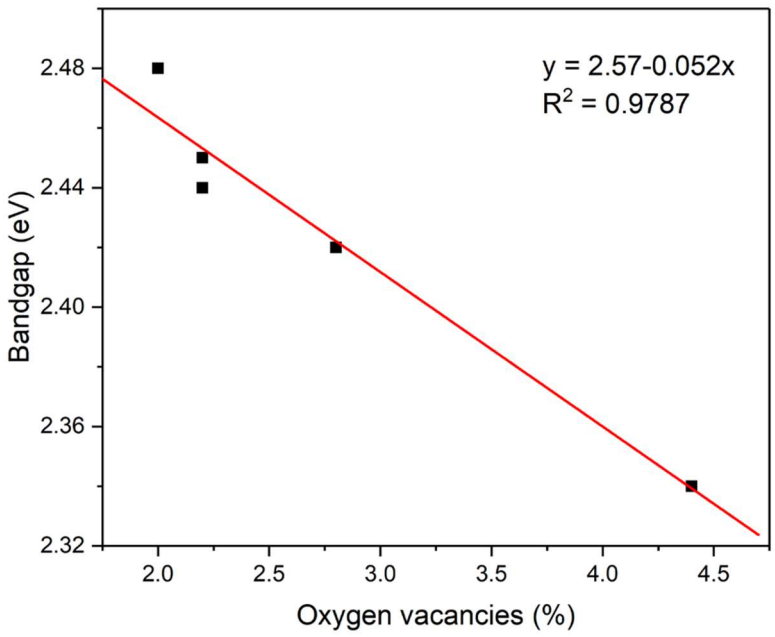

Fig. 5-9. Correlation between bandgap and oxygen vacancies of the samples.

Based on all results and analyses, it can be inferred that a large number of oxygen vacancies was produced during the sample preparation of $BiVO_4$ with the addition of KCl, which in turn narrows the bandgap of $BiVO_4$. The bandgap value of KCl-$BiVO_4$ can be restored to that of pristine $BiVO_4$ by heating the sample in air. When the KCl-$BiVO_4$ sample is calcined in air (oxygen-rich atmosphere), the oxygen from the air can effectively fill the oxygen vacancies [22,23] in the $BiVO_4$ system as temperature increases, leading to reducing some vacancy defects and restoring its E_g value close to that of pristine $BiVO_4$. Conversely, when the KCl-$BiVO_4$ sample is calcined in Ar gas (oxygen-deficient atmosphere), the oxygen vacancies remain in the system, resulting in no change in its E_g value. Therefore, it can be concluded that the addition of KCl during $BiVO_4$ preparation induces additional oxygen vacancies in the KCl-$BiVO_4$ sample and narrows the bandgap of the sample. The underlying cause behind this effect will be discussed in the next section. Additionally, the bandgap value of KCl-$BiVO_4$ can be tunable by heating the sample in different atmospheric conditions, as shown in Fig. 5-8.

5.3.5. Relationship between the addition of KCl and oxygen vacancies in the KCl-$BiVO_4$ samples

Based on study [18] in Chapter 4, KCl concentration could influence the bandgaps of $BiVO_4$ due to the defects in the $BiVO_4$ crystal structure. The study in this chapter suggests the defects could be the oxygen vacancies introduced via addition of KCl to the $BiVO_4$ precursor. Thus, there should be a connection between KCl concentration and formation of oxygen vacancies in the KCl-$BiVO_4$ sample. In order to confirm this point, the KCl-$BiVO_4$ samples were prepared with different concentrations of KCl (0, 1, 2, 3, 4, and 5 mmol). The E_g and V_o [Eq (5-1)] values of the samples produced with various KCl concentration are listed in Table 5-2, the values of which are determined using Tauc's's's plot (Fig. 1 in Appendix C) and XPS V $2p_{3/2}$ spectra (Fig. 2 in Appendix C).

Table 5-2. XPS peak areas of V^{5+} and V^{4+} from V $2p_{3/2}$, estimated % oxygen vacancies (V_o), and bandgaps (E_g) of the KCl-$BiVO_4$ with various concentrations of KCl.

KCl concentration in KCl-$BiVO_4$	Peak area V^{5+} (%)	Peak area V^{4+} (%)	V_o[a] from XPS V $2p_{3/2}$ (%)	E_g (eV)	V_o[b] from E_g value (%)
5 mmol	91.0	9.0	4.5	2.35	4.2
4 mmol	90.8	9.2	4.6	2.32	4.8
3 mmol	91.2	8.8	4.4	2.34	4.4
2 mmol	94.2	5.8	2.9	2.43	2.7
1 mmol	95.6	4.4	2.2	2.45	2.3
0 mmol	96.1	3.9	2.0	2.48	1.7

[a] oxygen vacancies, V_o, are estimated using XPS V $2p_{3/2}$ spectra and Eq (5-1);
[b] oxygen vacancies, V_o', are estimated using E_g and correlation between bandgap and oxygen vacancies in Fig. 5-9.

The relationship between oxygen vacancies and KCl concentration is demonstrated in Fig 5-10. There are two data plotted in the figure. One set of data is calculated using the Eq (5-1) and XPS V $2p_{3/2}$ spectra (Table 5-2), and the other is using the E_g values (Table 5-2) and correlation between bandgap and oxygen vacancies (Fig. 5-9). Both results are comparable and follow a similar trend, where oxygen vacancies increase along with an increase in KCl concentration up to 3 mmol and remain almost constant from 3 to 5 mmol of KCl.

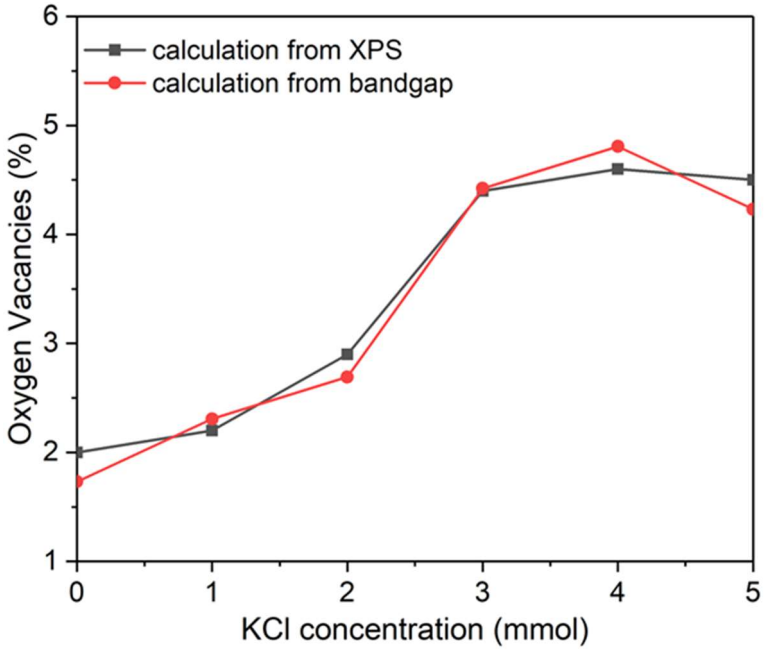

Fig. 5-10. Relationship between oxygen vacancies and KCl concentration of data calculated from XPS spectra and bandgap.

The increase in oxygen vacancies corresponding to the addition of KCl (Fig. 5-10) could be explained as follows. Generally, the formation of oxygen vacancies in metal oxides is involved with the oxygen-deficient environment, the chemical reduction, the dynamics of ionic defects, the plasma treatment, and the hydrogen treatment [14,20,46]. In case of this study, a plausible explanation of the increase in oxygen vacancies along with KCl concentration could be the reduction reaction of V^{5+} to V^{4+} by Cl^- during the synthesis. The existence of V^{4+} in the final product of $BiVO_4$ generates oxygen vacancies to retain charge neutrality in the $BiVO_4$ sample [37,47]. Considering the reaction (5-2) below, the formation reaction of VO^{2+} (V^{4+}) ions is favored, as the change in Gibbs free energy ($\Delta G° = -11.66$ kJ mol^{-1}) is negative at standard condition of 298.15 K and 1 bar (see the calculation (b) in Appendix A).

$$2VO_3^-\,(aq) + 2Cl^-\,(aq) + 8H^+\,(aq) \rightleftharpoons 2VO^{2+}\,(aq) + Cl_2\,(g) + 4H_2O\,(l) \qquad (5\text{-}2)$$

(V^{5+}) (V^{4+})

Moreover, earlier study has reported a small amount of V^{4+} was produced in a solution of V^{5+} and chlorine [48]. Thus, adding more Cl^- would result in generating more VO^{2+} with V^{4+}, which could contribute to the formation of oxygen vacancies in $BiVO_4$. Although this does not accurately represent the actual condition of synthesis, which involves other chemicals and hydrothermal conditions, it may provide an insight on the correlation between concentrations of Cl^- and V^{4+}, which is in good agreement with the increase in oxygen vacancies in the KCl-$BiVO_4$ sample.

On the other hand, the increase of oxygen vacancies is almost constant from 3 to 5 mmol of KCl (Fig. 5-10) because only the addition of KCl might not be able to induce more V^{4+} ions since the process also depends on acidity. It is also worth mentioning that there is a small decrease in oxygen vacancy levels calculated from bandgaps of the KCl-$BiVO_4$ sample with KCl of 5 mmol (Fig. 5-10). It might imply that the bandgap of KCl-$BiVO_4$ could be influenced by other minor factor besides oxygen vacancies. The minor factor might possibly be a Cl-doping effect caused by a small amount Cl existing in the KCl-$BiVO_4$ sample. The Cl observed in KCl-$BiVO_4$ (the XPS result) could correspond to both BiOCl and Cl elements in the sample. Earlier studies on the Cl-doping effect on optical properties of ZnO [49] and CdS [50] found that the bandgaps of both materials widened with the increase in Cl-doping concentration. This doping effect might also occur on $BiVO_4$, resulting in a slight increase in bandgap when KCl concentration increases. Therefore, the oxygen vacancies calculated using the bandgap of the sample might be underestimated and less accurate at a relatively high concentration of KCl (5 mmol).

The above analysis indicates that KCl concentration in the $BiVO_4$ precursor influences oxygen vacancies, in turn modifying the bandgap of $BiVO_4$. Therefore, oxygen vacancies and bandgap of $BiVO_4$ could be controlled not only by calcination conditions, but also by varying KCl concentration during the $BiVO_4$ preparation.

5.4. Conclusions

The KCl-$BiVO_4$ sample was synthesized via hydrothermal method with addition of KCl in the $BiVO_4$ precursor, and compared with pristine $BiVO_4$. The KCl-$BiVO_4$ sample exhibits narrower bandgap compared with pristine $BiVO_4$ sample. The bandgap modification is ascribed to the oxygen vacancies, which could be partially eliminated via calcination of the sample in air (oxygen-rich atmosphere) up to 600 °C. The linear correlation is found between the amount of oxygen vacancies in the KCl-$BiVO_4$ sample and the bandgap value, in which an increase in the former reduces the latter value. Since altering the KCl concentration in the $BiVO_4$ precursor and the calcination condition would influence the level of oxygen vacancies in $BiVO_4$, it is thus possible that the bandgap of $BiVO_4$ can be tunable via controlling these two factors. These findings are beneficial not only in the field of photocatalysis, but also in other potential applications that involve bandgap engineering.

Reference

[1] G. Xi, J. Ye, Synthesis of bismuth vanadate nanoplates with exposed {001} facets and enhanced visible-light photocatalytic properties, Chem. Commun. 46 (2010) 1893–1895. https://doi.org/10.1039/b923435g.

[2] T. Senasu, S. Youngme, K. Hemavibool, S. Nanan, Sunlight-driven photodegradation of oxytetracycline antibiotic by $BiVO_4$ photocatalyst, J. Solid State Chem. 297 (2021) 122088. https://doi.org/10.1016/j.jssc.2021.122088.

[3] T. Inoue, A. Fujishima, S. Konishi, K. Honda, Photoelectrocatalytic reduction of carbon dioxide in aqueous suspensions of semiconductor, Nature. 277 (1979) 637.

[4] S. Banerjee, D.D. Dionysiou, S.C. Pillai, Self-cleaning applications of TiO_2 by photo-induced hydrophilicity and photocatalysis, Appl. Catal. B Environ. 176–177 (2015) 396–428. https://doi.org/10.1016/j.apcatb.2015.03.058.

[5] C. Dette, M.A. Pérez-Osorio, C.S. Kley, P. Punke, C.E. Patrick, P. Jacobson, F. Giustino, S.J. Jung, K. Kern, TiO_2 anatase with a bandgap in the visible region, Nano Lett. 14 (2014) 6533–6538. https://doi.org/10.1021/nl503131s.

[6] W. Qin, D. Zhang, D. Zhao, L. Wang, K. Zheng, Near-infrared photocatalysis based on YF_3:Yb^{3+}, Tm^{3+}/TiO_2 core/shell nanoparticles, Chem. Commun. 46 (2010) 2304–2306. https://doi.org/10.1039/b924052g.

[7] Z. Wang, X. Mao, P. Chen, M. Xiao, S.A. Monny, S. Wang, M. Konarova, A. Du, L. Wang, Understanding the roles of oxygen vacancies in hematite-based photoelectrochemical processes, Angew. Chemie - Int. Ed. 58 (2019) 1030–1034. https://doi.org/10.1002/anie.201810583.

[8] Z. Zhang, C. Shao, X. Li, Y. Sun, M. Zhang, J. Mu, P. Zhang, Z. Guo, Y. Liu, Hierarchical assembly of ultrathin hexagonal SnS_2 nanosheets onto electrospun TiO_2 nanofibers: Enhanced photocatalytic activity based on photoinduced interfacial charge transfer, Nanoscale. 5 (2013) 606–618. https://doi.org/10.1039/c2nr32301j.

[9] X. Hao, Y. Hu, Z. Cui, J. Zhou, Y. Wang, Z. Zou, Self-constructed facet junctions on hexagonal CdS single crystals with high photoactivity and photostability for water splitting, Appl. Catal. B Environ. 244 (2019) 694–703. https://doi.org/https://doi.org/10.1016/j.apcatb.2018.12.006.

[10] G. Zhao, W. Liu, Y. Hao, Z. Zhang, Q. Li, S. Zang, Nanostructured shuriken-like $BiVO_4$ with preferentially exposed {010} facets: Preparation, formation mechanism, and enhanced photocatalytic performance, Dalt. Trans. 47 (2018) 1325–1336. https://doi.org/10.1039/c7dt04431c.

[11] H.L. Tan, R. Amal, Y.H. Ng, Alternative strategies in improving the photocatalytic and photoelectrochemical activities of visible light-driven $BiVO_4$: A review, J. Mater. Chem. A. 5 (2017) 16498–16521. https://doi.org/10.1039/c7ta04441k.

[12] J.K. Cooper, S.B. Scott, Y. Ling, J. Yang, S. Hao, Y. Li, F.M. Toma, M. Stutzmann, K. V. Lakshmi, I.D. Sharp, Role of hydrogen in defining the n-type character of $BiVO_4$ photoanodes, Chem. Mater. 28 (2016) 5761–5771. https://doi.org/10.1021/acs.chemmater.6b01994.

[13] T.W. Kim, Y. Ping, G.A. Galli, K.S. Choi, Simultaneous enhancements in photon absorption and charge transport of bismuth vanadate photoanodes for solar water splitting, Nat. Commun. 6 (2015) 1–10. https://doi.org/10.1038/ncomms9769.

[14] H.L. Tan, A. Suyanto, A.T. De Denko, W.H. Saputera, R. Amal, F.E. Osterloh, Y.H. Ng, Enhancing the photoactivity of faceted $BiVO_4$ via annealing in oxygen-deficient condition, Part. Part. Syst. Charact. 34 (2017). https://doi.org/10.1002/ppsc.201600290.

[15] C. Qin, H. Liao, F. Rao, J. Zhong, J. Li, One-pot hydrothermal preparation of Br-doped $BiVO_4$ with enhanced visible-light photocatalytic activity, Solid State Sci. 105 (2020) 106285. https://doi.org/10.1016/j.solidstatesciences.2020.106285.

[16] H. Liu, F. Zeng, Y. Lin, G. Wang, F. Pan, Correlation of oxygen vacancy variations to band gap changes in epitaxial ZnO thin films, Appl. Phys. Lett. 102 (2013). https://doi.org/10.1063/1.4804613.

[17] M.R.U.D. Biswas, W.C. Oh, Synthesis of $BiVO_4$-GO-PVDF nanocomposite: An excellent, newly designed material for high photocatalytic activity towards organic dye degradation by tuning band gap energies, Solid State Sci. 80 (2018) 22–30. https://doi.org/10.1016/j.solidstatesciences.2018.03.021.

[18] S. Meng, T. Ogawa, H. Okumura, K.N. Ishihara, The effect of potassium chloride on $BiVO_4$ morphology and photocatalysis, J. Solid State Chem. 302 (2021) 122291. https://doi.org/10.1016/j.jssc.2021.122291.

[19] C. Künneth, R. Batra, G.A. Rossetti, R. Ramprasad, A. Kersch, Thermodynamics of phase stability and ferroelectricity from first principles, 2019. https://doi.org/10.1016/B978-0-08-102430-0.00006-1.

[20] F. Gunkel, D. V. Christensen, Y.Z. Chen, N. Pryds, Oxygen vacancies: The (in)visible friend of oxide electronics, Appl. Phys. Lett. 116 (2020). https://doi.org/10.1063/1.5143309.

[21] S. Wang, T. He, P. Chen, A. Du, K. Ostrikov, W. Huang, L. Wang, In situ formation of oxygen vacancies achieving near-complete charge separation in planar $BiVO_4$ photoanodes, Adv. Mater. 32 (2020) 1–10. https://doi.org/10.1002/adma.202001385.

[22] W. Yu, F. Chen, Y. Wang, L. Zhao, Rapid evaluation of oxygen vacancies-enhanced photogeneration of the superoxide radical in nano-TiO_2 suspensions, RSC Adv. 10 (2020) 29082–29089. https://doi.org/10.1039/d0ra06299e.

[23] K. Yamada, H. Yamane, S. Matsushima, H. Nakamura, K. Ohira, M. Kouya, K. Kumada, Effect of thermal treatment on photocatalytic activity of N-doped TiO_2 particles under visible light, Thin Solid Films. 516 (2008) 7482–7487. https://doi.org/10.1016/j.tsf.2008.03.041.

[24] G. Wang, Y. Ling, X. Lu, F. Qian, Y. Tong, J.Z. Zhang, V. Lordi, C. Rocha Leao, Y. Li, Computational and photoelectrochemical study of hydrogenated bismuth vanadate, J. Phys. Chem. C. 117 (2013) 10957–10964. https://doi.org/10.1021/jp401972h.

[25] G. Wang, H. Wang, Y. Ling, Y. Tang, X. Yang, R.C. Fitzmorris, C. Wang, J.Z. Zhang, Y. Li, Hydrogen-treated TiO_2 nanowire arrays for photoelectrochemical water splitting, Nano Lett. 11 (2011) 3026–3033. https://doi.org/10.1021/nl201766h.

[26] W. Mtangi, F.D. Auret, W.E. Meyer, M.J. Legodi, P.J. Janse Van Rensburg, S.M.M. Coelho, M. Diale, J.M. Nel, Effects of hydrogen, oxygen, and argon annealing on the electrical properties of ZnO and ZnO devices studied by current-voltage, deep level transient spectroscopy, and Laplace DLTS, J. Appl. Phys. 111 (2012). https://doi.org/10.1063/1.4709728.

[27] T. Zhang, Y. Liu, S. Jiang, B. Li, J. Wang, X. Shao, D. Wang, K. Wang, Z. Yan, Bacitracin-assisted synthesis of spherical $BiVO_4$ nanoparticles with C doping for remarkable photocatalytic performance under visible light, CrystEngComm. 22 (2020) 1812–1821. https://doi.org/10.1039/c9ce01908a.

[28] C. Ravidhas, A. Juliat Josephine, P. Sudhagar, A. Devadoss, C. Terashima, K. Nakata, A. Fujishima, A. Moses Ezhil Raj, C. Sanjeeviraja, Facile synthesis of nanostructured monoclinic bismuth vanadate by a co-precipitation method: Structural, optical and photocatalytic properties, Mater. Sci. Semicond. Process. 30 (2015) 343–351. https://doi.org/10.1016/j.mssp.2014.10.026.

[29] S. Xie, Z. Shen, H. Zhang, J. Cheng, Q. Zhang, Y. Wang, Photocatalytic coupling of formaldehyde to ethylene glycol and glycolaldehyde over bismuth vanadate with controllable facets and cocatalysts, Catal. Sci. Technol. 7 (2017) 923–933. https://doi.org/10.1039/c6cy02510b.

[30] X. Liu, Y. Su, Q. Zhao, C. Du, Z. Liu, Constructing $Bi_{24}O_{31}Cl_{10}$/BiOCl heterojunction via a simple thermal annealing route for achieving enhanced photocatalytic activity and selectivity, Sci. Rep. 6 (2016) 1–13. https://doi.org/10.1038/srep28689.

[31] U. Eggenweiler, E. Keller, V. Krämer, Redetermination of the crystal structures of the "arppe compound" $Bi_{24}O_{31}Cl_{10}$ and the isomorphous $Bi_{24}O_{31}Br_{10}$, Acta Crystallogr. Sect. B Struct. Sci. 56 (2000) 431–437. https://doi.org/10.1107/S0108768100000550.

[32] P. Cui, J. Wang, Z. Wang, J. Chen, X. Xing, L. Wang, R. Yu, Bismuth oxychloride hollow microspheres with high visible light photocatalytic activity, Nano Res. 9 (2016) 593–601. https://doi.org/10.1007/s12274-015-0939-z.

[33] S. Sorokina, R.E. Enjalbert, P. Baules, A. Castro, J. Galy, Continuous structural evolution of $(Bi_2O_2)_2V_{2y}O_{4y+2}$ $(1 \leq y \leq 4)$ aurivillius phases in the Bi_2O_3–VO_2 system, J. Solid State Chem. 125 (1996) 54–62. https://doi.org/https://doi.org/10.1006/jssc.1996.0264.

[34] J. Galy, R. Enjalbert, P. Millan, A. Castro, New Aurivillius phases in the bismuth-vanadium-oxygen system crystal structure of $Bi_4V_2O_{10}$, Comptes Rendus l'Academie Des Sci. Ser. 2. 317 (1993) 43–48. http://inis.iaea.org/search/search.aspx?orig_q=RN:24068739.

[35] C. Satto, P. Millet, P. Sciau, C. Roucau, J. Galy, α-$Bi_4V_2O_{10}$ crystal structure and oxidation mechanism. X-ray and electron diffraction analysis, Mater. Res. Bull. 34 (1999) 655–664. https://doi.org/https://doi.org/10.1016/S0025-5408(99)00058-6.

[36] Y. Yuan, Y. Huang, F. Ma, Z. Zhang, X. Wei, Effects of oxygen vacancy on

the mechanical, electronic and optical properties of monoclinic $BiVO_4$, J. Mater. Sci. 52 (2017) 8546–8555. https://doi.org/10.1007/s10853-017-1069-7.

[37] S. Selim, E. Pastor, M. García-Tecedor, M.R. Morris, L. Francàs, M. Sachs, B. Moss, S. Corby, C.A. Mesa, S. Gimenez, A. Kafizas, A.A. Bakulin, J.R. Durrant, Impact of oxygen vacancy occupancy on charge carrier dynamics in $BiVO_4$ photoanodes, J. Am. Chem. Soc. 141 (2019) 18791–18798. https://doi.org/10.1021/jacs.9b09056.

[38] D.K. Ma, M.L. Guan, S. Sen Liu, Y.Q. Zhang, C.W. Zhang, Y.X. He, S.M. Huang, Controlled synthesis of olive-shaped $Bi_2S_3/BiVO_4$ microspheres through a limited chemical conversion route and enhanced visible-light-responding photocatalytic activity, Dalt. Trans. 41 (2012) 5581–5586. https://doi.org/10.1039/c2dt30099k.

[39] C. Feng, D. Wang, B. Jin, Z. Jiao, The enhanced photocatalytic properties of $BiOCl/BiVO_4$ p-n heterojunctions via plasmon resonance of metal Bi, RSC Adv. 5 (2015) 75947–75952. https://doi.org/10.1039/c5ra13886h.

[40] D.P. Jaihindh, B. Thirumalraj, S.M. Chen, P. Balasubramanian, Y.P. Fu, Facile synthesis of hierarchically nanostructured bismuth vanadate: An efficient photocatalyst for degradation and detection of hexavalent chromium, J. Hazard. Mater. 367 (2019) 647–657. https://doi.org/10.1016/j.jhazmat.2019.01.017.

[41] S. Sun, W. Wang, L. Zhou, H. Xu, Efficient methylene blue removal over hydrothermally synthesized starlike $BiVO_4$, Ind. Eng. Chem. Res. 48 (2009) 1735–1739. https://doi.org/10.1021/ie801516u.

[42] J. Cao, C. Zhou, H. Lin, B. Xu, S. Chen, Surface modification of m-$BiVO_4$ with wide band-gap semiconductor BiOCl to largely improve the visible light induced photocatalytic activity, Appl. Surf. Sci. 284 (2013) 263–269. https://doi.org/10.1016/j.apsusc.2013.07.092.

[43] Y. Li, B. Yang, B. Liu, Synthesis of $BiVO_4$ nanoparticles with tunable oxygen vacancy level: The phenomena and mechanism for their enhanced photocatalytic performance, Ceram. Int. 47 (2021) 9849–9855. https://doi.org/10.1016/j.ceramint.2020.12.126.

[44] D.D. Qin, T. Wang, Y.M. Song, C.L. Tao, Reduced monoclinic $BiVO_4$ for improved photoelectrochemical oxidation of water under visible light, Dalt. Trans. 43 (2014) 7691–7694. https://doi.org/10.1039/c3dt53575d.

[45] C. Cheng, Q. Fang, S. Fernandez-Alberti, R. Long, Controlling charge carrier trapping and recombination in $BiVO_4$ with the oxygen vacancy oxidation state, J. Phys. Chem. Lett. 12 (2021) 3514–3521. https://doi.org/10.1021/acs.jpclett.1c00713.

[46] Q. Wang, S. Zhang, H. He, C. Xie, Y. Tang, C. He, M. Shao, H. Wang, Oxygen vacancy engineering in titanium dioxide for sodium storage, Chem. - An Asian J. 16 (2021) 3–19. https://doi.org/10.1002/asia.202001172.

[47] S. Byun, G. Jung, Y. Shi, M. Lanza, B. Shin, Aging of a vanadium precursor solution: influencing material properties and photoelectrochemical water oxidation performance of solution-processed $BiVO_4$ photoanodes, Adv. Funct. Mater. 30 (2020) 1–7. https://doi.org/10.1002/adfm.201806662.

[48] S. Kim, M. Vijayakumar, W. Wang, J. Zhang, B. Chen, Z. Nie, F. Chen, J. Hu, L. Li, Z. Yang, Chloride supporting electrolytes for all-vanadium redox flow batteries, Phys. Chem. Chem. Phys. 13 (2011) 18186–18193. https://doi.org/10.1039/c1cp22638j.

[49] E. Chikoidze, M. Nolan, M. Modreanu, V. Sallet, P. Galtier, Effect of chlorine doping on electrical and optical properties of ZnO thin films, Thin Solid Films. 516 (2008) 8146–8149. https://doi.org/10.1016/j.tsf.2008.04.076.

[50] T. Sivaraman, V. Narasimman, V.S. Nagarethinam, A.R. Balu, Effect of chlorine doping on the structural, morphological, optical and electrical properties of spray deposited CdS thin films, Prog. Nat. Sci. Mater. Int. 25 (2015) 392–398. https://doi.org/10.1016/j.pnsc.2015.09.010.

6. Enhanced Photocatalytic Activity of $BiVO_4/Bi_2S_3/SnS_2$ Heterojunction for Photodegradation of Rhodamine B under Visible Light

6.1. Introduction

In recent years, a tremendous effort has been made to develop efficient photocatalysts due to their potential applications in water splitting [1–3], CO_2 reduction [4,5], and pollutant removal [6–8]. A good photocatalyst needs a suitable bandgap to work in the visible light region, in addition to satisfying other important criteria, e.g., abundance, low cost, nontoxicity, low electron–hole recombination rate, and stability. Photocatalysts such as SnS_2 and $BiVO_4$ fit most of these conditions; in particular, they can absorb visible light because their bandgaps are 2.18–2.4 eV [1,9]. Although both materials have many advantages as a single photocatalyst, incorporating them with different photocatalysts to form a heterojunction has proved very effective in attaining superior photocatalytic activity [1,10–12]. The interface can act as a bridge allowing electrons to migrate between photocatalysts, which, in turn, suppress the photoinduced electron–hole recombination and improve the performance of photocatalysts [11,13]. In addition, the heterojunction may also induce a Z-scheme system in which the redox ability is enhanced via coupling two or more narrow-bandgap semiconductors [1,14].

To date, no attempt has been made to fabricate the $BiVO_4/SnS_2$ heterojunction despite many publications on SnS_2 and $BiVO_4$ [7,15]. One of the reasons for this

could be an occurrence of the reaction between Bi^{3+} and S^{2-} that leads to formation of Bi_2S_3 at elevated temperatures [6,16]. It would be challenging to obtain a $BiVO_4/SnS_2$ heterojunction without formation of Bi_2S_3. However, the composites containing Bi_2S_3, such as Bi_2S_3/ZnS [17], Bi_2S_3/MoS_2 [5,18], and TiO_2/Bi_2S_3 [3], have been shown to promote photocatalytic activity. Furthermore, earlier researchers have demonstrated that both SnS_2 and $BiVO_4$ were successfully fabricated with Bi_2S_3 to produce Bi_2S_3/SnS_2 and $Bi_2S_3/BiVO_4$, respectively, exhibiting enhanced photocatalytic performance in dye degradation [15,19–21]. Additionally, ternary heterojunction based on Bi_2S_3 (e.g., $Bi_2O_3/Bi_2S_3/MoS_2$ [2], $Bi_2S_3/SnS_2/Bi_2O_3$ [6], and $Bi_2O_3/Bi_2S_3/MoS_2$ [16]) have also been proven to improve the photocatalytic activity. Therefore, viewed from a different perspective, Bi_2S_3 formation from the reaction between SnS_2 and $BiVO_4$ might enhance photocatalytic performance of the composite via formation of a ternary heterojunction.

In this study, the $BiVO_4/Bi_2S_3/SnS_2$ heterojunction was thus synthesized by combining SnS_2 and $BiVO_4$ via ultrasonic mixing and solvothermal synthesis. The formation of Bi_2S_3 during the synthesis would then constitute a ternary composite with SnS_2 and $BiVO_4$. Various molar ratios of $BiVO_4$ to SnS_2 were prepared to investigate the properties of three-phase photocatalysts ($BiVO_4$, Bi_2S_3, and SnS_2) and optimize the amount of $BiVO_4$ in the composite. The photocatalytic performance of the composite was compared with pure $BiVO_4$ and SnS_2, and the charge transfer pathway in the heterojunction system was examined. A dual Z-scheme model was then proposed to consistently explain the enhanced photocatalytic activity of $BiVO_4/Bi_2S_3/SnS_2$ heterojunctions.

6.2. Experimental

6.2.1. Preparation of SnS_2

Preparation of SnS_2 was conducted via a typical synthesis method. The powder of $SnCl_4 \cdot 5H_2O$ (5 mmol) was dissolved in 40 mL of 5% (v/v) acetic acids under magnetic stirring. Then, 10 mmol amount of thioacetamide was added to the

solution. After 30 min of vigorous stirring to achieve a homogeneous solution, the solution was transferred to a stainless-steel autoclave attached with a Teflon liner to fill 80% of its maximum capacity (50 mL). It was then put in a preheated electric oven at 150 °C for 12 h under autogenous pressure. After letting the autoclave cool to room temperature, SnS_2 precipitate was collected via centrifuge at 4000 rpm for 5 min. The SnS_2 was then washed several times with DI water and ethanol, and dried at 90 °C overnight.

6.2.2. Preparation of $BiVO_4$

Typical hydrothermal synthesis was used to prepare $BiVO_4$. The first solution was prepared by dissolving 2.43 g of $Bi(NO_3)_3 \cdot 5H_2O$ in 20 mL of 2 M HNO_3 acid, and the second solution was made by dissolving an equimolar amount of NH_4VO_3 in 2 M NaOH solution. Then, the second solution was poured drop by drop into the first solution. The clear solution turned yellow as $BiVO_4$ precipitate was formed. The mixture solution was continuously stirred for another 10 min before adding 1 mL of acetic acid into the solution. After 1 h of stirring, the solution was transferred to the stainless-steel autoclave with a Teflon liner. The autoclave was heated at 180 °C for 24 h. Finally, $BiVO_4$ precipitate was collected, washed, and dried at 90 °C overnight.

6.2.3. Preparation of $BiVO_4/Bi_2S_3/SnS_2$ composites

The composite was prepared using ultrasonic mixing and solvothermal synthesis. A specific amount of $BiVO_4$ (0.01, 0.03, 0.06, and 0.12 mmol) was mixed with 1 mmol of SnS_2 in 40 mL of ethylene glycol. The mixture was thoroughly mixed via ultrasonication at 45 kHz for 1 h before transferring to the autoclave. It was then sealed and heated at 150 °C for 8 h. The final product of the composite was obtained through washing and drying, following the same procedure as stated in Sections 6.2.1 and 6.2.2. The composites with different ratios of $BiVO_4$ to SnS_2 were denoted, respectively, as 0.01 $BiVO_4/SnS_2$, 0.03 $BiVO_4/SnS_2$, 0.06 $BiVO_4/SnS_2$, and 0.12 $BiVO_4/SnS_2$.

For reference, a bare Bi_2S_3 was synthesized as follows. First, 5 mmol of $Bi(NO_3)_3 \cdot 5H_2O$ was dissolved in 40 mL of ethylene glycol via sonication for 10 min. After that, Thiourea (10 mmol) was added to the solution and magnetically stirred for 10 min. The homogeneous solution was then transferred to a stainless steel autoclave attached with Teflon-liner and heated at 160 ℃ for 18 h. The Bi_2S_3 precipitates were then collected and washed several times with deionized water and ethanol, and dried at 90 ℃ overnight.

6.2.4. Characterization

X-ray diffraction (XRD) measurement was conducted using a Rigaku RINT2100 at 40 kV and 30 mA with Cu Kα radiation (λ = 0.15418 nm), where the diffractogram was obtained via scanning the sample in a 2θ angle range from 10° to 80°. Microstructures and morphologies of the samples were investigated using an FE-SEM (Hitachi SU6600 Scanning Electron Microscope) equipped with Bruker EDX operated at 15 and 20 kV for SEM and EDX, respectively, where all samples were coated with Au via sputtering prior to the analyses. UV–Vis diffuse reflectance spectra (DRS) were obtained using a Lambda 750S UV/Vis/NIR Spectrophotometer with $BaSO_4$ as reference. X-ray photoelectron spectroscopy (XPS, JPS-9030 X-ray photoelectron spectrometer) was conducted with Mg Kα radiation using C 1s = 284.8 eV as reference. The Brunauer–Emmett–Teller (BET) specific surface area was measured and evaluated using nitrogen gas adsorption with a FlowSorb III 2305 Micromeritics Instrument (Shimadzu, Japan).

6.2.5. Measurement of photocatalytic activity for rhodamine B degradation

Evaluation of photocatalytic activity was conducted via the photodegradation of RhB dye under visible light irradiation using a 500 W Xe lamp (Ushio, UXL-500D-O) equipped with a UV cutoff filter (λT = 420 nm). In each measurement process, 30 mg of the photocatalyst was put into 80 mL of RhB solution (5 mg/L, 0.01 mmol/L) in a beaker with 100 mL capacity. The sampling procedure is described in Section 3.3 (Chapter 3). Before irradiation, the establishment of

adsorption–desorption equilibrium between photocatalyst and RhB solution was achieved to ensure an accurate result of photocatalytic activity.

Since SnS_2 exhibits exceptionally strong adsorptivity for RhB dye [22], an initial dye concentration (C_0) for each photocatalytic test would be different, depending on the ratio of $BiVO_4/SnS_2$ composites, after achieving an adsorption–desorption equilibrium. To ensure that all samples had relatively similar initial concentrations at the start of illumination, all samples were subjected to the adsorption–desorption process twice. Each sample was added to a RhB solution, which was then agitated by sonication for 10 min and magnetically stirred for 60 min in the dark. Then, the sample was collected via centrifuge and put into a fresh RhB solution, where the adsorption–desorption procedure was performed again prior to the photocatalytic test. This devised method allowed an initial RhB concentration (C_0) to be similar for each photocatalytic test, using various composite ratios.

6.3. Results and discussion

6.3.1. Crystal structure of the samples

The crystalline phases of as-prepared samples with different ratios of $BiVO_4$ to SnS_2 were investigated through XRD (X-ray diffraction) patterns, as shown in Fig. 6-1. The characteristic peaks at 14.9°, 28.3°, 32.3°, 49.5°, and 52.4° correspond to (001), (100), (101), (110), and (111) planes of hexagonal SnS_2, respectively (ICDD PDF No. 00-023-0677). Other visible peaks can be observed at 18.7°, 19.0°, 28.8°, and 30.5°, assigned to (110), (011), ($\bar{1}$21), and (040) planes of monoclinic $BiVO_4$, respectively (ICDD PDF No. 00-014-0688). In addition to these obvious peaks, there are four small peaks at 22.3°, 23.6°, 24.9°, and 25.2°, which can be assigned to (202), (101), (130), and (310) planes of orthorhombic Bi_2S_3, respectively (ICDD PDF No. 01-089-8965). The XRD patterns of individual synthesized materials ($BiVO_4$, SnS_2, and Bi_2S_3) are shown in Fig. 6-2. These characteristic diffraction peaks confirm three crystal phases of SnS_2, B_2S_3, and $BiVO_4$ in the composites. As the content of $BiVO_4$ during the synthesis is reduced,

the diffraction intensities of $BiVO_4$ and Bi_2S_3 decrease and almost disappear for the 0.01 $BiVO_4/SnS_2$ sample due to the very low content of $BiVO_4$ and Bi_2S_3 in the composite. According to the result, the content of Bi_2S_3 depends on the initial concentration of $BiVO_4$ during the hydrothermal synthesis.

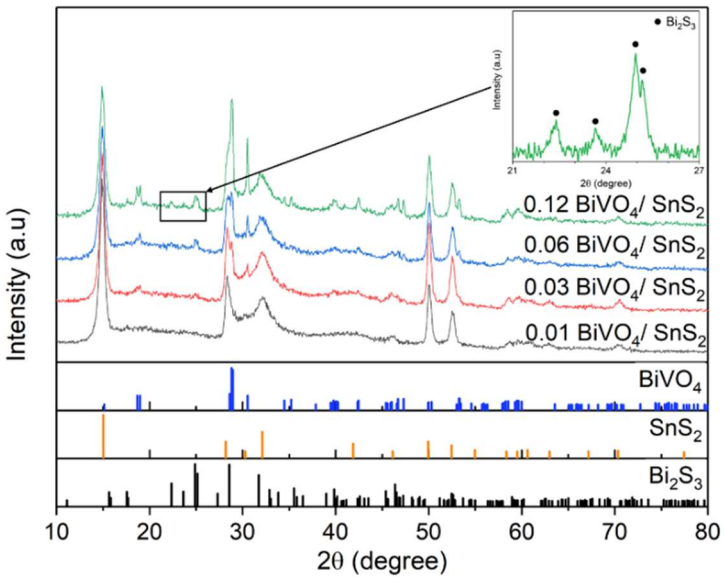

Fig. 6-1. XRD patterns of $BiVO_4/SnS_2$ samples with various ratios of $BiVO_4$ and SnS_2.

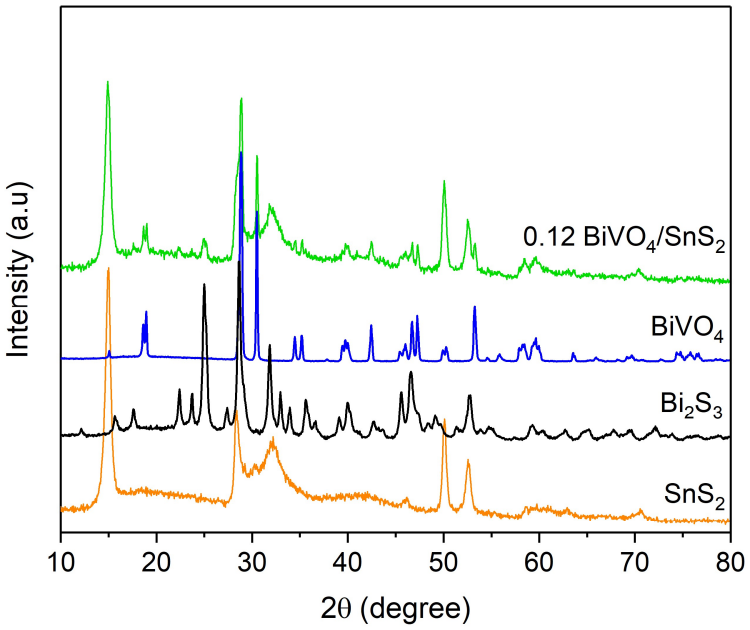

Fig. 6-2. XRD pattern comparisons of SnS_2, Bi_2S_3, $BiVO_4$, and 0.12 $BiVO_4/SnS_2$ composite.

6.3.2. Morphology and microstructure of the samples

Fig. 6-3a and 6-3b reveal agglomerates of SnS_2, composed of ultrafine nanoparticles with a diameter of approximately 50 nm. On the other hand, $BiVO_4$ exhibits micron-sized polyhedral particles with a smooth surface, i.e., particular features of microcrystals with many facets, as observed in Fig. 6-3c. The ultrafine nanoparticles of SnS_2 and microparticles of $BiVO_4$ explain a large difference (more than 100 times) in the specific surface area of SnS_2 and $BiVO_4$ in Table 6-1. Furthermore, Fig. 6-3d shows a micrograph image of the 0.03 $BiVO_4/SnS_2$ composite, in which the nanoparticles of SnS_2 are attached to, and cover, the particles of $BiVO_4$. Based on the EDS elemental mapping of 0.03 $BiVO_4/SnS_2$ in Fig. 6-4, the elements of Sn, S, Bi, V, and O are uniformly dispersed in the composite, indicating good distribution of $BiVO_4$ and SnS_2 after the incorporation.

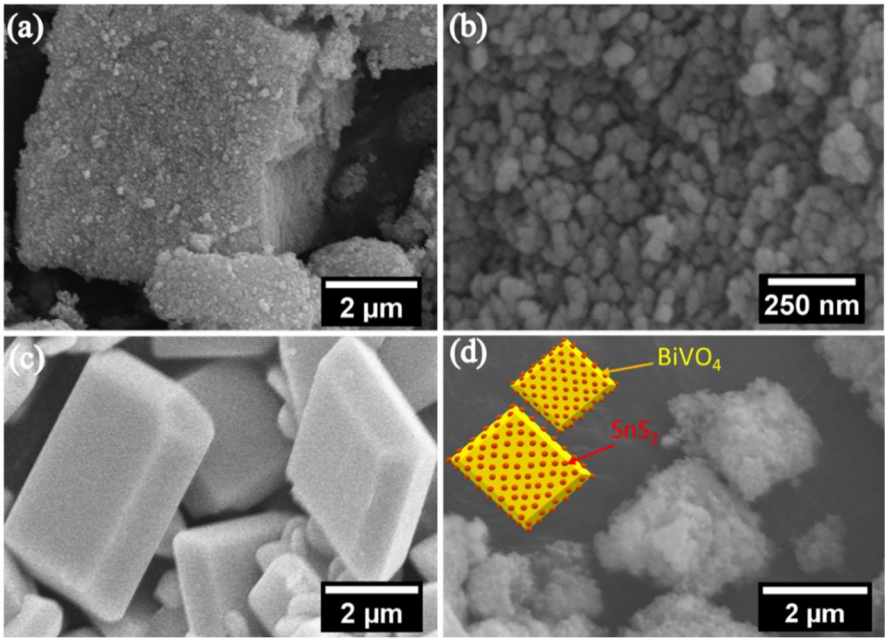

Fig. 6-3. FE-SEM micrographs of (a) SnS_2, (b) magnified image of SnS_2, (c) $BiVO_4$, and (d) 0.03 $BiVO_4/SnS_2$ with schematic illustration.

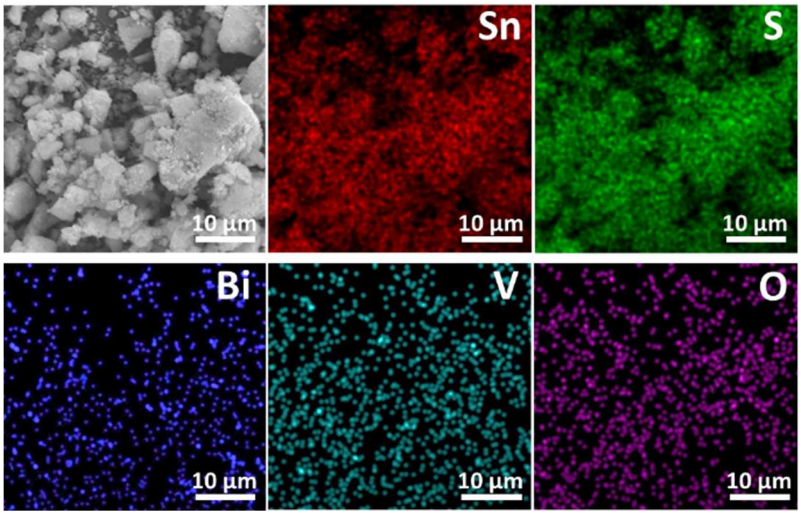

Fig. 6-4. EDS elemental mapping of Sn, S, Bi, V, and O elements in 0.03 $BiVO_4/SnS_2$.

Table 6-1. Comparison of molar/weight percent $BiVO_4$, specific surface area, and pseudo-first-order-kinetic degradation constant, for SnS_2, $BiVO_4$, and $BiVO_4/SnS_2$ composites with various $BiVO_4$-to-SnS_2 ratios.

Sample	Molar Percent of $BiVO_4$ (mole %)	Weight Percent of $BiVO_4$ (wt %)	S_{BET}[a] ($m^2\ g^{-1}$)	k[b] ($10^{-3}\ min^{-1}$)
SnS_2	0	0	75.7	0.60
0.01 $BiVO_4/SnS_2$	1.0	1.7	83.3	1.40
0.03 $BiVO_4/SnS_2$	2.9	5.1	74.7	1.60
0.06 $BiVO_4/SnS_2$	5.7	9.6	68.5	1.25
0.12 $BiVO_4/SnS_2$	10.7	17.5	56.3	0.68
$BiVO_4$	100	100	0.6	0.55

[a] S_{BET} is BET specific surface area; [b] k is photodegradation rate constant

6.3.3. Optical absorption properties of the samples

UV–Vis diffuse reflectance spectra (DRS) were used to study the optical properties of as-prepared samples. The reflectance spectra were converted to absorption spectra via the Kubelka–Munk function using Eq. (3.1). The absorption spectra of the samples are plotted in Fig. 6-5a; all composites exhibit absorption edges around the wavelength of 550 nm, indicating that they are photoactive in the

visible light region. The curves of 0.06 $BiVO_4/SnS_2$ and 0.12 $BiVO_4/SnS_2$ are noticeably different from the remainder as their absorption regions extend beyond 550 nm. This could be attributed to an increase in the content of Bi_2S_3 in the composite.

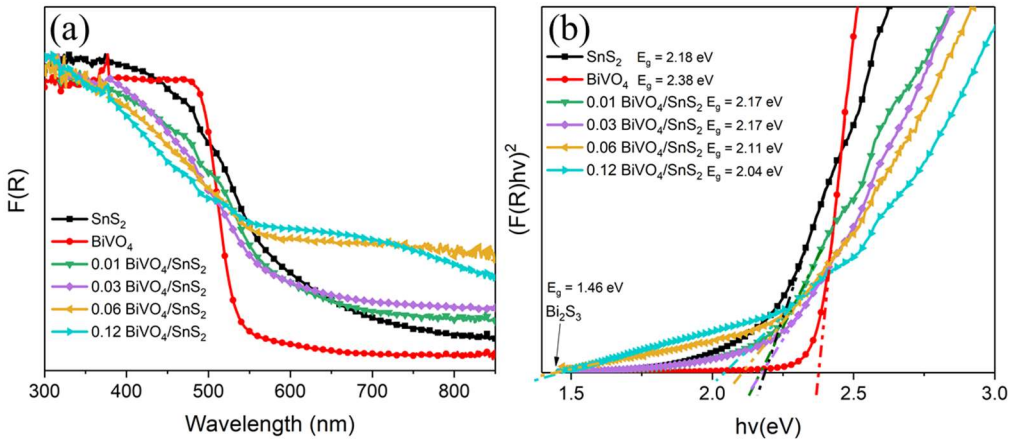

Fig. 6-5. (a) UV–Vis diffuse reflectance spectra and (b) $(F(R)hv)^2$ vs. hv plot of SnS_2, $BiVO_4$, and the $BiVO_4/SnS_2$ composites with various ratios of $BiVO_4$.

The bandgaps (E_g) can be estimated using Eq. (3.2). The $(F(R)h\upsilon)^2$ vs. $h\upsilon$ graph (Tauc's plot) can be plotted as in Fig. 6-5b, and the E_g values are evaluated by extrapolating the linear part of the curve to intercept the F(R) = 0 line. The E_g values of $BiVO_4$, SnS_2, and Bi_2S_3 are accordingly estimated to be 2.38, 2.18, and 1.46 eV, respectively, which are similar to those in previous reports [23,24]. In addition, the effective E_g values of 0.01 $BiVO_4/SnS_2$, 0.03 $BiVO_4/SnS_2$, 0.06 $BiVO_4/SnS_2$, and 0.12 $BiVO_4/SnS_2$ are estimated to be 2.17, 2.17, 2.11, and 2.04 eV, respectively. It appears that the apparent E_g value of the composite is decreased with an increase in $BiVO_4$. This bandgap modification may be ascribed to a small composition variation of SnS_2, $BiVO_4$, and Bi_2S_3, especially near the interface. This bandgap reduction effect is also reported in previous publications [3,16,19].

6.3.4. X-ray photoelectron spectroscopic (XPS) analyses of the samples

The XPS survey spectrum of 0.03 $BiVO_4/SnS_2$ composite is shown in Fig. 6-6a, demonstrating that it consists of Sn, S, Bi, V, and O elements, which are in

agreement with the EDS result. The chemical state of each element, investigated via the high-resolution XPS analyses, is shown in Fig. 6-6b and 6-6c. As observed in Fig. 6-6b, two separate spectra with peaks at 494.89 and 486.49 eV (with an energy difference of 8.4 eV) correspond to Sn $3d_{3/2}$ and Sn $3d_{5/2}$ of Sn^{4+}, respectively, for a common SnS_2 [4,10,19]. On the other hand, for the 0.03 $BiVO_4/SnS_2$ composite, it is noted that both Sn 3d peaks shift to the higher binding energy side by about 0.30–0.35 eV, compared with those of pure SnS_2. The blueshift observed in the Sn 3d spectra is also found in, and synchronous with, the S 2p spectra.

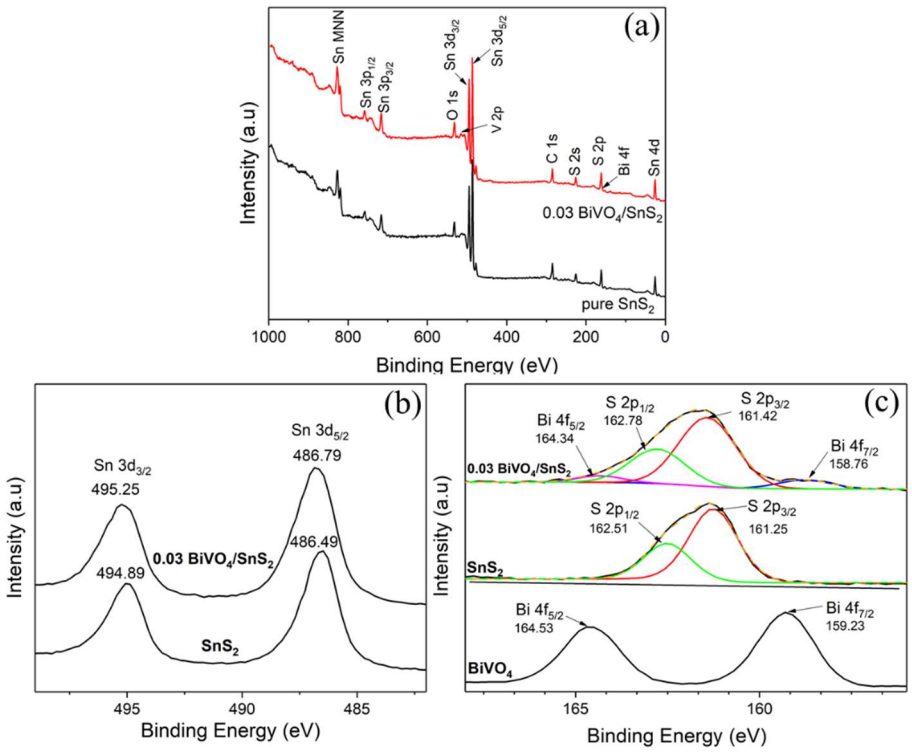

Fig. 6-6. (a) XPS survey spectra of 0.03 $BiVO_4/SnS_2$ and pure SnS_2 and high-resolution XPS spectra of (b) Sn 3d orbital and (**c**) Bi 4f and S 2p orbital.

As shown in Fig. 6-6c, the S $2p_{3/2}$ (161.34 eV) and S $2p_{1/2}$ (162.52 eV) peaks, corresponding to typical Sn-S bonds of pure SnS_2 [4,9,10], also exhibit a blueshift in the binding energy by 0.1–0.3 eV for the 0.03 $BiVO_4/SnS_2$ composite. Furthermore, the synchronized binding energy shift is also observed, with an opposite direction, for the Bi 4f spectra. The spectral peaks for the 0.03 $BiVO_4/SnS_2$ composite at 158.75 and 164.34 eV, which belong to Bi $4f_{7/2}$ and Bi $4f_{5/2}$ of $BiVO_4$,

respectively, exhibit the redshift, by 0.2–0.5 eV, compared with Bi 4f peaks (159.23 and 164.53 eV) of pure $BiVO_4$ [15]. Importantly, the synchronous phenomena are reproducible.

The shift of binding energy in the core-level of XPS spectra should be largely attributed to the change in electron concentration of semiconductors due to the interaction between SnS_2 and $BiVO_4$ [25]. As the electron concentration decreases, the binding energy of the semiconductor increases, and vice versa, due to the so-called electron screening effect [26]. When a heterojunction is formed through chemical interaction, the Fermi energy levels of both materials are adjusted, allowing the electron transfer between materials to achieve equilibrium [10,25,26]. In the case of the 0.03 $BiVO_4/SnS_2$ composite, it implies that SnS_2 has a higher Fermi energy level than that of $BiVO_4$, thus the electron migrates from SnS_2 to $BiVO_4$. This consequently reduces the electron concentration of SnS_2 and increases that of $BiVO_4$. As a result, the Sn 3d and S 2p spectra of the composite exhibit the blueshift, while Bi 4f spectra exhibit the redshift.

Furthermore, the broad peaks of the Bi 4f exhibited in the 0.03 $BiVO_4/SnS_2$ composite may be caused by the presence of Bi_2S_3. The Bi $4f_{7/2}$ and Bi $4f_{5/2}$ spectral peaks of a typical Bi_2S_3 are reported to be at 158.4 and 163.8 eV [27], respectively, which are slightly lower than those of $BiVO_4$. Moreover, the S 2p peaks at 161.45 and 162.81 eV in the 0.03 $BiVO_4/SnS_2$ composite could also correspond to S^{2-} of Bi_2S_3 [28]. The results from XPS spectra and XRD patterns (Section 6.3.1) strongly suggest the coexistence of SnS_2, Bi_2S_3, and $BiVO_4$ in the composite. Additionally, the shifts in binding energy indicate that the interaction among SnS_2, Bi_2S_3, and $BiVO_4$ in the 0.03 $BiVO_4/SnS_2$ composite involves a chemical bonding rather than a physical contact only.

Fig. 6-7 illustrates valence band XPS spectra of pristine SnS_2, Bi_2S_3, and $BiVO_4$. The difference between the Fermi level and VBMs (valence band maximums) of SnS_2, Bi_2S_3, and $BiVO_4$ is found to be 1.3, 0.3, and 2 eV, respectively. Fermi level positions of SnS_2, Bi_2S_3, and $BiVO_4$ with respect to their VBs (valence bands) can be determined from the potential difference between VBM

and Fermi level from the valence band XPS spectra [12]. The result indicates that SnS_2 and $BiVO_4$ are n-type semiconductors, whereas Bi_2S_3 is a p-type semiconductor, which is in agreement with prior studies [2,6,16].

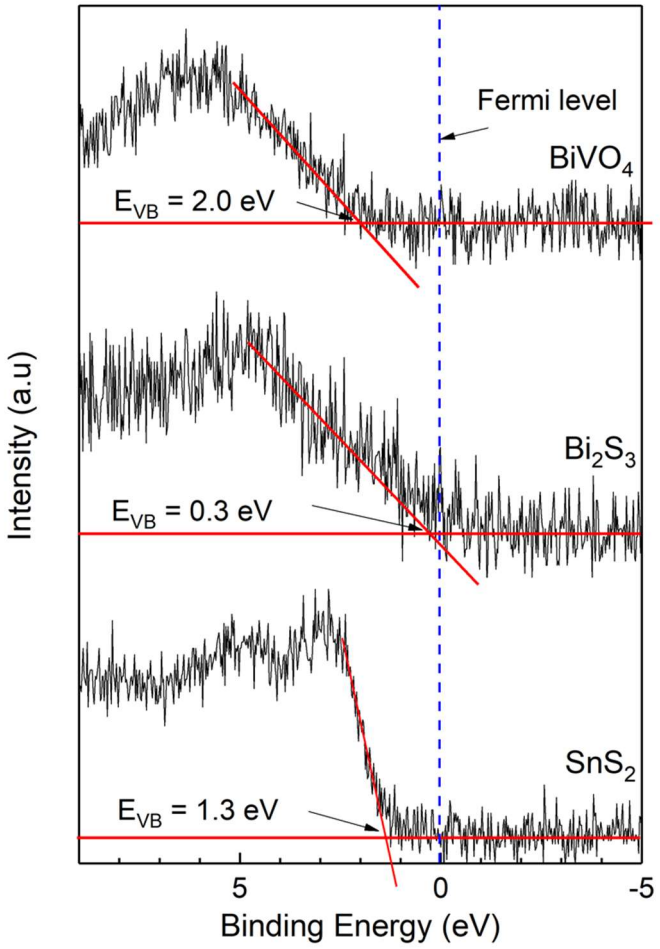

Fig. 6-7. Valence band XPS spectra of bare $BiVO_4$, Bi_2S_3, and SnS_2.

6.3.5. Photocatalytic activities of the samples for rhodamine B degradation

Photocatalytic activity was evaluated via concentration reduction in RhB (rhodamine B) dye solution over time, as shown in Fig. 6-8a, where C_0 is the initial RhB concentration at the time of light irradiation (t = 0), and C_t is the RhB concentration at any sampling time during irradiation. Blank RhB (a control test) in Fig. 6-8a demonstrates that the RhB dye solution was stable under this test condition without any photocatalyst in the solution and that the photolysis of RhB dye was negligible over 240 min of visible light irradiation. Conversely, the

concentration of RhB decreased over time for all other RhB solutions containing any photocatalyst, evidencing that photocatalysts used in this study respond to visible light ($\lambda > 420$ nm). Importantly, all composited powders exhibit higher photocatalytic degradation of RhB than that of bare SnS_2, Bi_2S_3, or $BiVO_4$ under visible light irradiation for over 240 min. The temporal evolution of RhB absorption spectra for each photocatalyst can be seen in Fig. 2 of Appendix B.

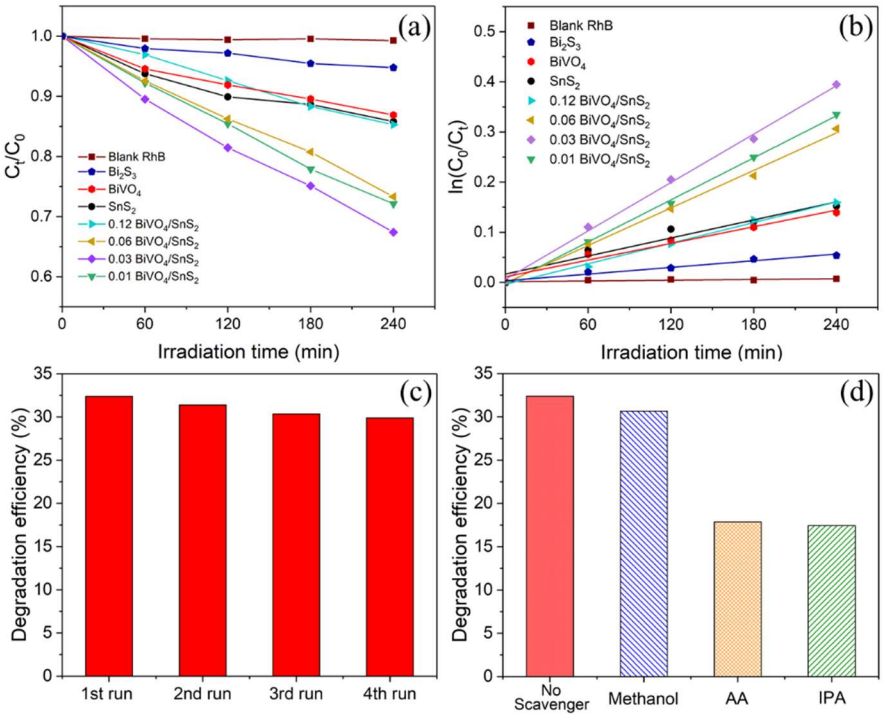

Fig. 6-8. (a) Photocatalytic RhB degradation for various photocatalysts; (b) pseudo-first-order-kinetics for RhB photodegradation; (c) RhB degradation efficiency of 0.03 $BiVO_4/SnS_2$ over four cycles; and (d) the effect of methanol, ascorbic acid (AA), and isopropyl alcohol (IPA) on RhB photodegradation by 0.03 $BiVO_4/SnS_2$ under visible light irradiation ($\lambda > 420$ nm) for 240 min.

The degradation rates were compared using a photodegradation rate constant (k), assuming a pseudo-first-order reaction model, $\ln(C_0/C_t) = kt$, as shown in Fig. 6-8b. The kinetic model fits the data well, and the k value of the 0.03 $BiVO_4/SnS_2$ sample is about 2.3 times or 2.9 times greater than that of a single SnS_2 or $BiVO_4$, respectively (Table 6-1). As shown in Fig. 6.9, the photocatalytic activity of the composite is enhanced as the content of $BiVO_4$ is increased from 0.01 to 0.03,

whereas further addition of $BiVO_4$ leads to a reduction in photocatalytic activity of the composites (0.06 $BiVO_4/SnS_2$ and 0.12 $BiVO_4/SnS_2$). It is thus reasonable to consider that an optimal molar ratio exists at a relatively low concentration of $BiVO_4$. One possible reason could be the variation in the "effective" specific surface area. As shown in Table 6-1, the specific surface area of the composites mostly decreases with an addition of $BiVO_4$, ascribed to the significantly small value of bare $BiVO_4$ (0.6 m^2/g). Furthermore, the interfacial reaction and agglomeration of powders may affect the effective active area for photocatalytic activity. As previously mentioned, the formation of Bi_2S_3 is intensive as the amount of $BiVO_4$ in the composite is increased. Although a small amount of Bi_2S_3 would be favorable for the composite, excess content may lead to deterioration of the photocatalytic performance because Bi_2S_3 has a low photocatalytic activity of RhB degradation compared to SnS_2 and $BiVO_4$, possibly due to its rapid recombination rate of the photogenerated electron-hole [17]. Thus, excessive Bi_2S_3 could act as a recombination center for electron-hole pairs in the composite, which is similar to the findings of previous studies [13,19].

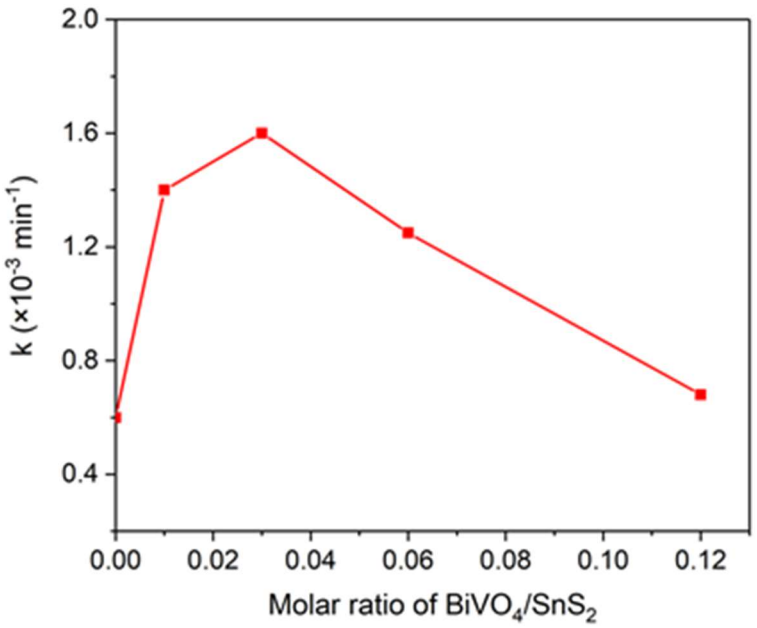

Fig. 6-9. Variation of photodegradation rate constant (k) with respect to molar ratio of $BiVO_4/SnS_2$.

In addition to the photocatalytic activity of the material, stability and reusability are also important to determine its value in practical applications. Thus, the reusability test was also conducted by collecting the used sample (0.03 $BiVO_4/SnS_2$) after irradiation via centrifuge and putting it back into the fresh RhB solution. The same procedure for the photocatalytic activity measurement was repeated in this reusability test. Fig. 6-8c shows the degradation efficiencies of 0.03 $BiVO_4/SnS_2$ composite over four cycles, illustrating stability and reusability of the 0.03 $BiVO_4/SnS_2$ composite. A slight loss (around 6%) of the degradation efficiency in the 4th run could be due to a loss of photocatalyst during the recovery process. Furthermore, the stability of the composite was also confirmed by XRD pattern before and after irradiation (Fig. 6-10), in which the crystal structure of 0.03 $BiVO_4/SnS_2$ was not significantly altered after RhB degradation process.

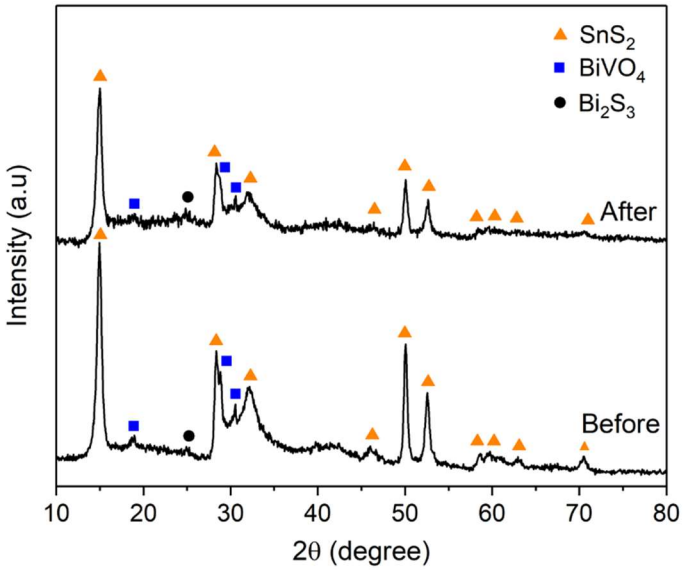

Fig. 6-10. XRD patterns of 0.03 $BiVO_4/SnS_2$ before and after RhB photodegradation.

To determine main reactive species responsible for RhB photodegradation by 0.03 $BiVO_4/SnS_2$ during irradiation, scavenger tests were conducted using various types of scavengers. In this study, methanol (10 mM) [6], ascorbic acid (AA, 10 mM) [29], and isopropyl alcohol (IPA, 10 mM) [16] were used as the scavengers for superoxide radicals ($O_2^{\bullet-}$), holes (h^+), and hydroxyl radicals (•OH), respectively. As shown in Fig. 6-8d, the addition of methanol into the system has only a slight

effect on RhB degradation, indicating that $O_2^{\bullet-}$ radicals play a minor role in the degradation process. Conversely, AA (h^+ scavenger) and IPA (•OH scavenger) greatly suppress photocatalytic RhB degradation. The result strongly suggests that h^+ and •OH radicals are the main reactive species for the RhB photodegradation process with the 0.03 $BiVO_4/SnS_2$ photocatalyst under visible light ($\lambda > 420$ nm) irradiation.

6.3.6. Possible mechanism for photocatalytic activity enhancement of $BiVO_4/Bi2S_3/SnS_2$ heterojunction for rhodamine B degradation

A plausible photocatalytic mechanism of the $BiVO_4/Bi_2S_3/SnS_2$ heterojunction could be explained by understanding the band energy structures of the photocatalysts, as illustrated in Fig. 6-11. The empirical equations (6.1) and (6.2) are often used to estimate the band edge of the semiconductor, such as conduction band edge potential (E_{CB}) and valence band edge potential (E_{VB}) [15,19]:

$$E_{VB} = \chi - E^e + 0.5E_g \quad (6.1)$$

$$E_{CB} = E_{VB} - E_g \quad (6.2)$$

where, χ is absolute electronegativity of a semiconductor, determined by the geometric mean of absolute electronegativity values of constituent atoms. E_g values of SnS_2, Bi_2S_3, and $BiVO_4$ are 2.18, 1.46, and 2.38 eV, respectively (in Section 6.3.3). The absolute electronegativity values of Bi, V, O, Sn, and S are 4.69, 3.6, 7.54, 4.3, and 6.22 eV, respectively, taken from Pearson's experimental data [30]. The value E^e is the energy of the free electron on the hydrogen scale, which is 4.5 eV. According to this calculation, E_{CB} and E_{VB} of SnS_2 are estimated to be −0.09 and 2.09 eV, respectively, whereas $BiVO_4$ exhibits E_{CB} of 0.47 eV and E_{VB} of 2.85 eV, and Bi_2S_3 possesses E_{CB} of 0.33 eV and E_{VB} of 1.79 eV.

The calculated values of band positions of SnS_2 in the present study are similar to those in earlier research [11]. Moreover, the calculated values are similar to the experiment ones reported by Huang et al. [31]. Likewise, the calculated values (band positions) of the $BiVO_4$ are also closed to those reported in the literature

[32,33]. In comparison with experiment values (E_{CB} = 0.21 eV and E_{VB} = 2.56 eV) [34], they are about 0.2−0.3 eV difference. In contrast, the calculated values (E_{CB} = 0.33 eV and E_{VB} = 1.79 eV) of Bi_2S_3 in the current work are not matched with those (E_{CB} ~ 0.1 eV and E_{VB} ~ 1.5 eV) in previous reports [13,35,36] because they used different value of the absolute electronegativity of Bi, which was 4.12 eV [37,38] instead of 4.69 eV (Pearson's data) [30]. In fact, the band positions values of Bi_2S_3 calculated using 4.12 eV are closer to those (E_{CB} = −0.18 eV and E_{VB} = 1.22 eV) measured in experiment results [39], compared with those (E_{CB} of 0.33 eV and E_{VB} of 1.79 eV) using 4.69 eV. Thus, it may be more reasonable to use 4.12 eV (the absolute electronegativity of Bi) specifically for Bi_2S_3 in the present study. Thus, the more suitable E_{CB} and E_{VB} values of Bi_2S_3 are 0.05 eV, and 1.51 eV, respectively. Additionally, including the positions of Fermi levels of SnS_2, Bi_2S_3, and $BiVO_4$ from XPS results in section 6.3.4, the band energy structures (calculation model) of $BiVO_4$, SnS_2, and Bi_2S_3 can be constructed, as shown in Fig. 6-11.

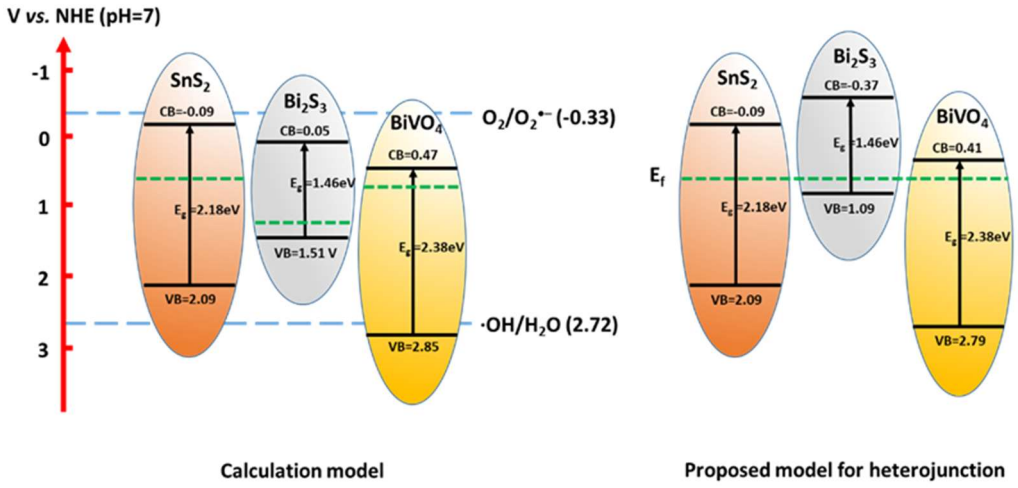

Fig. 6-11. Calculation model (left) and proposed model for heterojunction (right) of band energy structures of $BiVO_4$, Bi_2S_3, and SnS_2 of

In the calculation model of the band energy structures (Fig. 6-11), the conduction bands (CBs) of $BiVO_4$, Bi_2S_3, and SnS_2 are less negative than −0.33 eV (O_2/ $O_2^{\bullet-}$) to generate $O_2^{\bullet-}$, which is inconsistent with the scavenger test in Section 6.3.5. It is worth noting that the XPS results (Section 6.3.4) suggest that the photocatalysts are chemically bonded at the interface, and their Fermi levels are

aligned in the heterojunction. Thus, another model with consideration of the heterojunction in the composite is proposed to fit the experiment results. For this study, the Fermi levels of $BiVO_4$ and Bi_2S_3 are assumed to be aligned with that of SnS_2, thus that the CB potential of Bi_2S_3 (after adjustment) could possess an overpotential to reduce dissolved O_2 to $O_2^{\bullet-}$ for consistency with the result of scavenger test (Section 6.3.5). Therefore, their band energy structures are accordingly adjusted, creating a heterojunction as depicted in Fig. 6-11. It is worth mentioning that it is possible for the CB position of Bi_2S_3 in the composite to be more negative than −0.33 eV (O_2/ $O_2^{\bullet-}$), as reported by previous research [6,40].

To understand the charge-transfer pathway in the $BiVO_4/Bi_2S_3/SnS_2$ heterojunction system, two possible models are explored and examined for the charge transfer process, as proposed in Fig. 6-12. All of the photocatalysts in both models are capable of generating electron-hole pairs upon visible light illumination due to their narrow bandgaps. In model A, the photogenerated electrons (e^-) would migrate from the CB (conduction band) of Bi_2S_3 to CBs of SnS_2 and $BiVO_4$. Thus, $O_2^{\bullet-}$ radicals would not be produced by the heterojunction since the CBs of both SnS_2 and $BiVO_4$ are incapable of reducing dissolved O_2 to produce $O_2^{\bullet-}$ because their CBs are less negative than −0.33 eV (O_2/ $O_2^{\bullet-}$) [16]. On the other hand, the generated holes (h^+) would move from the VBs of both SnS_2 and $BiVO_4$ to the VB of Bi_2S_3. In this scenario, the heterojunction also could not oxidize H_2O to form •OH because VB of Bi_2S_3 is less positive than 2.72 eV (for •OH/H_2O) [8,16]. It has been reported that $O_2^{\bullet-}$, •OH, and h^+ play major roles in the RhB photodegradation process [16,32,33]. Although model A might improve charge separation of photoinduced electrons and holes, it would be less efficient as the composite would be unable to produce $O_2^{\bullet-}$ and •OH to degrade the RhB dye. Moreover, the model is inconsistent with the trapping experiment (the scavenger test in Section 6.3.5) in which $O_2^{\bullet-}$ and h^+, •OH were observed in the RhB degradation process.

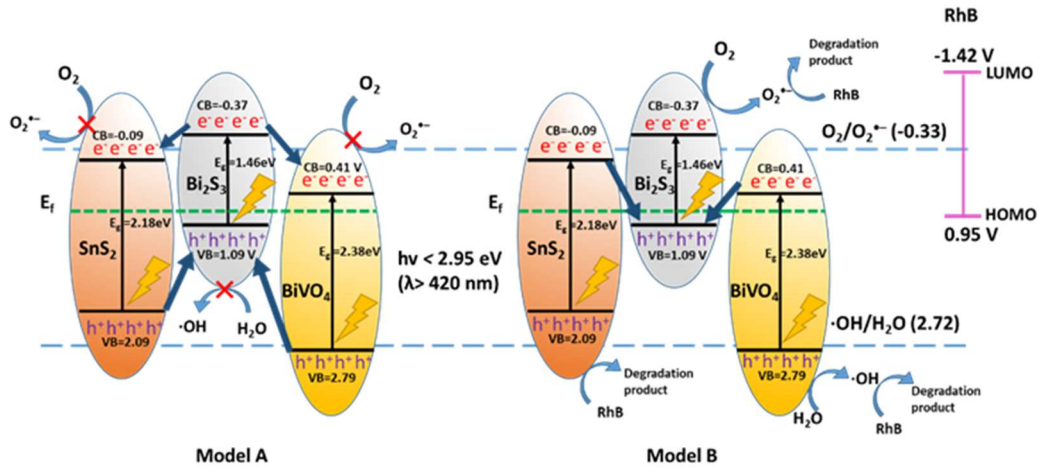

Fig. 6-12. Proposed charge-transfer pathway models, RhB degradation mechanism of $BiVO_4/Bi_2S_3/SnS_2$ under visible light illumination, and band energy diagram of RhB [43–45].

A more plausible scenario might be that of model B in Fig. 6-12, involving a dual Z-scheme process. Based on this model, we can explain the presence of $O_2^{\bullet-}$, •OH, and h^+ for the RhB degradation process. In the dual Z-scheme process, the photoinduced e^- from the CBs of both SnS_2 and $BiVO_4$ could migrate to and recombine with h^+ in the VB of Bi_2S_3. Consequently, e^- from the CB of Bi_2S_3 would be able to react and reduce the dissolved O_2 in H_2O to produce $O_2^{\bullet-}$ because the CB of Bi_2S_3 is more negative than −0.33 eV. According to the scavenger test, $O_2^{\bullet-}$ played only a minor role in the RhB degradation process by the 0.03 $BiVO_4/SnS_2$ heterojunction, which fits well with the current model in which there is the low optimal content of Bi_2S_3 in the composite. Meanwhile, since h^+ in the VB of Bi_2S_3 quickly recombine with e^- transferred from $BiVO_4$ and SnS_2, it would leave h^+ in the VBs of $BiVO_4$ and SnS_2, the former of which would oxide H_2O to generate •OH (2.72 V vs. NHE). Although the VB of SnS_2 is not negative enough to produce •OH, the h^+ would decompose RhB directly because the VB of SnS_2 (2.09 eV) is more negative than HOMO of RhB (0.95 V vs. NHE) [43–45]. Thus, the dual Z-scheme model is consistent with the experimental result, and may be used to explain the charge-transfer pathway of the $BiVO_4/Bi_2S_3/SnS_2$ heterojunction system.

6.4. Conclusion

In summary, three-phase photocatalysts consisting of $BiVO_4$, Bi_2S_3, and SnS_2 were prepared by the chemical reaction between $BiVO_4$ and SnS_2 via solvothermal synthesis. The composite photocatalyst produced via a molar ratio of 1:0.03 (SnS_2:$BiVO_4$) demonstrates the highest photocatalytic performance for RhB degradation among the prepared samples. The composite is proved to be stable after several cycles under visible light irradiation. The main reactive species for the photocatalytic degradation of RhB for 0.03 $BiVO_4$/SnS_2 are h^+ and •OH, whereas $O_2^{\bullet-}$ also plays a minor role in the degradation process. The enhanced photocatalytic activity is attributed to the formation of Bi_2S_3, allowing a suitable condition for the electron pathway (the dual Z-scheme model) in the $BiVO_4$/Bi_2S_3/SnS_2 heterojunction. I believe this discovery of beneficial formation of Bi_2S_3 could encourage more research that focuses on materials prone to reaction with each other at elevated temperature and pressure. The finding may provide a different approach for preparing ternary composite by taking advantage of the chemical reaction between combined photocatalysts.

Reference

[1] N. Kumar, N. Krishnarao, S.A. Singh, Cocatalyst free Z-schematic enhanced H_2 evolution over $LaVO_4/BiVO_4$ composite photocatalyst using Ag as an electron mediator, Appl. Catal. B Environ. 220 (2018) 512–523. https://doi.org/10.1016/j.apcatb.2017.08.082.

[2] J. Ke, J. Liu, H. Sun, H. Zhang, X. Duan, P. Liang, X. Li, M.O. Tade, S. Liu, S. Wang, Facile assembly of $Bi_2O_3/Bi_2S_3/MoS_2$ n-p heterojunction with layered n-Bi_2O_3 and p-MoS_2 for enhanced photocatalytic water oxidation and pollutant degradation, "Applied Catal. B, Environ. 200 (2017) 47–55. https://doi.org/10.1016/j.apcatb.2016.06.071.

[3] G. Ai, R. Mo, Q. Chen, H. Xu, S. Yang, H. Li, J. Zhong, TiO_2/Bi_2S_3 core-shell nanowire arrays for photoelectrochemical hydrogen generation, RSC Adv. 5 (2015) 13544–13549. https://doi.org/10.1039/c4ra15820b.

[4] I. Shown, S. Samireddi, Y.C. Chang, R. Putikam, P.H. Chang, A. Sabbah, F.Y. Fu, W.F. Chen, C.I. Wu, T.Y. Yu, P.W. Chung, M.C. Lin, L.C. Chen, K.H. Chen, Carbon-doped SnS_2 nanostructure as a high-efficiency solar fuel catalyst under visible light, Nat. Commun. 9 (2018). https://doi.org/10.1038/s41467-017-02547-4.

[5] R. Kim, J. Kim, J.Y. Do, M.W. Seo, M. Kang, Carbon Dioxide Photoreduction on the Bi_2S_3/MoS_2 Catalyst, (2019) 1–18. https://doi.org/10.3390/catal9120998.

[6] C. Yu, K. Wang, P. Yang, S. Yang, C. Lu, Y. Song, S. Dong, J. Sun, J. Sun, One-pot facile synthesis of $Bi_2S_3/SnS_2/Bi_2O_3$ ternary heterojunction as advanced double Z-scheme photocatalytic system for efficient dye removal under sunlight irradiation, Appl. Surf. Sci. 420 (2017) 233–242. https://doi.org/10.1016/j.apsusc.2017.05.147.

[7] C.M. Kgoetlana, S.P. Malinga, L.N. Dlamini, Photocatalytic Degradation of Chlorpyrifos with Mn-WO_3/SnS_2 Heterostructure, Catalysts. 10 (2020) 699. https://doi.org/10.3390/catal10060699.

[8] J. Cao, B. Xu, H. Lin, B. Luo, S. Chen, Novel Bi_2S_3-sensitized BiOCl with highly visible light photocatalytic activity for the removal of rhodamine B, Catal. Commun. 26 (2012) 204–208. https://doi.org/10.1016/j.catcom.2012.05.025.

[9] C. Lin, M. Zhu, T. Zhang, Y. Liu, Y. Lv, X. Li, M. Liu, Cellulose/SnS_2

composite with enhanced visible-light photocatalytic activity prepared by microwave-assisted ionic liquid method, RSC Adv. 7 (2017) 12255–12264. https://doi.org/10.1039/c7ra00558j.

[10] Z. Zhang, C. Shao, X. Li, Y. Sun, M. Zhang, J. Mu, P. Zhang, Z. Guo, Y. Liu, Hierarchical assembly of ultrathin hexagonal SnS_2 nanosheets onto electrospun TiO_2 nanofibers: Enhanced photocatalytic activity based on photoinduced interfacial charge transfer, Nanoscale. 5 (2013) 606–618. https://doi.org/10.1039/c2nr32301j.

[11] Y.C. Zhang, Z.N. Du, K.W. Li, M. Zhang, D.D. Dionysiou, High-performance visible-light-driven SnS_2/SnO_2 nanocomposite photocatalyst prepared via in situ hydrothermal oxidation of SnS_2 nanoparticles, ACS Appl. Mater. Interfaces. 3 (2011) 1528–1537. https://doi.org/10.1021/am200102y.

[12] J. Safaei, H. Ullah, N. Aida, M. Firdaus, M. Noh, M. Fairus, A.A. Tahir, N. Ahmad, M. Adib, Enhanced photoelectrochemical performance of Z-scheme g-C_3N_4/$BiVO_4$ photocatalyst, Appl. Catal. B Environ. 234 (2018) 296–310. https://doi.org/10.1016/j.apcatb.2018.04.056.

[13] X. Li, Y. Li, J. Shen, M. Ye, A controlled anion exchange strategy to synthesize Bi_2S_3 nanoparticles/plate-like Bi_2WO_6 heterostructures with enhanced visible light photocatalytic activities for rhodamine B, Ceram. Int. 42 (2016) 3154–3162. https://doi.org/10.1016/j.ceramint.2015.10.105.

[14] Q. Xu, L. Zhang, J. Yu, S. Wageh, A.A. Al-Ghamdi, M. Jaroniec, Direct Z-scheme photocatalysts: Principles, synthesis, and applications, Mater. Today. 21 (2018) 1042–1063. https://doi.org/10.1016/j.mattod.2018.04.008.

[15] D.K. Ma, M.L. Guan, S. Sen Liu, Y.Q. Zhang, C.W. Zhang, Y.X. He, S.M. Huang, Controlled synthesis of olive-shaped Bi_2S_3/$BiVO_4$ microspheres through a limited chemical conversion route and enhanced visible-light-responding photocatalytic activity, Dalt. Trans. 41 (2012) 5581–5586. https://doi.org/10.1039/c2dt30099k.

[16] J. Wang, J. Jin, X. Wang, S. Yang, Y. Zhao, Y. Wu, S. Dong, J. Sun, J. Sun, Facile fabrication of novel $BiVO_4/Bi_2S_3/MoS_2$ n-p heterojunction with enhanced photocatalytic activities towards pollutant degradation under natural sunlight, J. Colloid Interface Sci. 505 (2017) 805–815. https://doi.org/10.1016/j.jcis.2017.06.085.

[17] Z. Wu, L. Chen, C. Xing, D. Jiang, J. Xie, M. Chen, Controlled synthesis of Bi_2S_3/ZnS microspheres by an in situ ion-exchange process with enhanced

visible light photocatalytic activity, J. Chem. Soc. Dalt. Trans. 42 (2013) 12980–12988. https://doi.org/10.1039/c3dt50984b.

[18] S.V.P. Vattikuti, C. Byon, Bi_2S_3 nanorods embedded with MoS_2 nanosheets composite for photodegradation of phenol red under visible light irradiation, Superlattices Microstruct. 100 (2016) 514–525. https://doi.org/10.1016/j.spmi.2016.10.012.

[19] X. Gao, G. Huang, H. Gao, C. Pan, H. Wang, J. Yan, Y. Liu, H. Qiu, N. Ma, J. Gao, Facile fabrication of Bi_2S_3/SnS_2 heterojunction photocatalysts with efficient photocatalytic activity under visible light, J. Alloys Compd. 674 (2016) 98–108. https://doi.org/10.1016/j.jallcom.2016.03.031.

[20] L.Z. Ren, D.E. Zhang, X.Y. Hao, X. Xiao, J.Y. Gong, M.Y. Wang, Z.W. Tong, Synthesis and photocatalytic performance of Bi_2S_3/SnS_2 heterojunction, Funct. Mater. Lett. 10 (2017) 3–7. https://doi.org/10.1142/S1793604717500047.

[21] C. Zhuang, L. Tang, Z. Yu, T. Peng, Y. Zhang, L. Li, Y. Zhou, Z. Zou, Hollow $BiVO_4/Bi_2S_3$ cruciate heterostructures with enhanced visible-light photoactivity, Catal. Sci. Technol. 9 (2019) 182–187. https://doi.org/10.1039/c8cy01899e.

[22] G. Zhang, X. Du, Y. Wang, H. Wang, W. Wang, Z. Fu, Controllable synthesis of SnS_2 nanostructures with high adsorption and photocatalytic activities, Mater. Sci. Semicond. Process. 64 (2017) 77–84. https://doi.org/10.1016/j.mssp.2017.03.010.

[23] Y.C. Zhang, Z.N. Du, K.W. Li, M. Zhang, Size-controlled hydrothermal synthesis of SnS_2 nanoparticles with high performance in visible light-driven photocatalytic degradation of aqueous methyl orange, Sep. Purif. Technol. 81 (2011) 101–107. https://doi.org/10.1016/j.seppur.2011.07.016.

[24] H.Q. Chen, L.Y. Lin, S.L. Chen, Direct growth of $BiVO_4/Bi_2S_3$ nanorod array on conductive glass as photocatalyst for enhancing the photoelectrochemical performance, ACS Appl. Energy Mater. 1 (2018) 6089–6100. https://doi.org/10.1021/acsaem.8b01146.

[25] Y. Zheng, L. Zheng, Y. Zhan, X. Lin, Q. Zheng, K. Wei, Ag/ZnO heterostructure nanocrystals: Synthesis, characterization, and photocatalysis, Inorg. Chem. 46 (2007) 6980–6986. https://doi.org/10.1021/ic700688f.

[26] X.H. Li, H.Y. Xu, X.T. Zhang, Y.C. Liu, J.W. Sun, Y.M. Lu, Local chemical

states and thermal stabilities of nitrogen dopants in ZnO film studied by temperature-dependent x-ray photoelectron spectroscopy, Appl. Phys. Lett. 95 (2009). https://doi.org/10.1063/1.3259644.

[27] S.V.P. Vattikuti, J. Shim, C. Byon, Synthesis , characterization , and optical properties of visible light-driven Bi_2S_3 nanorod photocatalysts, J. Mater. Sci. Mater. Electron. 28 (2017) 14282–14292. https://doi.org/10.1007/s10854-017-7287-6.

[28] S.V.P. Vattikuti, J. Shim, C. Byon, 1D Bi_2S_3 nanorod/2D e-WS_2 nanosheet heterojunction photocatalyst for enhanced photocatalytic activity, J. Solid State Chem. 258 (2018) 526–535. https://doi.org/10.1016/j.jssc.2017.11.017.

[29] Z. Zhang, R. Xu, Z. Wang, M. Dong, B. Cui, M. Chen, Visible-light neural stimulation on graphitic-carbon nitride/graphene photocatalytic fibers, ACS Appl. Mater. Interfaces. 9 (2017) 34736–34743. https://doi.org/10.1021/acsami.7b12733.

[30] R.G. Pearson, Absolute electronegativity and hardness: application to inorganic chemistry, Inorg. Chem. 27 (1988) 734–740. https://doi.org/10.1021/ic00277a030.

[31] E. Huang, X. Yao, W. Wang, G. Wu, N. Guan, SnS_2 nanoplates with specific facets exposed for enhanced visible-light-driven photocatalysis, ChemPhotoChem. (2017) 60–69. https://doi.org/10.1002/cptc.201600026.

[32] Y. Zhang, L. Shi, Z. Geng, T. Ren, Z. Yang, The improvement of photocatalysis O_2 production over $BiVO_4$ with amorphous FeOOH shell modification, Sci. Rep. 9 (2019) 2–11. https://doi.org/10.1038/s41598-019-54940-2.

[33] K. Ding, B. Chen, Y. Li, Y. Zhang, Z. Chen, Comparative density functional theory study on the electronic and optical properties of $BiMO_4$ (M = V, Nb, Ta), J. Mater. Chem. A. 2 (2014) 8294–8303. https://doi.org/10.1039/c3ta15367c.

[34] Y. lei Li, Y. Liu, Y. juan Hao, X. jing Wang, R. hong Liu, F. tang Li, Fabrication of core-shell $BiVO_4$@Fe_2O_3 heterojunctions for realizing photocatalytic hydrogen evolution via conduction band elevation, Mater. Des. 187 (2020) 108379. https://doi.org/10.1016/j.matdes.2019.108379.

[35] F. Dong, X. Feng, Y. Zhang, C. Gao, Z. Wu, An anion-exchange strategy for 3D hierarchical $(BiO)_2CO_3$/amorphous Bi_2S_3 heterostructures with increased

solar absorption and enhanced visible light photocatalysis, RSC Adv. 5 (2015) 11714–11723. https://doi.org/10.1039/c4ra15798b.

[36] X. Wang, N. Zhang, G. Wang, Visible light Bi_2S_3 /$BiFeO_3$ photocatalyst for effective removal of Rhodamine B, MATEC Web Conf. 238 (2018) 0–5. https://doi.org/10.1051/matecconf/201823803007.

[37] C. Kittel, Introduction to solid state physics. Fifth edition, Wiley,Sussex, Eng., United Kingdom, 1976.

[38] J. Zhang, P. Deng, M. Deng, H. Shen, Z. Feng, H. Li, Hybrid density functional theory study of native defects and nonmetal (C, N, S, and P) Doping in a Bi_2WO_6 Photocatalyst, ACS Omega. 5 (2020) 29081–29091. https://doi.org/10.1021/acsomega.0c03685.

[39] Z. Grubač, J. Katić, M. Metikoš-Huković, Energy-band structure as basis for semiconductor n-Bi_2S_3/n-Bi_2O_3 photocatalyst design, J. Electrochem. Soc. 166 (2019) H433–H437. https://doi.org/10.1149/2.0481910jes.

[40] Z. Liu, K. Xu, H. Yu, M. Zhang, Z. Sun, In-situ preparation of double Z-scheme Bi_2S_3/$BiVO_4$/TiO_2 ternary photocatalysts for enhanced photoelectrochemical and photocatalytic performance, Appl. Surf. Sci. 545 (2021) 148986. https://doi.org/10.1016/j.apsusc.2021.148986.

[41] Y. Bessekhouad, M. Mohammedi, M. Trari, Hydrogen photoproduction from hydrogen sulfide on Bi_2S_3 catalyst, Sol. Energy Mater. Sol. Cells. 73 (2002) 339–350. https://doi.org/10.1016/S0927-0248(01)00218-5.

[42] F.A. Liu, Y.C. Yang, J. Liu, W. Huang, Z.L. Li, Preparation of Bi_2O_3@Bi_2S_3 core-shell nanoparticle assembled thin films and their photoelectrochemical and photoresponsive properties, J. Electroanal. Chem. 665 (2012) 58–62. https://doi.org/10.1016/j.jelechem.2011.11.015.

[43] A. Pandey, G. Naresh, T.K. Mandal, Sunlight responsive new Sillén-Aurivillius A1X1 hybrid layered oxyhalides with enhanced photocatalytic activity, Sol. Energy Mater. Sol. Cells. 161 (2017) 197–205. https://doi.org/10.1016/j.solmat.2016.11.040.

[44] L. Pan, J.J. Zou, X.Y. Liu, X.J. Liu, S. Wang, X. Zhang, L. Wang, Visible-light-induced photodegradation of rhodamine B over hierarchical TiO_2: Effects of storage period and water-mediated adsorption switch, Ind. Eng. Chem. Res. 51 (2012) 12782–12786. https://doi.org/10.1021/ie3019033.

[45] T. Shen, Z.G. Zhao, Q. Yu, H.J. Xu, Photosensitized reduction of benzil by

heteroatom-containing anthracene dyes, J. Photochem. Photobiol. A Chem. 47 (1989) 203–212. https://doi.org/10.1016/1010-6030(89)87066-2.

7. Comparison of $BiVO_4/Bi_2S_3/SnS_2$ Composites with Different Morphologies of $BiVO_4$

7.1. Introduction

Composite photocatalyst has garnered much attention in recent decades due to its advantages over a single photocatalyst, such as the suppression of electron-hole recombination [1,2], efficient charge separation [3,4], and enhanced light absorption [5]. Among the composites, $BiVO_4$-based composites have demonstrated a promising result by many research in pollutant degradation [4], water splitting [6], H_2 production [7], and CO_2 reduction [8], attributed to the favorable properties of $BiVO_4$, including photostability, narrow bandgap (~2.4 eV), and non-toxicity [9].

The study [10] in Chapter 6 has demonstrated that an enhanced $BiVO_4/Bi_2S_3/SnS_2$ composite can be produced by the chemical reaction between $BiVO_4$ and SnS_2 via a solvothermal method. Earlier report [6,11] have suggested that the photocatalytic activity of the composite depends on the morphology of its individual components. Thus, the $BiVO_4$ with different morphologies would be able to influence the photocatalytic performance of $BiVO_4/Bi_2S_3/SnS_2$ composites. It is worth mentioning that the process of $BiVO_4/Bi_2S_3/SnS_2$ synthesis involves the chemical reaction between two materials to produce the third one, the expected outcome may differ from the conventional process.

In this work, the $BiVO_4/Bi_2S_3/SnS_2$ composites with two different morphologies of $BiVO_4$ (shuriken-like $BiVO_4$ and polyhedral $BiVO_4$) were prepared by incorporating each of them with SnS_2 using solvothermal synthesis. Based on previous research [10], the $BiVO_4/Bi_2S_3/SnS_2$ composite with a molar

ratio of 1:0.03 (SnS_2:$BiVO_4$) exhibits the highest photocatalytic activity. Thus, the molar ratio of 1:0.03 (SnS_2:$BiVO_4$) was used in this study. Both composites were measured and characterized via various methods to compare and study their properties, such as morphology, crystal structure, optical absorption, surface chemical state, and photocatalytic activity. The results show the photocatalytic degradation of RhB in the presence of the $BiVO_4$/Bi_2S_3/SnS_2 composite depends on the morphology of $BiVO_4$.

7.2. Experimental

The preparation of the shuriken-like $BiVO_4$ is described in Section 4.2 of Chapter 4, whereas the preparations of polyhedral $BiVO_4$, Bi_2S_3, and SnS_2 are shown in Section 6.2 of Chapter 6.

7.2.1. Preparation of $BiVO_4$/Bi_2S_3/SnS_2 composites

The $BiVO_4$/Bi_2S_3/SnS_2 composite was prepared via the method used in Chapter 6. The preparation of the composite with different morphologies of $BiVO_4$ started with mixing 0.03 mmol of either shuriken-like $BiVO_4$ (denoted as S-$BiVO_4$) or polyhedral $BiVO_4$ (denoted as P-$BiVO_4$) with 1 mmol of SnS_2 in 40 ml of ethylene glycol via ultrasonication for 1 h. Then, the suspension was transferred to a Teflon-liner inside a stainless steel autoclave, which was heated in a pre-heated oven at 150 °C for 8 h. The obtained composite was collected via a centrifuge, washed several times with DI water and ethanol, and then dried at 90 °C overnight. Finally, the powder sample was ground for 1 min. The composites prepared with S-$BiVO_4$ and P-$BiVO_4$ were denoted as S-$BiVO_4$/SnS_2 and P-$BiVO_4$/SnS_2, respectively.

7.2.2. Characterization

The crystal structures of the samples were measured using a Rigaku RINT2100 with Cu Kα radiation (λ = 0.15418 nm) to record X-ray diffraction (XRD) diffractogram. Microstructures and morphologies of the samples were analyzed using an FE-SEM (Hitachi SU6600 Scanning Electron Microscope)

equipped with Bruker EDX operated at 20 kV. Prior to the analyses, each sample was sputtered with Au to avoid the charging effect. A Lambda 750S UV/Vis/NIR spectrophotometer equipped with a 60 mm integrating sphere was used to record UV-vis diffuse reflectance spectra (DRS. a JPS-9030 X-ray photoelectron spectrometer was used to measure X-ray photoelectron spectra. It was conducted with Mg Kα radiation using C 1s = 284.8 eV as reference. A Flowsorb III 2305 Micromeritics instruments (Shimadzu, Japan) with N_2 gas adsorption was used to determine the specific surface area (S_{BET}) of the samples.

7.2.3. Measurement of photocatalytic activity for rhodamine B degradation

Photocatalytic degradation of rhodamine B (RhB) was used to evaluate the photocatalytic activity of the samples. The experimental setup consisted of A 500 W light source (Xe lamp, UXL-500D-O, Ushio), a water filter, a UV cutoff filter (λT = 420 nm), and a 100ml beaker on a magnetic stirrer. The measurement was conducted at room temperature (25 °C). The light intensity (source) with 100 mW/cm^2 (calibration with a spectroradiometer, S-2440 model II) was used to illuminate the sample solution, with around 40 mW/cm^2 after passing through water and cutoff filters. Powder of photocatalyst (30 mg) was dispersed in 40 ml of RhB solution (0.01 mmol L^{-1}), agitated with ultrasonication (10 min), and magnetically stirred (50 min) in dark to attain adsorption-desorption equilibrium. As SnS_2 demonstrates strong adsorptivity for RhB dye [12], we followed the previous method [10] by performing adsorption-desorption procedure twice with fresh RhB solution in order to allow initial RhB concentration (C_0) to be similar for all samples. During the irradiation, around 3 ml of RhB solution was taken every 60 min. The supernatant was filtered with a syringe filter (0.22 μm, PTFE) and analyzed using the Lambda 750S UV/Vis/NIR Spectrophotometer.

7.3. Results and discussion

7.3.1. Crystal structure of the samples

Crystal phases of S-$BiVO_4$/SnS_2 and P-$BiVO_4$/SnS_2 composites are illustrated in Fig. 7-1. The XRD diffractograms of both composites display similar

patterns. The characteristic peaks correspond to hexagonal SnS_2 (ICDD PDF No. 00-023-0677) can be seen in both composites at 14.9°, 28.3°, 32.3°, 49.5°, and 52.4°. Other noticeable peaks at 19.0°, 28.8°, and 30.5°, corresponding to (011), ($\bar{1}$21), and (040) planes of the standard monoclinic $BiVO_4$, respectively (ICDD PDF No. 00-014-0688). In addition, a small peak at 25° can be assigned (130) plane of orthorhombic Bi_2S_3 (ICDD PDF No. 01-089-8965). This peak would become more visible if the $BiVO_4$ content was increased, based on the previous study [10]. There is a visible difference between both composites around the peak at 30.5°, assigned to (040) plane of $BiVO_4$, where the peak intensity of S-$BiVO_4$/SnS_2 is higher than that of P-$BiVO_4$/SnS_2. It can be ascribed to the relative intensity ratio $I_{(040)}/I_{(\bar{1}21)}$ of S-$BiVO_4$, which is greater than that of P-$BiVO_4$, as shown in Fig. 7-2. The high $I_{(040)}/I_{(\bar{1}21)}$ indicates the preferential orientation along {010} planes of $BiVO_4$ [13,14]. It should be noticeable that the relative intensity ratio $I_{(040)}/I_{(\bar{1}21)}$ of S-$BiVO_4$, 2.46, reduces to that of 1.14 of S-$BiVO_4$/SnS_2, perhaps because the S-$BiVO_4$/SnS_2 composite was ground into smaller particles, which could lose its preferential orientation. Nevertheless, both composites retain crystal structures of both SnS_2 and their respective $BiVO_4$.

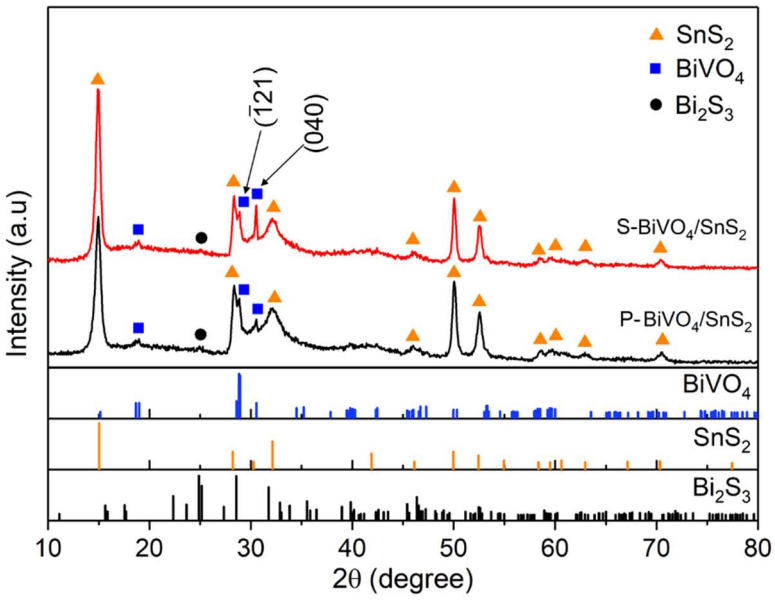

Fig. 7-1. XRD patterns of composites with different types of $BiVO_4$.

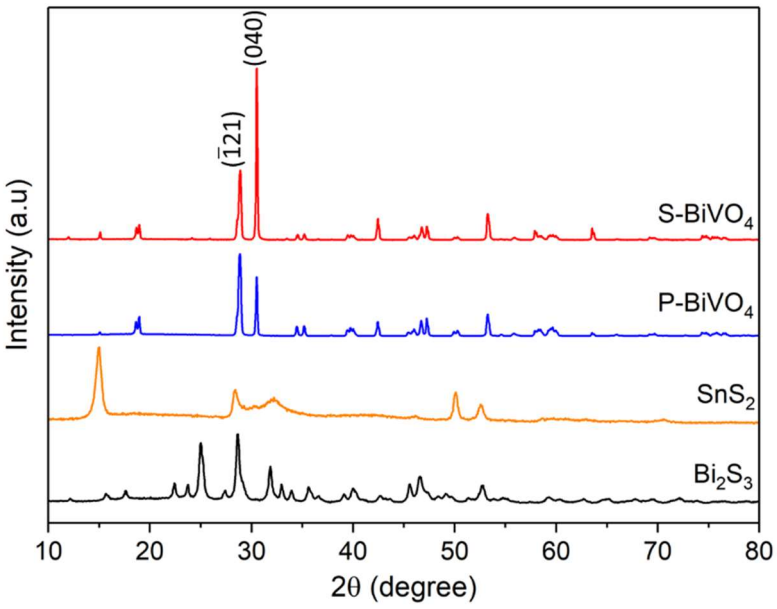

Fig. 7-2. XRD patterns of Bi_2S_3, SnS_2, P-$BiVO_4$, and S-$BiVO_4$.

7.3.2. Morphology and microstructure of samples

Fig. 7-3 depicts micrograph images of SnS_2, P-$BiVO_4$, P-$BiVO_4$/SnS_2, S-$BiVO_4$, and S-$BiVO_4$/SnS_2. In Fig. 7-3a, SnS_2 possesses nanoparticles with a size of ~50 nm, while P-$BiVO_4$ (Fig. 7-3b) and S-$BiVO_4$ (Fig. 7-3e) exhibit polyhedron with a diagonal length of ~5 μm and shuriken shape with a diagonal length of ~12, respectively. Fig. 7-3c and 7-3f illustrate the P-$BiVO_4$/SnS_2 and S-$BiVO_4$/SnS_2, respectively, demonstrating the micro-sized particles covered with the nanoparticles of SnS_2. Moreover, the shapes of P-$BiVO_4$ and S-$BiVO_4$ are still visible after being covered by the nanoparticles of SnS_2. It is further confirmed by EDS mapping in Fig. 7-4 and Fig. 7-5, demonstrating the existence of Sn, S, Bi, V, and O elements.

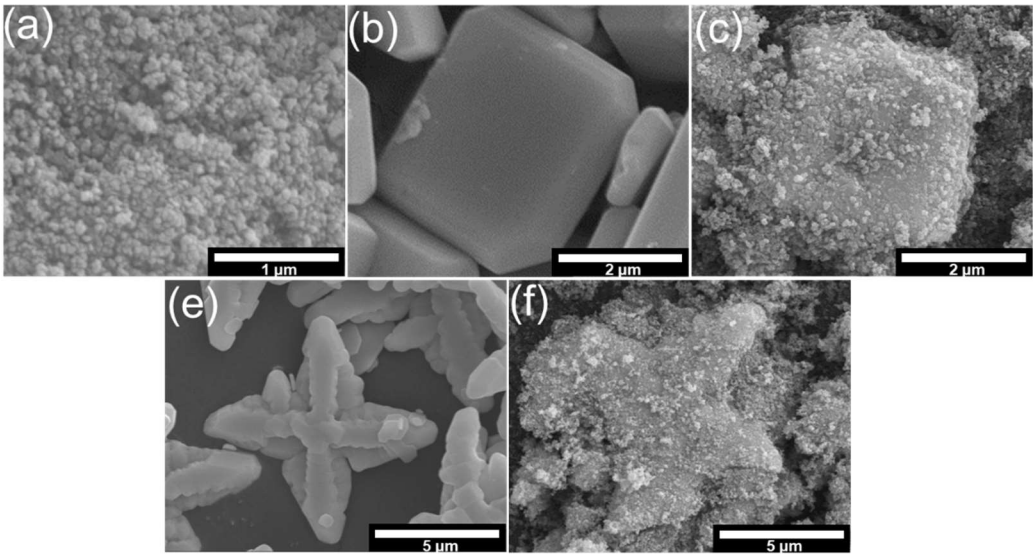

Fig. 7-3. FE-SEM micrographs of (a) SnS_2, (b) P-$BiVO_4$, (c) P-$BiVO_4$/SnS_2, (d) S-$BiVO_4$, and (e) S-$BiVO_4$/SnS_2.

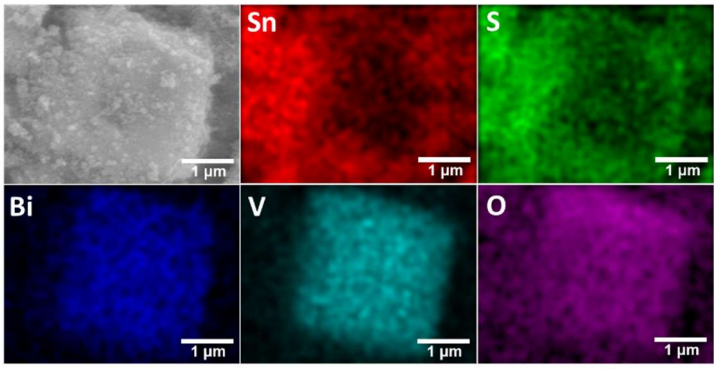

Fig. 7-4. EDS elemental mapping of Sn, S, Bi, V, and O elements in P-$BiVO_4$/SnS_2.

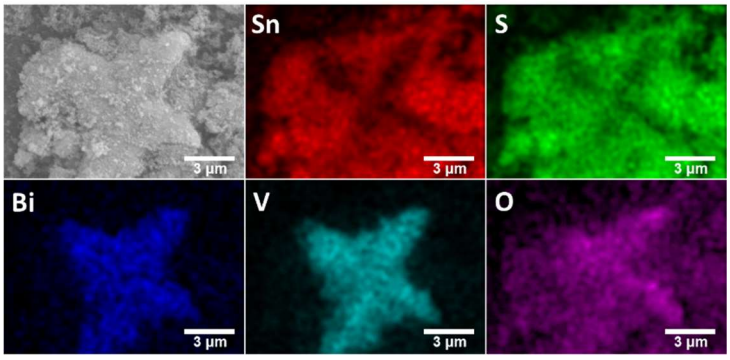

Fig. 7-5. EDS elemental mapping of Sn, S, Bi, V, and O elements in S-$BiVO_4$/SnS_2.

7.3.3. Optical absorption properties of the samples

Absorption spectra of the samples were transformed from reflectance spectra using Kubelka-Munk function in Eq. (3.1), and the absorption spectra were plotted in Fig. 7-6a. According to the figure, all the samples are capable of absorbing visible light because their absorption edges are in a range of 520–570 nm. It is worth mentioning that S-$BiVO_4$ exhibits tailing in the absorption spectrum due to the presence of the oxygen vacancies (confirmed in Chapter 5). The absorption spectrum can be used to estimate bandgaps of each sample is using equation Eq (3.2). Since SnS_2 and $BiVO_4$ are direct transition materials (n = 1, described in Section 3.2.4 of Chapter 3) [15,16], *(F(R)hv)^2 vs. hv* graph can be used for Tauc's plot, as shown in Fig. 7-6b [13,17,18].

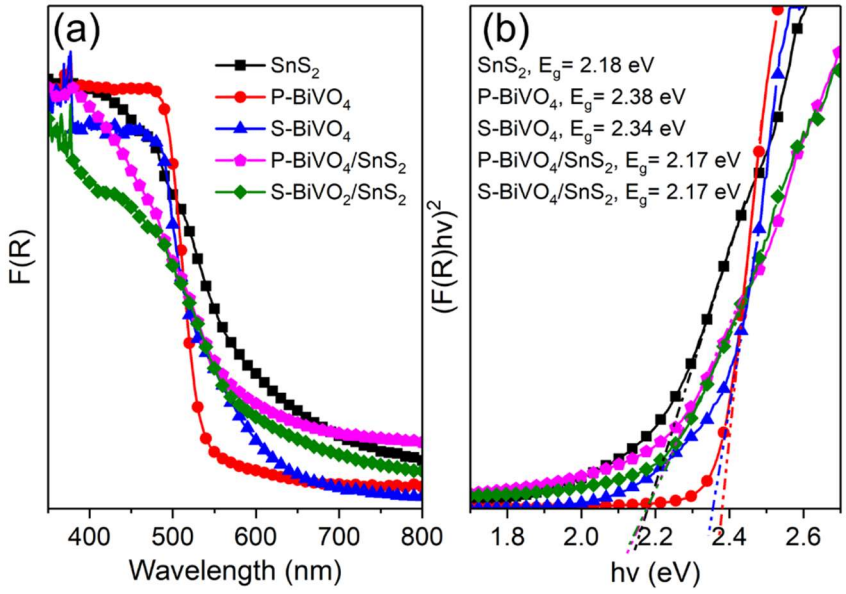

Fig. 7-6. (a) UV-vis absorption spectra and (b) $(F(R)hv)^2$ vs hv plot of SnS_2, P-$BiVO_4$, S-$BiVO_4$, P-$BiVO_4$/ SnS_2, and S-$BiVO_4$/ SnS_2.

Bandgap value of each sample can be determined by extrapolating the linear part of the curve to intercept x-axis. The estimated E_g values of SnS_2, S-$BiVO_4$, and P-$BiVO_4$ are 2.18, 2.34, and 2.38 eV, respectively, similar to earlier reports [14,19,20]. On the other hand, effective E_g values of S-$BiVO_4$/SnS_2 and P-$BiVO_4$/SnS_2 are around 2.17 eV. Based on the results in Chapter 6, Bi_2S_3 exists in

the $BiVO_4/Bi_2S_3/SnS_2$ composite, and its bandgap (1.46 eV) could be determined in the composites with higher content of $BiVO_4$. Since this work uses low content of $BiVO_4$ with the ratio of 1:0.03 (SnS_2:$BiVO_4$), the effect of Bi_2S_3 is too small to observe in the Tauc's plot. Based on the above result, there is no significant difference in terms of the bandgap between S-$BiVO_4/SnS_2$ and P-$BiVO_4/SnS_2$.

7.3.4. X-ray photoelectron spectroscopic (XPS) analyses of the samples

The XPS survey spectra of SnS_2, S-$BiVO_4/SnS_2$, and P-$BiVO_4/SnS_2$ are shown in Fig. 7-7a. The survey spectra indicate that the samples are composed of Sn, S, Bi, V, and O elements, which are consistent with the result from EDS. High-resolution XPS spectra in Fig. 7-7b (Sn 3d) and 7-7c (Bi 4f and S2p) demonstrate the chemical state of the samples.

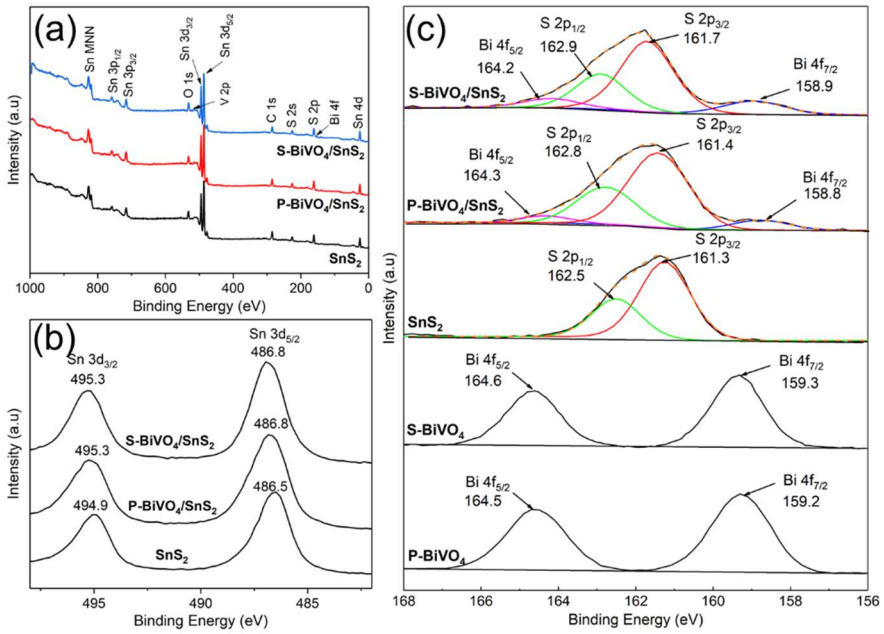

Fig. 7-7. (a) XPS survey spectra of SnS_2, P-$BiVO_4/SnS_2$, and S-$BiVO_4/SnS_2$; and high-resolution XPS spectra of (b) Sn 3d, and (c) Bi 4f and S 2p orbitals of the samples.

As can be seen in Fig. 7-7b, the two peaks at 494.9 and 486.5 eV correspond to the splitting peaks of Sn 3d, belonging to Sn^{4+} of a typical SnS_2 [15,21,22]. Both S-$BiVO_4/SnS_2$, and P-$BiVO_4/SnS_2$ composite also possess the splitting peaks of Sn 3d at 495.3 and 486.8 eV, which have a blueshift to the higher binding energy by

0.4 eV, compared with SnS_2. In Fig. 7-7c, the blueshift is also observed in S 2p spectra of both composites, where both peaks of S 2p shift by about 0.1–0.4 eV, compared with those of SnS_2 (162.5 and 161.3 eV). The S 2p peak fittings can be found in Fig. 2 of Appendix D. Fig. 7-7c also shows the splitting peaks (Bi 4f) of P-$BiVO_4$ (164.5 and 159.2 eV) and S-$BiVO_4$ (164.6 and 159.3 eV) are similar in value and only different by 0.1 eV. The splitting peaks of Bi 4f correspond to Bi^{3+} of a common $BiVO_4$ [23]. After forming composite, those Bi 4f peaks have redshift to lower binding energy, 159.2→158.8 eV and 164.5→164.3 eV for P-$BiVO_4$/SnS_2, and 159.3→158.9 eV and 164.6→164.2 eV for S-$BiVO_4$/SnS_2. These shifts are in the opposite direction, compared to Sn 3d and S 2p. The shift of binding energy in the composites is likely due to the electron screening effect [24], which has been explained in Section 6.3.4 of Chapter 6. It also indicates a formation of the heterojunction in the composite [10]. It should be mentioned that the broad peak of Bi 4f may also be caused by the existence of Bi_2S_3, whose peaks located at 158.4 and 163.8 eV [25].

XPS results demonstrate Both S-$BiVO_4$/SnS_2, and P-$BiVO_4$/SnS_2 composites exhibit similar chemical states at the core level of XPS spectra and the heterojunction of $BiVO_4$/Bi_2S_3/SnS_2. Therefore, different morphologies of $BiVO_4$ in $BiVO_4$/Bi_2S_3/SnS_2 composites do not have any significant change in the chemical state.

7.3.5. Photocatalytic activities of the samples for rhodamine B degradation

RhB degradation was used to evaluate the photocatalytic performance of the as-synthesized samples. Fig. 7-8a shows the degradation of RhB over time in the presence of the photocatalyst. After 4 h of irradiation, SnS_2, P-$BiVO_4$, P-$BiVO_4$/SnS_2, S-$BiVO_4$, and S-$BiVO_4$/SnS_2 exhibit the RhB degradation efficiency of 14.2%, 13.1%, 32.6%, 41.1%, and 48.8%, respectively. The S-$BiVO_4$/SnS_2 composite demonstrates the highest RhB degradation efficiency among the samples.

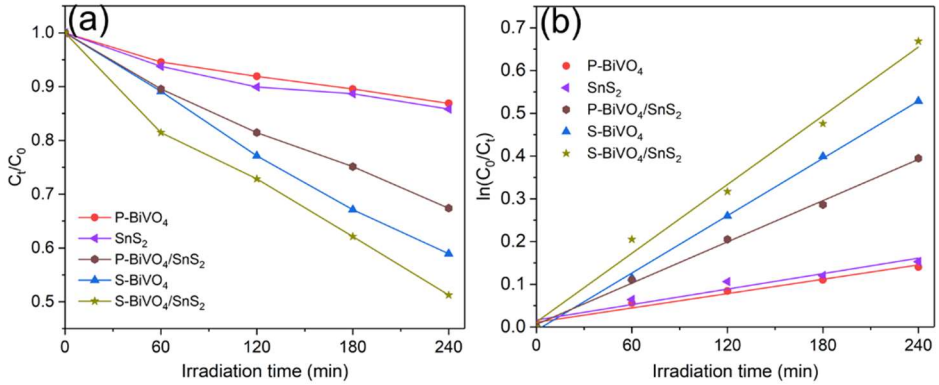

Fig. 7-8. (a) Photodegradation of RhB solution in presence of SnS_2, P-$BiVO_4$, S-$BiVO_4$, P-$BiVO_4$/ SnS_2, and S-$BiVO_4$/ SnS_2 photocatalysts under visible light (λ >420 nm); and (b) their pseudo-first-order kinetic degradation.

For comparison, photodegradation constant rate (k) of each sample was calculated using pseudo-first-order reaction in Eq. (3.4), producing a graph in Fig. 7-8b. Thus, the slopes from linear lines of all samples are their *k* values, which are shown in Table 7-1. The samples can be arranged in the descending order of *k* values from big to small, as follows: S-$BiVO_4$/SnS_2 > S-$BiVO_4$ > P-$BiVO_4$/SnS_2 > SnS_2 > P-$BiVO_4$. It is worth mentioning that the *k* value of P-$BiVO_4$/SnS_2 is 2.9 times greater than that of P-$BiVO_4$, while S-$BiVO_4$/SnS_2 exhibits the *k* value only 1.2 times that of S-$BiVO_4$. Both P-$BiVO_4$/SnS_2 and S-$BiVO_4$/SnS_2 are improved over their individual components in terms of photocatalytic degradation of RhB likely due to the dual Z-scheme model proposed in Chapter 6. Moreover, the *k* value of S-$BiVO_4$/SnS_2 is higher than that of P-$BiVO_4$/SnS_2 by 1.7 times although their bandgaps and specific surface areas (S_{BET}) values are equal. Although single S-$BiVO_4$ exhibits high photocatalytic activity, the amount of S-$BiVO_4$ used in the composite is rather low. Thus, its individual photocatalytic activity may not contribute to the composite unless it possesses morphology, which can enhance the charge-transfer pathway in the composite. Furthermore, S-$BiVO_4$ possesses a large number of oxygen vacancies (Chapter 5), narrowing the bandgap and promoting light absorption efficiency. To some extent, this may also contribute to the improved photocatalytic activity of S-$BiVO_4$/SnS_2. Therefore, the enhanced photocatalytic activity of S-$BiVO_4$/SnS_2 may be attributed to the narrower bandgap

and higher $I_{(040)}/I_{(\bar{1}21)}$ ratio of S-$BiVO_4$ (increase in {010} facets [13,14,26]), compared with those of P-$BiVO_4$. This will be discussed in a later section. Finally, both composites exhibit their stability by showing no significant alteration in the crystal structure after being used in the RhB degradation process, as shown in Fig. 7-9.

Table 7-1. Bandgap, specific surface area, RhB degradation efficiency and photodegradation constant rate of the samples.

Sample	E_g[a] (eV)	S_{BET}[b] ($m^2\ g^{-1}$)	RhB degradation efficiency (%)	k[c] ($\times 10^{-3}\ min^{-1}$)
P-$BiVO_4$	2.38	0.6	13.1	0.55
S-$BiVO_4$	2.34	0.6	41.1	2.2
SnS_2	2.18	75.7	14.2	0.60
P-$BiVO_4$/SnS_2	2.17	74.7	32.6	1.6
S-$BiVO_4$/SnS_2	2.17	74.7	48.8	2.7

[a] E_g is Bandgap value; [b] S_{BET} is BET specific surface area; [c] k is photodegradation rate constant

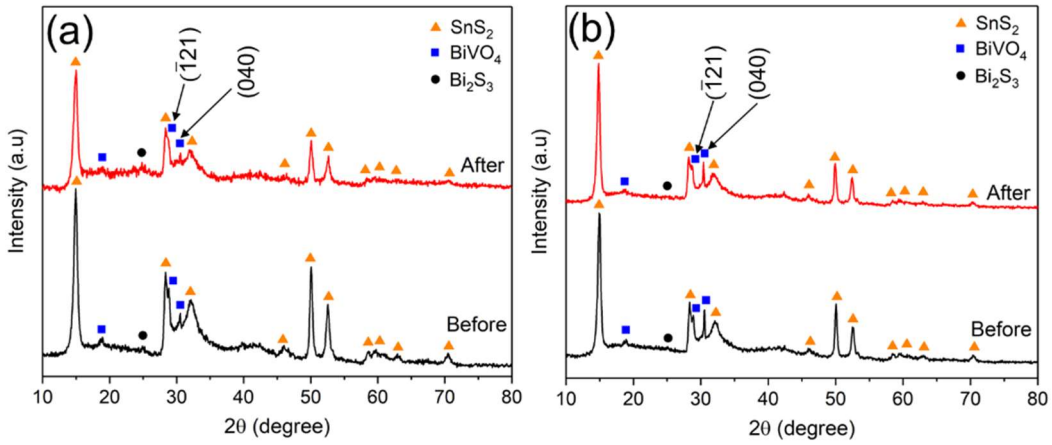

Fig. 7-9. XRD patterns of (a) P-$BiVO_4$/SnS_2 and (b) S-$BiVO_4$/SnS_2 before and after irradiation

7.3.6. Possible explanation for enhanced photocatalytic activities in S-$BiVO_4$/SnS_2 composites for rhodamine B degradation

Both P-$BiVO_4$/SnS_2 and S-$BiVO_4$/SnS_2 possess some similarities in terms of the surface chemical states, effective bandgaps, crystal structure, and specific surface area, based on XPS, optical absorption, XRD, and BET results, respectively. According to SEM results, their morphologies are different due to their source of $BiVO_4$. Thus, it is plausible that both composites are likely to follow the same model (dual Z-scheme), which is proposed for $BiVO_4$/Bi_2S_3/SnS_2 composite (P-$BiVO_4$/SnS_2) in Chapter 6. In addition, Fig. 7-10 displays XPS valence band spectra of S-$BiVO_4$ and P-$BiVO_4$ and demonstrates that their differences between the Fermi level and valence band maximum (VBM) are almost the same (2 eV). Since their bandgap values are different (2.34 and 2.38 eV for S-$BiVO_4$ and P-$BiVO_4$, respectively), their band edge potentials are slightly different. However, as S-$BiVO_4$ and P-$BiVO_4$ possess the same energy gap value of 2 eV between the Fermi level and VBM, their E_{VB} would be the same after the alignment of the band energy structures. Using these results and the data from Chapter 6, charge-transfer pathway models of both composites can be made and compared, as shown in Fig. 7-1.

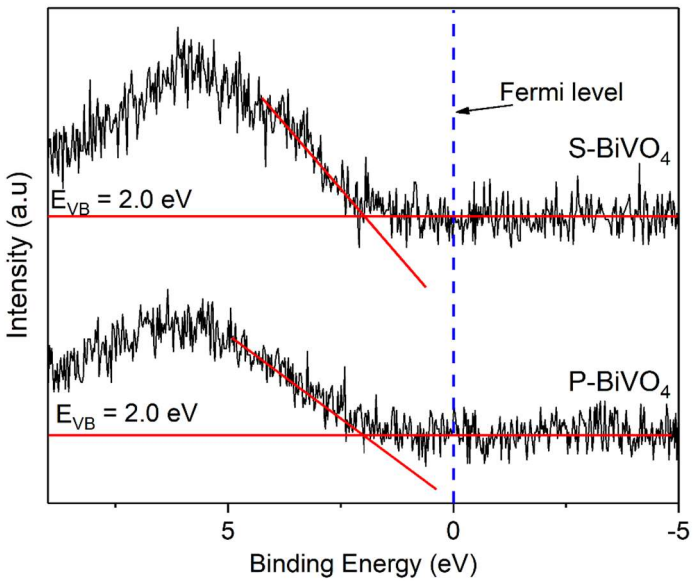

Fig. 7-10. Valence band XPS spectra of S-$BiVO_4$ and P-$BiVO_4$

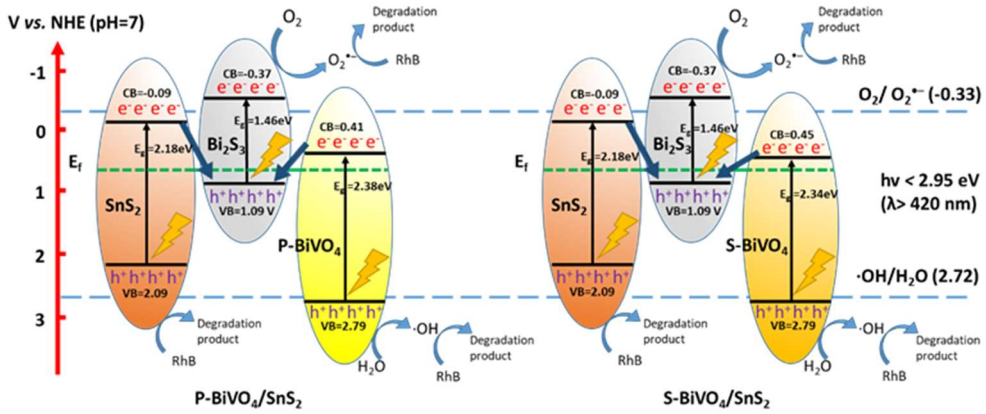

Fig. 7-11. Proposed charge-transfer pathway models of P-$BiVO_4$/SnS_2 (left) and S-$BiVO_4$/SnS_2 (right) composites.

The enhanced photocatalytic activity of the S-$BiVO_4$/SnS_2 composite, compared with that of the P-$BiVO_4$/SnS_2 composite, could be explained as follows. As mentioned above, the S-$BiVO_4$ possesses large number of oxygen vacancies, introducing defect levels that produce tailing in the absorption spectrum (Fig. 7-6a) and narrow bandgap of S-$BiVO_4$. Thus, S-$BiVO_4$ exhibits superior light absorption efficiency than that of P-$BiVO_4$, which in turn may contribute to the enhanced photocatalytic activity of the S-$BiVO_4$/SnS_2 composite. In addition, S-$BiVO_4$ exhibits higher relative intensity ratio of $I_{(040)}/I_{(\bar{1}21)}$, indicating the higher exposed {010} facets. The {010} facets have been known to be active reduction sites, accumulating electrons after photoexcitation [27–31]. The XRD results demonstrate the S-$BiVO_4$/SnS_2 composite exhibit higher $I_{(040)}/I_{(\bar{1}21)}$ ratio of the S-$BiVO_4$, compared with that of the P-$BiVO_4$ in the P-$BiVO_4$/SnS_2 composite. Thus, the more exposed {010} facets, the more accumulation of electrons at conduction band (CB) of S-$BiVO_4$, leads to the enhanced electron transfer from CB of S-$BiVO_4$ to VB of Bi_2S_3 (Fig. 7-11), consequently suppressing recombination rate and promoting charge separation efficiency [27]. As a result, the photocatalytic performance of the S-$BiVO_4$/SnS_2 composite is improved. The chemical reaction between S-$BiVO_4$ and SnS_2 might modify the surface of S-$BiVO_4$ in the composite to some extent, however, the majority (bulk) of crystal structures of the individual components (S-$BiVO_4$ and SnS_2) in the composite remain unchanged (XRD result). Thus, the enhanced photocatalytic activity of the S-$BiVO_4$/SnS_2 composite,

compared to that of P-$BiVO_4$/SnS_2, could happen at the sites, in which the chemical reaction induces only mild effect, and the exposed {010} facets of S-$BiVO_4$ still remain and in contact with Bi_2S_3.

Based on the above analyses, the photocatalytic performance of the $BiVO_4$/Bi_2S_3/SnS_2 composite can be further enhanced using different morphologies of $BiVO_4$ with superior morphology (e.g., high exposed {010} facets) and narrower bandgap. Nevertheless, it should be pointed out that this method may only work if the particle size or the specific surface area of $BiVO_4$ is similar to that of $BiVO_4$ used in the present study because small particle size or high specific surface area of $BiVO_4$ could lead to an increase in the reaction rate of $BiVO_4$ and SnS_2, resulting in a substantial change of the composite properties. Consequently, more optimization of the solvothermal method may be required to achieve a desirable result.

7.4. Conclusion

The $BiVO_4$/Bi_2S_3/SnS_2 composites with different morphologies of $BiVO_4$ were prepared via solvothermal route. The results show that the surface chemical states, effective bandgaps, crystal structures, and specific surface areas of both P-$BiVO_4$/SnS_2 and S-$BiVO_4$/SnS_2 samples do not significantly differ from each other. The composites could retain morphologies of their respective $BiVO_4$ to some extent, which in turn influences their photocatalytic performance. The S-$BiVO_4$/SnS_2 sample exhibits higher photocatalytic degradation of RhB than that of the P-$BiVO_4$/SnS_2 sample, where the bandgap and morphology of S-$BiVO_4$ were attributed to for facilitating the electron-transfer pathway in S-$BiVO_4$/SnS_2. These findings indicate that the $BiVO_4$/Bi_2S_3/SnS_2 composite can be further improved using $BiVO_4$ with morphology that can promote electron migration in the composite.

Reference

[1] Y.C. Zhang, Z.N. Du, K.W. Li, M. Zhang, D.D. Dionysiou, High-performance visible-light-driven SnS_2/SnO_2 nanocomposite photocatalyst prepared via in situ hydrothermal oxidation of SnS_2 nanoparticles, ACS Appl. Mater. Interfaces. 3 (2011) 1528–1537. https://doi.org/10.1021/am200102y.

[2] X. Li, Y. Li, J. Shen, M. Ye, A controlled anion exchange strategy to synthesize Bi_2S_3 nanoparticles/plate-like Bi_2WO_6 heterostructures with enhanced visible light photocatalytic activities for Rhodamine B, Ceram. Int. 42 (2016) 3154–3162. https://doi.org/10.1016/j.ceramint.2015.10.105.

[3] B. Chai, J. Yan, G. Fan, G. Song, C. Wang, In situ fabrication of $CdMoO_4$/g-C_3N_4 composites with improved charge separation and photocatalytic activity under visible light irradiation, Chinese J. Catal. 41 (2020) 170–179. https://doi.org/10.1016/S1872-2067(19)63383-8.

[4] J. Wang, J. Jin, X. Wang, S. Yang, Y. Zhao, Y. Wu, S. Dong, J. Sun, J. Sun, Facile fabrication of novel $BiVO_4/Bi_2S_3/MoS_2$ n-p heterojunction with enhanced photocatalytic activities towards pollutant degradation under natural sunlight, J. Colloid Interface Sci. 505 (2017) 805–815. https://doi.org/10.1016/j.jcis.2017.06.085.

[5] C. Yu, K. Wang, P. Yang, S. Yang, C. Lu, Y. Song, S. Dong, J. Sun, J. Sun, One-pot facile synthesis of $Bi_2S_3/SnS_2/Bi_2O_3$ ternary heterojunction as advanced double Z-scheme photocatalytic system for efficient dye removal under sunlight irradiation, Appl. Surf. Sci. 420 (2017) 233–242. https://doi.org/10.1016/j.apsusc.2017.05.147.

[6] Q. Jia, A. Iwase, A. Kudo, $BiVO_4$-Ru/$SrTiO_3$:Rh composite Z-scheme photocatalyst for solar water splitting, Chem. Sci. 5 (2014) 1513–1519. https://doi.org/10.1039/c3sc52810c.

[7] F. Li, D.Y.C. Leung, Highly enhanced performance of heterojunction $Bi_2S_3/BiVO_4$ photoanode for photoelectrocatalytic hydrogen production under solar light irradiation, Chem. Eng. Sci. 211 (2020) 115266. https://doi.org/10.1016/j.ces.2019.115266.

[8] Z.H. Wei, Y.F. Wang, Y.Y. Li, L. Zhang, H.C. Yao, Z.J. Li, Enhanced photocatalytic CO_2 reduction activity of Z-scheme CdS/$BiVO_4$ nanocomposite with thinner $BiVO_4$ nanosheets, J. CO_2 Util. 28 (2018) 15–25. https://doi.org/10.1016/j.jcou.2018.09.008.

[9] H.L. Tan, R. Amal, Y.H. Ng, Alternative strategies in improving the photocatalytic and photoelectrochemical activities of visible light-driven $BiVO_4$: a review, J. Mater. Chem. A. 5 (2017) 16498–16521. https://doi.org/10.1039/c7ta04441k.

[10] S. Meng, T. Ogawa, H. Okumura, K.N. Ishihara, Enhanced photocatalytic activity of $BiVO_4/Bi_2S_3/SnS_2$ heterojunction under visible light, Catalysts. 10 (2020) 1294. https://doi.org/10.3390/catal10111294.

[11] C. Li, P. Zhang, R. Lv, J. Lu, T. Wang, S. Wang, H. Wang, J. Gong, Selective deposition of Ag_3PO_4 on monoclinic $BiVO_4$ (040) for highly efficient photocatalysis, Small. 9 (2013) 3951–3956. https://doi.org/10.1002/smll.201301276.

[12] G. Zhang, X. Du, Y. Wang, H. Wang, W. Wang, Z. Fu, Controllable synthesis of SnS_2 nanostructures with high adsorption and photocatalytic activities, Mater. Sci. Semicond. Process. 64 (2017) 77–84. https://doi.org/10.1016/j.mssp.2017.03.010.

[13] G. Zhao, W. Liu, Y. Hao, Z. Zhang, Q. Li, S. Zang, Nanostructured shuriken-like $BiVO_4$ with preferentially exposed {010} facets: preparation, formation mechanism, and enhanced photocatalytic performance, Dalt. Trans. 47 (2018) 1325–1336. https://doi.org/10.1039/c7dt04431c.

[14] S. Meng, T. Ogawa, H. Okumura, K.N. Ishihara, The effect of potassium chloride on $BiVO_4$ morphology and photocatalysis, J. Solid State Chem. 302 (2021) 122291. https://doi.org/10.1016/j.jssc.2021.122291.

[15] X. Gao, G. Huang, H. Gao, C. Pan, H. Wang, J. Yan, Y. Liu, H. Qiu, N. Ma, J. Gao, Facile fabrication of Bi_2S_3/SnS_2 heterojunction photocatalysts with efficient photocatalytic activity under visible light, J. Alloys Compd. 674 (2016) 98–108. https://doi.org/10.1016/j.jallcom.2016.03.031.

[16] A. Walsh, Y. Yan, M.N. Huda, M.M. Al-Jassim, S.H. Wei, Band edge electronic structure of $BiVO_4$: Elucidating the role of the Bi s and V d orbitals, Chem. Mater. 21 (2009) 547–551. https://doi.org/10.1021/cm802894z.

[17] S. Sun, W. Wang, L. Zhou, H. Xu, Efficient methylene blue removal over hydrothermally synthesized starlike $BiVO_4$, Ind. Eng. Chem. Res. 48 (2009) 1735–1739. https://doi.org/10.1021/ie801516u.

[18] D.P. Jaihindh, B. Thirumalraj, S.M. Chen, P. Balasubramanian, Y.P. Fu, Facile synthesis of hierarchically nanostructured bismuth vanadate: An efficient photocatalyst for degradation and detection of hexavalent chromium, J. Hazard. Mater. 367 (2019) 647–657. https://doi.org/10.1016/j.jhazmat.2019.01.017.

[19] Y.C. Zhang, Z.N. Du, K.W. Li, M. Zhang, Size-controlled hydrothermal synthesis of SnS_2 nanoparticles with high performance in visible light-driven photocatalytic degradation of aqueous methyl orange, Sep. Purif. Technol. 81 (2011) 101–107. https://doi.org/10.1016/j.seppur.2011.07.016.

[20] H.Q. Chen, L.Y. Lin, S.L. Chen, Direct growth of $BiVO_4/Bi_2S_3$ nanorod array on conductive glass as photocatalyst for enhancing the photoelectrochemical performance, ACS Appl. Energy Mater. 1 (2018) 6089–6100. https://doi.org/10.1021/acsaem.8b01146.

[21] I. Shown, S. Samireddi, Y.C. Chang, R. Putikam, P.H. Chang, A. Sabbah, F.Y. Fu, W.F. Chen, C.I. Wu, T.Y. Yu, P.W. Chung, M.C. Lin, L.C. Chen, K.H. Chen, Carbon-doped SnS_2 nanostructure as a high-efficiency solar fuel catalyst under visible light, Nat. Commun. 9 (2018). https://doi.org/10.1038/s41467-017-02547-4.

[22] Z. Zhang, C. Shao, X. Li, Y. Sun, M. Zhang, J. Mu, P. Zhang, Z. Guo, Y. Liu, Hierarchical assembly of ultrathin hexagonal SnS_2 nanosheets onto electrospun TiO_2 nanofibers: Enhanced photocatalytic activity based on photoinduced interfacial charge transfer, Nanoscale. 5 (2013) 606–618. https://doi.org/10.1039/c2nr32301j.

[23] D.K. Ma, M.L. Guan, S. Sen Liu, Y.Q. Zhang, C.W. Zhang, Y.X. He, S.M. Huang, Controlled synthesis of olive-shaped $Bi_2S_3/BiVO_4$ microspheres through a limited chemical conversion route and enhanced visible-light-responding photocatalytic activity, Dalt. Trans. 41 (2012) 5581–5586. https://doi.org/10.1039/c2dt30099k.

[24] X.H. Li, H.Y. Xu, X.T. Zhang, Y.C. Liu, J.W. Sun, Y.M. Lu, Local chemical states and thermal stabilities of nitrogen dopants in ZnO film studied by temperature-dependent x-ray photoelectron spectroscopy, Appl. Phys. Lett. 95 (2009). https://doi.org/10.1063/1.3259644.

[25] S.V.P. Vattikuti, J. Shim, C. Byon, Synthesis, characterization , and optical properties of visible light-driven Bi_2S_3 nanorod photocatalysts, J. Mater. Sci. Mater. Electron. 28 (2017) 14282–14292. https://doi.org/10.1007/s10854-017-7287-6.

[26] L. Xia, J. Li, J. Bai, L. Li, S. Chen, B. Zhou, $BiVO_4$ photoanode with exposed (040) facets for enhanced photoelectrochemical performance, Nano-Micro Lett. 10 (2018) 1–10. https://doi.org/10.1007/s40820-017-0163-3.

[27] H.L. Tan, X. Wen, R. Amal, Y.H. Ng, $BiVO_4$ {010} and {110} relative exposure extent: governing factor of surface charge population and photocatalytic activity, J. Phys. Chem. Lett. 7 (2016) 1400–1405. https://doi.org/10.1021/acs.jpclett.6b00428.

[28] R. Li, H. Han, F. Zhang, D. Wang, C. Li, Highly efficient photocatalysts constructed by rational assembly of dual-cocatalysts separately on different facets of $BiVO_4$, Energy Environ. Sci. 7 (2014) 1369–1376. https://doi.org/10.1039/c3ee43304h.

[29] B. Baral, K. Parida, {040/110} Facet isotype heterojunctions with monoclinic scheelite $BiVO_4$, Inorg. Chem. (2020). https://doi.org/10.1021/acs.inorgchem.0c01465.

[30] H.L. Tan, A. Suyanto, A.T. De Denko, W.H. Saputera, R. Amal, F.E. Osterloh, Y.H. Ng, Enhancing the photoactivity of faceted $BiVO_4$ via annealing in oxygen-deficient condition, Part. Part. Syst. Charact. 34 (2017). https://doi.org/10.1002/ppsc.201600290.

[31] R. Li, F. Zhang, D. Wang, J. Yang, M. Li, J. Zhu, X. Zhou, H. Han, C. Li, Spatial separation of photogenerated electrons and holes among {010} and {110} crystal facets of $BiVO_4$, Nat. Commun. 4 (2013). https://doi.org/10.1038/ncomms2401.

8. Discussion and Prospect for Future

This work aims to improve the photocatalytic activity of $BiVO_4$-based photocatalysts for the RhB photodegradation. The present study demonstrates two main approaches to enhance the photocatalytic performance (RhB photodegradation) of $BiVO_4$-based photocatalysts via hydrothermal/solvothermal method. One utilized KCl as a directing agent during $BiVO_4$ preparation to control the various properties of $BiVO_4$ and produce the shuriken-like $BiVO_4$ (Chapter 4 and 5). Another realized a $BiVO_4$-based composite ($BiVO_4/Bi_2S_3/SnS_2$) by incorporating $BiVO_4$ and SnS_2 through a chemical reaction (Chapter 6). Additionally, further enhanced photocatalytic performance of $BiVO_4$-based composite can be achieved by combining the shuriken-like $BiVO_4$ and SnS_2 (Chapter 7). This chapter discusses the findings identified in both techniques. It also compares photocatalytic activity (RhB photodegradation) of $BiVO_4$-based photocatalysts in this study and their potential application. The last part presents recommendations for future work.

8.1. Discussion of findings

The discussion is organized into two subsections for both techniques: $BiVO_4$ preparation using KCl as a directing agent and preparation of $BiVO_4$-based composite via incorporation with SnS_2.

8.1.1. Preparation of $BiVO_4$ using KCl as a directing agent

This study revealed the shuriken-like $BiVO_4$ with a narrow bandgap exhibited superior photocatalytic degradation of RhB among the samples, mainly due to its high exposed {010} facets (high relative intensity ratio $I_{(040)}/I_{(\bar{1}21)}$). The increase in exposed {010} facets appears to enhance the photocatalytic performance of $BiVO_4$,

which is consistent with many studies [1–7]. Wang et al. [7] and Yao et al. [3] found the photocatalytic activity of $BiVO_4$ for O_2 evolution was enhanced with the increase in exposed {010} facets. However, the {010} facets of $BiVO_4$ are known for the site for reduction reaction, while {110} facets are responsible for oxidation reaction [5,6,8]. At first glance, it seems counter institutive to increase the reduction site ({010} facets) to enhance O_2 evolution (oxidation reaction). However, Tan et al. [6] argued that enlarging the {010} facets allowed a larger number of surfaces available for photogenerated electrons. It facilitated the electron transfer to the {010} facets and suppressed the electron trapping on {110} facets, which led to the loss of photogenerated holes through recombination of electron-hole pair. As a result, the increase in the {010} facets improved both photo-reduction and photo-oxidation efficiency. The high exposed {010} facets are beneficial not only for the O_2 evolution, but also for the degradation of organic dyes, such as methylene blue [1] and RhB [9,10], which are in line with the results found in this study.

The result of this study also found that the KCl concentration used in the precursor could influence the morphology and the {010} facets of $BiVO_4$. Previous studies used $TiCl_3$ [7] and NaCl [11] as directing agents and found that the {010} facets could be controlled by modifying the concentration of the directing agent. Xie et al. [11] claimed that Cl^- ions in the Cl-containing agents played the main role in controlling the {010} facets of $BiVO_4$. Their DFT calculation revealed that the Cl^- ions reduced surface energy of the {010} facets of $BiVO_4$ when the Cl^- ions were adsorbed on the said facets. Thus, more Cl^- ions in the solution suppressed the growth rate in [010] direction, leading to the increase in {010} facets. Therefore, Cl^- ions in KCl could also play a key role, influencing {010} facets in the present study.

Unpon Comparison with the mentioned literature [7,11], Cl^- ions in this study had another function for controlling morphology. It is worth mentioning that the agent containing Cl^- used in the literature [7,11] was added into the precursor at the later stage of $BiVO_4$ preparation, in which tetragonal zircon-type $BiVO_4$ had already formed [12], as described in Chapter 4. In contrast, this study added Cl^-

ions (from KCl) to the precursor of $BiVO_4$ before VO_3^- addition (from NH_4VO_3). Since the BiOCl readily forms by the reaction of Bi^{3+} and Cl^- in water [13], the BiOCl intermediate could form first before Bi^{3+} reacts with VO_3^-. This synthetic route is similar to $BiVO_4$ preparation using $BiCl_3$, containing both Bi^{3+} and Cl^- [9,14]. In this synthetic route, the final morphology of $BiVO_4$ was found to depend on the number of BiOCl (intermediate) particles. Ackermann [15] claimed that the concentration of H_3O^+ ions and Cl^- dictated the formation and dissolution of BiOCl, in turn influencing the number of BiOCl particles in the precursor. The morphology of $BiVO_4$ was drastically changed when Xi and Ye [9] varied the acidity (H_3O^+ ions) of the precursor solution and used $BiCl_3$ (containing Cl^- ions) as a source of Bi^{3+} for $BiVO_4$. In the case of this study, controlling Cl^- concentration could also alter the morphology of $BiVO_4$ because Cl^- ions are another factor affecting the number of BiOCl particles. Therefore, this study suggests that, in addition to the role of controlling {010} facets, Cl^- concentration plays another major role in shaping the final morphology of $BiVO_4$ in various forms, such as rod-like, cruciate, shuriken-like and tabular structures.

Among various morphologies of $BiVO_4$ produced in this study, the shuriken-like structure was found to exhibit the highest photocatalytic degradation of RhB due to its facetted structure that maximizes the relative intensity ratio $I_{(040)}/I_{(\bar{1}21)}$ and exposed {010} facets. This finding is in agreement with that obtained by Zhao et al. [1], producing a similar shuriken-like $BiVO_4$ using ethylenediamine tetraacetic acid disodium (EDTA) as a directing agent in glycerol/water mixed solvent. In fact, many other studies [3,16–20], synthesizing similar cruciate or dendritic structure, often found the structure exhibiting the high relative intensity ratio $I_{(040)}/I_{(\bar{1}21)}$ and high exposed {010} facets of $BiVO_4$. However, a result obtained by Li et al. [21] revealed that if the cruciate or dendritic structure was made by small irregular particles, it would not increase the relative intensity ratio $I_{(040)}/I_{(\bar{1}21)}$. Therefore, it suggests that $BiVO_4$ should either be a single crystal with the exposed {010} facets or a particle consisting of smaller particles with the {010} planes facing the same direction to increase the relative intensity ratio $I_{(040)}/I_{(\bar{1}21)}$.

Furthermore, the results in this work demonstrated that KCl concentration in precursor also influenced the optical properties of $BiVO_4$. The increase in the KCl concentration reduced the bandgap of $BiVO_4$ due to the formation of oxygen vacancies. These results do not match those observed in the previous studies [7,11], in which the bandgap of $BiVO_4$ remained unchanged regardless of differences in Cl^- concentration (in the precursor). This could also be attributed to the different synthetic routes (the order of adding Cl^- ions in the precursor) used in the previous studies and this work. As discussed in Chapter 5, the decrease in bandgap in this study was caused by oxygen vacancies induced by Cl^- ions, which might reduce VO_3^- (V^{5+}) to VO^{2+} (V^{4+}) ions during hydrothermal synthesis. Since the previous study [7,11] added Cl^- ions to the precursor where tz-$BiVO_4$ had already formed [12], there would be few to no VO_3^- ions left to interact with the Cl^- ions; then, oxygen vacancies may not be induced by increasing concentration of Cl^- ions, leading to the unchanging in bandgap of $BiVO_4$.

The present work also found that the concentration of KCl could tune the bandgap of $BiVO_4$ via introduction of oxygen vacancies in $BiVO_4$ during the hydrothermal synthesis. Furthermore, a linear relationship between bandgap and oxygen vacancies in $BiVO_4$ was also discovered. Liu et al. [22] reported a similar linear relationship between bandgap and oxygen vacancies in ZnO thin films, produced via varying the oxygen partial pressure. Thus, it is also possible to modify the bandgap of the $BiVO_4$ sample with the addition of KCl in the precursor by altering oxygen vacancy levels in $BiVO_4$. The results in Chapter 5 demonstrated that oxygen vacancies could be reduced by calcining the sample at a temperature range of 400-600 °C in air (oxygen-rich atmosphere). The result is in line with other works on TiO_2 [23,24], which suggested that oxygen from air could effectively fill the oxygen vacancies in the oxide materials with the increase in temperature, resulting in widening the bandgap of the materials. The current study also found that the $BiVO_4$ sample with relatively low levels of oxygen vacancies could be further induced by thermal treatment in Ar gas (oxygen-deficient atmosphere), which is consistent with an earlier study by Tan et al. [25]. However, the $BiVO_4$ sample with a large number of oxygen vacancies could not be further increased via

calcination in Ar gas. These findings suggest bandgap of $BiVO_4$ can be tunable by both KCl concentration in precursor and calcination conditions via controlling oxygen vacancies in $BiVO_4$.

In this study, besides the main factor (the exposed {010} facets) enhancing the photocatalytic performance (RhB degradation) of $BiVO_4$, some minor factors might also affect the photocatalytic activity of $BiVO_4$. It was found that there was residual BiOCl (XRD and XPS results in Chapter 4) present in the $BiVO_4$ samples, prepared with a high concentration of KCl. Thus, there was a possibility that the residual BiOCl might be able to form BiOCl/$BiVO_4$ composite. He et al. [26] and Song et al. [27] reported in their respective studies that BiOCl/$BiVO_4$ composite exhibited enhanced photocatalytic activity for dye photodegradation. Thus, it might have a minor effect on the photocatalytic activity of the $BiVO_4$ samples in this study. In addition to this, the Cl elements observed in XPS results indicate the presence of Cl in not only BiOCl, but also in $BiVO_4$ powder. Thus, we could not rule out the possibility of Cl^- modification or Cl-doping effect on $BiVO_4$. Li et al. [28] discovered that Cl^- modification on the surface of $BiVO_4$ improved photocurrent density of $BiVO_4$ because it facilitated a carrier transfer and enhanced a charge separation efficiency. Therefore, the effect might also influence the photodegradation of RhB in the present study. Future research may conduct a detailed investigation on the effect of both BiOCl/$BiVO_4$ composite and Cl^- modification on $BiVO_4$ to further explore the benefits of the synthetic technique used in this study.

This study demonstrates the synthetic technique for $BiVO_4$ preparation, using KCl as a directing agent and involving BiOCl intermediate. The technique is useful for controlling not only the morphology of $BiVO_4$ (the exposed {010} facets and particle shape of $BiVO_4$), but also the oxygen vacancies and bandgap of $BiVO_4$. In addition, the oxygen vacancies and bandgap of the as-synthesized $BiVO_4$ could be modified via calcination conditions. Controlling these factors is essential for improving the photocatalytic activity of $BiVO_4$ and designing a high performance $BiVO_4$ for practical use. Moreover, there may be other interesting effects (involving

residual BiOCl and Cl in $BiVO_4$) produced by the mentioned method to be further explored in the future research.

8.1.2. Preparation of $BiVO_4$-based composites via incorporation with SnS_2

The results in Chapter 6 found the photocatalytic activity (RhB degradation) of $BiVO_4$-based composite ($BiVO_4/Bi_2S_3/SnS_2$) was higher than those of the single $BiVO_4$, Bi_2S_3, and SnS_2. Earlier works have also reported that the composite photocatalysts exhibit superior photocatalytic activity [29–32] because the composite interface allows electrons to migrate between photocatalysts, in turn enhancing the charge separation efficiency and suppressing the photoinduced electron-hole recombination [30,33].

The results demonstrated Bi_2S_3 was produced from $BiVO_4$ and SnS_2 during solvothermal synthesis because Bi^{3+} ($BiVO_4$) and S^{2-} (SnS_2) are rather reactive at elevated temperatures to form Bi_2S_3 [34,35]. It was found that the Bi_2S_3 may play the main role in improving the photocatalytic activity (RhB degradation) of the $BiVO_4$-based composite because it might act as a bridge to connect SnS_2 and $BiVO_4$. The results are in agreement with those of previous studies [36–41], which fabricated composites involving Bi_2S_3. Although Bi_2S_3 may be beneficial for the composite, the high content of Bi_2S_3 could act as a recombination center for electron-hole pairs in the composite due to its rapid recombination rate of the photogenerated electron-hole [33,38,41]. This could be the reason that the optimal ratio of $BiVO_4$:SnS_2 for the high photocatalytic performance is rather low (0.03:1) since Bi_2S_3 content rises with the increase in the molar ratio of $BiVO_4$:SnS_2, as evidently shown in the XRD result in Chapter 6.

In this work, the dual Z-scheme model was proposed to explain the possible charge-transfer pathway in the $BiVO_4/Bi_2S_3/SnS_2$ composite. A method used for building the model relied on the individual band energy structure of each photocatalyst and the experimental scavenger test (identifying the reactive oxygen species). This kind of method is widely used by numerous studies [34,35,37,42,43].

However, after forming heterojunction (especially a chemical contact), the properties of the interphase of the composite may be altered. Moreover, B_2S_3 was formed from Bi of $BiVO_4$ and S of SnS_2, hence, there might be vacancies of Bi and S in their respective site at the interphase. Thus, the bandgap of each component of composite may not be the same as it was before the component was incorporated into the composite. Hence, using the bandgap of the single photocatalysts to explain the band energy structure of the composite might not be accurate. However, it is rather difficult to investigate or measure the actual bandgap of composite interphase. As a result, the current method is used with an assumption that the bandgap of each component approximately remains the same after being incorporated into a composite. Although the method might be flawed and far from perfect, it is still a commonly used method to explain the charge-transfer pathway in the composite [34,35,37,42,43] because it is useful to estimate the band energy structure of each semiconductor in the composite and predict the direction of charge migration. Nevertheless, future research may need to develop an effective technique to investigate the electronic properties of the composite interphase in order to construct an accurate representation of the band energy structure of the composite.

The results in Chapter 7 revealed that the shuriken-like $BiVO_4$-based composite exhibited superior photocatalytic activity in RhB degradation, compared with the polyhedral $BiVO_4$-based composite that possesses a wider bandgap and lower exposed {010} faceting. Previous studies [44,45] reported that the photocatalytic activity of the composite depended on the morphology of its individual components. However, since the production of composite in this study involved a chemical reaction, it could not exclude the possibility that some damage has been done to the surface of the shuriken-like $BiVO_4$. Thus, the enhanced photocatalytic degradation of RhB might be attributed to mildly affected sites on {010} facets, which still could accumulate the photogenerated electrons and transfer them to Bi_2S_3. The findings suggest that using a $BiVO_4$ with high exposed {010} facets and narrower bandgap for building $BiVO_4/Bi_2S_3/SnS_2$ composite could further improve the photocatalytic performance (RhB degradation) of the composite.

The present study demonstrates an incorporating technique for producing $BiVO_4/Bi_2S_3/SnS_2$ composite using a chemical reaction between $BiVO_4$ and SnS_2 via solvothermal method. The formation of Bi_2S_3 plays a crucial role in connecting both $BiVO_4$ and SnS_2 to create a dual Z-scheme system, which facilitates electron transfer to enhance charge separation efficiency. As a result, the photocatalytic performance in RhB degradation of the $BiVO_4/Bi_2S_3/SnS_2$ composite has an improvement over those of the single photocatalysts. Moreover, the further enhancement of the photocatalytic activity can be attained by producing the $BiVO_4/Bi_2S_3/SnS_2$ composite, using the $BiVO_4$ with high exposed {010} facets and narrower bandgap. Therefore, these findings could provide a different approach for preparing composite by taking advantage of the chemical reaction between combined photocatalysts.

8.2. Photocatalytic performance (rhodamine B degradation) comparison of $BiVO_4$-based photocatalysts and their potential applications

Among the $BiVO_4$-based photocatalysts synthesized in this thesis, the shuriken-like $BiVO_4$ (S-$BiVO_4$) and the $BiVO_4/Bi_2S_3/SnS_2$ composite with shuriken-like $BiVO_4$ as a source (S-$BiVO_4/SnS_2$) exhibit the highest photocatalytic performance in photodegradation of RhB. It is worth mentioning that the S-$BiVO_4/SnS_2$ composite has a slightly better photodegradation rate (k) than that of the single S-$BiVO_4$ by around 1.2 times. Even though the composite shows better performance, the enhancement over S-$BiVO_4$ is rather small after incorporating with SnS_2. Thus, it may not be worth adding additional steps to produce the S-$BiVO_4/SnS_2$ composite for RhB degradation. Therefore, the S-$BiVO_4$ may be sufficient to use for this purpose in order to avoid an unnecessary increase in time and cost of production. Furthermore, S-$BiVO_4$ may have a potential application in O_2 generation, as its valence band potential is suitable to oxidize water to O_2 [46]. Although it could not reduce H^+, it may still be used as the photoanode in a photoelectrochemical cell for water splitting [47].

On the other hand, the S-$BiVO_4$/SnS_2 composite may be potentially useful in other applications, compared with single S-$BiVO_4$, considering their band energy structures. In this study, the conduction band potential of Bi_2S_3 in the composite was estimated to be slightly more negative than $O_2/O_2^{\bullet-}$ (-0.33 V) due to the scavenger test in Chapter 6; it is consistent with a previous study [48]. In addition, Liu et al. [49] reported the conduction band potential of Bi_2S_3 to be slightly below $2H^+/H_2$ potential (-0.41 V). Thus, the conduction band potential of Bi_2S_3 might locate between $2H^+/H_2$ and $O_2/O_2^{\bullet-}$ potentials and may not be able to generate H_2, as shown in Fig. 8-1. Based on the figure, although $BiVO_4$ alone can oxidize H_2O to produce O_2 due to its valence band (VB) potential being more positive than that of H_2O/O_2, the conduction band (CB) potential of $BiVO_4$ is not negative enough for CO_2 reduction [50,51]. The S-$BiVO_4$/SnS_2 composite, on the other hand, could utilize the CB potential of Bi_2S_3 via the dual Z-scheme process for CO_2 reduction. Previous research [52] has reported the CB potential of Bi_2S_3 was suitable for such a reductive reaction. Additionally, similar to the single S-$BiVO_4$, the S-$BiVO_4$/SnS_2 composite might be potentially used for O_2 evolution, however, it might need a sacrificial electron acceptor such as $AgNO_3$.

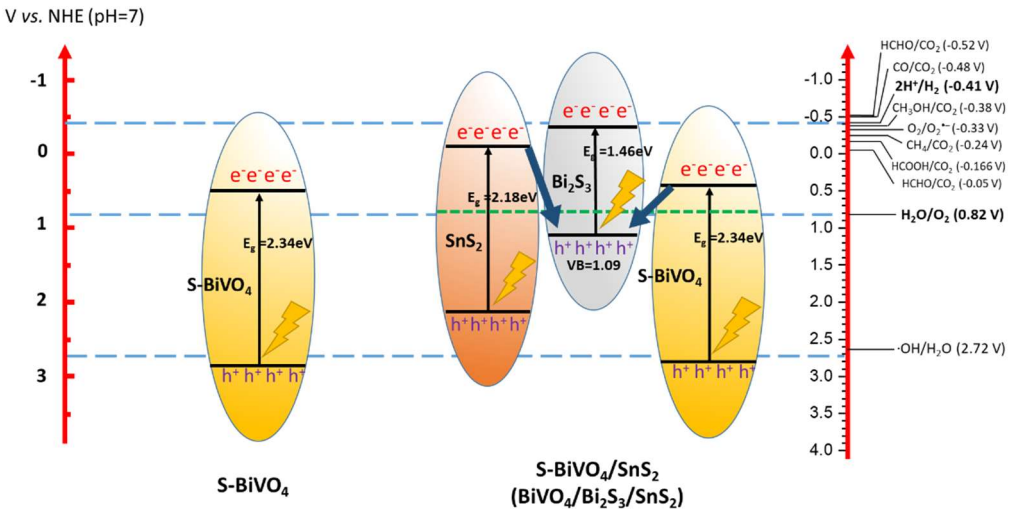

Fig. 8-1. Band energy structures of shuriken-like $BiVO_4$ (S-$BiVO_4$) and $BiVO_4$/Bi_2S_3/SnS_2 (S-$BiVO_4$/SnS_2) composite relative to energy level of the redox couples [53].

This study explores the possibility of the S-$BiVO_4$/SnS_2 composite used in CO_2 reduction. Iwase et al. [54] reported CO_2 reduction to form CO, using a Z-scheme system made of a CoO_x/$BiVO_4$, metal sulfides, and a reduced graphene oxides (RGO) as electron mediator. Compared with the said system, the S-$BiVO_4$/SnS_2 composite may have a slight advantage since the current work demonstrates the direct Z-scheme in the composite without electron mediators. Sasaki [55] suggested that electron mediators may provide negative effects such as light-shielding effect. However, the CO_2 reduction in this work might depend on Bi_2S_3, which is relatively low in quantity in the composite. This issue may be remedied by increasing Bi_2S_3 content via either increasing the molar ratio of $BiVO_4$:SnS_2 or prolonging hydrothermal duration. In addition, although the S-$BiVO_4$/SnS_2 composite may not be able to generate CH_3OH or CO because the conduction band potential of Bi_2S_3 might lack the overpotential for such reduction, it may produce formic acid (HCOOH) or formaldehyde (HCHO) from CO_2 and methanol (as a solvent), as reported by Chen et al. [52]. Moreover, to increase its effectiveness, a metal nanoparticle cocatalyst, such as Pt, Au, Ag, or Rh, may be selectively photodeposited on Bi_2S_3 in the S-$BiVO_4$/SnS_2 composite to engineer active sites for CO_2 reduction [56]. Since the bandgap of Bi_2S_3 is the narrowest among other components in the composite, the suitable light energy can be used to excite only Bi_2S_3 for the selective photodeposition. Base on the analyses, the S-$BiVO_4$/SnS_2 composite may have a potential application in CO_2 reduction, and its effectiveness and photocatalytic activity for CO_2 reduction may be enhanced with some modifications.

8.3. Recommendations for future work

The suggestions for further study are presented as follows:

The photocatalytic degradation of organic pollutants in this study was mainly based on the degradation of rhodamine B. Although it represents one of the most common dye in industrial wastewater, there are other dyes whose properties are different than those of rhodamine B, which in turn could influence the photocatalytic activity of the photocatalyst. Thus, various dyes with different

properties, for example, cationic and anionic dyes, should be used to measure the photocatalytic degradation of pollutants in the presence of photocatalyst in order to determine the effectiveness of the photocatalyst.

The changing in the exposed {010} facets of the $BiVO_4$ samples was indirectly determined by measuring the relative intensity $I_{(040)}/I_{(\bar{1}21)}$ ratio from XRD pattern. Although this technique is effective and used by many research, the direct identification and observation of the {010} facets and other facets of the $BiVO_4$ samples could further improve the understanding of their interaction, which contributes to the enhanced photocatalytic activity of $BiVO_4$.

The incorporation of $BiVO_4$ and SnS_2 via chemical reaction produced Bi_2S_3, resulting in the formation of heterojunction and the enhanced photocatalytic activity, based on the results from various characterization techniques. However, the detailed interfacial study at the contact zone (interphase) has not been done due to difficulty in measurement and observation. Therefore, there is a need for a direct investigation on the morphology, optical properties, and other properties at the interphase of the composite to further promote the understanding of the charge-carrier migration in the composite photocatalyst.

As mentioned in Section 8.2, the shuriken-like $BiVO_4$ and the $BiVO_4/Bi_2S_3/SnS_2$ composite may have potential applications in O_2 production and CO_2 reduction. Thus, future work may extend the measurement of the photocatalytic performance beyond the pollutant degradation to CO_2 reduction and O_2 generation.

As the specific surface area of a photocatalyst can influence its photocatalytic activity, further improvement on the photocatalytic performance of the $BiVO_4/Bi_2S_3/SnS_2$ composite could be realized using nano-sized particles of $BiVO_4$ as a source. However, since the incorporation technique involves producing a third component via a chemical reaction, the size of particles will affect the reaction rate of the materials. Therefore, future research may need to use different synthesis

parameters (molar ratio of $BiVO_4$ to SnS_2, heating duration, and temperature) to obtain the optimal result for the photocatalytic activity of the composite.

Reference

[1] G. Zhao, W. Liu, Y. Hao, Z. Zhang, Q. Li, S. Zang, Nanostructured shuriken-like $BiVO_4$ with preferentially exposed {010} facets: Preparation, formation mechanism, and enhanced photocatalytic performance, Dalt. Trans. 47 (2018) 1325–1336. https://doi.org/10.1039/c7dt04431c.

[2] S.M. Thalluri, M. Hussain, G. Saracco, J. Barber, N. Russo, Green-synthesized $BiVO_4$ oriented along {040} facets for visible-light-driven ethylene degradation, Ind. Eng. Chem. Res. 53 (2014) 2640–2646. https://doi.org/10.1021/ie403999g.

[3] Y. Li, Z. Sun, S. Zhu, Y. Liao, Z. Chen, D. Zhang, Fabrication of $BiVO_4$ nanoplates with active facets on graphene sheets for visible-light photocatalyst, Carbon N. Y. 94 (2015) 599–606. https://doi.org/10.1016/j.carbon.2015.07.042.

[4] L. Xia, J. Li, J. Bai, L. Li, S. Chen, B. Zhou, $BiVO_4$ photoanode with exposed (040) facets for enhanced photoelectrochemical performance, Nano-Micro Lett. 10 (2018) 1–10. https://doi.org/10.1007/s40820-017-0163-3.

[5] R. Li, F. Zhang, D. Wang, J. Yang, M. Li, J. Zhu, X. Zhou, H. Han, C. Li, Spatial separation of photogenerated electrons and holes among {010} and {110} crystal facets of $BiVO_4$, Nat. Commun. 4 (2013). https://doi.org/10.1038/ncomms2401.

[6] H.L. Tan, X. Wen, R. Amal, Y.H. Ng, $BiVO_4$ {010} and {110} relative exposure extent: governing factor of surface charge population and photocatalytic activity, J. Phys. Chem. Lett. 7 (2016) 1400–1405. https://doi.org/10.1021/acs.jpclett.6b00428.

[7] D. Wang, H. Jiang, X. Zong, Q. Xu, Y. Ma, G. Li, C. Li, Crystal facet dependence of water oxidation on $BiVO_4$ sheets under visible light irradiation, Chem. - A Eur. J. 17 (2011) 1275–1282. https://doi.org/10.1002/chem.201001636.

[8] B. Zhang, Y. Xiang, M. Guo, J. Wang, K. Liu, W. Lin, G. Ma, Fabrication of a facet-oriented $BiVO_4$ photoanode by particle engineering for promotion of charge separation efficiency, ACS Appl. Energy Mater. 4 (2021) 4259–4268. https://doi.org/10.1021/acsaem.1c00694.

[9] G. Xi, J. Ye, Synthesis of bismuth vanadate nanoplates with exposed {001} facets and enhanced visible-light photocatalytic properties, Chem. Commun.

46 (2010) 1893–1895. https://doi.org/10.1039/b923435g.

[10] M. Hojamberdiev, G. Zhu, Z.C. Kadirova, J. Han, J. Liang, J. Zhou, X. Wei, P. Liu, Morphology-controlled growth of $BiVO_4$ crystals by hydrothermal method assisted with ethylene glycol and ethylenediamine and their photocatalytic activity, Mater. Chem. Phys. 165 (2015) 188–195. https://doi.org/10.1016/j.matchemphys.2015.09.015.

[11] S. Xie, Z. Shen, H. Zhang, J. Cheng, Q. Zhang, Y. Wang, Photocatalytic coupling of formaldehyde to ethylene glycol and glycolaldehyde over bismuth vanadate with controllable facets and cocatalysts, Catal. Sci. Technol. 7 (2017) 923–933. https://doi.org/10.1039/c6cy02510b.

[12] A. Kudo, K. Omori, H. Kato, A novel aqueous process for preparation of crystal form-controlled and highly crystalline $BiVO_4$ powder from layered vanadates at room temperature and its photocatalytic and photophysical properties, J. Am. Chem. Soc. 121 (1999) 11459–11467. https://doi.org/10.1021/ja992541y.

[13] D. Diemente, Why is bismuth subchloride soluble in acid?, J. Chem. Educ. 74 (1997) 398–399. https://doi.org/10.1021/ed074p398.

[14] X. Zhu, F. Zhang, M. Wang, X. Gao, Y. Luo, J. Xue, Y. Zhang, J. Ding, S. Sun, J. Bao, C. Gao, A shuriken-shaped m-$BiVO_4$/{001}-TiO_2 heterojunction: Synthesis, structure and enhanced visible light photocatalytic activity, Appl. Catal. A Gen. 521 (2016) 42–49. https://doi.org/10.1016/j.apcata.2015.10.017.

[15] M.N. Ackermann, Why is Bismuth Subchloride Soluble in Acid?, J. Chem. Educ. 75 (1998) 523. https://doi.org/10.1021/ed075p523.

[16] L. Chen, J. Wang, D. Meng, X. Wu, Y. Wang, E. Zhong, The pH-controlled {040} facets orientation of $BiVO_4$ photocatalysts with different morphologies for enhanced visible light photocatalytic performance, Mater. Lett. 162 (2016) 150–153. https://doi.org/10.1016/j.matlet.2015.09.138.

[17] Y. Lu, H. Shang, F. Shi, C. Chao, X. Zhang, B. Zhang, Preparation and efficient visible light-induced photocatalytic activity of m-$BiVO_4$ with different morphologies, J. Phys. Chem. Solids. 85 (2015) 44–50. https://doi.org/10.1016/j.jpcs.2015.04.016.

[18] Y. Zhu, M.W. Shah, C. Wang, Insight into the role of Ti^{3+} in photocatalytic performance of shuriken-shaped $BiVO_4$/TiO_{2-x} heterojunction, Appl. Catal.

B Environ. 203 (2017) 526–532. https://doi.org/10.1016/j.apcatb.2016.10.056.

[19] S. Sun, W. Wang, L. Zhou, H. Xu, Efficient methylene blue removal over hydrothermally synthesized starlike $BiVO_4$, Ind. Eng. Chem. Res. 48 (2009) 1735–1739. https://doi.org/10.1021/ie801516u.

[20] C. Regmi, Y.K. Kshetri, R.P. Pandey, S.W. Lee, Visible-light-driven S and W co-doped dendritic $BiVO_4$ for efficient photocatalytic degradation of naproxen and its mechanistic analysis, Mol. Catal. 453 (2018) 149–160. https://doi.org/10.1016/j.mcat.2018.05.008.

[21] D. Li, W. Shi, W. Zheng, Controlled synthesis of m-$BiVO_4$ dendrites for enhanced photocatalytic activity, J. Cryst. Growth. 448 (2016) 93–96. https://doi.org/10.1016/j.jcrysgro.2016.05.028.

[22] H. Liu, F. Zeng, Y. Lin, G. Wang, F. Pan, Correlation of oxygen vacancy variations to band gap changes in epitaxial ZnO thin films, Appl. Phys. Lett. 102 (2013). https://doi.org/10.1063/1.4804613.

[23] W. Yu, F. Chen, Y. Wang, L. Zhao, Rapid evaluation of oxygen vacancies-enhanced photogeneration of the superoxide radical in nano-TiO_2 suspensions, RSC Adv. 10 (2020) 29082–29089. https://doi.org/10.1039/d0ra06299e.

[24] K. Yamada, H. Yamane, S. Matsushima, H. Nakamura, K. Ohira, M. Kouya, K. Kumada, Effect of thermal treatment on photocatalytic activity of N-doped TiO_2 particles under visible light, Thin Solid Films. 516 (2008) 7482–7487. https://doi.org/10.1016/j.tsf.2008.03.041.

[25] H.L. Tan, A. Suyanto, A.T. De Denko, W.H. Saputera, R. Amal, F.E. Osterloh, Y.H. Ng, Enhancing the photoactivity of faceted $BiVO_4$ via annealing in oxygen-deficient condition, Part. Part. Syst. Charact. 34 (2017). https://doi.org/10.1002/ppsc.201600290.

[26] Z. He, Y. Shi, C. Gao, L. Wen, J. Chen, S. Song, BiOCl/$BiVO_4$ p-n heterojunction with enhanced photocatalytic activity under visible-light irradiation, J. Phys. Chem. C. 118 (2014) 389–398. https://doi.org/10.1021/jp409598s.

[27] L. Song, Y. Pang, Y. Zheng, C. Chen, L. Ge, Design, preparation and enhanced photocatalytic activity of porous BiOCl/$BiVO_4$ microspheres via a coprecipitation-hydrothermal method, J. Alloys Compd. 710 (2017) 375–

382. https://doi.org/10.1016/j.jallcom.2017.03.283.

[28] Z. Li, Q. Zhang, X. Chen, F. Yang, D. Wang, L. Liu, J. Ye, Cl-modification for effective promotion of photoelectrochemical water oxidation over $BiVO_4$, Chem. Commun. 56 (2020) 13153–13156. https://doi.org/10.1039/d0cc05334a.

[29] Z. Zhang, C. Shao, X. Li, Y. Sun, M. Zhang, J. Mu, P. Zhang, Z. Guo, Y. Liu, Hierarchical assembly of ultrathin hexagonal SnS_2 nanosheets onto electrospun TiO_2 nanofibers: Enhanced photocatalytic activity based on photoinduced interfacial charge transfer, Nanoscale. 5 (2013) 606–618. https://doi.org/10.1039/c2nr32301j.

[30] Y.C. Zhang, Z.N. Du, K.W. Li, M. Zhang, D.D. Dionysiou, High-performance visible-light-driven SnS_2/SnO_2 nanocomposite photocatalyst prepared via in situ hydrothermal oxidation of SnS_2 nanoparticles, ACS Appl. Mater. Interfaces. 3 (2011) 1528–1537. https://doi.org/10.1021/am200102y.

[31] J. Safaei, H. Ullah, N. Aida, M. Firdaus, M. Noh, M. Fairus, A.A. Tahir, N. Ahmad, M. Adib, Enhanced photoelectrochemical performance of Z-scheme g-$C_3N_4/BiVO_4$ photocatalyst, Appl. Catal. B Environ. 234 (2018) 296–310. https://doi.org/10.1016/j.apcatb.2018.04.056.

[32] N. Kumar, N. Krishnarao, S.A. Singh, Cocatalyst free Z-schematic enhanced H_2 evolution over $LaVO_4/BiVO_4$ composite photocatalyst using Ag as an electron mediator, Appl. Catal. B Environ. 220 (2018) 512–523. https://doi.org/10.1016/j.apcatb.2017.08.082.

[33] X. Li, Y. Li, J. Shen, M. Ye, A controlled anion exchange strategy to synthesize Bi_2S_3 nanoparticles/plate-like $Bi2WO_6$ heterostructures with enhanced visible light photocatalytic activities for Rhodamine B, Ceram. Int. 42 (2016) 3154–3162. https://doi.org/10.1016/j.ceramint.2015.10.105.

[34] C. Yu, K. Wang, P. Yang, S. Yang, C. Lu, Y. Song, S. Dong, J. Sun, J. Sun, One-pot facile synthesis of $Bi_2S_3/SnS_2/Bi_2O_3$ ternary heterojunction as advanced double Z-scheme photocatalytic system for efficient dye removal under sunlight irradiation, Appl. Surf. Sci. 420 (2017) 233–242. https://doi.org/10.1016/j.apsusc.2017.05.147.

[35] J. Wang, J. Jin, X. Wang, S. Yang, Y. Zhao, Y. Wu, S. Dong, J. Sun, J. Sun, Facile fabrication of novel $BiVO_4/Bi_2S_3/MoS_2$ n-p heterojunction with enhanced photocatalytic activities towards pollutant degradation under natural sunlight, J. Colloid Interface Sci. 505 (2017) 805–815.

https://doi.org/10.1016/j.jcis.2017.06.085.

[36] R. Kim, J. Kim, J.Y. Do, M.W. Seo, M. Kang, Carbon Dioxide Photoreduction on the Bi_2S_3/MoS_2 Catalyst, (2019) 1–18. https://doi.org/10.3390/catal9120998.

[37] S.V.P. Vattikuti, C. Byon, Bi_2S_3 nanorods embedded with MoS_2 nanosheets composite for photodegradation of phenol red under visible light irradiation, Superlattices Microstruct. 100 (2016) 514–525. https://doi.org/10.1016/j.spmi.2016.10.012.

[38] Z. Wu, L. Chen, C. Xing, D. Jiang, J. Xie, M. Chen, Controlled synthesis of Bi_2S_3/ZnS microspheres by an in situ ion-exchange process with enhanced visible light photocatalytic activity, J. Chem. Soc. Dalt. Trans. 42 (2013) 12980–12988. https://doi.org/10.1039/c3dt50984b.

[39] G. Ai, R. Mo, Q. Chen, H. Xu, S. Yang, H. Li, J. Zhong, TiO_2/Bi_2S_3 core-shell nanowire arrays for photoelectrochemical hydrogen generation, RSC Adv. 5 (2015) 13544–13549. https://doi.org/10.1039/c4ra15820b.

[40] D.K. Ma, M.L. Guan, S. Sen Liu, Y.Q. Zhang, C.W. Zhang, Y.X. He, S.M. Huang, Controlled synthesis of olive-shaped $Bi_2S_3/BiVO_4$ microspheres through a limited chemical conversion route and enhanced visible-light-responding photocatalytic activity, Dalt. Trans. 41 (2012) 5581–5586. https://doi.org/10.1039/c2dt30099k.

[41] X. Gao, G. Huang, H. Gao, C. Pan, H. Wang, J. Yan, Y. Liu, H. Qiu, N. Ma, J. Gao, Facile fabrication of Bi_2S_3/SnS_2 heterojunction photocatalysts with efficient photocatalytic activity under visible light, J. Alloys Compd. 674 (2016) 98–108. https://doi.org/10.1016/j.jallcom.2016.03.031.

[42] J. Ke, J. Liu, H. Sun, H. Zhang, X. Duan, P. Liang, X. Li, M.O. Tade, S. Liu, S. Wang, Facile assembly of $Bi_2O_3/Bi_2S_3/MoS_2$ n-p heterojunction with layered n-Bi_2O_3 and p-MoS_2 for enhanced photocatalytic water oxidation and pollutant degradation, "Applied Catal. B, Environ. 200 (2017) 47–55. https://doi.org/10.1016/j.apcatb.2016.06.071.

[43] Q.Y. Tang, R. Huo, L.Y. Ou, X.L. Luo, Y.R. Lv, Y.H. Xu, One-pot synthesis of peony-like $Bi_2S_3/BiVO_4$(040) with high photocatalytic activity for glyphosate degradation under visible light irradiation, Chinese J. Catal. 40 (2019) 580–589. https://doi.org/10.1016/S1872-2067(19)63296-1.

[44] Q. Jia, A. Iwase, A. Kudo, $BiVO_4$-Ru/$SrTiO_3$:Rh composite Z-scheme

photocatalyst for solar water splitting, Chem. Sci. 5 (2014) 1513–1519. https://doi.org/10.1039/c3sc52810c.

[45] C. Li, P. Zhang, R. Lv, J. Lu, T. Wang, S. Wang, H. Wang, J. Gong, Selective deposition of Ag_3PO_4 on monoclinic $BiVO_4$(040) for highly efficient photocatalysis, Small. 9 (2013) 3951–3956. https://doi.org/10.1002/smll.201301276.

[46] K. Maeda, Z-scheme water splitting using two different semiconductor photocatalysts, ACS Catal. 3 (2013) 1486–1503. https://doi.org/10.1021/cs4002089.

[47] S.P. Berglund, D.W. Flaherty, N.T. Hahn, A.J. Bard, C.B. Mullins, Photoelectrochemical oxidation of water using nanostructured $BiVO_4$ films, J. Phys. Chem. C. 115 (2011) 3794–3802. https://doi.org/10.1021/jp1109459.

[48] S. Sharma, N. Khare, Sensitization of narrow band gap Bi_2S_3 hierarchical nanostructures with polyaniline for its enhanced visible-light photocatalytic performance, Colloid Polym. Sci. 296 (2018) 1479–1489. https://doi.org/10.1007/s00396-018-4362-3.

[49] C. Liu, Y. Yang, W. Li, J. Li, Y. Li, Q. Chen, In situ synthesis of Bi_2S_3 sensitized WO_3 nanoplate arrays with less interfacial defects and enhanced photoelectrochemical performance, Sci. Rep. 6 (2016) 1–12. https://doi.org/10.1038/srep23451.

[50] B. Xu, A. Zada, G. Wang, Y. Qu, Boosting the visible-light photoactivities of $BiVO_4$ nanoplates by Eu doping and coupling CeO_x nanoparticles for CO_2 reduction and organic oxidation, Sustain. Energy Fuels. 3 (2019) 3363–3369. https://doi.org/10.1039/C9SE00409B.

[51] Y. Park, K.J. Mc Donald, K.-S.S. Choi, K.J. McDonald, K.-S.S. Choi, Progress in bismuth vanadate photoanodes for use in solar water oxidation, Chem. Soc. Rev. 42 (2013) 2321–2337. https://doi.org/10.1039/C2CS35260E.

[52] J. Chen, S. Qin, G. Song, T. Xiang, F. Xin, X. Yin, Shape-controlled solvothermal synthesis of Bi_2S_3 for photocatalytic reduction of CO_2 to methyl formate in methanol, Dalt. Trans. 42 (2013) 15133–15138. https://doi.org/10.1039/C3DT51887F.

[53] W. Tu, Y. Zhou, Z. Zou, Photocatalytic conversion of CO_2 into renewable hydrocarbon fuels: State-of-the-art accomplishment, challenges, and

prospects, Adv. Mater. 26 (2014) 4607–4626. https://doi.org/10.1002/adma.201400087.

[54] A. Iwase, S. Yoshino, T. Takayama, Y.H. Ng, R. Amal, A. Kudo, Water Splitting and CO_2 Reduction under Visible Light Irradiation Using Z-Scheme Systems Consisting of Metal Sulfides, CoO_x-Loaded $BiVO_4$, and a Reduced Graphene Oxide Electron Mediator, J. Am. Chem. Soc. 138 (2016) 10260–10264. https://doi.org/10.1021/jacs.6b05304.

[55] Y. Sasaki, H. Nemoto, K. Saito, A. Kudo, Solar water splitting using powdered photocatalysts driven by Z-schematic interparticle electron transfer without an electron mediator, J. Phys. Chem. C. 113 (2009) 17536–17542. https://doi.org/10.1021/jp907128k.

[56] Y. Bo, C. Gao, Y. Xiong, Recent advances in engineering active sites for photocatalytic CO_2 reduction, Nanoscale. 12 (2020) 12196–12209. https://doi.org/10.1039/d0nr02596h.

9. Conclusion

Photocatalytic performance of $BiVO_4$-based photocatalysts was enhanced via two different techniques. First one was used to control crystal growth, morphology and bandgap of $BiVO_4$ using KCl as a directing agent in hydrothermal synthesis. KCl concentration is found to influence the formation of BiOCl intermediate, which in turn alters the crystal growth and morphology of the final production of $BiVO_4$. In addition, the concentration of KCl in the precursor also introduces the defects which reduces the bandgap of $BiVO_4$. Shuriken-like $BiVO_4$ exhibits the highest photocatalytic degradation of RhB under visible light owing to its high exposed {010} facets and narrow bandgap.

The shuriken-like $BiVO_4$ was calcined at various temperature in different atmospheric conditions (either in air or in Ar gas) to study the defects and optical properties. The defects are found to be oxygen vacancies, which influence the bandgap of $BiVO_4$. Calcining the $BiVO_4$ sample in air reduces the level of oxygen vacancies, subsequently widening the bandgap of the sample, while Ar calcination of the sample retains the level of oxygen vacancies and maintains its bandgap value. Moreover, KCl concentration in the precursor also affects the oxygen vacancies in $BiVO_4$. Therefore, KCl concentration and calcination can be used to control the oxygen vacancies and alter the bandgap of the $BiVO_4$.

Second technique utilized chemical reaction between $BiVO_4$ and SnS_2 via solvothermal synthesis to produce $BiVO_4/Bi_2S_3/SnS_2$ composite. The heterojunction was formed in the composite. The composite with the molar ratio of 0.03:1 ($BiVO_4$:SnS_2) demonstrates the highest photocatalytic activity in RhB degradation among the composites and the single photocatalysts ($BiVO_4$, Bi_2S_3, and SnS_2) in this study. The dual Z-scheme model is proposed to explain the enhanced photocatalytic preformation of the composites with formation of Bi_2S_3 as a key role.

Two $BiVO_4/Bi_2S_3/SnS_2$ composites with different morphologies of $BiVO_4$ (shuriken-like and polyhedral $BiVO_4$) were prepared, using the same incorporation

technique and molar ratio of $BiVO_4$:SnS_2 (0.03:1). Both composites share a lot of similarities in terms of their properties except for morphology and photocatalytic activity. The composite with shuriken-like $BiVO_4$ exhibits superior photocatalytic degradation of RhB, compared with that of the composite with polyhedral $BiVO_4$, attributed to the narrow bandgap and morphology (high exposed {010} facets) of the shuriken-like $BiVO_4$, which might facilitate the charge transfer in the composite. Although the photodegradation rate of RhB for the shuriken-like $BiVO_4$-based composite is only slightly enhanced by 1.2 times that of the single shuriken-like $BiVO_4$, the shuriken-like $BiVO_4$-based composite with the dual Z-scheme process might be able to reduce CO_2. Therefore, the applications of the shuriken-like $BiVO_4$-based composite may potentially extend beyond pollutant degradation to CO_2 reduction.

List of Publications

This thesis is based on following papers:

Peer-reviewed Journal Papers

1. Chapter 4

   S. Meng, T. Ogawa, H. Okumura, K.N. Ishihara,

   "The effect of potassium chloride on $BiVO_4$ morphology and photocatalysis"

   Journal of Solid State Chemistry ***2021****, 302, 122291.*

   (Published on May 21, 2021)

   https://doi.org/10.1016/j.jssc.2021.122291

2. Chapter 5

   S. Meng, T. Ogawa, H. Okumura, K.N. Ishihara,

   "The effect of calcination on optical properties of $BiVO_4$ prepared via hydrothermal route"

   Journal of Solid State Chemistry

   (Manuscript under review, submitted on Aug. 1, 2021)

3. Chapter 6

   S. Meng, T. Ogawa, H. Okumura, K.N. Ishihara,

   "Enhanced photocatalytic activity of $BiVO_4/Bi_2S_3/SnS_2$ heterojunction under visible light"

   Catalysts ***2020****, 10(11), 1294*

   (Published online on November 9, 2020)

   https://doi.org/10.3390/catal10111294

4. Chapter 7

   S. Meng, T. Ogawa, H. Okumura, K.N. Ishihara,

   "Comparison of $BiVO_4/Bi_2S_3/SnS_2$ composites with different morphologies of $BiVO_4$" (Manuscript to be submitted)

International workshop presentation (Oral presentation)

1. Sopheak MENG, **"Synthesis of $SnS_2/Bi_2S_3/BiVO_4$ ternary heterojunction for efficient Rhodamine-B removal under visible light irradiation"**, *5th Japan-ASEAN Science, Technology and Innovation Platform, Work Package 2 (JASTIP-WP2) Annual Workshop,* January 20, 2020, Bangkok, Thailand

2. Sopheak MENG, **"The effect of KCl content on morphology and Photocatalytic performance of $BiVO_4$"**, *6h Japan-ASEAN Science, Technology and Innovation Platform, Work Package 2 (JASTIP-WP2) Annual Workshop,* March 3, 2021, (online workshop).

Appendix A

a. Calculation of $BiCl^-$ concentration at equilibrium (298.15 K and 1 bar) when the amount of KCl increases

Table 1 Standard Gibbs free energies of formation ($\Delta G_f°$) for various species.

Species	$\Delta G_f°$, kJ mol^{-1} (298.15 K and 1 bar)[1]
Cl^- (aq)	-131.23
Cl_2 (g)	0
H_2O (aq)	-237.13
Bi^{3+} (aq)	82.80
BiO^+ (aq)	-146.4
$BiCl_4^-$ (aq)	-481.5
BiOCl (s)	-322.1
VO_3^- (aq)	-783.6
VO^{2+} (aq)	-446.4

Using the Gibbs energies in Table 1, we could obtain the Gibbs energy change ($\Delta G°$) of the reaction. The equilibrium constant (K) was then calculated using the relationship between $\Delta G°$ and K through the following equation (1):

$$\Delta G° = -RTlnK \qquad (1)$$

where $\Delta G°$ is the Gibbs energy change, R is the gas constant (8.314 J mol^{-1} K^{-1}), T is the absolute temperature (298.15 K), and K is the equilibrium constant. The results of the calculation were shown in Table 2.

Table 2 Reactions, Gibbs energy change, equilibrium constant K, and equilibrium expression for the reaction.

Reactions	ΔG° kJ mol^{-1} (298.15 K and 1 bar)	Equilibrium constant K	Equilibrium expression
Bi^{3+} (aq)+ H_2O (l) ⇌ BiO^+ + $2H^+$ (aq)	7.93	0.0408	$\frac{[BiO^+][H^+]^2}{[Bi^{3+}]}$
BiO^+ (aq) + $2H^+$ (aq)+ $4Cl^-$ (aq) ⇌ $BiCl_4^-$ (aq)+ H_2O (aq)	-47.31	19.4×10^7	$\frac{[BiCl_4^-]}{[BiO^+][H^+]^2[Cl^-]^4}$

The total volume of the precursor was adjusted to 30 ml for all samples, and the initial concentrations of Bi^{3+} and Cl^- in the precursor were listed in Table 3. Since the pH of the solution at equilibrium was about 1.8, the concentration of $[H^+]$ is then approximately 0.016 M. Consequently, we can determine the concentration of BiO^+, H^+, Cl^-, and $BiCl_4^-$ at equilibrium (Table 3) using the equilibrium expression in Table 2. The remaining BiO^+ and Cl^- can react with each other and form BiOCl. Therefore, we can conclude that the increase in Cl^- content reduces the amount of BiOCl and raises the $BiCl_4^-$ ions in the solution.

Table 3 Initial concentration and calculated concentration of various species at equilibrium (298.15 K and 1 bar).

Sample	Initial concentration of various species in solution (mol L^{-1})		Concentration of various species in the solution at equilibrium at 298.15 K and 1 bar (mol L^{-1})			
	Bi^{3+}	Cl^-	BiO^+	H^+	Cl^-	$BiCl_4^-$
Bi1	0.033	0.033	0.032	0.016	0.029	0.001
Bi2	0.033	0.067	0.027	0.016	0.045	0.005
Bi3	0.033	0.100	0.022	0.016	0.056	0.011
Bi5	0.033	0.167	0.011	0.016	0.080	0.022

b. Calculation of Gibbs energy change for possible reduced reaction from VO_3^- (V^{5+}) to VO^{2+}(V^{4+}) at equilibrium (298.15 K and 1 bar)

Gibbs energy change (ΔG°) of the reaction is calculated by using the known Gibbs energies of each species in Table 1. The equilibrium constant (K_{eq}) was then calculated using the equation (1):

The reduced reaction from V^{5+} to V^{4+} is expressed in reaction (2):

$$2VO_3^- (aq) + 2Cl^- (aq) + 8H^+ (aq) \rightleftharpoons 2VO^{2+} (aq) + Cl_2 (g) + 4H_2O \qquad (2)$$

$\Delta G° = -11.66$ kJ mol^{-1}, (298.15 K and 1 bar)

$K_{eq} = 110.37$

Reference

[1] D.D. Wagman, W.H. Evans, V.B. Parker, R.H. Schumm, I. Halow, S.M. Bailey, K.L. Churney, R.L. Nuttall, Erratum: The NBS tables of chemical thermodynamic properties. Selected values for inorganic and C1 and C2 organic substances in SI units [J. Phys. Chem. Ref. Data 11, Suppl. 2 (1982)], J. Phys. Chem. Ref. Data. 18 (1989) 1807–1812. https://doi.org/10.1063/1.555845.

Appendix B

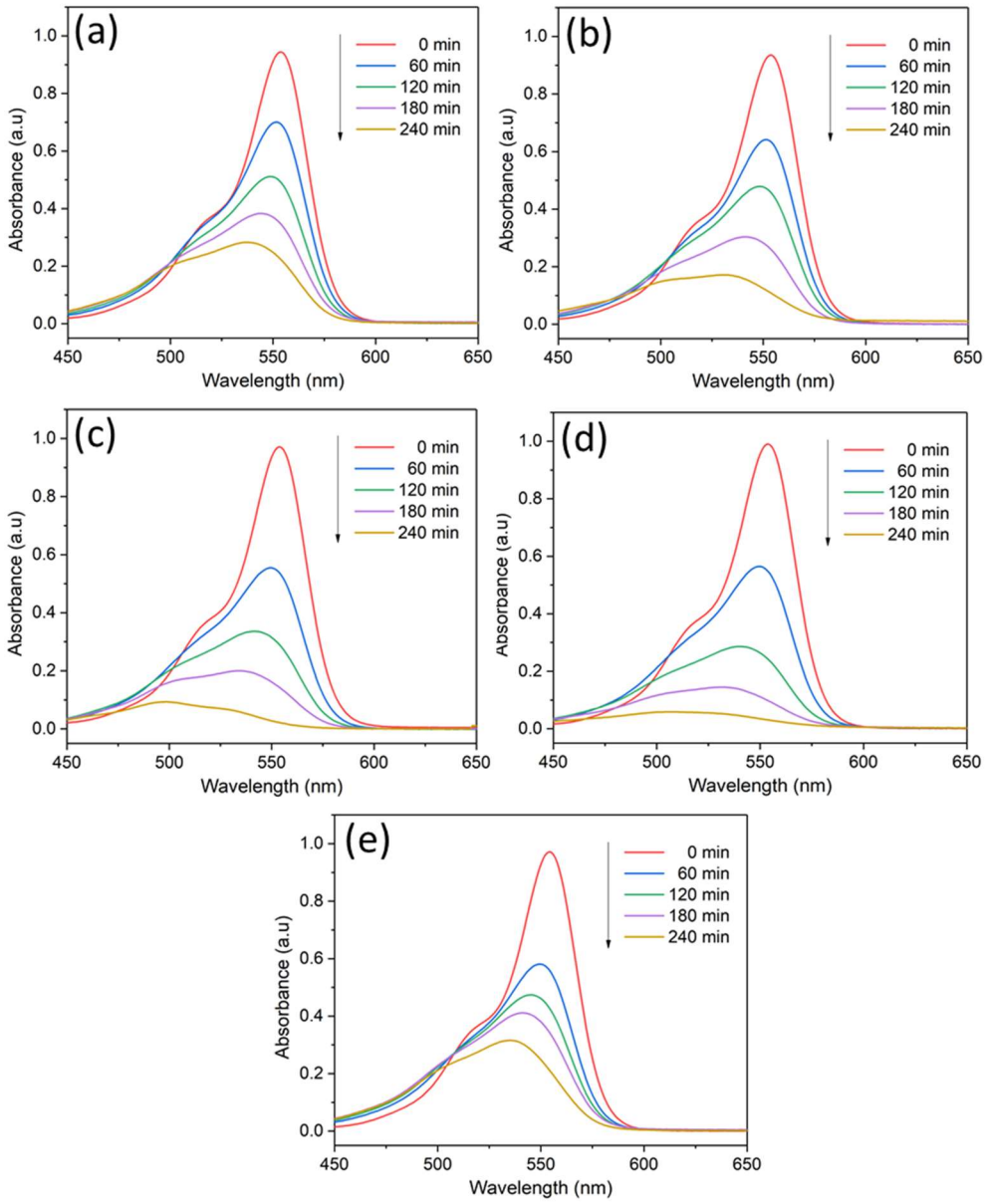

Fig. 1. Absorbance spectra of RhB dye solution (40 ml)as a function of irradiation time under visible light (λ > 420 nm) in the presence of (a) Bi0, (b) Bi1, (c) Bi2, (d) Bi3, and (e) Bi5 samples.

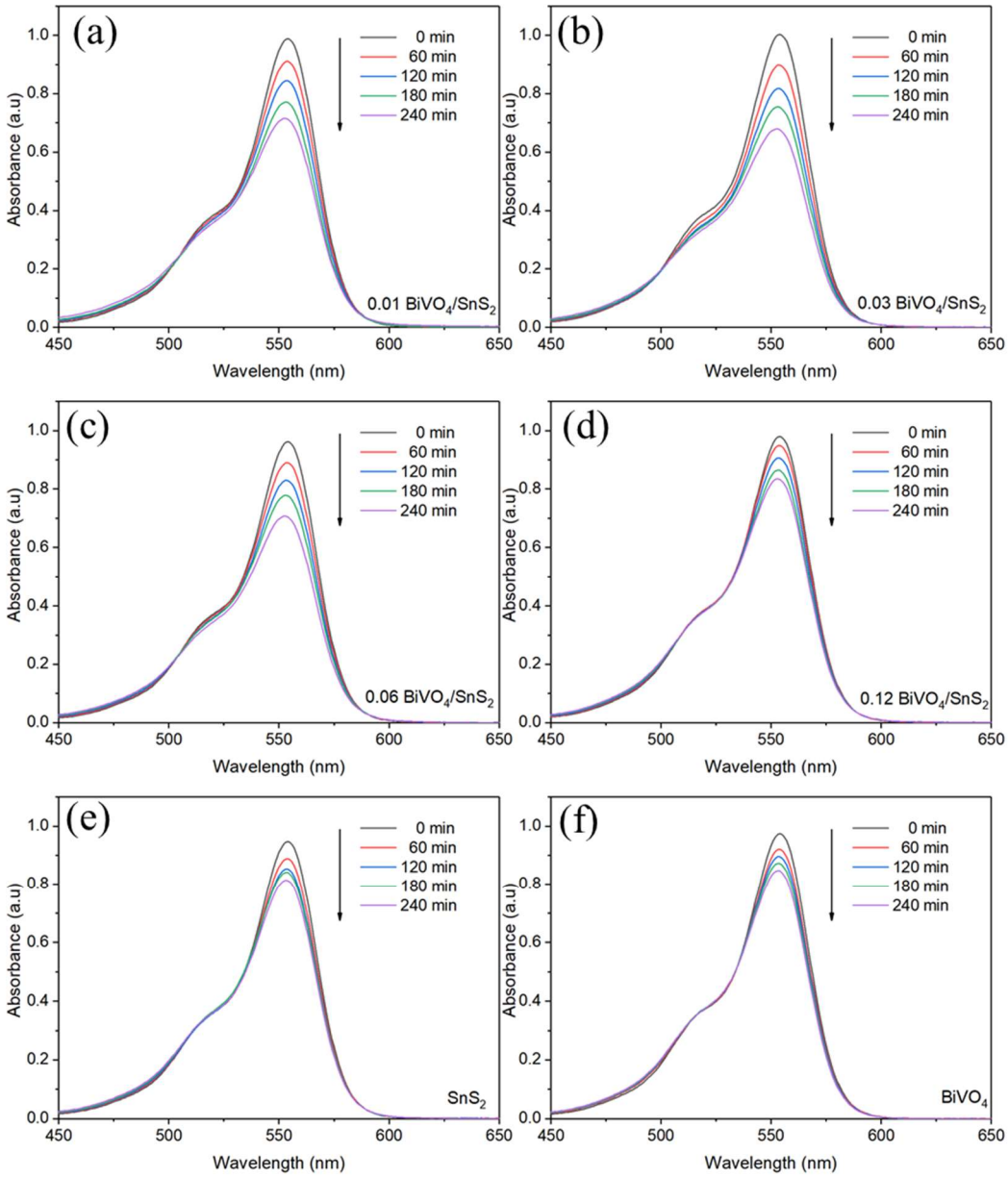

Fig. 2. Absorbance spectra of RhB solution (80 ml) as a function of time during the degradation process under visible light ($\lambda > 420$ nm) in the presence of (a) 0.01 $BiVO_4/SnS_2$, (b) 0.03 $BiVO_4/SnS_2$, (c) 0.06 $BiVO_4/SnS_2$ (d) 0.12 $BiVO_4/SnS_2$, (e) SnS_2, and (f) $BiVO_4$.

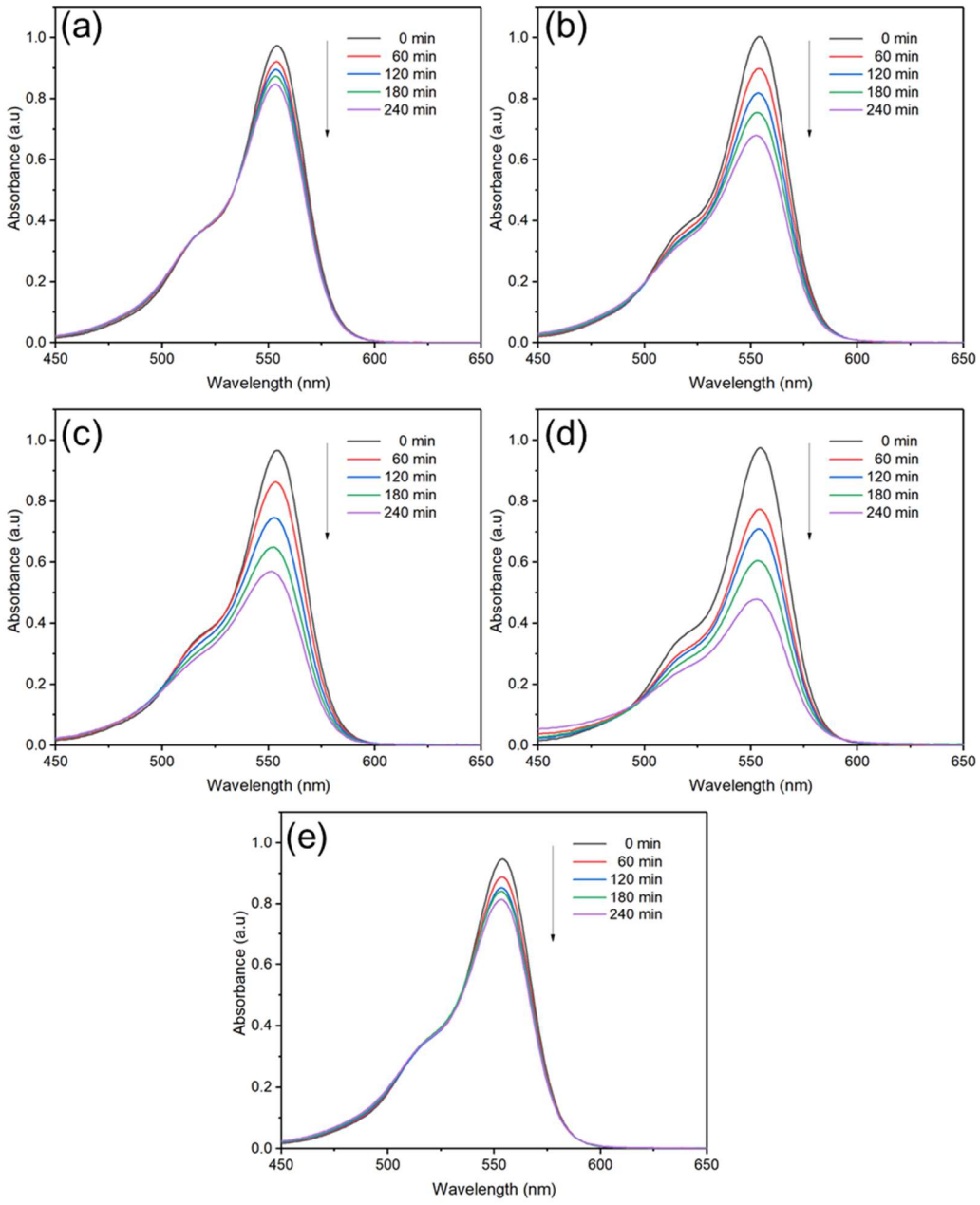

Fig. 3. Absorbance spectra of RhB solution (80 ml) as a function of time during the degradation process under visible light (λ > 420 nm) in the presence of (a) P-$BiVO_4$, (b) P-$BiVO_4$/SnS_2, (c) S-$BiVO_4$ (d) S-$BiVO_4$/SnS_2, and (e) SnS_2.

Appendix C

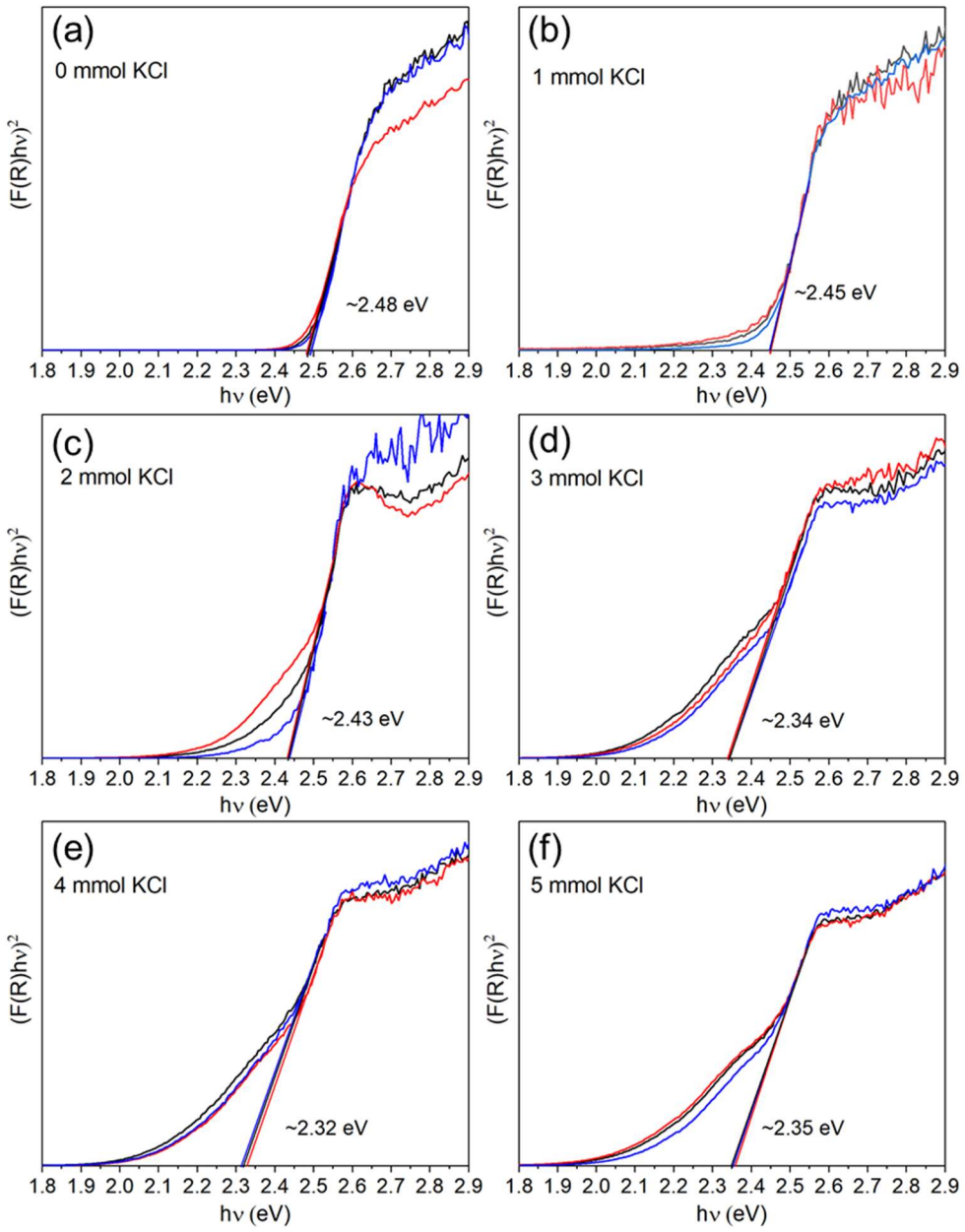

Fig. 1. $(F(R)hv)^2$ vs hv plots and average bandgap values of KCl-$BiVO_4$ with KCl concentrations of (a) 0 mmol, (b) 1 mmol, (c) 2 mmol, (d) 3 mmol, (e) 4 mmol, and (f) 5 mmol. Each sample was measured three times, and the bandgap value of each sample was determined using the average value.

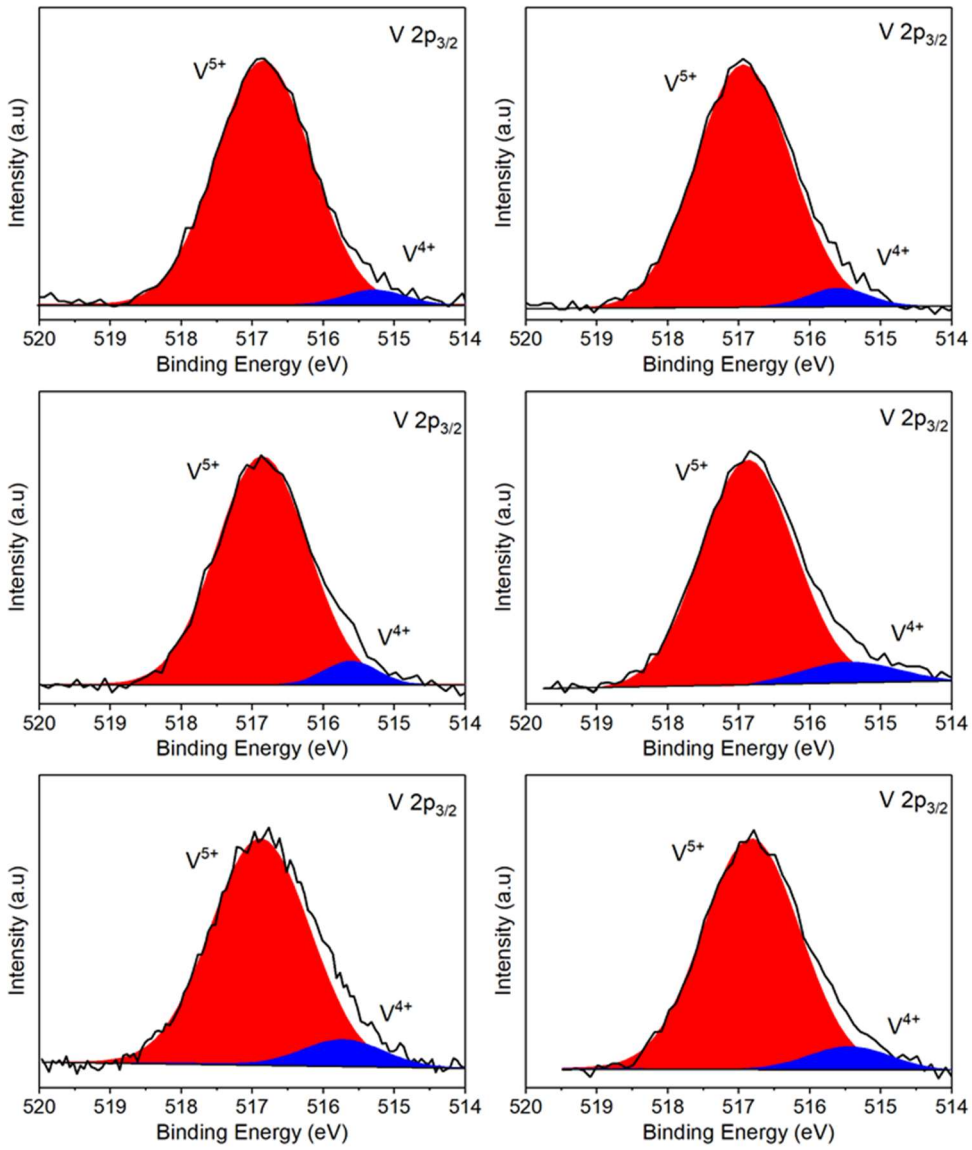

Fig. 2. High-resolution XPS spectra of V $2p_{3/2}$ of KCl-$BiVO_4$ samples with KCl concentration of (a) 0 mmol, (b) 1 mmol, (c) 2 mmol, (d) 3 mmol, (e) 4 mmol, and (f) 5 mmol.

Appendix D

Fig. 1 shows Tauc's plots of materials using either n = 1 (direct transition) or n = 4 (indirect transition) in equation 3.2. The estimated bandgap values of $BiVO_4$, SnS_2, and 0.03 $BiVO_4/SnS_2$ (n = 1, direct transition) are 2.38 eV, 2.18 eV, and 2.17 eV, respectively. These values are closed to those of pure $BiVO_4$ (2.38–2.48 eV) and pure SnS_2 (~2.2 eV) reported by earlier studies [1-5]. On the other hand, if n = 4 (indirect transition) is used, the bandgap values are smaller and not matched with those of previous reports [1-5]. It indicates that n = 1 is more suitable to estimate the bandgap of the samples.

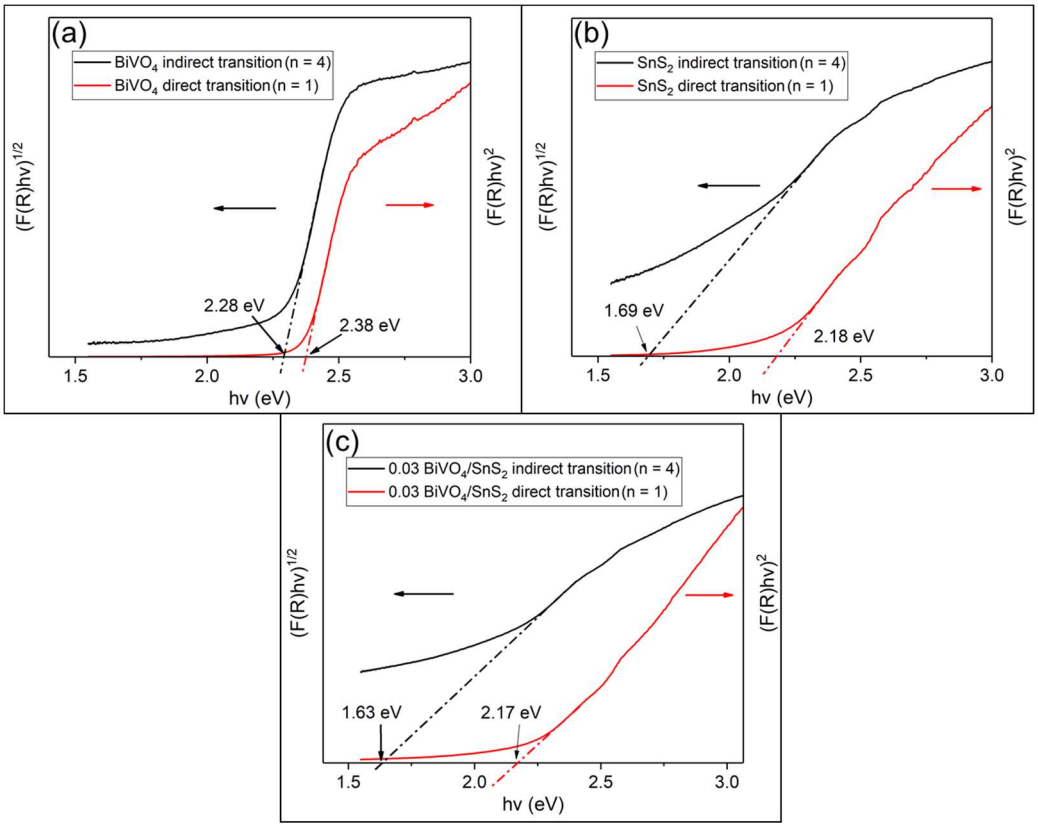

Fig. 1. Tauc's plot using n = 1 (direct bandgap) and n = 4 (indirect bandgap) of (a) pure SnS_2, (b) pure $BiVO_4$, and (c) 0.03 $BiVO_4/SnS_2$ ($BiVO_4/Bi_2S_3/SnS_2$).

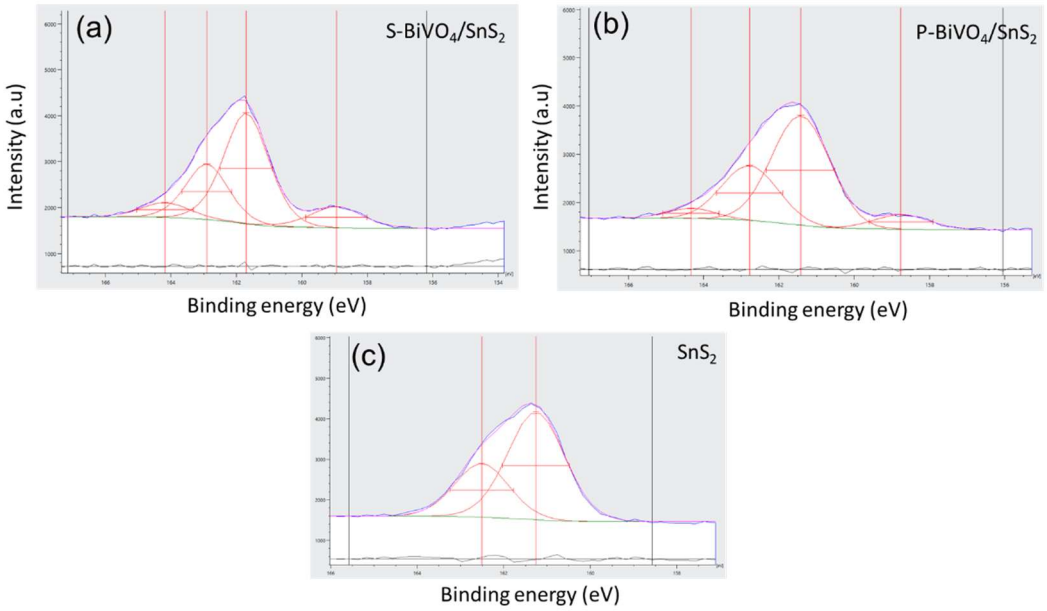

Fig. 2. High resolution XPS spectra of S 2p orbitals with peak fittings of (a) S-$BiVO_4/SnS_2$, (b) P-$BiVO_4/SnS_2$, and (c) SnS_2. S-$BiVO_4/SnS_2$ is $BiVO_4/Bi_2S_3/SnS_2$ with shuirken-like $BiVO_4$, and P-$BiVO_4/SnS_2$ is $BiVO_4/Bi_2S_3/SnS_2$ with polyhedral $BiVO_4$.

Reference

[1] Z.Y. Bian, Y.Q. Zhu, J.X. Zhang, A.Z. Ding, H. Wang, Visible-light driven degradation of ibuprofen using abundant metal-loaded $BiVO_4$ photocatalysts, Chemosphere. 117 (2014) 527–531. https://doi.org/10.1016/j.chemosphere.2014.09.017.

[2] S. Tokunaga, H. Kato, A. Kudo, Selective preparation of monoclinic and tetragonal $BiVO_4$ with scheelite structure and their photocatalytic properties, Chem. Mater. 13 (2001) 4624–4628. https://doi.org/10.1021/cm0103390.

[3] G. Zhao, W. Liu, Y. Hao, Z. Zhang, Q. Li, S. Zang, Nanostructured shuriken-like $BiVO_4$ with preferentially exposed {010} facets: Preparation, formation mechanism, and enhanced photocatalytic performance, Dalt. Trans. 47 (2018) 1325–1336. https://doi.org/10.1039/c7dt04431c.

[4] Y.C. Zhang, Z.N. Du, K.W. Li, M. Zhang, Size-controlled hydrothermal synthesis of SnS_2 nanoparticles with high performance in visible light-driven photocatalytic degradation of aqueous methyl orange, Sep. Purif. Technol. 81 (2011) 101–107. https://doi.org/10.1016/j.seppur.2011.07.016.

[5] N.G. Deshpande, A.A. Sagade, Y.G. Gudage, C.D. Lokhande, R. Sharma, Growth and characterization of tin disulfide (SnS_2) thin film deposited by successive ionic layer adsorption and reaction (SILAR) technique, J. Alloys Compd. 436 (2007) 421–426. https://doi.org/10.1016/j.jallcom.2006.12.108.